CLEANING PRINCIPLES IN AUTOMATIC DISHWASHERS

By

Raúl Pérez Mohedano

A thesis submitted to the University of Birmingham for the degree of Doctor of Engineering

Department of Chemical Engineering

College of Engineering and Physical Sciences

University of Birmingham

June 2015

ABSTRACT

This thesis aims to illustrate and expand the in-depth knowledge required to better understand the wash process occurring inside automatic dishwashers (ADWs) by studying the different mechanical and chemical factors involved.

The project started with the analysis of the water motion via Positron Emission Particle Tracking (PEPT). Tests showed that the initial distribution of water occurs via coherent jets from the nozzles in the spray arms. From a particular position, a jet follows a defined trajectory that can be estimated by using trigonometric principles. Also, these impact locations only represent a small fraction of the inner volume of the appliance. A mathematical model was then built to investigate the design factors associated with this phenomenon. Three dimensionless numbers were defined: the time efficiency factor (τ_{vis}) to evaluate the time a specific jet is impacting a crockery element; the impact length efficiency factor (δ) to measure the coverage produced; and the overall efficiency parameter (α) that combines both previous factors.

Egg yolk was selected as the soil material to study. Experiments in small scale were done using the scanning Fluid Dynamic Gauge (sFDG). By applying Partial Least Squares (PLS) methodology, temperature and mainly pH were identified as the main contributors to the initial hydration-swelling. Enzyme level, the frequency factor (ratio of time an external mechanical action is applied over the sample), and again temperature, showed a noticeable effect during removal. A novel algorithm was introduced to model the behaviour observed. Swelling was described using a non-linear partial differential equation. That allowed the introduction of 'theoretical layers' (number of virtual layers in which the soil thickness is divided). sFDG experiments identified two different mechanisms of cleaning: shear stress removal and soil dissolution. Both were modelled empirically and incorporated to the algorithm. The 'theoretical layers' previously defined were removed over time as cleaning occurred. Therefore, the simulations of cleaning and thickness changes over time were possible.

Finally, an image analysis system was designed to online evaluate cleaning in ADWs. Results were compared with simulations performed from the swelling-removal algorithm. Good predictions were obtained for most of the cases studied indicating the success in the development of a first 'full-scale' predictive model.

ACKNOWLEDGEMENTS

I will never forget that morning in late September 2010 when I left Spain in order to start the amazing journey that has been this Engineering Doctorate. Many days have passed since then in which I have worked hard, learnt more and even most importantly met fabulous people.

I would like to start thanking Serafim Bakalis, Richard Greenwood and Carlos Amador for giving me this opportunity. They have been really helpful during this period, both personally and professionally, and my gratitude will always be with them. In extension, I would like to thank Anju Brooker and Zayeed Alam from Procter & Gamble and specially Nathalie Letzelter who has been the best industrial supervisor I could ever have had. Thanks for all the patient and good advice. Thanks as well to Chad T. VanderRoest and Blair D. Mikkelsen from Whirlpool Corporation.

I wish to also dedicate some words to my colleagues and staff from the Department of Chemical Engineering at the University of Birmingham and from the ADW department in Procter & Gamble Newcastle Innovation Centre. It has been a real pleasure to work with you and to share precious moments and conversations. Borja, Jon, Isa, Luke, Flora and the rest of the Eng.D/PhD guys, thanks for all the fun during my stay at the university in Birmingham. Elena, Olgun, Emilio, Camilo, Iván, Edu, Pepe, Sarah, Graham, Nina, thanks for the same in Newcastle.

I would not have reached this moment in my life if it were not for my friends back home in Plasencia. Friends are the family you choose, and I could not have taken a better decision in my life. Álvaro, Laura, Juanny, Guille, Paula, Alberto, Dami, Macarena, Mario, Isa, Rocio, Marta, Alba, you will always be part of my life-journey and hopefully all my successes to come. I must say the same to Laura, Julia, Rubén and Amanda in Salamanca.

As per my family, I could not be luckier. All the support and affection they always show me has kept me going throughout these years. This is dedicated to my grandparents, Agapito and Julia

and Eusebio and Milagros. I feel very lucky to get to this stage and to still be able of sharing these experiences with them. They have been an example of resilience, care and love for the family. All my gratitude goes as well to my aunts, uncles and cousins from both the Perez and Mohedano's sides. Thanks as well to Fernando for his continuous support. Lastly, I wish to dedicate a special memory to my aunt Herminia to whom I could not say goodbye.

This is also dedicated to my dad, Pedro, who taught me to be passionate and to aim for my best in any work to be done since I was a child. He also got blessed with a daughter, Lara, after my first year in the UK. I hope I can set a good example to her.

Nacho, brother, this is also for you. You are the most talented person I know and growing-up with you has been the best experience ever. Thank you.

Finally, this is dedicated to two really important persons in my life. Irene, I met you during this journey and wish that this is just the beginning of many stories together. Thank you for all the support while writing this thesis, for all the love you give me and most importantly for the great memories already shared. Isabel, madre, you have always been an example to me. You have showed me the most important things in my life and have always been with me in the good and not so good moments. I have no words to express all the love I have for you and I could never do enough to give you back everything you have given me. Thanks.

And thanks to you, reader, to find interest in my research. Hope you enjoy the reading.

NOMENCLATURE

Symbol

a	Nozzle-sample surface separation.
A	Cross sectional area.
C	Mass concentration expressed as dry basis moisture content (water mass uptake / dry sample mass).
C_0	Initial moisture content (water mass at 'time 0'/ dry sample mass).
d	Separation between plates.
d_c	Characteristic dimension of a rectangular duct.
dir_x	x-axis direction vector component.
dir_y	y-axis direction vector component.
dir_z	z-axis direction vector component.
d_o	Duct diameter.
d_p	Tracer diameter.
D_{cr}	Diameter of a crockery element.
D_{PL}	Diamater of a plate.
D_{DW}	Depth of a dishwasher.
D_{NZ}	Nozzle diameter.
D	Generic effective diffusion coefficient.
D_0	Maximum effective diffusion coefficient.
D_F	Effective diffusion coefficient for Fick's equation.
D_L	Effective diffusion coefficient for linear poroelasticity theory.
D_{NL}	Effective diffusion coefficient for non-linear poroelasticity theory.
E_A	Activation energy.
f	Frequency function. Step function (0 or 1).
F	Deformation gradient.
g	Gravitational acceleration.
G_{SM}	Shear modulus.
G_{FE}	Gibbs free energy.
h	Height.
h_0	Initial thickness. Thickness at time 't=0'.
h_{dry}	Sample thickness at dry state.
$h(t)$	Thickness at time 't'.
$\overline{h(t)}$	Normalised thickness at time 't'.
h_∞	Thickness at equilibrium.
H_{cr}	Height of a crockery element.
H_{DW}	Height of a dishwasher.
i	Counter.
J_z	Diffusion flux.

k, k’	Constants incorporating characteristics of macromolecule and penetrant system.
k_{ds}	Removal rate by soil dissolution.
k_{ss}	Removal rate by shear stress action.
L_d	Length of a rectangular duct.
L_{impact}	Impact distance on plates.
$\dot{m}$	Mass flow rate.
M_0	Initial sample mass. Sample mass at time ‘t=0’.
M_{dry}	Dry sample mass.
$M(t)$	Total sample mass at time ‘t’.
$\overline{M(t)}$	Normalised sample mass at time ‘t’.
M_∞	Total sample mass at equilibrium (t=∞).
n, n’	Diffusional exponents.
N	Number of polymer chains per unit volume. (nº chains/m^3).
Nt_s	Normalised start time of application of shear within an interval.
Nt_e	Normalised end time of application of shear within an interval.
P	Pressure.
Q	Volumetric flow rate in the tube.
r	Radial distance.
R	Gas constant.
R^2	Coefficient of determination.
R_{FJ}	Film jump radius.
R_{NZ}	Radial nozzle position.
R_{PL}	Radial plate position.
*R	Nozzle-Plate relative position.
R_w	External circumferential radius.
s	Nominal stress.
St	Stokes number.
S	Swelling function.
SS	Shear Stress function.
SD	Soil Dissolution function.
t	Time.
t_s	Start time of application of shear within an interval.
t_e	End time of application of shear within an interval.
t_{vis}	Time travelling in vision area.
T	Temperature.
T_{impact}	Time impacting plates.
v	Fluid velocity.
W	Free energy function of the gel.
W_{DW}	Width of a dishwasher.
W_d	Width of a rectangular duct.

W_G	Gravity flow film width.
W_R	Rivulet flow film width.
W_s	Width of a surface.
x,y,z	Cartesian coordinates.
x_{impact}	Impact locations on x-axis
y_{impact}	Impact locations on y-axis
z_{impact}	Impact locations on z-axis
x_{PL}	Width plate position.
y_{PL}	Depth plate position.
z_{PL}	Height plate position.
z_{nz}	Height nozzle position.
Z	Frame at z-axis.

Greek Symbols

α	Overall efficiency.
$\beta\ (\beta_1; \beta_2)$	Angular position of a nozzle at any time.
β_{in}	Angle at which a nozzle enters the defined vision area.
β_{out}	Angle at which a nozzle exits the defined vision area.
δ	Effective impact length.
Γ	Wetting rate
Δt	Time step.
Δz	Thickness step.
θ_{jet}	Theta angle (x-y angle)
λ	Stretch in uniaxial direction (thickness at time 't' / dry state thickness).
λ_0	Initial stretch in uniaxial direction – Initial swelling ratio (initial thickness / dry state thickness).
λ_∞	Stretch at equilibrium – Equilibrium swelling ratio (equilibrium thickness / dry state thickness).
μ_0	Chemical potential at the initial state.
$\hat{\mu}$	Chemical potential of the solvent in the environment.
μ	Chemical potential of the gel.
μ_f	Fluid viscosity.
ρ_{jet}	Rho angle (radius-z angle)
ρ_s	Tracer density.
ρ_{WS}	Density of the wash solution.
τ	Characteristic time scale of diffusion.
τ_p	Particle response time.
τ_f	Fluid response time to an external disturbance.
τ_{vis}	Effective impact time in vision area.
τ_{lap}	Effective impact time per lap.

τ_{wall}	Shear stress imposed at the sample surface.
υ	Poisson's ratio (measurement of stretch changes).
υ_i	Time length of the interval.
χ	Flory-Huggins parameter (interaction between the solvent and the polymer).
ω	Spray arm rotation rate.
Ω	Volume of a solvent molecule.

Abbreviations

ADW	Automatic Dishwasher.
AHAM	Association of Home Appliance Manufacturers.
ß-lg	ß-lactoglobulin.
CFD	Computational Fluid Dynamics.
CFT	Centre For Testmaterials.
CIE	Commission on Illumination (as stands for the original French).
CIP	Cleaning In Place.
DAED	Diacetyl ethylene diamine
DFBI	Dynamic Fluid Body Interaction.
DNA	Deoxyribonucleic acid.
DOE	Design Of Experiments.
HDL	High-Density Lipoproteins.
LDL	Low-Density Lipoproteins.
NMR	Nuclear Magnetic Resonance.
PAP	Phthalimidoperhexanoic acid
PDE	Partial Differential Equation.
PEPT	Positron Emission Particle Tracking.
PLS	Partial Least Squares.
PVA	Polyvinyl alcohol.
RGB	Red-Green-Blue.
RS	Response Surface.
sFDG	Scanning Fluid Dynamic Gauge.
SRI	Stain Removal Index.
STTP	Sodium Tripolyphosphate
TACN	1,4,7-triazacyclononane
TAED	Tetraacetyl ethylene diamine
VIP	Variable Importance Plot.
VOF	Volume of Fluid.
WPI	Whey Protein Isolate.

CONTENTS

LIST OF TABLES

LIST OF FIGURES

CHAPTER 1

INTRODUCTION

1.1. CONTEXT

Since the last half of the 20th century, the use of household appliances has increased considerably. They have helped with daily home tasks and have contributed to a more efficient use of time. According to a recent study of consumers in the UK, the use of automatic dishwashers shows important advantages in time and water savings (Berkholz *et al*., 2010). For a standardised load (EN 50242), the study reported a mean water and energy consumption of 49.2 (±27.9) litres and 1.7 (±1.0) kWh for hand washing, while for automatic dishwashing these values were reduced to 13.2 (±1.7) litres and 1.3 (±0.1) kWh. Time spent to load and unload the dishes to the appliance was 9 minutes on average. On the contrary, 60 minutes were required to completely clean them by hand.

It is estimated that 42% of homes in the UK have an automatic dishwasher (Mintel Group, 2011). If there are approximately 25 million homes (BBC, 2005), and it is assumed that a complete washing cycle is run daily with an estimated use of water of 13 litres, the amount of water used per year reaches approximately 50 millions m^3. This is equivalent to the volume of 13,000 Olympic swimming pools. Thus, important costs and environmental benefits will be achieved by reducing the amount of water, chemistry or waste produced during a typical cleaning cycle.

Despite its common use, cleaning processes occurring inside automatic dishwashers (ADW) are not simple nor well understood. Scientific information related to dishwashers is scarce and mostly associated to energy consumption and water savings (Asteasu *et al*., 1993; De Paepe *et al*., 2003; Weiss *et al*., 2010). Dishwashers are complex systems in which a combination of chemistry, temperature, water flow and inner properties of soils are evolving dynamically during a wash cycle. Four areas can be identified: (1)dishwasher design and operation parameters, (2)dishwasher load and type, (3)types of food soils and (4)detergent formulation. Water represents the key element linking all four areas together. It is responsible for influencing the total cleaning time as it distributes detergent components and provides the mechanical force to remove soils. A detailed study of the characteristics of an ADW is necessary to build the in-depth knowledge and fully understand the wash process.

1.2. PROJECT OBJECTIVES

The project aims to reduce the existing gap in current knowledge for a typical cleaning cycle in automatic dishwashing. The development of new tools, methods and models will help the optimisation and integration of mechanical and chemical factors involved. More specifically, project deliverables are:

1. To describe water motion phenomena. The understanding of flow fields and water mechanical action inside an ADW is a fundamental stage to increase current knowledge.
2. To understand and model the influence of mechanical design factors on water distribution. Highlighting current design constraints will help to establish action steps to optimise chemical formulation and mechanical design.
3. To use existing tools or to develop new ones to analyse cleaning online. This aims to incorporate time as a factor in the analysis of cleaning performance within ADW. Current cleaning evaluation is based on measurements at the end of the cleaning cycle, thus no information is collected during the process.
4. To develop fundamental and statistical cleaning models incorporating all physical and chemical factors highlighted as important. The integration of mechanical and chemical parameters and the use of a theoretical background will help to understand their interactions and influence at each stage of a typical cleaning cycle.

1.3. RELEVANCE FOR INDUSTRY

A first evaluation of physical and chemical aspects in a typical ADW wash cycle reveals a clear need for optimisation. Appliance manufacturers design cleaning cycles to give the optimum mechanical performance with very little consideration on the chemical aspect of cleaning. Moreover, detergent companies design current formulations in a way that all chemical agents are released together once the tablet dispenser opens. In addition, drain stages are frequent during typical wash cycles, thus chemistry added is eliminated to a large degree. The carryover of wash solution after a drainage process is typically between 0.3 to 0.5 litres (Letzelter, N. (2015, Personal communication). Inefficiencies arise as the integration of chemical and

mechanical actions is not done in parallel. There are multiple appliances manufacturers developing unique appliances' designs and cycles, while different detergent companies develop their own formulated products. However, there is no combined front-to-end design process. As a result, an optimum performance is hard to achieve.

A similar analogy is found in computer industry. Multiple hardware providers (HP, Acer, Lenovo, Samsung…) need software developers (Windows, Linux) to work correctly. The performance optimisation in this environment is complex as hardware components need to interact with software elements, each of them designed independently. In this context, appliances manufacturers could be seen as hardware providers while detergent companies as software suppliers. Both are required to perform a complete cleaning of the toughest soils found.

Additionally, industry standardised cleaning tests (AHAM, 1992) only evaluate the performance of an appliance or detergent once the cleaning cycle is finished. Timescale is not considered. Therefore, the introduction of time as a factor and the necessity of understanding the limitations and interactions of mechanical and chemical components become obvious.

1.4. STRUCTURE OF THIS DISSERTATION

Chapter 2 reviews the state-of-art in current automatic dishwashing technology. It explains the stages commonly found in a wash cycle, the main features of an ADW and the future trends in industry. The literature review also focuses on cleaning mechanisms and principles. From a mechanical perspective, impingement jets are explained. Fundamentals on the characteristics of different soils, main components included in current formulated detergents and their relation to mass transfer and chemical reaction phenomena leading to removal are commented as well.

Chapter 3 focuses on the materials and methodology used during the realisation of the experimental work. It describes the commercially available ADW considered as the unit operation to study. A technical egg-yolk soil is also introduced as a representative protein-based stain typically used in product development tests. Different research techniques are also presented. Positron Emission Particle Tracking (PEPT) is described as the technique selected

to analyse water motion in a typical wash cycle. Data processing is explained on a step-by-step basis as a particular approach is considered. Its results support a Computational Fluid Dynamic (CFD) model developed by the appliance manufacturer. CFD methodology is also explained. Scanning Fluid Dynamic Gauge (sFDG) is introduced as a small-scale technique to study swelling and removal mechanisms in protein-based soils. In parallel, gravimetric studies are considered to support sFDG findings. The statistical methodology based on Partial Least Squares (PLS) method to develop dynamic models is also presented. Finally, a waterproof camera used for the online evaluation of cleaning inside an ADW is introduced. Experimental conditions selected and operational procedures are described for each of the techniques given.

Chapter 4 begins the experimental work section with the description of water motion using Positron Emission Particle Tracking (PEPT) as a technique. Results show the typical water pattern produced as described by the motion of the radioactive tracer. Impingement jets trajectories are characterised. Velocity flow fields are given in the form of Eulerian contour plots and different factors such as pump speed, packing and detergent used are studied. Computational Fluid Dynamics data is also compared with PEPT data. The concluding discussion establishes the limitations of both techniques (PEPT and CFD) and shows the foundational principles of current automatic dishwashing processes.

Chapter 5 describes the development of a mathematical model to understand the influence of the main mechanical design parameters on water distribution via impingement jets. The chapter presents the basic principles of ADW's design by applying geometry and trigonometry fundamentals. The assumptions made are based on results provided from PEPT experiments. The methodology developed includes the identification of the main design factors and the introduction of dimensionless numbers to evaluate design efficiency. A generic case study is presented to analyse the effect of some key parameters affecting water distribution. Optimum designs for the case study given are also calculated. The concluding remarks summarise the main constraints existing in current ADW design. Extensions on the model are also presented to address for the issues highlighted.

Chapter 6 focuses on the analysis and modelling of swelling and removal mechanisms occurring in technical protein-based soils. Factors analysed involve temperature, chemistry (pH, Enzyme), shear stress and frequency of application of shear stress. The use of Partial Least Squares (PLS) as a modelling tool is presented to initially evaluate a Design of Experiments (DOE) approach to measure the thickness evolution of the samples using the sFDG. The main parameters affecting each of the phenomena seen (swelling and removal stages) and their interactions over time are also identified. Studies on swelling phenomenon are further expanded. Specific studies undertaken in egg yolk technical samples using both the sFDG and gravimetric tests are also reported. Degrees and rates of swelling obtained from both techniques are compared. Four different theories are considered to evaluate data: power law model, Fick's second law and linear and non-linear theories based on poroelasticity theory. Effective diffusion coefficients are reported and compared. Finally, the initial modelling work is expanded by introducing a mathematical swelling-removal model for the sFDG. A case study is shown to ease the understanding on the development of the model and its functionality. A mathematical equation is proposed to explain the phenomena occurring. Swelling and removal mechanisms are modelled independently and further integrated via the developed algorithm. Simulations results, including thickness predictions and other outputs, are shown as examples of the benefits provided by the model. The concluding remarks summarise the importance of understanding cleaning constrains in protein-based soils and the main factors affecting each of the cleaning stages.

Chapter 7 concludes the experimental work. Initially, results from the waterproof camera to continuously assess for cleaning inside an ADW are presented. The effect of temperature, pH and the level of enzyme on the removal of egg yolk technical soils are reported. Models developed throughout the thesis are compiled and used together to build predictions on full-scale results. A comparative from these models and full-scale results are finally presented.

Chapter 8 discusses project conclusions and gives future recommendations. The Appendix section compiles main MATLAB® codes used for the analysis of the data and includes the

description and methodology of another technique developed to evaluate cleaning in carbohydrate-based soils.

1.5. DISSEMINATION OF RESULTS

Results obtained through this research have been published as follows:

Peer-review journals

- Pérez-Mohedano, R., Letzelter, N., Amador, C., VanderRoest, C. T., & Bakalis, S. (2014). Positron Emission Particle Tracking (PEPT) for the analysis of water motion in a domestic dishwasher. *Chemical Engineering Journal*, *259*, 724–736. doi: 10.1016/j.cej.2014.08.033
- Pérez-Mohedano, R., Letzelter, N., & Bakalis, S. (2014). Development of a swelling-removal model for the Scanning Fluid Dynamic Gauge. *Food and Bioproducts Processing, 93, 269-282.* doi: 10.1016/j.fbp.2014.10.001
- Pérez-Mohedano, R., Letzelter, N., & Bakalis, S. (2015). Swelling and hydration studies on egg yolk samples via Scanning Fluid Dynamic Gauge and gravimetric tests. *Journal of Food Engineering, 169, 101-113*. doi: 10.1016/j.jfoodeng.2015.08.014

Conference proceedings

- Pérez-Mohedano, R., Letzelter, N., & Bakalis, S. (2013). Fundamentals on water motion inside a commercial dishwasher. *9th European Congress of Chemical Engineering. Poster*. The Hague, Netherlands. April, 2013.
- Pérez-Mohedano, R., Letzelter, N., & Bakalis, S. (2013). Using PEPT Technique to Visualize Water Motion Inside an Automatic Dishwasher. *9th World Congress of Chemical Engineering.* Book of Proceedings, pag. 383. Seoul, South Korea (August, 2013)
- Pérez-Mohedano, R., Letzelter, N., & Bakalis, S. (2014). Development of mechanistic swelling-removal model for the Scanning Fluid Dynamic Gauge. *Fouling and cleaning in food processing 2014. Green Cleaning* Cambridge, (UK). ISBN 978-0-9542483-3-8

CHAPTER 2

LITERATURE REVIEW

2.1. THE AUTOMATIC DISHWASHER

The invention of automatic dishwashing dates back to the mid 19th century. In 1850, Joel Houghton first patented a wooden device, hand-powered, that splashed water onto the dishes. It was the first concept of a semi-automatic dishwasher, however it was hardly workable. Later on in 1865 Levi A. Alexander patented an upgraded machine (Alexander, 1865). The device, also hand-powered, consisted in a circular wooden rack where dishes were placed. It was sealed to prevent any leakage to the exterior and water was splashed to the dishes from the top. The concave bottom part allowed an easy drainage of the wash liquor. It was not until 1887 when the first fully automatic dishwasher was invented. Josephine Cochran, a wealthy woman worried about the preservation of her china, patented an automated appliance to clean dishes. The invention consisted in a motor-powered appliance that rained down soapy water into different compartments where crockery was placed. The device was exposed in 1893's World's Columbian Exposition in Chicago, gaining recognition and commercial success (D'Ambrosio, 2011).

Modern dishwasher features were incorporated in 1924 by Livens William Howard (Howard, 1924). The improvements consisted in the utilisation of rotating arms to spread water, heating and drying (later in 1940) elements, household water piping and electrical energy input. Despite the significant advances, it was not a commercial success. In the 1950s, household appliances became smaller, cheaper and therefore, more affordable. It was then when the use of these machines started within the middle classes. Since then, multiple manufacturing companies have grown the business.

Current Automatic Dishwashers' (ADWs) penetration rate is quite spread among developed countries. 78% of US households own a dishwasher while the distribution is more inhomogeneous in Europe: 77% Germany, 52% France, 49% Spain, 42% UK or 25% Turkey (Mintel, 2011). This compares with the averaged 2% penetration rate for developing countries, indicating significant growth potential.

Contemporary automatic dishwashing technology consists of the distribution of water via the formation of jets on rotating spray arms. Crockery items are placed typically in two baskets located at the bottom and middle part of the dishwasher. Large and heavy items such as saucepans, bowls and dinner plates are typically placed at the lower basket. Delicate glassware and small items are usually located at the medium/upper basket. Cutlery is loaded in special designed trays found at the top, door or at the bottom crockery basket. Detergent is placed in a dispenser compartment found at the door (Dixon, 2009). **Figure 2.1** shows these main elements in a commercially available ADW.

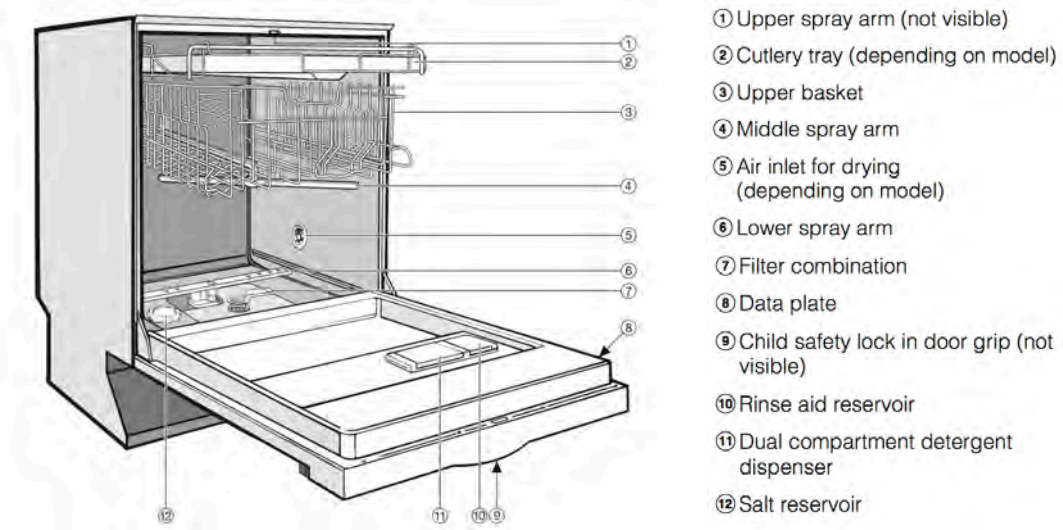

Figure 2.1. Schematic of an Automatic Dishwasher. Image retrieved from Miele G1222C model operating instructions (Miele, 2011).

A typical cleaning wash cycle consists of a series of rinse and main wash stages in which the degetergent is released from its compartment and temperatures are varying during the length of the cycle. **Figure 2.2** illustrates the temperature profile of water and cumulative water inlet of a typical wash cycle and the actions occurring at a given time. Temperature was measured at the bottom, next to the filter combination, with the aid of waterproof digital thermometers.

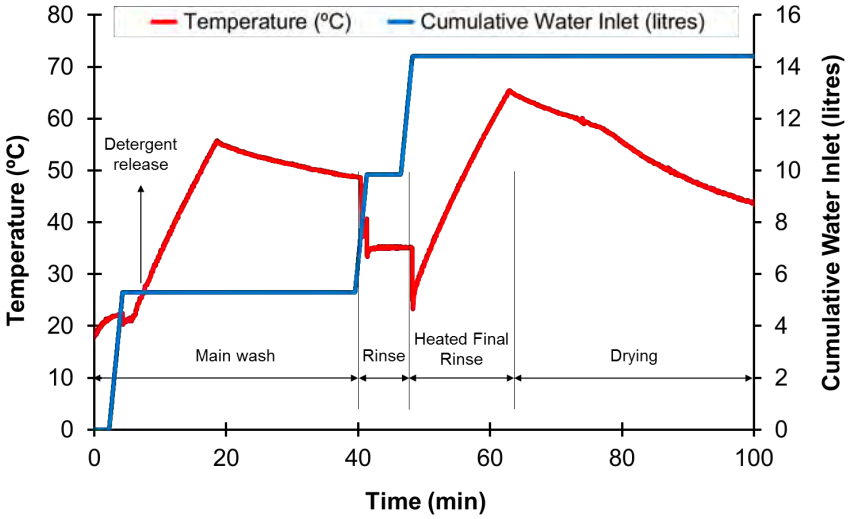

Figure 2.2. Temperature profile of water and cumulative water inlet in a typical ADW wash cycle.

A great performance of an ADW would involve the complete cleaning and drying of a wide variety of items in the least time possible and consuming low amounts of water and energy. The result is influenced by the water coverage and physical energy input (which depends on the appliance design), the distribution of items (partially user-dependant) and the performance of the formulated detergent used. As environmental concerns arise, a reduction of water and energy consumption is being imposed. Consequently, a reduction of cycle lengths is also occurring. New trends seen in the market aim to solve these issues by better distributing water using newly designed spray systems. A double rotating spray arm system by Frigidaire® claims four times better coverage than traditional spray arms. The design involves a circular spray arm rotating around its axis while this turns in circles around the dishwasher (Frigidaire, 2014). The use of a sweeping water-wall at the bottom where jets are reflected also claims better coverage (Samsung, 2014). The issue between a rectangular distribution of crockery and a circular distribution of water seems to be addressed in this case.

2.2. FACTORS AFFECTING CLEANING

2.2.1. Impingement jets

Rotating jet spray arms are used to distribute water in ADWs. Water jets are also widely used in manufacturing industry for cleaning purposes. Its use has been strengthened for tanks and other vessels via the development of spray balls (Jensen, 2011). The coverage produced on the surface by the water jets and the shear stress thus generated are believed to be key factors for the effectiveness of cleaning (Wang *et al*., 2013a). The impact of an impinging jet over a flat vertical surface makes the liquid move outward radially in a thin film at high velocity. After some distance 'R_{FJ}', the fluid forms a thicker film as it reaches the *film jump*. The *film jump* is defined as the point where a fast moving liquid converges with a small velocity profile area, producing a sudden decrease in its velocity and thus, an abrupt increase in the liquid height. Then, the liquid drains downwards and forms a falling film of certain width. The term *film jump* is differentiated from the traditional *hydraulic jump* as the latter typically refers to the transition region over horizontal surfaces, where gravity does not affect the fluid flow (Liu and Lienhard, 1993).

Net contributions from gravity, surface effects and the inclination of the impingement coherent jets create a range of downflow behaviours (Wang *et al*., 2013b; Wilson *et al*., 2012). **Figure 2.3** shows three common types known as 'gravity flow', 'rivulet flow' and 'dry patch'. The latter two cases are undesirable for cleaning purposes.

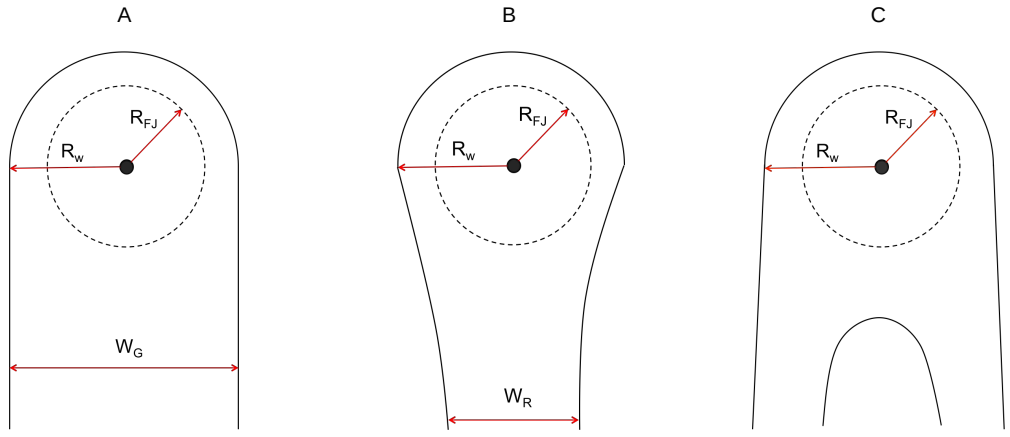

Figure 2.3. Drainage flow patters after impingement of a jet over a vertical surface. Black dot represents impingement point. A – Gravity flow. B – Rivulet flow. C – Dry patch. Legend: R_{FJ} = Radius of the film jump; R_W = Radius of the corona at the impingement level; W_G = Gravity flow film width; W_R = Rivulet flow film width. Definitions and schematics were retrieved from Wilson *et al*. (2012) and Wang *et al*. (2013b) .

- *Gravity flow:* The liquid drains as a thin film with a width 'W_G'. This width is related to the maximum liquid radius at the impingement proximities. Gravity contributions dominate over surface effects.
- *Rivulet flow:* The liquid film shrinks and forms one or more tails of width 'W_R'. Surface tension effects are in the range of gravity contributions.
- *Dry patch:* The falling film splits into two. Again surface tension effects are equally important than gravity contributions.

Morison & Thorpe (2002) analysed the wetting patterns generated by a horizontal jet produced through a sprayball and its impact over a vertical surface. A parameter called 'Wetting rate' ($\Gamma=\dot{m}/W_s$) was defined as the mass flow rate ($\dot{m}$) required to completely wet a surface of width 'W_s'. The authors found that an increase in temperature decreased the wetting rate. The viscosity reduction produced by increasing temperature makes the fluid move faster as a thinner film. In consequence, a higher wet width for the same mass flow was produced, giving a lower wetting rate value.

These studies were extended initially by Wilson *et al*. (2012), where a model of the radial flow zone and subsequent downfall film was developed. 'Gravity flow' and 'rivulet flow' patterns were analysed. The use of dimensionless correlations allowed the calculation of the wetted width for a given flow rate. Flow patterns produced by inclined impinging water jets over vertical surfaces were also reported by Wang *et al*. (2013b). Studies were also performed on the flow patterns generated by horizontal jets impinging on angled surfaces (Wang *et al*., 2014). The work expanded previous models by incorporating the effect of gravity and the impingement jet inclination angle. Flow rates used were higher (up to 480 l/h and jet velocities of 10.6 m/s) and close to those used in industrial cleaning devices. A circular jet impinging obliquely to a flat surface produces an elliptical radial flow zone. Experiments demonstrated that for low flow rates, film patterns created were sensitive to the nature of the soil, whereas this effect was negligible at high flow rates. Moreover, Wang *et al*. (2013a) evaluated the effect of surfactants on impingement flow and estimated the distribution of shear stress over the different flow areas. A significant effect by the surfactant on the downwards film shape was reported, promoting

‘gravity flow’. Shear stress values showed a significant difference between the outward radial flow and the falling film.

Within ADWs, impinging jets may impact the different surfaces at a wide range of angles. Overall, the same principles are applied. Also, other water distribution patterns are produced: splashing of water due to a jet breaking or falling film generated due to the accumulation of water from top positions. These aspects are hardly quantifiable, and therefore the scope of this work will be focused only on jets movement and characterisation.

Different angles of ejection are obtained by varying the design of the individual nozzles present in a spray arm and by changing the pump pressure. This produces different ejection paths depending on the nozzle considered. Also, the spray arm rotation rate is a consequence of the total torque generated. Generally, the presence of one or more ‘driving nozzles’ at the bottom of a spray arm creates a net force due to the reaction force (third Newton’s law) that is produced on the spray arm once the water is ejected.

Work on cleaning of soft soil layers produced by coherent jets impinging vertically on horizontal surfaces and horizontally on vertical surfaces has also been reported recently by Wilson *et al*. (2014). Three different soil-substrate systems were evaluated: (i) PVA glue on glass and polymethylmethacrylate (Perspex), (ii) Xatham gum on stainless steel and (iii) petroleum jelly on glass. Results showed a rapid adhesive removal from the impingement location to further radial positions, being the rate of removal proportional to the flow momentum. An important difference in cleaning rates between the inside and outside areas of the film jump was also observed. For the first two cases, removal was achieved all over the flow pattern once the absorption of water and the subsequent weakening of the soil structure occurred. However, the petroleum jelly showed no cleaning outside the film jump. The force imposed by the water film was insufficient to produce removal. This highlighted the important role of the nature of the soil in cleaning operations. The model was recently extended to incorporate the effect produced by a constantly moving impingement jet (Wilson *et al*., 2015).

2.2.2. Soil nature and characterisation

Foods are complex examples of soft condensed matter (Mezzenga *et al*., 2005; van der Sman and van der Goot, 2009; Van Der Sman, 2012). Their physical and chemical properties show a strong dependence on moisture content (Labuza and Hyman, 1998). State diagrams characterise the different states of a food sample as a function of water content and temperature (Rahman, 2006). It allows the identification of not only phase changes, but also of internal changes within a phase. An important region to look up in these systems is the glass state and the glass transition temperature. Glass state is commonly found at low temperatures and low water content regions. Materials in this state are hard and fragile. When increasing the water content and temperature, a transition from glass to rubber state occurs. This phenomenon is a second-order thermodynamic transition. The discontinuity does not happen at a constant temperature (i.e. boiling water) but at a range of temperatures (the first derivate is not zero, but the second is). Rubber state is characterised by being softer and with lower mechanical strength than the glass state. This is a consequence of the increase in molecular mobility and the decrease in viscosity. These changes might not only affect the shelf-life or texture of different foods, but also the energy input needed when cleaned from hard surfaces (Liu *et al*., 2006b)

Main food soils found in ADWs can be categorised in four different groups: protein-based, carbohydrate-based, lipid-based and mineral-based types.

2.2.2.1. Protein-based soils

Proteins are large polyamide chains characterised by the presence of peptide bonds. Their molecular weight can range from hundred to millions of Daltons. They are typically presented in folded complex networks where the primary, secondary and subsequent bonding structures are organised in a unique way (Phillips and Williams, 2011). They present a wide functionality in nature. Proteins conforms the basic structure of DNA, biological catalysts (enzymes), plants or microorganisms. Among food, examples with high protein content are: egg, milk, meat, cheese or nuts. **Figure 2.4** illustrates the peptide bond formation or hydrolysis process and a schematic of a polypeptide chain.

A

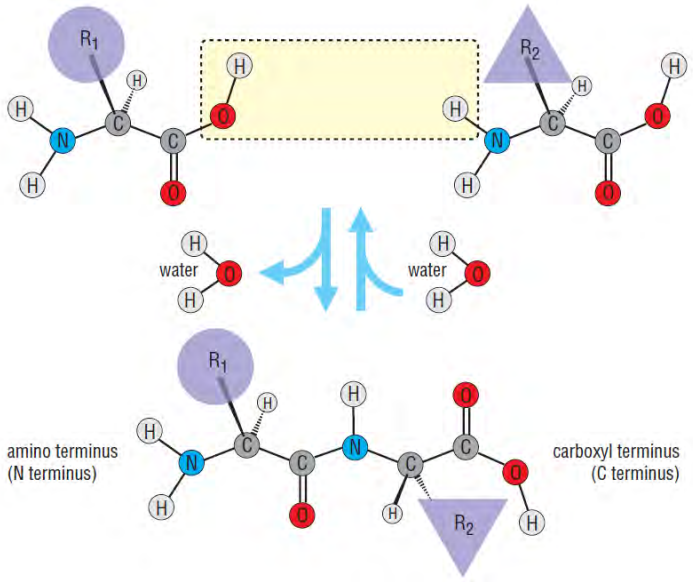

B

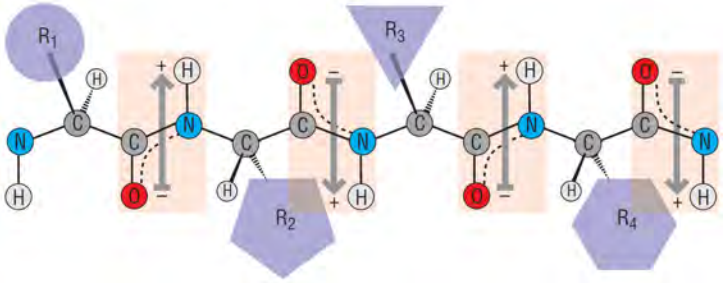

Figure 2.4. A – Peptide bond formation and hydrolysis. B – Schematic of an extended polypeptide bond. Figure was retrieved from Petsko and Ringe, (2004).

Cleanability of protein-based food soils is complex. Highly attached layers are formed through thermal and drying processes requiring a special treatment for their removal. These problems have been widely studied in milk industry where specific cleaning-in-place (CIP) actions take place (Fryer *et al*., 2006). Typically, a CIP sequence involves the following cycles (Goode *et al*., 2010): (i) rinse stage to remove those low attached substances, (ii) detergent wash to chemically attack the soil, (iii) post rinse to eliminate soil and detergent residues, (iv) sanitization to avoid microbial contamination and (v) final rinse to prepare the system for its restart. The detergent stage is typically done by circulating alkali-based solutions.

Specifically for ADW, egg yolk soil represents a challenge. This material is highly difficult to remove from a hard surface when dried and is one of the typical consumer complaints within the automatic dishwasher industry (DuPont, 2012). Burnt-on type of soils (Sen *et al*., 2014) also present highly difficult solutions. Therefore, these types of soils are commonly used in technical test to evaluate the performance of different detergent formulations. Apart from alkaline conditions, current detergent formulations incorporate specially designed enzymes to address these issues.

2.2.2.2. Carbohydrate-based soils

Carbohydrates are simple organic compounds based on the empirical formula $C_X(H_2O)_Y$ (Daintith and Martin, 2010). They range a wide variety of food constituents: from the simplest ones known as sugars to more complex structures such as starches or celluloses. In nature, their functionality is to store energy in living organisms. Some examples of carbohydrate-based foods are rice, bread, potatoes, pasta or tomatoes.

These components are hydrophilic and commonly easy to clean. They typically do not require external agents to be removed. However, denaturation and ageing processes can lead to undesirable foodstuff conditions, increasing the cleanabilty issues. Drying or Maillard reactions (IFIS, 2009), produced as a consequence of high temperatures, result in highly attached soil layers over a substrate. These Maillard reactions involve reducing sugars in multiple reactions with proteins. The chemical paths followed have not been fully described yet due to the complexity of the process. Caramelization, non-enzymatic browning and changes in aroma and texture are direct consequences of this phenomenon (Arnoldi, 2001).

2.2.2.3. Lipid-based soils

Lipids are carbon chains insoluble in water. They are also commonly known as fats. Complex structures are found as esters of long-chain fatty acids. Simple structures also exist as smaller chains without fatty acids (Daintith and Martin, 2010). Oils, dairy products, mayonnaise and other oil-in-water emulsions are examples of food containing lipids. Their main functionality in living organisms is to store energy, but they are also present in cell membranes or as vitamins.

Their hydrophobicity represents a challenge when cleaning. The use of surfactants is required to create micelles and remove the fatty content from water.

Also, the removal of burnt-on/baked-on fat type of food soils represent another difficult task in ADW industry. These residues can be found in pans or cooking items where high temperature conditions occur. Typically fat structures burn and adhere heavily to the surface of the crockery item. High mechanical energy input from water jets and enzymatic treatment is required in order to achieve a complete cleaning (Ali *et al*., 2015).

2.2.2.4. Mineral-based soils

Minerals are inorganic compounds containing ions. Their presence is common in a wide variety of foods and additives, such as table salt, fruits or regenerative drinks. They are important to grow, maintain and repair living cells. Their presence in automatic dishwashing produce the formation of dry films or spots on the glassware at the end of a wash cycle. However, the cleaning challenge provided by these compounds does not come directly from foodstuff. Hard waters containing ions (i.e. Ca^{2+} or Mg^{2+}) need to be treated during the cleaning cycle to avoid this issue. Chemical builders are typically use to encapsulate and remove these ions and to softer the water.

2.2.3. Formulated cleaning products

Commercially ADW's formulated cleaning products were firstly introduced in the 1950's (Procter&Gamble, 2014). Initially, detergents were sold as powders during 25 years. These products gave good cleaning but were used in high quantities and produced some damage in glassware and diverse crockery elements after repeated cycles. These were highly alkaline (understood as the stoichiometric sum of bases in the solution) and incorporated phosphates. At the end of 1980's, liquid detergents were marketed. Alkalinity was reduced and product became less aggressive to preserve crockery quality. In the early 1990's, compact powders were introduced. These became more environmentally friendly as alkalinity was again reduced and first commercially available cleaning enzymes were incorporated. However, consumers tended to overdose thus the price per wash cycle increased. Concentrated liquids were later on

developed. pH was reduced and became less of an irritant though the problem of overdosing still persisted. Finally, unit dose and tablets were commercialised. Different powder and liquid compartments were created to preserve chemistry quality (i.e. separate enzyme from bleach components to avoid its denaturation). The overdosing problem was also addressed as detergent quantities were standardised. These commercial standards are still preserved nowadays. Current detergent formulations encompass a wide range of ingredients (Tomlinson and Carnali, 2007). They can be grouped according to the role they play during a wash cycle. Main components found are:

- *Buffers.* These chemicals aim to maintain pH. At high pH, swelling and gelification phenomena in protein and starch-based soils occur. Cohesive forces are reduced as a consequence of the lower bonding energy density. The number of bonds per unit volume decreases when volume increases. Hydrolysis reactions on protein-based soils (Mercadé-Prieto *et al*., 2007a) and the deprotonation of hydroxyl groups which cross-link starch network (Carnali and Zhou, 1997) might also happen if conditions are adequate. Thus, a further reduction in the cohesiveness of the soil is also possible. The presence of negative charge ions in solution also charges negatively glass and ceramic items. This produces a reduction in the adhesive forces between the soil and substrate which eases the removal using the mechanical forces provided by the ADW. Main formulations used to boost pH are based on carbonate, bicarbonate and silicates. The use of silicates act as inhibitors of metal corrosion by creating a passive layer. However, these compounds are known to deteriorate china items. Overall, buffer level should also preserve enzyme stability, bleach performance and minimise the environmental impact.

- *Builders.* The main functionality of a builder component is the removal of hardness ions (Ca^{2+} and Mg^{2+}). At basic conditions, calcium ions can bridge protein-based soils to stainless steel substrates and hydrolysed starches to glass or ceramic. These ions can also form precipitates that adhere to washware creating unwanted films or deposits that affect the shine and final look of these items. The removal of mineral-based soils, such

as tea deposits, is also aided by the presence of builders in the detergent. These compounds are typically deprotonated acids and can be classified in three categories depending on the chemical route they use (Broze, 1999): formation of precipitates such as sodium carbonate or potassium oleate; ion exchange mechanism, mainly produced by zeolites; and sequestrant builders such as phosphates, polycarboxylates or citrates. These latter are the most commonly used due to the cost, availability and chemical performance. Current regulations towards zero phosphate formulas are generating a trend for these components disappear from commercial detergents.

- *Antiscalants.* These components specifically aim to avoid the formation of calcium carbonate ($CaCO_3$) and calcium phosphate ($CaPO_4$) precipitates on glassware. High pH found in wash conditions can lead to the formation of supersaturated calcium carbonate which precipitates and forms deposits. Antiscalants are clearly related to builders components. Typically, chemicals such as sodium tripolyphosphate (STTP) were used due to their high Ca^{2+} building capacity. However, the move towards none phosphate formulations is enhancing the filming problem again. Mechanisms involved are based on electrostatic forces where bulk solution ionic strength and particle diameters play an important role in the process (Riley and Carbonell, 1993).

- *Bleaches*. Their aim is to perform a germicidal action and to remove tea stains. The mechanism occurring during their reaction is a nucleophilic attack to a molecule double bond. The sanitization process is also enhanced by the high temperatures found in a typical ADW wash cycle. For detergency purposes, two big groups of bleach systems can be identified: active chlorine compounds and oxygen systems. The first were used initially, however they were incompatible with enzymes, presented non-ionic surfactants degradation and self-storage stability. They are characterised by the production of ROCl molecules in solution. The second group (oxygen systems), also known as oxidising bleaches are the ones used nowadays. They can be divided as well into three smaller categories: peroxide sources; peracids and their precursors; and catalysed systems of previous groups. Peroxide sources are characterised by the presence of the

active group –O-O-H which dissociates to form $O\text{-}O^-$. Their kinetics is slow below 60ºC and high pH levels are also necessary for an optimum performance. Peracid precursors are added into the formulation to speed-up kinetics. The principal compound used is TAED (tetraacetyl ethylene diamine) which forms peracetic acid and DAED (diacetyl ethylene diamine) in its reaction with a peroxide group. For lower pH conditions, the use of PAP (phthalimidoperhexanoic acid) has also been considered. The use of catalysed systems in commercial applications has been developed recently. Mn Me TACN (1,4,7-trimethyl-1,4,7-triazacyclononane) is the first peroxide catalyst attempt in industry.

- *Surfactants*. The use of surfactants in ADW detergents targets different functions: control of foaming during the wash cycle, increase the wettability of the crockery items and minimise the segregation of powder components. Excessive foaming in an ADW can cause a malfunction of the spray arms as bubbles are displaced to the pump, reducing the flow rate and decreasing the wash efficiency. Surfactants added to ADW formulations typically perform an antifoaming or defoaming action. In the presence of high contents of protein-based soils, excessive foam can be produced. By controlling this phenomenon, a proper operation of the machine is guaranteed. Also, the presence of surfactants lowers the water surface tension, thus increases the wettability of the different items. This promotes a reduction in the spots/films created at the end of the wash cycle. However, the particular nature of the surfactants used in ADW's detergents makes them to reduce the surface tension to values between 40-45 mN/m, while for hand-washing, values between 26-30 mN/m are achieved. Typical surfactants used are non-ionic compounds that must be analysed in terms of their solubility. That is characterised by a threshold temperature known as cloud point. This means that above the cloud point, the solution becomes turbid, as a consequence of a phase separation where a richer water phase with low surfactant content and a richer surfactant phase with low water content are formed. This produces problems of detergent solubility when high temperatures (above the cloud point) are achieved. In consequence, surfactants used are aimed to dissolve within the range of temperatures typically found in ADWs. Chemical ways to produce surfactants involve the condensation reaction between

ethylene oxide and an organic hydrophobic group, a condensation between aliphatic alcohols and ethylene or propylene oxides or the co-formation of polyoxyethylene/polyoxypropylene block copolymers.

- *Enzymes*. They are required to enhance soil hydrolysis and increase washing performance. Enzymes are commonly found across automatic dishwashing industry nowadays (Aehle, 2007; Olsen and Falholt, 1998). The low levels set in formulation made possible their inclusion in commercial detergents. Enzymes help the reduction of wash times, lower the required pH and provide a more environmentally friendly effluent. Enzymes used in ADWs industry should comply with the following properties: perform correctly in a wide range of temperatures (20ºC to 70ºC) and with an optimum temperature performance around 60ºC; show high activity at basic conditions; be stable in the presence of other detergent ingredients; and target a wide variety of soils. Two major groups of enzymes are used in ADW industry: *proteases and amylases*. *Proteases* aim to enhance the hydrolysis of peptide bonds from protein-based soils (i.e. egg yolk). Typical commercially available proteases belong to the serine family and the subtilisin sub-group (Tavano, 2013). The reaction mechanism is described by an initial adsorption of the enzyme molecule onto the soil surface, followed by the reaction with a protein peptide bond to conform a metastable intermediate product. This complex molecule is later on disintegrated back to give the enzyme molecule and the protein with a hydrolysed peptide bond. The same enzyme molecule can still be catalysing subsequent reactions without leaving the soil surface. *Amylases* aim to enhance the hydrolysis of starch-based soils (i.e. pasta). They target (1→4) glycosidic bonds and catalyse their hydrolysis reaction. The reaction mechanism is similar than for proteases, distinguishing between α–amylases that target bonds in the middle of the chain and ß-amylases that target end bonds of the starch chain. Both types of enzymes require free Ca^{2+} ions for an optimum performance. They also offer good stability in powders whilst amylases show higher instability than proteases in liquid products. The type of cleaning produced is a layer-by-layer removal of the soil. The evolution of these enzymes is

critical in the progress of the detergent industry. With the aid of computational programs and new technologies, the development of new molecules can occur much faster.

Overall, formulated cleaning products need to comply with the following (Fuchs, 1981):

- Provide good cleaning by removing all sort of foodstuff.
- Prevent spotting or filming on glassware and dishes.
- Avoid the deterioration/marking of crockery.
- Operate in a wide range of temperatures and water hardness.
- Produce low foaming during a wash cycle.
- Present a satisfactory shelf-life.

2.3. CLEANING MECHANISMS

To remove soft soil deposits off a hard surface it is necessary to overcome the cohesive forces that bind the soil together and the adhesive forces that bind the soil to the substrate. Factors affecting the effectiveness of the removal include: the nature and state of the soil to physical and chemical factors such as flow rate (shear stress applied), concentration of chemicals (pH, enzymes) or temperature (Wilson, 2005).

Fryer & K.Asteriadou (2009) proposed a classification for cleaning phenomena based on types of soils and mechanisms of removal. Soils were classified based on their physical properties, ranging from *low viscosity fluids* to *cohesive solids*. Cleaning fluids were classified from *water at ambient* to *hot chemicals*. The cleaning mechanism occurring varies depending on the case given: a *fluid mechanic removal* happens when fluid flow is enough and no chemicals are needed. However, a *diffusion-reaction removal* involves the presence of chemicals. Different dynamic processes might occur in parallel, involving mass transfer from the bulk of wash solution to the soil, a subsequent diffusion of the actives species, the change of the soil inner properties due to chemical reactions and the increase in moisture content (phase changes). This leads to a weakening of the soil structure that facilitates the cleaning process. Once the soil molecules are disengaged, a reverse mass transfer phenomena occurs. Released particles

must travel to the boundary soil-wash solution layer and then be completely removed. The rate limiting stage controls the total removal time.

Particularly, for protein-based soils, three stages can be identified in the cleaning process (Bird and Fryer, 1991):

1) Swelling: An initial swelling process occurs when the soil and the wash solution are put into contact. The diffusion of the liquid containing the active species causes the increase in thickness of the soil.

2) Erosion: Once the active species (e.g. enzymes) have had enough time to act and the increase in moisture content has weakened the soil structure, the removal of the substance starts to occur. A constant removal rate is reached for constant cleaning conditions. Swelling might still be occurring in parallel.

3) Decay: In the final stages of the removal process, adhesive forces become important. For protein-based soils, adhesive forces are typically higher than cohesive forces (Liu *et al*., 2006a). Therefore, higher energy input is required to remove the same soil amount. If cleaning conditions are invariant, then the removal rate is reduced in this latter stage until cleaning is complete.

Extensive research has been done to study swelling and dissolution mechanisms on simple and common protein soil deposits such as ß-lactoglobulin (ß-lg). Studies performed (Mercadé-Prieto *et al*., 2007a) showed the presence of a dissolution threshold below which the gel swelled but did not dissolve. This threshold is dependent on pH and the volume fraction available inside the protein network. It establishes the limit for the stability and dissolution of these protein gels. When pH was increased, charges on the polymer chain increased and swelling was promoted. A significant swelling degree occurred above pH 10. However, when salts were added and the ionic strength increased, a screening effect between cations from solution and the polymer network occurred and swelling degree decreased. pH and volume fraction thresholds were

suggested when the dissolution of ß-lg occurred at different rates for different pH and solution ionic strengths. The importance of swelling was highlighted. Dissolution occurred when pH was high enough (pH threshold) and a certain degree of swelling was achieved (volume fraction threshold).

pH threshold was studied in detail (Mercadé-Prieto *et al*., 2007b). A sharp transition in the dissolution rate was found between pH 11 and 12. The disruption of non-covalent intermolecular bonds due to alkali denaturation was established as the main dissolution mechanism. This disengagement was favoured by the repulsion produced as the number of charges increased and the unfolding of the protein structure occurred. Dissolution rates also varied for different protein structures obtained (i.e. length of protein aggregates), which in essence were dependent on the temperature of formation of the gel and the gelation time (Mercadé-Prieto *et al*., 2006).

The volume fraction threshold was also explored (Mercadé-Prieto *et al*., 2009, 2007c). For the same pH, higher concentrations of salts produced a repulsion effect due to the presence of more counter ions in the network. Screening effect lowered swelling degree thus less space was available. Therefore the dissolution rate of the polymer chain reduced. The disentanglement process (reptation of the polymer chains) was proposed as the dissolution rate limiting removal mechanism. At high pH (pH > 13.3) an anomalous behaviour was also observed (Mercadé-Prieto *et al*., 2007c, 2006). A maximum pH for dissolution was found and the dissolution rate decreased with the increase of pH beyond that point. Also, the dissolution rate was not uniform and dropped over time. To explain this, it was proposed that a reduction in the free volume in the gel network occurred due to the high concentration of cations from the alkaline solution (typically NaOH). Transport of the disengaged molecules outside the affected gel network was restricted. As penetration of alkaline solution occurred, shrinking of the gel happened and mobility of the protein molecules was reduced.

Therefore, the work also expanded the limiting criteria for the dissolution and removal of protein based soils. Three scenarios were established including the effect on removal of an external mechanical action (a flow over the soil sample) (Mercadé-Prieto *et al*., 2006). The first one

considered high temperature, low dissolution pH and a minimum flow. In this case, results suggested that the rate limiting stage was a mass transfer process. The diffusion of sodium hydroxide molecules into the network or the protein diffusion into the bulk solution were considered as the two possible limiting mechanisms. The second case assumed high temperatures and high pH. For a low flow, the diffusion of the disengaged molecules into the bulk solution was established as the rate limiting stage. However, for a high flow the extra mechanical action enhanced the removal rate and the limiting stage was the reaction-controlled formation of small aggregates. Finally, a third case considered mild conditions of temperature and pH. For high flow, the erosion of the swollen layers occurred and the kinetics of swelling was considered as limiting mechanism. Similar studies were also performed on slightly more complex protein systems (Whey Protein Isolate/Concentrate) (Saikhwan *et al*., 2010). Work reported different swelling behaviours depending on the complexity of the protein gels. Fickian to more linear diffusion profiles were observed.

Modelling cleaning processes over time is a complex task as different transport mechanisms are combined. Not many attempts have been considered so far and semi-empirical approaches are frequent. Dürr & Graßhoff (1999) developed a two-parameter exponential type model as an easy-to-use tool to predict cleaning. A specific time constant was defined as the time required to reach 63.2% of total removal. As a second parameter, a logarithmic-type slope characterising cleaning behaviour was also defined. The model showed high flexibility for describing different cleaning patterns. It was further expanded (Dürr, 2002) to re-appraise the model approach by using a Weibull distribution analysis.

Xin *et al*. (2004) proposed a mathematical model for the removal of milk protein deposits. Disengagement of protein molecules and subsequent mass transfer to the bulk of the wash solution (boundary layer) were considered to be the rate limiting stages. The initial swelling stage was constrained to occur before a ‘reptation time’ was reached and no cleaning was observed during this period. The ‘reptation time’ is linked to the initial time required for the first molecules to disengage. A first-order equation was proposed to characterise the removal rate and a disengagement rate constant introduced. This constant was considered as a function of

the volume fraction of the disengaged protein molecules at the soil-solution interface. As the rate limiting stage is the movement of these molecules to the interface and their subsequent detachment, a critical concentration would be reached in this area and a constant removal rate obtained. This agreed with the results seen in experiments. Finally, the decay stage was modelled as a function of the surface area of the remaining film. By integrating the three steps, good correlations (no error given) were obtained with experimental data.

2.4. DIFFUSIONAL THEORIES

Across the different mechanisms highlighted previously, swelling phenomena represents the activating stage for cleaning to occur in protein-based soils. Penetration of the active species is necessary to perform an optimum clean. The reader must differentiate between *degree* of swelling and *kinetic* of swelling when a hydration phenomenon with an associated change in thickness occurs. *Degree* of swelling indicates the net increase in volume occurring in the sample over time. A swelling-ratio coefficient, typically defined as the ratio between the thickness at equilibrium and the thickness at dry state of the sample, is used to characterise this process. *Kinetic* of swelling relates to the speed at which the equilibrium is reached. It is typically characterised by a diffusion coefficient (Ganji, 2010).

Numerous approaches have been done to model the swelling/hydration phenomena in different foods. They can be listed as a function of the complexity of the equations and approach used. There are empirical models that fit experimental data (Chen *et al*., 2007; Davey *et al*., 2002; Kruif *et al*., 2015; Malumba *et al*., 2013); theoretical approaches to estimate intrinsic parameters (i.e. diffusion coefficients) (Bakalis *et al*., 2009; Bello *et al*., 2010; Oztop and McCarthy, 2011); theoretical models fully developed and validated (Briffaz *et al*., 2014; Chapwanya and Misra, 2015); or other theoretical models developed for the simulation of swelling using advanced computational systems (Mitchell and O'Brien, 2012; Van Der Sman, 2014).

A classification depending on the rate limiting stage was proposed by Alfrey *et al*. (1966). A *Case I or Fickian diffusion* occurs when the solvent diffusion rate is clearly slower than the network relaxation rate. Relaxation time describes the time required for the sample network to

accommodate to the increase in liquid content. It is related to the transition from glass to rubber state of the sample. A *Case II or Non-Fickian* transport process takes place when liquid mobility is much higher than the structure relaxation time (Thomas and Windle, 1982, 1980). In between these two extreme cases, an *anomalous transport* can also be defined. Liquid movement and relaxation time are in the same order of magnitude.

Four different diffusional theories are presented next. They show an increasing complexity and provide different information regarding the dynamics of the diffusion process. Different subscripts will be used to distinguish the different diffusion coefficients estimated from each theory. The solutions to each of the equations next shown can be found in Chapter 3, section 3.10.

2.4.1. Power-law model

Peppas & J.L.Sinclair (1983) presented a semi-empirical equation (Eq. 2.1) to assess the type of transport occurring in one-dimensional (thin slabs) isothermal processes. The equation is valid for the first 60% of the mass uptake $\left(\frac{M(t)}{M_\infty} < 60\%\right)$ under perfect sink conditions (i.e. infinite supply of solvent).

$$\frac{M(t)}{M_\infty} = kt^n \qquad \text{Eq. 2.1}$$

Where:

- $M(t)$ = Total sample mass at time 't'.
- M_∞ = Total sample mass at equilibrium (t=∞).
- k = Constant incorporating characteristics of the macromolecule and the penetrant system.
- t = Time.
- n = Diffusional exponent.

Depending on the value of the diffusional exponent 'n', any transport mechanism can be identified. **Table 2.1** illustrates the different cases.

Table 2.1. Types of mass transport as function of the diffusional exponent 'n' value. Coefficients are valid for one-dimensional (slab geometry) isothermal processes.

TYPE OF TRANSPORT	DIFFUSIONAL EXPONENT (n)	TIME DEPENDENCE
Fickian Diffusion (Case I)	0.5	$t^{1/2}$
Anomalous transport	0.5 < n < 1	t^{n-1}
Non-Fickian transport (Case II)	1	Time independent

Different geometries (other than the slab) or in particular, the increase of thickness of the sample when hydrating, can lead to a variation in the estimated values of 'n' (Peppas and Brannon-Peppas, 1994). The increase of thickness over time implies longer distances for a solvent molecule to travel, but also higher holding capacity of the sample, as the volume achieved at equilibrium is higher. The presence of a higher number of solvent molecules implies an extra resistance for the network to adapt to the changes. In consequence, its relaxation time increases with the increase of swelling-ratio. Other factors affecting the diffusional exponent 'n' are the use of monodisperse or polydisperse solvent systems. In the presence of a particle size distribution in the solvent, small molecules are able to diffuse faster through the sample network at early stages, but the equilibrium might be delayed as larger molecules move slower in the final stages. A change in the assumption of boundary perfect sink conditions can lead to variations in the diffusional exponent 'n' as well. This assumes an instantaneous equilibrium between the solvent and the top layer of the sample once they come into contact. However, even though the equilibrium might be reached fast, it cannot be instant.

Eq. 2.1 was also adapted in this work to fit thickness data by replacing mass by height. The analogue expression is shown in Eq. 2.2.

$$\frac{h(t)}{h_{\infty}} = k' t^{n'} \qquad \text{Eq. 2.2}$$

Where:

- $h(t)$ = Thickness at time 't'.
- h_{∞} = Thickness at equilibrium (t=∞).

- k' = Constant (for thickness data).
- t = Time.
- n' = Diffusional exponent (for thickness data).

2.4.2. Fick's second law

If Fickian diffusion is the predominant type of transport, Fick's second law (Eq. 2.3) can be used to fit experimental data (Bird *et al*., 2007). Eq. 2.3 describes the uniaxial concentration change over time occurring for a thin slab geometry.

$$\frac{\partial C}{\partial t} = D_F \frac{\partial^2 C}{\partial z^2} \qquad \text{Eq. 2.3}$$

Where:

- C = $\frac{M(t)}{M_{dry}}$ = Mass concentration (expressed relative to the initial dry weight of the soil).
- M_{dry} = Dry sample mass.
- t = Time
- D_F = Effective diffusion coefficient for Fick´s equation.
- z = Uniaxial diffusion direction.

A series of assumptions are typically made when this equation is used (Sam Saguy *et al*., 2005). The most common ones involve:

- No other transport mechanisms are considered (e.g. capillarity).
- The effective diffusion coefficient is constant and independent of the moisture content in the network.
- Only the diffusion of unreacted liquid is modelled.
- The initial moisture content in the network is uniform (i.e. isotropic state).
- No resistances to the flux are found at the top layer and therefore the equilibrium occurs instantly.

- Swelling or shrinkage phenomena are typically not considered.
- The geometry is simplified to slab, spheres or cylindrical shapes.
- Heat transfer equations are commonly ignored.

In a diffusion process with a change in volume (thickness) of the sample, boundary conditions are constantly varying. If the degree of swelling reaches a significant level (e.g. doubles up), and this is not considered by the model, wrong conclusions can be made when analysing the results. The assumption of molecular incompressibility (additive volumes) can relate the thickness change with the mass gained for a uniaxial swelling case via a density relationship. This is expressed in Eq. 2.4.

$$M_f = M(t) - M_0 = \rho_f \cdot A \cdot (h(t) - h_0) \qquad \text{Eq. 2.4}$$

Where:

- $M(t)$ = Total sample mass at time 't'.
- M_0 = Initial sample mass. Sample mass at time 't=0'.
- ρ_f = Density of the fluid.
- A = Cross sectional area.
- $h(t)$ = Thickness at time 't'.
- h_0 = Initial thickness. Thickness at time 't=0'.

The incorporation of Eq. 2.4 into Eq. 2.3 allows the calculation of diffusion profiles considering moving boundaries.

2.4.3. Linear poroelasticity theory

More complex theories have been developed to study the swelling kinetics of polymer gels. Classical Biot's theory of poroelasticity (Biot, 1941), adapted from Gibbs (1906), in combination with statistical mechanics (Flory and Rehner Jr., 1943) has been used extensively to analyse solvent migration in polymer systems (Hong *et al*., 2009). At time zero, the polymer network is considered to be stress free, isotropically swollen and at a constant chemical potential (μ_0). In the presence of an adequate solvent, a chemical potential gradient is established and a flux of

the solvent into the network is created. This results in a deformation gradient in the network, which can be correlated with the concentration distribution if molecular incompressibility is assumed. The theory is developed for neutral gels, thus interaction effects between solvent ions and the gel are not considered. The constitutive equations are linearized at the vicinities of the initial state, when small perturbations happen. The increase of thickness over time for the case of constrained swelling to one direction is expressed as shown in Eq. 2.5 (Yoon *et al*., 2010). The right side of the equation is formed by two terms. The first one indicates the total thickness change at equilibrium (Eq. 2.6). The second is related to the dynamics of the diffusion process (equilibrium ratio achieved at any time) and ranges from 0 to 1. The effective diffusion coefficient (D_L) is included in the characteristic time scale of diffusion (τ=h_{dry}^2/D_L).

$$\Delta h(t) = h(t) - h_0 = \frac{(1-2\upsilon)(\hat{\mu}-\mu_0)h_0}{2(1-\upsilon)G_{SM}\Omega} \cdot \left\{1 - \frac{8}{\pi^2}\sum_{n=0}^{\infty}\frac{1}{(2n+1)^2} exp\left[-(2n+1)^2\frac{\pi^2 t}{4\tau}\right]\right\} \quad \text{Eq. 2.5}$$

$$\Delta h_{\infty}^{eq} = h_{\infty} - h_0 = \frac{(1-2\upsilon)(\hat{\mu}-\mu)h_0}{2(1-\upsilon)G_{SM}\Omega} \quad \text{Eq. 2.6}$$

Where:

- $h(t)$ = Thickness at time ‘t’.
- h_0 = Initial thickness. Thickness at time ‘t=0’.
- h_{∞} = Thickness at equilibrium.
- υ = Poisson’s ratio (measurement of stretch changes).
- μ_0 = Chemical potential at the initial state.
- $\hat{\mu}$ = Chemical potential of the solvent in the environment.
- G_{SM} = Shear modulus.
- Ω = Volume of a solvent molecule.
- t = Time
- $\tau = h_{dry}^2/D_L$ = Characteristic time scale of diffusion.
- h_{dry} = Sample thickness at dry state.
- D_L = Effective diffusion coefficient.

This theory has been reported to be limited to small deformation cases (Bouklas and Huang, 2012). For more detailed information in the mathematical development, the reader is referred to Yoon *et al*. (2010).

2.4.4. Non-linear poroelasticity theory

Hong *et al*. (2008) developed a non-linear approach that combines a non-equilibrium thermodynamic theory with a Fickian kinetic law to analyse the diffusion of small molecules into a neutral polymer gel. Mass transport was analysed together with the deformation of the polymer. The authors considered a field of markers (Z) along the network of the gel, which provides an initial reference state. As the polymer swells, the markers (Z) move and a deformation gradient (F) is established. A nominal stress (s) is then defined to comply with the on-going forces and to give a force balance in the network. It defines a 'field of weights'. They also consider a flux of solvent molecules into the gel at a given chemical potential (μ) such that the concentration (C) of these molecules in the polymer would be a function of the flux and the stretch given. This motion defines a 'field of pumps'. A free-energy function of the gel W(F,C) can be given as the combination of the deformation and the concentration gradients. The gel, the 'field of weights' and the 'field of pumps' form a thermodynamic system. Thus, the free energy of the system (G_{FE}) can be given by the sum of the free energy of the polymer and the potential energy for both the deformation and concentration fields. Overall, thermodynamics laws are applied $\left({}^{dG_{FE}}/_{dt} \leq 0\right)$ and the energy of the system should never increase.

The assumption of molecular incompressibility was also considered when looking specifically into the gel. Therefore, all volumetric change given in the system is due to the absorption/desorption of the solvent molecules in the network. By applying Flory & Rehner Jr. (1943) theory, the stretch in the polymer network can be calculated for any direction. The theory considers the free energy of the gel as a combination of two molecular processes: stretching of the network and the mixing of the small solvent molecules with the polymer. Intrinsic properties of the solvent and polymer are included:

- N = Effective number of polymer chains per unit volume of the polymer (nº chains/m^3 polymer). It is defined as a constant value and refers to a reference condition at dry state.
- Ω = Volume per solvent molecule (m^3/solvent molecule).
- χ = Flory-Huggins parameter (interaction between the solvent and the polymer).

The kinetics of the solvent molecules were considered to follow a Fickian diffusion model. It is characterised by a diffusion coefficient, $D_{NL,}$ which is isotropic and independent of the concentration and deformation gradients. In a swollen gel, the main resistance found for a molecule to diffuse comes from other solvent molecules, as they are the major component in the system. Resistance between the polymer network and the solvent molecules are lower except at the initial stage. Therefore, the theory considers a liquid diffusing into itself. The flux is a function of the chemical potential gradient available in the system.

By considering a uniaxial swelling (constraint in 2 directions) and an isotropically initially swollen state, the stretch of the network as a function of time and position is given by Eq. 2.7.

$$\lambda_0^2 \frac{\partial \lambda}{\partial t} = D_{NL} \frac{\partial}{\partial Z}\left(\xi(\lambda) \frac{\partial \lambda}{\partial Z}\right) \qquad \text{Eq. 2.7}$$

Where:

$$\xi(\lambda) = \frac{1}{\lambda_0^2 \lambda^4} - \frac{2\chi\left(\lambda_0^2 \lambda - 1\right)}{\lambda_0^4 \lambda^5} + N\Omega \frac{\left(\lambda_0^2 \lambda - 1\right)\left(\lambda^2 + 1\right)}{\lambda_0^2 \lambda^4} \qquad \text{Eq. 2.8}$$

Where:

- D_{NL} = Effective diffusion coefficient.
- λ = Stretch in uniaxial direction (thickness at time 't' / dry state thickness).
- λ_0 = Initial stretch in uniaxial direction (initial thickness / dry state thickness).

The total thickness of the sample can be calculated as:

$$h(t) = \int_0^{h_{dry}} \lambda(z,t)dz \qquad \text{Eq. 2.9}$$

Where:

- $h(t)$ = Thickness at time 't'.
- h_{dry} = Layer thickness in the dry state.

Also, an algebraic equation (Eq. 2.10) relates the equilibrium swelling ratio, λ_∞, with λ_0, N, Ω and χ as follows:

$$ln\left(\frac{\lambda_0^2\lambda_\infty - 1}{\lambda_0^2\lambda_\infty}\right) + \frac{1}{\lambda_0^2\lambda_\infty} + \frac{\chi}{\lambda_0^2(\lambda_\infty)^2} + \frac{N\Omega}{\lambda_0^2}\left(\lambda_\infty - \frac{1}{\lambda_\infty}\right) = 0 \qquad \text{Eq. 2.10}$$

A relationship between the diffusion coefficients calculated through both linear and non-linear approaches is given by the following equation (Eq. 2.11):

$$D_{NL} = \frac{D_L}{\xi\left(\lambda_0^*\right)} \qquad \text{Eq. 2.11}$$

Where:

$$\lambda_0^* = \frac{(\lambda_0 + \lambda_\infty)}{2} \qquad \text{Eq. 2.12}$$

This theory was further expanded to incorporate the effect of different charges in the gel (polyelectrolytes) and the mobility of different ions across the network (Hong *et al*., 2010) but it was not considered in this study.

2.4.5. Temperature dependence

For the case of the diffusion of a fluid into a solid, the effective diffusion coefficient at different temperatures typically follows an Arrhenius equation (Mehrer, 2007) (Eq. 2.13).

$$D = D_0 \cdot e^{-E_A/RT} \qquad \text{Eq. 2.13}$$

Where:

- D = Effective diffusion coefficient.
- D_0 = Maximum effective diffusion coefficient.
- E_A = Activation energy.
- R = Gas constant
- T = Temperature.

2.5. SUMMARY

Cleaning in ADWs involves a wide range of areas of knowledge that must be joined together: distribution of water and mechanical cleaning via coherent jets, detergent formulations (chemical cleaning) and type of food soils. Detergent formulations have made important progress in the past 25 years as the research in food technology has expanded and the development of advanced designed enzymes were introduced to the market. Describing the interactions between detergent chemistry and type of food soils is becoming more important both in industrial and household scales. The idea is to drive this knowledge to propose optimisation scenarios resulting in important cost savings and more environmentally friendly processes. Understanding cleaning mechanisms and its evolution over time seems essential to achieve that aim. ADW design has remained almost invariant during the same period of time. Their evolution has mainly focused on reducing water and energy usage, with its correspondent positive environmental impact, but without focusing on a better distribution of water and integration with detergents. However, in the past few years there has also been significant progress in modelling the cleaning occurring via impingement jets. This could be implemented in newly design appliances. The state of the art in the field of automatic dishwashing clearly lacks an integrated study that combines the physical and chemical processes occurring. There is a necessity of deeply understanding the fundamental knowledge and principles involved.

CHAPTER 3

MATERIALS & METHODS

3.1. INTRODUCTION

This chapter provides detailed information on the different equipment and materials used. It also explains the methodology followed for the experimental set-up as well as the different factor levels selected in each of the studies considered. Firstly, it introduces the ADW used as a unit operation of study. Typical technical protein-bases soils are also presented as the soil system evaluated. The various analytical methods considered are explained next. Finally, the different design of experiments implemented for the study of protein-based soils behaviour under a range of alkaline and cleaning conditions are detailed.

3.2. AUTOMATIC DISHWASHER (ADW) UNIT

Water motion experiments via Positron Emission Particle Tracking (PEPT) *(Chapter 4)* and cleaning studies on a full scale ADW *(Chapter 7)* were carried out in a customised Whirlpool (DU750) dishwasher with internal loading area dimensions of 560 x 500 x 620 mm (Width x Depth x Height). The interior consisted in two baskets to place the crockery, a cutlery basket situated at the door and three spray arms (lower, medium and upper) to distribute water. The software controlling the different washing cycles was modified to offer different water pump speeds and the selection of the spray arm ejecting water. Washing time of the customised cycles could be up to 3 hours. The heating element was also controlled by the programming software, allowing to set-up temperature profiles for the running cycle. **Figure 3.1** illustrates the ADW model used and its view of the interior.

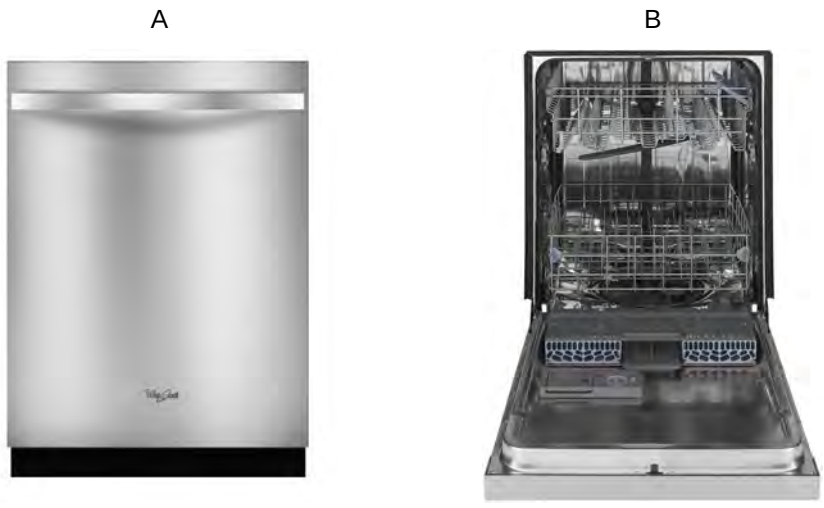

Figure 3.1. Whirlpool DU 750 Automatic Dishwasher. A – Front view. B – Interior view.

3.3. TECHNICAL SOIL

Egg yolk was chosen as the food material subjected to study. As discussed in *Chapter 2*, these soils represent a challenge within ADW industry, as they are particularly hard to remove. It is a complex mixture of proteins and lipids. Its typical dry composition comprises 33% of proteins, 62.5% of fats, less than 3.5% of minerals and 1% of carbohydrates approximately (Mine and Zhang, 2013). Despite the larger proportion of fats, samples are considered protein-based as their physico-chemical properties depend on the protein network that forms the main structure. Egg yolk is formed by high (HDL) and low-density (LDL) lipoproteins consisting on spherical particles that surround a lipid core. LDLs are the essential components that allow the emulsification of egg yolk due to their amphiphilic properties. Also, preheated samples above 70ºC have been reported to form a gel system due to the aggregation of protein networks occurring at high temperatures (Denmat *et al*., 1999; Tsutsui, 1988). At alkaline conditions, the network hydrates and swells.

Samples were obtained from Centre for Testmaterials (product DS-22/DM-22, C.F.T, BV, Vlaardingen, the Netherlands). They were made by spraying layers of egg yolk over a stainless steel or melamine base. Stainless steel substrate was used for scanning fluid dynamic gauge and gravimetric experiments as a completely flat and non-swellable surface was needed. Melamine substrates were used in tests in the ADW unit due to the white background required for colour measurements. Samples were kept in a fridge at temperatures below 5ºC until its usage. Size of the tiles were 120 mm x 100 mm with an approximate egg yolk mass of 1.75 g (±0.04 g) and an estimated initial thickness of 68 µm (±14 µm). The initial thickness was estimated by extrapolating the data obtained from scanning Fluid Dynamic Gauge (sFDG) experiments.

The initial moisture content was obtained by weighing 3 samples before and after they were deposited in a vacuum oven at 60ºC during 24 hours (Booth, 2003). 0.11 grams (±0.03 g) were lost as an average during this process. Therefore, the initial moisture content (C_0) was estimated as 0.067 g. water / g. dry sample. The amount of water initially present in the samples corresponds to a layer thickness of 9 µm.

Tiles were found to have slight different behaviour among batches. According to the supplier, a batch consisted of products prepared at the same time and with the same expiration date (6 months). As the length of the experimental work exceeded the expiration date periods, different batches were purchased over time. Two stainless steel batches (DS-22) were used for experiments shown in *Chapter 6*, while one melamine batch (DM-22) was used for experiments in *Chapter 7*. Among the stainless steel batches, the differences highlighted are reported in *Chapter 6* where the data gathered is analysed.

3.4. POSITRON EMISSION PARTICLE TRACKING (PEPT)

3.4.1. Technique principles

For the analysis of fluid motion, the University of Birmingham has developed a technique called Positron Emission Particle Tracking (PEPT), which enables non-invasive 3D spatial detection of a radioactively labelled particle (tracer). One of the greatest advantages of this technique is that it can be used for the analysis of flow within opaque systems containing metals (Parker *et al*., 1993)

These tracers are prepared by bombarding water in the Birmingham 'in-house' cyclotron producing the following reaction:

$$^{16}O + {}^{3}He \rightarrow {}^{18}F + \text{neutron}$$

^{18}F is an unstable element that decays by positron emission (ß-decay). Its half-life is approximately 110 min. These positrons are annihilated with surrounding electrons, generating emissions of back-to-back 511 keV gamma rays that can be detected. These gamma rays are emitted in couples with an angle of approximately 180 degrees and have the ability to penetrate both opaque fluids and thick metals (up to 10 cm thick)

To perform an experiment, a small (~250 to 600 µm) isokinetic radioactive tracer is placed into the system to study and a sensitive camera follows its movement. These particles are designed to be sufficiently small and insufficiently dense as to be considered isokinetic with most viscous

fluid flows. The PEPT camera consists of two parallel detectors with an effective area of 600 x 300 mm^2. Each detector is able to accurate determine the 2D spatial impact location of the gamma rays generated by the tracer. The emission angle of approximately 180 degrees makes possible to apply a triangulation method and determine the 3D spatial location of the radioactive tracer over time. The accuracy of the method can be as low as less than a millimetre with a time resolution of milliseconds.

Figure 3.2 illustrates the sequence followed to the 3D spatial detection of the radioactive tracer.

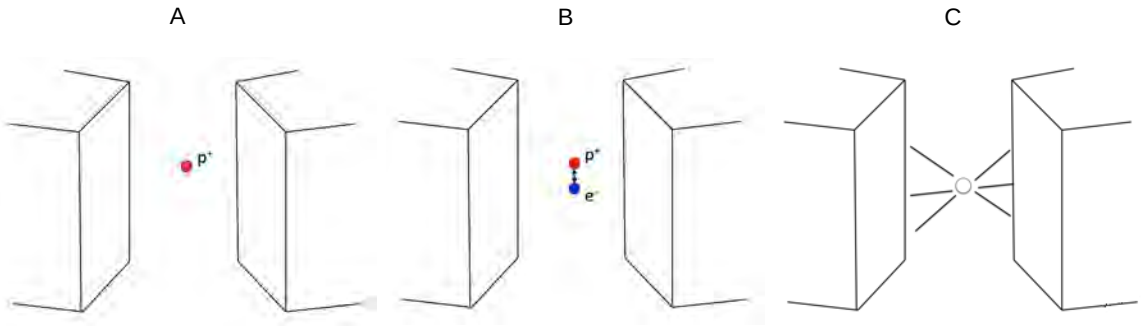

Figure 3.2. Schematic of the sequence followed to the 3D spatial detection of the radioactive tracer. A – A positron-emitting tracer is placed in the system between PEPT cameras. B – A positron particle annihilates with an electron. C – Back-to-back gamma rays are generated after the annihilation process and are detected by the two cameras.

Throughout the years, the technique has been used successfully in a wide range of experimental set-ups. Barigou (2004) gave a good overview of the capabilities of PEPT. As an example, a widely studied field has been mixing systems. Bakalis *et al.* (2004) were able to measure velocity distributions of different viscous fluids within a pipe. Extensive research has also been done in rotating systems (Ingram *et al.*, 2005; Parker *et al.*, 1997), such as in tumbling mills (Bbosa *et al.*, 2011), or for studying the segregation of different sized particles (Ding *et al.*, 2002). Additionally, PEPT has been recently used to characterise the motion of textiles in a front-loading washing machine showing its capability to describe flow in household appliances (Mac Namara *et al*., 2012).

3.4.2. Experimental procedure

Particularly, for the studies of water motion in an ADW, a radioactive tracer having a size between 250 μm – 400 μm was used per experiment. Tracers were made using the resin ion-exchange procedure explained in Parker & Fan (2008). They were coated with blue paint to enhance their visibility and to prevent the spread of activity in the aqueous environment. Each tracer was introduced at the beginning of every experiment in the bulk of water that remains at the bottom of the dishwasher.

Given the flexibility provided by the customised Whirlpool ADW, different tests conditions could be analysed. **Table 3.1** shows those variables controlled that were considered. Combinations of them were studied during the realisation of these tests.

Table 3.1. Experimental variables considered for PEPT experiments.

VARIABLE	CONDITION
Pump speed	High
	Medium
	Low
Presence of Load	'No load'
	'With load'
Detergent Use	'No detergent'
	'With detergent'.

5 litres of water were added at the beginning of each test with a temperature varying between 18-20 $^{\circ}$C. The water-heating element was disabled, as the purpose of the experiments was not to analyse the effect of temperature. Variations in water density and viscosity, which could affect the flow, were negligible in the range of temperatures used. They were measured and remained constant through the cycles. A typical concentration of 3.4 g/l of powder detergent was used to identify the effect of cleaning formulation with flow. The lower spray arm was selected to be the only one spraying water due to the constraints in the field of view of PEPT cameras. Also, as at the edges of the cameras the quality of the data can be highly compromised (Parker *et al.*, 1993), only the flow between the lower and medium spray arm was analysed.

When needed, crockery was distributed in two baskets situated at different heights. **Figure 3.3** illustrates the ADW set-up between the two PEPT cameras, the distribution of crockery and the coordinate system used as a reference. The origin of it was located at the middle bottom side of the ADW, in line with the axis of rotation of the spray arms.

A B

Figure 3.3. A - Dishwasher in between PEPT cameras. B - Dishwasher loaded with crockery and coordinates reference system.

Commercially available crockery used was a combination of 12 dinner plates (D_{cr} = 270 mm), 24 dessert plates (D_{cr} = 160 mm), 12 teacups (D_{cr} = 70 mm; H_{cr} = 60 mm), 12 glasses (D_{cr} = 65 mm; H_{cr} = 120 mm) and 12 bowls (D_{cr} = 120 mm), that are used in standardised AHAM (Association of Home Appliance Manufacturers) industry tests. Loading of the dishwasher took place according to the method: dinner plates and dessert plates were placed in the lower basket and small crockery items in the upper basket (AHAM, 1992).

The ability of a tracer to follow the fluid flow was characterised by the Stokes number (Eq. 3.1):

$$St = \frac{\tau_p}{\tau_f} \qquad \text{Eq. 3.1}$$

Where:

- $\tau_p = \frac{\rho_s \cdot d_p^2}{18 \cdot \mu_f}$ = Particle response time. Eq. 3.2
- $\tau_f = \frac{d_o}{v}$ = Fluid response time to an external disturbance. Eq. 3.3

Where:

- ρ_s = Tracer density.
- d_p = Tracer diameter.
- μ_f = Fluid viscosity.
- d_o = Duct diameter.
- v = Fluid velocity.

For St < 1, the particle is considered to follow closely the fluid streamlines while for St > 1, particle's inertia forces will start to influence particle's movement (Schetz and Fuhs, 1996).

For these calculations, the worst cases were considered for every experimental setup: highest particle diameter (d_p = 400 µm) and highest velocities found experimentally (v). Tracers' densities (ρ_s) were ~1100 kg/m^3 and water viscosity (μ_f) was ~0.001 Pa·s. To calculate the characteristic dimension of the spray arm, a rectangular duct was assumed ($d_c = 2L_dW_d/(L_d+W_d)$) with L_d = 0,01 m and W_d = 0,035 m. The characteristic dimension in the ejection step was assumed to be the most common nozzle diameter (0.002 m) in the design of the lower spray arm. For the down flow over the walls or plates, the characteristic dimension was interpreted as the thickness given when a homogeneous distribution of the amount of ejected fluid (not at the bottom or in the internal pipes) was covering all those surfaces (estimated thickness = 0.0009 m). **Table 3.2** summarises maximum Stokes numbers calculated for every condition.

Table 3.2. Stokes values.

	HIGH PUMP SPEED	MEDIUM PUMP SPEED	LOW PUMP SPEED
Spray Arm	1.1	0.88	0.63
Ejection	39.1	26.1	13.0
Down flow over walls/plates		10.3	

Results showed low values for the spray arm flow, which agreed with the isokinetic assumption. For the ejection part and downfall stages, higher values than 1 were found. A deviation of the

particle's behaviour from the fluid flow was therefore expected. The higher density of the tracer might make the particle exhibit higher resistance in the ejection path and to travel within the lowest layers (slower) of the fluid film during the downfall. However, the ejection step was very rapid in time, as it will be discussed in *Chapter 4, section 4.5.1*, and the deviation due to the inertia forces of the particle was assumed negligible.

3.4.3. Data Analysis

3.4.3.1. Pre-processing

Raw data obtained with PEPT consists of two-dimensional locations corresponding to the position of gamma-ray detections in each of the cameras. A series of algorithms were used to transform the original data with the aim of increasing the quality of the analysis carried out later. Thus, the logic behind this process focused on, firstly, transforming the data into three-dimensional locations, and then, on enhancing the quality of it by reducing its noise via smoothing and selective linear interpolation methods.

A previously developed algorithm (Parker *et al*., 1993) was used to transform this initial raw data into three dimensional tracer locations. Another algorithm was then developed to process the obtained positions. The steps taken were as follows:

I. An initial step removed all data with a spatial ***location error*** higher than 3 mm. Remaining data was hereinafter filtered out if its spatial location error was higher than the average spatial error value plus two times the standard deviation of the data not filtered initially.
II. Data was further ***smoothed*** following the procedure below:
    a. Initially, moving average intervals of **5** to **25** points were created with respect to a central point (P_o).
    b. These intervals were then fitted using **1st, 2nd** and **3rd** order polynomial equations (based on least squares method) and a new central point obtained (P_{new}).

c. Then, for every specific combination of intervals sizes and fitting orders a matrix was created with new central points (P_{new}) for each original location. Distances between consecutive points were calculated and associated to every combination. The one that showed the smallest standard deviation was the combination selected at the end of the process and its new central points replaced the original data.

d. As a restriction criterion, data was only smoothed if the 3D spatial distance within the moving average interval was less than **30** mm and/or if time difference for consecutive points was less than **0.1** seconds.

Figure 3.4 shows an example of the smoothing process for a small amount of data. A new central point (black dot) is created for the case of an interval of 9 points (blue-green dots) and the use of a 2nd order polynomial equation (green dash-line). The new central points (red dots) for that combination are shown as well. The figure also shows the data not modified due to the application of the restriction criteria (coincidence of blue and red dots).

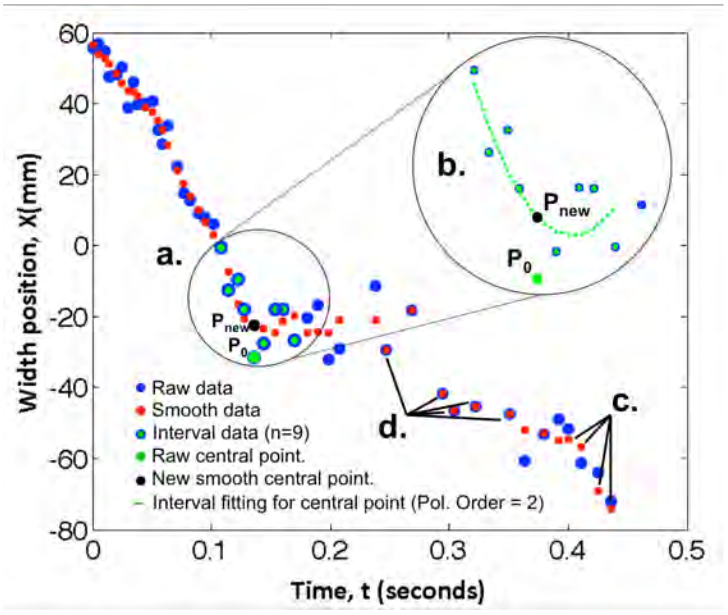

Figure 3.4. Smooth data example. Blue dots – Original Raw data; Red dots – New smoothed data; Blue-Green dots – Interval example (n=9); Green dot – Interval central point (P_0); Black dot – New central point (P_{new}); Dotted green line – Second order polynomial fitting for interval considered. a, b, c and d refer to the explanation just given in section II.

III. It was expected to get fast moving tracers at the water jets. Due to the constant data acquisition time of PEPT cameras, the number of data points was lower at that stage. To solve a similar problem (systems with a wide range of velocities), Chiti *et al*. (2011) applied a ***selective linear interpolation*** method. The authors achieved a more homogeneous spatial distribution of data points and increased the quality of the results. With that in mind, the application of this interpolation algorithm was used for spatial distances of consecutive locations between 5 mm to 20 mm. These values were chosen to be half and double the cell size (10 mm) for further Eulerian analysis. When spatial distances were smaller than the low limit, no need for generating new points was required as data spatial distribution was good enough. When, on the contrary, spatial distances were bigger than the high limit, important errors could have been introduced due to the linear trajectory considered for the interpolation.

3.4.3.2. Lagrangian velocities

Lagrangian velocities were estimated according to the method used by Mac Namara *et al*. (2012). A 'best fit' second order polynomial line was generated for every data point as a function of time and then, the gradient of which was used as the Lagrangian velocity of the tracer. These values were optimised by taking different intervals of size 'n', where 'n' is the number of points used, and minimising the least squares error in the velocity calculation.

Depending on the situation, 'n' value can be high or low. If the tracers were moving in a straight line, a high value of 'n' would give a more accurate velocity. Whereas, if there was a sudden change in the trajectory, as for example in the spray arm ejection area (nozzles), less points would be required to accurately follow this change. Illustrations can be found in the paper cited above.

3.4.3.3. Eulerian analysis

Eulerian velocity data was represented graphically in a user-defined 2D cell grid, which divided the loading area into cells of equal size (10 mm). Lagrangian velocities were time-weighted average throughout each cell providing time independent Eulerian velocity values.

Considering the rotation of the spray arm, data was represented using a cylindrical coordinate system. Angular projection was disregarded, as the ejection pattern is not modified at different angular positions. This allowed a simpler way to look at the data: a 2D grid representation of it as a function of the tracer distance from the rotation axe (middle of the spray arm) and its height was possible. **Figure 3.5** illustrates this transformation process.

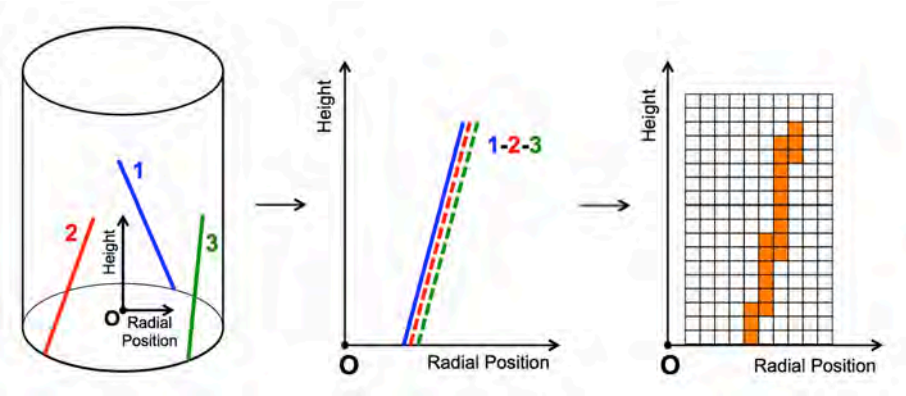

Figure 3.5. Schematic of ejection patterns.

Residence time plots represent the average time the tracer stays in every cell. These values were calculated as the tracer cumulative residence time divided by the number of passes.

3.5. COMPUTATIONAL FLUID DYNAMICS (CFD)

Computational Fluid Dynamics (CFD) complemented PEPT studies. The appliance manufacturer generated simulated data in an effort to correlate real experiments with computer modelling. PEPT data was used to refine and validate CFD results provided.

For this study, an unsteady state Eulerian multiphase model with VOF (volume of fluid) was considered. A Dynamic Fluid Body Interaction (DFBI) module was used to simulate the motion of the spray arm in response to the pressure and shear forces that the fluid exerted. The

rotational motion around the vertical axis was made free, while the motion over other axes was constrained. The moment of inertia was defined for the spray arm and the values were calculated in Pro-E software. The mass flow condition was applied at the inlet of the spray arm. A volume mesh was generated with polyhedral and prism layers, giving a total number of elements of 5 million. The time step size was kept constant at 10^{-4} sec. The simulation was run in Star-CCM+ with parallel processing on a cluster with 96 processors for 48 hrs. Post-processing was also done in Star-CCM+.

The current simulation was carried out only for the lower spray arm with an empty (no dish-load, racks & silverware basket) dishwasher. Firstly, the flow field was developed through VOF multiphase simulation for two rotations of the spray arm. Then, a Lagrangian multiphase particle tracking was performed by using water particles (with all their physical properties defined). Particle diameters were decided based on water flow rate. Particles were sent through the inlet of the spray arm and tracked through each nozzle. The same coordinates system was created in Star-CCM+ as for PEPT experimental setup. Cartesian coordinates (x, y & z) of path traced as well as the velocity component associated to every location were recorded for each particle. A total number of 106 particles were sent through the inlet of the spray arm. A comparison between PEPT and CFD data is reported in *Chapter 4, section 4.6.*

3.6. SCANNING FLUID DYNAMIC GAUGE (sFDG)

Scanning Fluid Dynamic Gauge (sFDG) was the technique selected for the analysis of the cleaning evolution of technical protein samples in a small-scale and controlled environment.

3.6.1. Technique principles

Figure 3.6 shows a picture and a schematic of the sFDG.

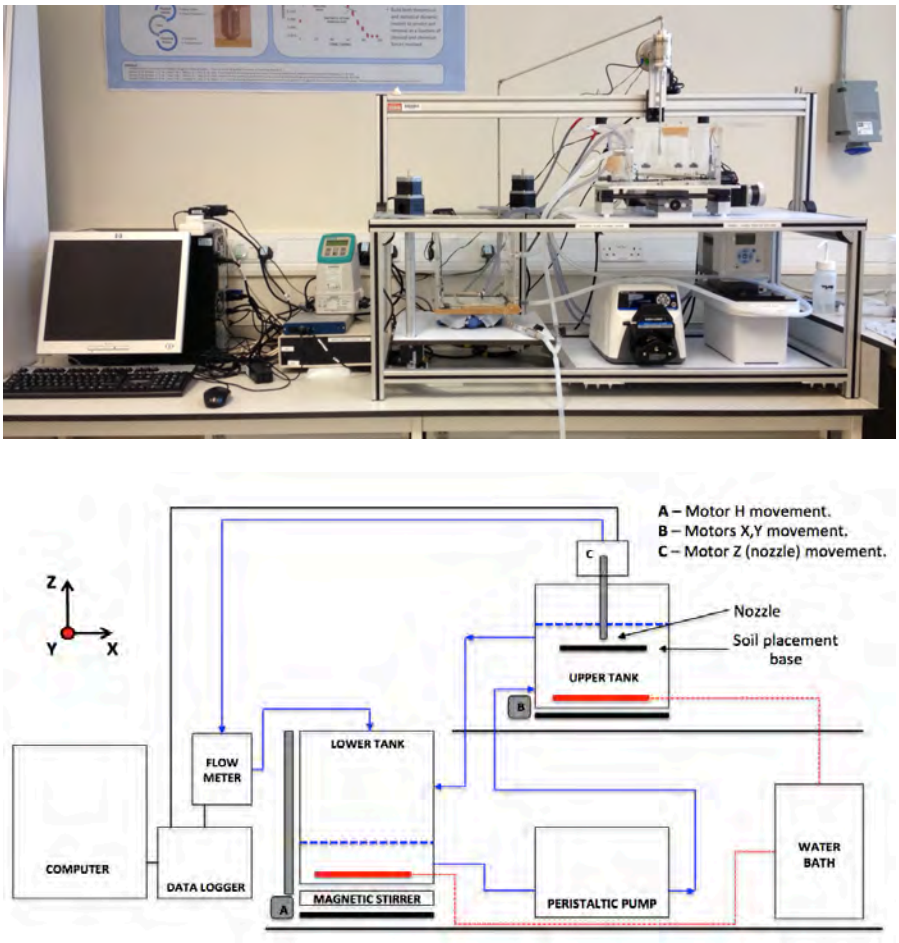

Figure 3.6. Schematic of the scanning Fluid Dynamic Gauge (sFDG).

The technique measures the change in thickness of an immobile soil sample submerged in a wash solution, in situ and in real time (Gordon *et al*., 2010). The soil sample is placed in the upper tank and a nozzle is sited on top of it. A gravity-controlled flow rate is created through the nozzle and is maintained constant over time. Any change occurring in the sample, as a consequence of its contact with the wash solution and the surface shear stress generated by the gauging fluid, produces a variation in the soil thickness (swelling or removal). A highly precise motor moves the nozzle up and down (z-axis) to compensate for this change and its consequent effect on the flow rate through nozzle. The variation in height is recorded through a data logger to a computer and transformed to the thickness of the soil. Programmable routines can be loaded via LabView^{TM}. The nozzle can track different locations over time and at different frequencies (scanning mode) as the system is equipped with two motors to move the upper tank in the ‘x’ and ‘y’ directions.

For different experimental runs, different solutions can be prepared in the lower tank. A peristaltic pump and a magnetic stirrer continuously mix the liquid through the system. The temperature of the liquid is also controlled by the presence of a water bath. Shear stress profiles generated over the sample can be changed by varying the height of the lower tank or the diameter of the nozzle, producing different flow rates through the nozzle. The shear stress applied at any time is calculated by the software controlling the sFDG according to Eq. 3.4 (Chew *et al*., 2005).

$$\tau_{wall} = \mu_f \left(\frac{3Q}{4\pi\left(a/2\right)^2} \right) \frac{1}{r} \qquad \text{Eq. 3.4}$$

Where:

- τ_{wall} = Shear stress imposed at the sample surface.
- μ_f = Fluid viscosity.
- Q = Volumetric flow rate in the tube.
- a = Nozzle-sample surface separation.
- r = Radial distance.

The following parameters can be studied: temperature, chemistry (pH, enzyme level, surfactants…), shear stress and frequency of application of the shear stress over a single point (frequency factor). The frequency factor is defined as the ratio of time the gauging fluid is imposing a surface shear stress on a particular location over the total experimental time. For more specific information, the reader is referred to (Gordon *et al*., 2012a; Tuladhar *et al*., 2000, 2002).

3.6.2. Experimental procedure

Thickness measurements over time were obtained by using the sFDG. 5 litres of deionised water were used in each experimental run. This corresponds to the typical amount of water present in an ADW during a main wash cycle. The length of the experimental runs was up to 3 hours.

The water hardness was set at 8.5 US gpg ($4.4 \cdot 10^{-3}$ M) with 0.236 g/l of $CaCl_2 \cdot 6H_20$ and 0.076 g/l of $MgCl_2 \cdot 6H_20$ (molar ratio between $CaCl_2 \cdot 6H_20$ and $MgCl_2 \cdot 6H_20$ was 3:1). Before running the experiments, all chemicals were added to the lower tank and stirred and recirculated through the system for 10 minutes. Temperatures in both tanks were monitored constantly with the aid of waterproof digital thermometers.

To provide the necessary pH, buffer solutions were prepared and pH measured with a pH meter (product Orion 4 Star™, Thermo Scientific Orion).

- For pH 9.5, 0.112 g/l of Na_2CO_3 and 0.150 g/l of $NaHCO_3$ were used ($[Na_2CO_3]$ = 1.10 mM and $[NaHCO_3]$ = 1.80 mM).
- For pH 10.5, 0.106 g/l of Na_2CO_3 were added ($[Na_2CO_3]$ = 1.00 mM).
- For pH 11.5, 0.13 g/l of NaOH were added ([NaOH] = 3.25 mM).

A detergent formulated protease was selected as the enzyme to study. The material was provided internally by Procter & Gamble. They were supplied as prills and were dissolved in water before adding them to the bulk solution.

Different shear stresses were established by varying the height of the lower tank in the sFDG and the diameter of the nozzle used (1 mm or 2 mm). Ranges of shear stresses imposed were from 12 to 65 Pa. Also, shear stress over the different locations analysed was applied at different frequencies. The frequency factor can range from 0% to 100%. A value of 0% indicates no external action on the sample during the experimental time, while a value of 100% establishes a continuous application of shear stress on the sample during the length of the experiment.

3.6.3. Typical thickness profiles. Data handling.

Figure 3.7 represents a typical thickness profile for a pure swelling process.

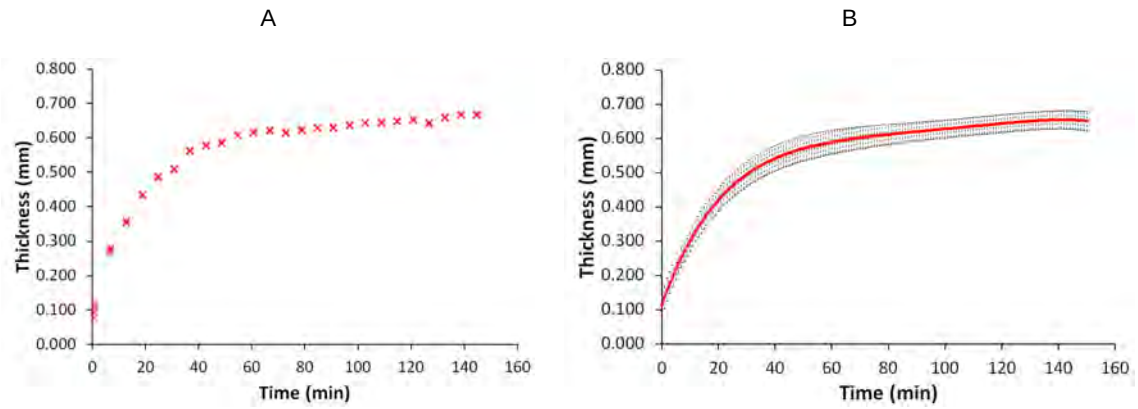

Figure 3.7. Typical thickness profile for swelling phenomenon. A – Raw data values and polynomial fitting for a single location in the run at 50ºC, pH = 10.5, [Enzymes] = None, Shear Stress Frequency = 8.5%, Net Shear Stress = 24 Pa. B – Averaged fitted experimental results and error bars for the four locations analysed in the experimental run.

Figure 3.7A illustrates thickness values of a single location for a test at 50ºC, pH 10.5, with no enzymes added and a shear stress applied of 24 Pa at a frequency of 8.5%. sFDG raw data consists of thickness values grouped at different times per location. The dispersion of each group per location corresponds to the frequency at which shear stress is applied. To determine the variability within each sample, a polynomial correlation was established for each of the locations studied (red line). Thickness values were calculated then at fixed times (i.e. every minute). The degree of the polynomial fit was set as the lowest possible to give an accurate fitting ($R^2 > 0.98$), being always 6^{th} order or lower. The use of this approach also allowed the comparison of measurements from different repetitions. Data fitted for specific times and for different samples can be further averaged. **Figure 3.7B** shows the averaged fitted data from all the six locations studied in the example and their triplicates results. By obtaining thickness values at fixed times, building mathematical models is also simplified. The same approach was used for all the experimental cases studied.

3.7. GRAVIMETRIC TESTS

Gravimetric tests were done to correlate swelling studies from sFDG *(Chapter 6, section 6.3)*. They were conducted in the upper tank of the sFDG apparatus. Samples were placed on the soil platform without any gauging action occurring. They were taken out at specific times for their weight measurement: 3, 6, 10, 15, 20, 25, 30, 40, 50, 60, 80, 100, 120, 150 and 180 minutes. Prior to the measurement, the base was dried and the excess surface water was removed by soft-shaking the tiles 10 times. They were weighed on a digital scale (product EP201, Ohaus) with an error of ±0.01 g. Once an experiment was completed, the tile was cleaned, dried and weighed again so the net sample mass could be estimated.

3.8. STATISTICAL METHODS

3.8.1. Partial Least Squares (PLS).

Statistical analyses were carried out by using JMP® software (v. Pro 11.1.1). Partial Least Squares was the method selected to analyse output data from the scanning Fluid Dynamic Gauge *(Chapter 6, section 6.2)*. This technique is a regression method typically more robust than classical principal components approaches (Geladi and Kowalski, 1986). It was initially developed for its use in econometric studies and further expanded to chemical applications. In order to gain a better insight on the method development and principles, the reader is referred to Wold (1985).

The method bases its analysis on creating alternative factors that are linear combinations of the input parameters (Xs) and interactions. The criterion to obtain these factors is to maximise the covariance existing between them and the output(s) responses (Ys). When constructing the model, software requires the input of different model effects. Depending on the experimental design selected, the availability of more or less interactions is possible. PLS approach used a NIPALS (Non-linear Iterative Partial Least Squares) algorithm (Geladi and Kowalski, 1986) to build the model, which reduced the computational time by only considering the first few principal components.

This method offers a quick and reliable prediction model and incorporates dynamic responses to the analysis. Thus, rather than single outputs, the technique enables the processing of time-evolving results (single points vs. curves responses).

As alternative information, different plots were built to prove the consistency of the analysis, the significance of the different factors analysed (overall and at a specific time) and the predictions given by the developed model.

- *Scores plots*: they represent the different X factors scores against the Y scores. Score values are typically related with the sensitivity of the different X factors extracted. These plots are used to identify any cluster of data that could be considered odd. A linear tendency indicates no unusual observations within the data set.

- *Variable Importance Plot (VIP)*: it indicates how significant a factor or interaction is independently of the fitting method used and the model construction effects. This type of plot illustrates the time-weighted contribution to the response analysed of the different factors considered. This means that the overall contribution of a factor to the response is shown, but not its impact at a specific time. A red dashed line is typically drawn at a Variable Importance score of 0.8, indicating the limit below which a variable is a candidate for deletion in the model (Eriksson *et. al*, 2006).

- *Spectral profilers:* Using PLS as a modelling technique for time-evolving responses allows spectral profilers to be made. This tool creates interactive response curves rather than single output predictions. Therefore, the time evolution of a system studied can be predicted quickly as a function of the different inputs considered. The effect of the different factors at different times and their interactions can also be observed from these graphs.

- *Normalised effect plot*: JMP software also discretises and normalises each effect studied along the different time responses obtained. These plots represent the

significance of each factor over time. Values are normalised between -1 to +1. A negative value indicates a negative effect on the response while a positive value indicates the opposite. The closer the value to -1 or +1, the higher the influence of a factor at that time.

3.8.2. Response surface (RS).

Response Surface (RS) models were built to estimate removal rates in full-scale tests *(Chapter 7, section 7.3.1)*. The RS methodology consists of the empirical modelling of one or more responses as a function of the different input factors (Bezerra *et al*., 2008). The methodology combines mathematical and statistical techniques to build the final predictions. Depending on the main factors and interactions considered, linear, quadratic of higher degree functions are inputted to describe the system. The term 'response surface' was selected as the graphical representation of the model built simulates a curve that adapts to the different input data.

3.9. KINETICS AND DEGREE OF SWELLING

The *kinetics* (time to equilibrium) of both sFDG and gravimetric data was studied through a dimensionless approach. Data was transformed and normalised by applying Eq. 3.3 and Eq. 3.4:

For sFDG data: $$\overline{h(t)} = \frac{h(t) - h_0}{h_\infty - h_0}$$ Eq. 3.3

For Gravimetric data: $$\overline{M(t)} = \frac{M(t) - M_0}{M_\infty - M_0}$$ Eq. 3.4

Where:

- $\overline{h(t)}$ = Normalised thickness at time 't'.
- $h(t)$ = Thickness at time 't'.
- h_0 = Initial thickness. Thickness at time 't=0'.
- h_∞ = Thickness at equilibrium.
- $\overline{M(t)}$ = Normalised sample mass at time 't'.
- $M(t)$ = Total sample mass at time 't'.

- M_0 = Initial sample mass. Sample mass at time 't=0'.
- M_∞ = Total sample mass at equilibrium (t=∞).

The new relative values (0-1 scale) indicate the equilibrium degree achieved at any experimental time. The approach makes all experiments comparable independently of the degree of swelling. By plotting thickness dimensionless values versus gravimetric ones for pairs of data at the same experimental time, a graphical comparison is also possible. Data from both experimental techniques is in agreement if they follow a line with a slope of 1 and the intercept is at 0. This means that the same equilibrium degree is achieved at the same time independently of the technique used. The addition of a time-based scale to the figures, also allowed the comparison of the time to the equilibrium for the different experimental conditions. **Figure 3.8** represents a schematic of the possible scenarios.

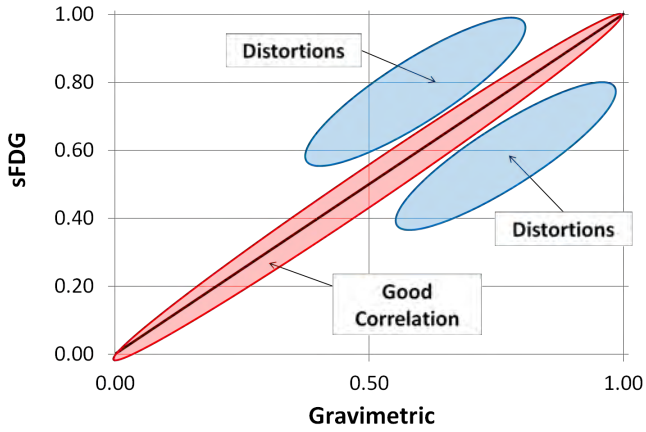

Figure 3.8. Dimensionless comparative approach.

The black line represents a line which slope equals to 1. Distortions are highlighted when values are found above or below it. For pairs of data found above the line, the theoretical equilibrium would be reached faster by sFDG tests than by gravimetric measurements. Thickness relative increase would be much higher than water uptake for the same experimental conditions. The opposite case would happen when values are seen below the line.

To study the *degree* of swelling, the comparison was done in absolute values. To do so, mass was estimated from the thickness data (sFDG) by applying Eq. 2.4 and values were directly compared.

3.10. SOLUTION OF EQUATIONS FROM DIFFUSIONAL THEORIES

Equations from Fick's second law (Eq. 2.3 and Eq.2.4) were solved via an algorithm developed in MATLAB® (see Appendix A.3) by applying a forward finite difference method. It was assumed that the bottom face of the sample $(z = 0)$ was attached to a rigid surface with no diffusion occurring at this position. Also, the top face $\big(z = h(t)\big)$ was considered to be freely exposed to the solvent. Thus, liquid penetration occurred from top to bottom. The sample was considered to swell uniformly in one direction (z), with a constrained or negligible lateral stretch. At each time step, swelling of the sample (Eq. 2.4) was incorporated and the total thickness was discretised again to compute for this change. The assumption of an instantaneous equilibrium at the boundary layer between the network and the fluid together with a zero flux at the bottom layer were considered as boundary conditions. Additionally, the diffusional coefficient was assumed to be constant and independent of the moisture gradient. The initial condition assumed a homogeneous distribution of the initial moisture content within the sample. The boundary and initial conditions are expressed as follows:

- Initial Condition: $t = 0 \rightarrow C = C_0$
- Boundary Condition 1: $C\big(z = h(t)\big) = C_{eq}$
- Boundary Condition 2: $z = 0 \rightarrow \frac{\partial C}{\partial z} = 0$

The effective diffusion coefficient values (D_F) were calculated by minimising the error between experimental and numerical results.

The estimation effective diffusion coefficients from linear poroelasticity theory (D_L) (Eq. 2.5) was also carried out by minimising the error between experimental and numerical data. Parameters included in the first term $(\upsilon, \hat{\mu}, G_{SM})$ on the right side were not estimated as the rheological

characterisation of the soil samples was out of the scope of this study. Knowing these parameters was not necessary as the thickness increase between the equilibrium and the initial conditions (Eq. 2.6) was estimated from experimental data.

Finally, the same assumptions used for Fick´s second law were considered to solve the equations from non-linear theory (Eq. 2.7 to Eq. 2.12). A forward finite difference method was used to determine a solution for Eq. 2.7. The initial condition assumed an isotropically swollen state with an initial swelling ratio of λ_0. Boundary conditions established the instantaneous equilibrium at the top surface ((BC1: $\lambda\left(z = h(t)\right) = \lambda_\infty$) and the condition of zero flux at the bottom surface (BC2: $J_z\,(z = 0) = 0$). After a long time $(t \to \infty)$ the system evolved to an equilibrium state ($\lambda = \lambda_\infty$). Stretch profiles obtained (λ) were integrated over the layer thickness in the dry state (h_{dry}) by applying Eq. 2.9 to calculate net thickness values over time. Finally, Eq. 2.10 was used to relate the equilibrium stretch (λ_∞) with λ_0 and other intrinsic parameters: N, Ω and χ.

Three variables were unknown: Flory-Huggins parameter (χ), the effective number of polymer chains per unit volume of the polymer (N) and the non-linear effective diffusion coefficient (D_{NL}). To estimate them, an iterative process between the two available equations (Eq. 2.7 and Eq. 2.10) was established. The range of values considered was 10^{-13} to 10^{-9} m^2/s for D_{NL}, 0 to 1.2 for χ, and 10^{25} to 10^{28} for N, according to previously reported values in literature (Hong *et al.*, 2009). The estimation process started by obtaining stretch profiles ($\lambda(z,t)$) using Eq. 2.7 for multiple combinations of the three unknown variables. These results were then used to calculate thickness values over time by applying Eq. 2.9. Finally, experimental and predicted values were compared and a coefficient of determination (R^2) calculated. Additionally, it was checked that Eq. 2.10 gave a value close to zero. From an assumed value of N, χ could be estimated and vice versa. However, this would not take into account any experimental error in λ_0 and λ_∞ and would reduce the number of possible combinations. Therefore, a sensitivity analysis was performed in order to define an acceptable margin around zero that satisfies Eq. 2.10. The iteration showing the highest coefficient of determination (R^2) and satisfying the margin error was the chosen solution.

Figure 3.9 illustrates, for different iterations, the coefficient of determination (R^2) calculated and the left side value from Eq. 2.10.

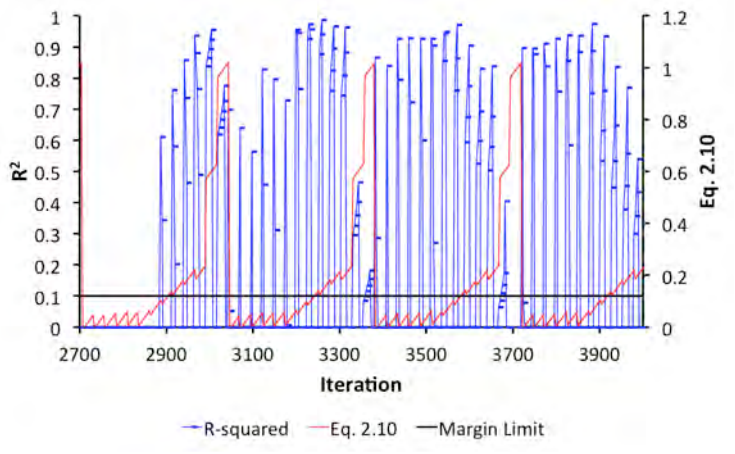

Figure 3.9. Variability of the iterations. Coefficients of determination (R^2 – y-main axis) estimated by using Eq. 2.7 and Eq. 2.9 and values from the left side of Eq. 2.10 (y-secondary axis) for different iterations.

Local maximums were seen for R^2. The first term of Eq. 2.9 oscillated around values close to 0, except for some iterations where it increased suddenly to values up to 1. As the range given was around 1, a threshold value of 0.12 (black line) was established as a margin error. This was in accordance with the experimental error ($\sim 12\%$) calculated. This margin allowed most of the combinations possible between and χ and N in the range considered for each factor.

3.11. IMAGE ANALYSIS (IA)

Image analysis was carried out in full-scale tests *(Chapter 7, section 7.2)* for the cleaning evaluation of technical protein-based soils.

3.11.1. Technique principles

When possible, visual techniques always represent an alternative to measure cleaning. Traditional approaches are based on individual visual judgements that tend to be very subjective. To avoid this, the International Commission on Illumination (CIE as it stands for its original French title 'Commission Internationale de l'Eclairage') (CIE, 2014) developed a colour

space named CIELAB (Tkalcic and Tasic, 2003). The space introduces three vectors to describe colours: a luminance vector (L) and two chromatic components (a & b). It was designed as a quantitative measurement of colour equivalent to the human eye. The main characteristic is that the human visual perception is highly correlated with the Euclidean distance between two defined positions in the L*a*b reference space. The introduction of CIELAB space established a more consistent way to visually characterise cleaning as reproducibility increased.

Figure 3.10 shows the schematic representation of the L*a*b colour space defined.

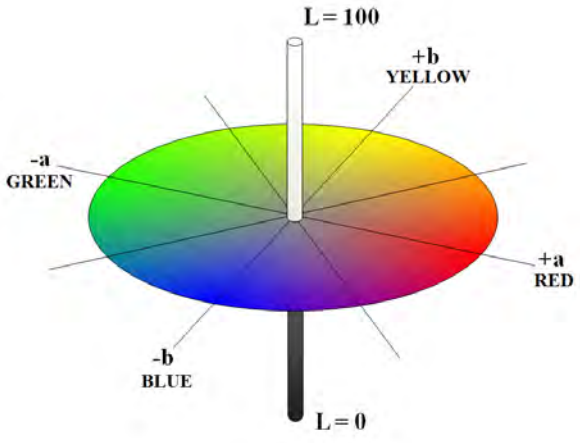

Figure 3.10. Schematic representation of the CIELab colour space.

Pictures are typically taken in RGB colour spectra, where a particular colour is expressed by a combination of the three primary colours: Red, Green and Blue (Sharifzadeh and Clemmensen, 2014). RGB spectrum is a device-dependent colour space and therefore alternative set-ups are not comparable. Contrarily, CIELAB (or commonly know as L*a*b) colour scale is a device-independent colour space, thus the use of this method is more suitable. The range of the luminosity vector (L) goes from 0 to 100, while the range of 'a' and 'b' vectors go from -128 to +128. The colour contrast between two different points given is calculated as the Euclidean distance between them. Therefore, it can be expressed as follows:

$$Contrast = \sqrt{(\Delta L)^2 + (\Delta a)^2 + (\Delta b)^2} \qquad \text{Eq. 3.5}$$

3.11.2. Camera kit

A waterproof camera was the tool used to gathered online images through the wash cycle. A waterproof torch with good resistance to high temperatures was also used as the light source inside the ADW. Specific details on the design and set-up of the camera kit have been intentionally avoided to preserve its confidentiality. The system aimed to evaluate the cleaning evolution of technical CFT tiles.

3.11.3. Experimental procedure

Full scale cleaning tests studied temperature, pH and enzyme level effects on egg yolk samples over a melamine substrate. The customised Whirlpool ADW was programmed to run at two constant washing temperatures (30ºC and 55ºC) with only the lower spray arm ejecting water. Three different pH values (9.5, 10.5 and 11.5) were selected. The same protease as for sFDG experiments was used and three different concentrations established: 0.02 g/l, 0.06 g/l and 0.10 g/l. The camera, torch and CFT sample were placed in the dishwasher at the back-left side of the lower basket. Experiments were done for a spray arm rotation rate of approximately 35 rpm. The length of the cycles was up to 2 hours without any initial or final rinse stage. The torch light was set at its lowest intensity and lit up at least 15 minutes before the start of any experiment to compensate for its initial decay in intensity (Schubert, 2006). Deionised inlet water was preheated in an external tank at the desired temperature so no extra heating effort from the dishwasher was needed. The water hardness was initially established at 8.5 US gpg ($4.4 \cdot 10^{-3}$M) by following the same procedure as for sFDG tests. Chemistry required was added at the bulk water at the bottom once the dishwasher finished filling it up. Chemicals were mixed during 5 minutes before the camera, torch and CFT sample were placed internally. Pictures were taken every 5 seconds and information collected until the camera shut down (typically 65-70 minutes). Triplicates were done for each experimental condition considered. Once a experiment was completed, images were loaded to a computer for further processing.

3.11.4. Image processing and data analysis

A customised software was used to analyse the pictures taken during a test. Initially, the software requires the selection of the area of interest (tile area) to crop the images around it. Typical cropped areas were 1250 x 750 pixels approximately. Cropped images were evaluated by transforming their initial RGB colour values into L*a*b ones (Jin and Li, 2007). The white colour reference was established by selecting the picture of a completely cleaned tile. Colour contrasts between the white reference and images taken at different times were then estimated. A Stain Removal Index (SRI) scale was defined as expressed in Eq. 3.6 (Neiditch *et al*., 1980). The definition established a range of values between 0 and 100. A value of 0 indicates no cleaning (or colour change) when compared to the initial soiled tile. A value of 100 indicates a complete cleaning or complete colour matching with the 'cleaned white tile' used as a reference. As the initial colour starting point might differ from tile to tile, pure contrast changes are not comparable. By normalising the values with regard of the initial colour contrast, a homogeneous scale was then obtained. The representation of the SRI over time allowed the estimation of cleaning rates. The slope of the curve represents the cleaning percentage change over time (i.e. %/min).

$$SRI\ (\%) = \frac{(Contrast)_{t=0} - (Contrast)_{t=t}}{(Contrast)_{t=0}} \cdot 100 \qquad \text{Eq. 3.6}$$

As cleaning was evaluated by comparing all the area of interest, average values of L, 'a' and 'b' vectors were calculated per cropped image. This reduced the noise and the computational cost.

3.12. DESIGN OF EXPERIMENTS

Swelling and removal studies in protein-based samples *(Chapter 6)* were initially performed by establishing different Design of Experiments (DOE). A first approach considered the development of statistical models on the data collected via sFDG. Swelling mechanism was further studied in detail by correlating sFDG and gravimetric data. The following describes the experimental design selected for each of these cases.

3.12.1. Dynamic Statistical models

Two different approaches were considered. Firstly, only swelling phenomenon was analysed via sFDG. Screening studies showed no decrease in thickness without the addition of enzymes, except at high alkaline and temperature conditions (i.e. 55ºC and pH 11.5). A 3 level full-factorial DOE was established to study the influence of temperature and pH as main contributors to swelling. pH levels were: 9.5, 10.5 and 11.5. Temperatures levels selected were: 30ºC, 42.5ºC and 55ºC. These ranges were within typical values in an ADW wash cycle. Net shear stress applied and the frequency factor were considered to have a negligible influence over the initial (most important) stage of the swelling process (i.e. first 30 minutes). A total number of 9 experiments were run. 4 different locations were studied in each experimental run. The position of the nozzle changed every minute and shear stress over a particular location was applied for approximately 30 seconds in intervals of 4 minutes. This corresponded to a frequency of application of shear stress of 12.5%. Shear stress imposed over the tile was 18 Pa. No enzymes were added. **Figure 3.11** illustrates the locations studied over the samples.

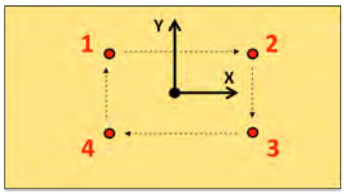

POINT	X (mm)	Y (mm)
1	-20	20
2	20	20
3	20	-20
4	-20	-20

Figure 3.11. Schematic of points analysed while using sFDG.

A second DOE was developed to incorporate the removal stage in the analysis of the soil evolution. A 22 experiments custom-design was established. Temperature and pH ranges remained the same. Enzyme levels were set between 0.02 g/l and 0.10 g/l, being the commercial formulated level somewhere in between these concentrations. Shear stress imposed was established from 12 Pa to 65 Pa. This matched the lowest and highest shear stress exerted by the gauging fluid. Frequency factor ranged from 8.5% to 100%. A frequency factor of 8.5% was set by tracking 6 different locations per sample. As the nozzle needed time to move from one location to another, the imposition of external shear stress lasted again approximately 30 seconds per location. The scanning sequence was repeated every 6 minutes.

A frequency factor of 100% means that the nozzle was sited over a single location for the duration of the experiment. **Figure 3.12** shows a schematic of the movement of the nozzle for each of the extreme frequency factors considered.

A

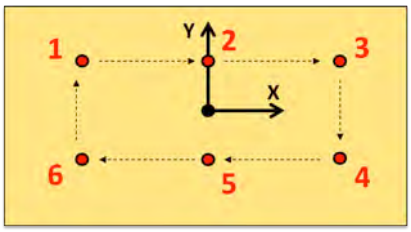

POINT	X (mm)	Y (mm)
1	-30	20
2	0	20
3	30	20
4	30	-20
5	0	-20
6	-30	-20

B

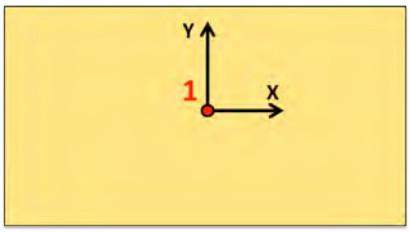

POINT	X (mm)	Y (mm)
1	0	0

Figure 3.12. Experimental set-up for different frequencies of application of shear stress. A – Six points analysed for frequency factor at 8.5%. Movement of the nozzle from point to point occurred every minute. B – Single location analysed for frequency factor at 100%. Nozzle was constantly sited on top of the location studied.

Table 3.3 summarises the two different experimental approaches taken:

Table 3.3. Summary of the two different Design of Experiments considered.

MODEL	FACTORS	RANGE CONSIDERED	TYPE OF DESIGN
Swelling (Nil enzyme)	*Temperature*	30ºC – 55ºC	Full Factorial (9 experiments)
	pH	9.5 – 11.5	
Swelling + Removal (With enzymes)	*Temperature*	30ºC – 55ºC	Custom design (22 experiments)
	pH	9.5 – 11.5	
	Enzyme	0.02 g/l – 0.1 g/l	
	Shear Frequency	8.5% - 100%	
	Shear Stress	12 Pa – 65 Pa	

3.12.2. Swelling studies

Temperature and pH were selected as the factors to study for both sFDG and gravimetric tests. Preliminary statistical studies showed that the effect of pH on swelling was higher than temperature. Therefore, for the design of the experiments 3 levels were selected for pH (9.5, 10.5 and 11.5) and 2 levels for temperature (30^{o}C and 55^{o}C). This resulted in a combination of 6 different set-ups as shown in **Table 3.4**. Triplicates were measured for each case and the order of the experiments randomized. Tests were run for 180 minutes.

Table 3.4. Design of experiments for swelling studies.

EXPERIMENT	TEMPERATURE	pH
1	30ºC	9.5
2	55ºC	9.5
3	30ºC	10.5
4	55ºC	10.5
5	30ºC	11.5
6	55ºC	11.5

For the sFDG runs, 4 points were analysed per sample to asses the variability within a tile. The frequency factor was again set about 12.5% of the total experimental time. Shear stress applied over the samples was kept constant at 18Pa. Gravimetric tests were performed according to the procedure explained in *section 3.7*.

CHAPTER 4

ANALYSIS OF WATER MOTION INSIDE AN ADW

4.1. INTRODUCTION

In this chapter, Positron Emission Particle Tracking (PEPT) is used for the analysis of water flow in a typical dishwasher. The description of water flow in ADWs is critical to create the foundational knowledge required to link physical and chemical phenomena as water is the key element driving both. A typical water sequence is determined and Lagrangian velocities estimated. Eulerian flow-field studies are performed to determine velocity profiles and residence time distributions over the inner volume of the ADW. Finally, PEPT data is compared with Computational Fluid Dynamic (CFD) data at the same experimental conditions. ADWs show the peculiarity of not being completely filled with water. Therefore, this study can also be used as a proof of concept for similar systems (i,e. sprinklers or pipe cleaning spray-balls). This chapter also aims to understand the role that direct impingement jets might have on cleaning phenomenon in these appliances.

4.2. MOTION OF THE TRACER PARTICLE

Figure 4.1 shows a typical tracer path sequence.

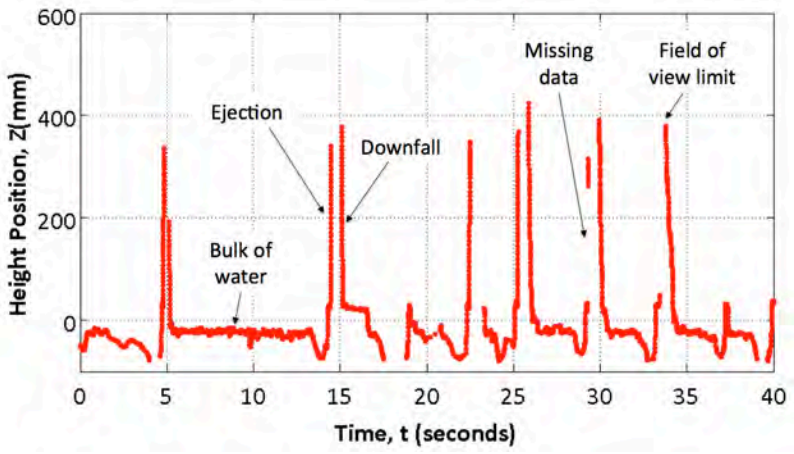

Figure 4.1. Time series of a typical tracer path during an interval of 40 seconds in a wash cycle.

The rapid increase in 'z' direction indicates an ejection from the lower spray arm and the decrease the downfall. The tracer was ejected every few seconds and appeared to follow a straight line (see further *section 4.3*). Sometimes, parts of the particle paths were missing (i.e.

time = 25s.), as particle locations could not be accurately detected. Above 400 mm, the tracer was outside the field of view of PEPT cameras and locations were not collected either. Most of the time the tracer was located at negative 'z' values, which corresponds to the bulk of water remaining at the bottom of the dishwasher.

Figure 4.2 describes the different steps of a typical ejection.

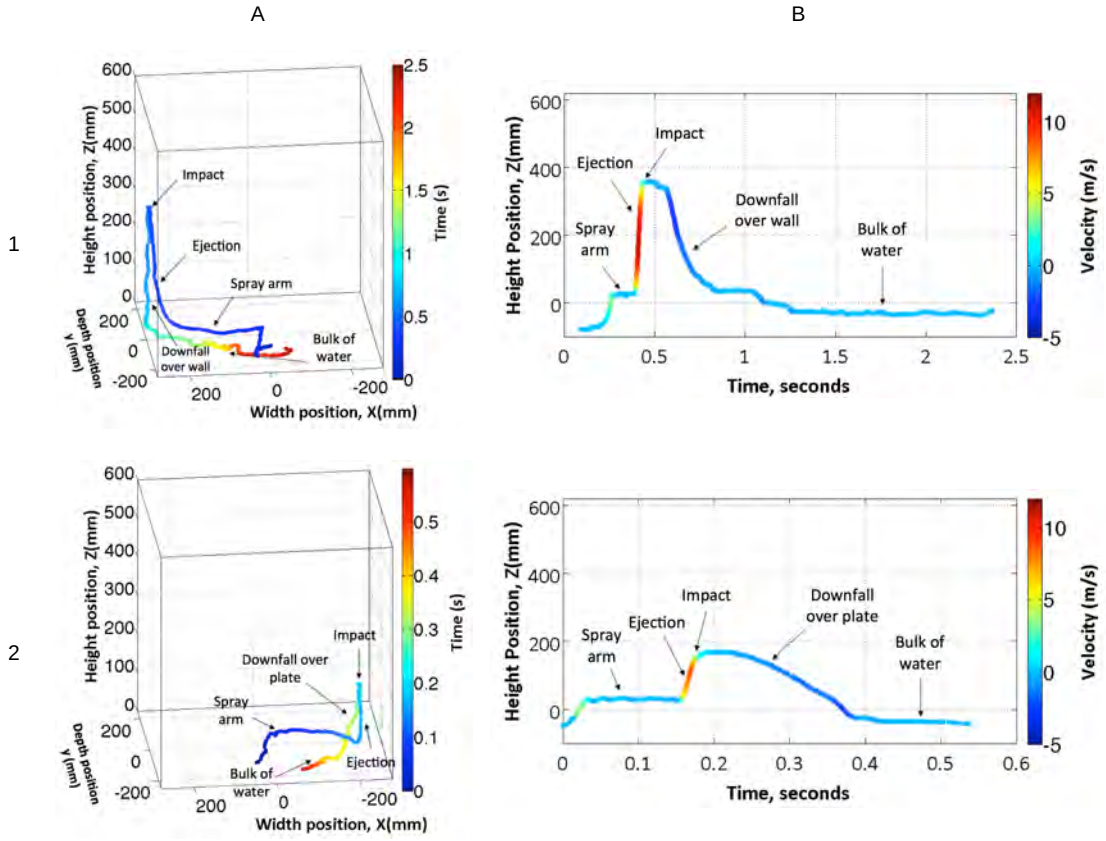

Figure 4.2. Typical water sequence inside an ADW. 1 - 'No load'; 2 - 'With load'; A- 3D plot scattered over time; B – Time sequence scattered over velocity.

Regardless of the presence of load (crockery and cutlery), the same pattern was observed: namely movement inside the pump and spray arm, ejection, impact on the wall or crockery, downfall (either over crockery, walls or free falling) and back to the bulk of water. The time scale of the process was typically less than 3 seconds and the highest velocity values were found upon ejection.

The ‘downfall over plate’ stage (***Figure 4.2B2***) happened within tenths of a second. The residence time is of importance in terms of the mechanism of transfer of surfactant/enzymes over the soils. As the amount of water present is not constant, cleaning phenomena are likely to differ from situations where soils are submerged constantly in cleaning solutions.

4.3. CHARACTERISATION OF JETS

Figure 4.3 represents the path typically followed by the tracer during its movement inside the spray arm and the subsequent ejection from three different points of view.

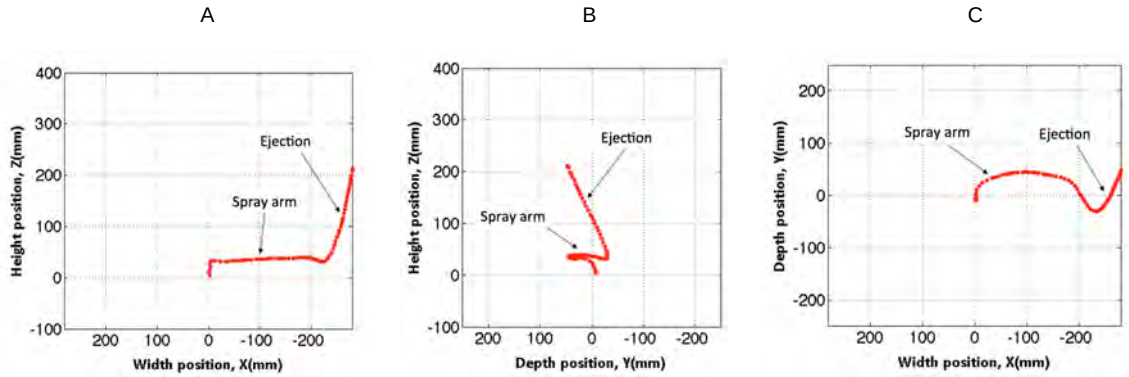

Figure 4.3. Typical water jet path. A – Front view. B – Side view. C – Plan view.

Plots illustrate that, once water was ejected, the tracer moved in a straight line, with no effect on its trajectory from the rotation of the spray arm. This suggests that the rotational inertia given can be disregarded with respect to the vertical and radial components (considering a cylindrical coordinates system). Therefore, specific locations are targeted from specific ejection points. For a given time, jets trajectories can be considered as fixed vectors. A complete and continuous coverage of all areas with direct impingement jets was also impossible due to this fact. Jets impact a specific location with a frequency related to the rotation rate of the spray arm.

Figure 4.4 shows the fitting of a 3D line over multiple particle locations corresponding to a water jet ejection.

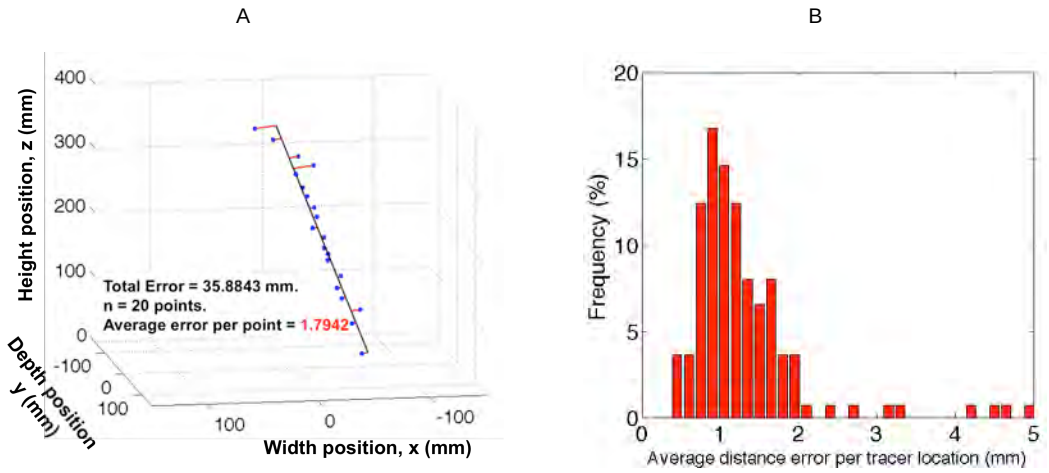

Figure 4.4. A – 3D fitting of tracer locations in an ejection stage. B - Histogram error values for the fitting of all ejection paths obtained.

The analysis was done before the 'smoothing' and 'interpolation' steps *(see Chapter 3, section 3.4.3)*, so any artificial change in the data that can cause interactions in the linearity was avoided. Linear fitting was done by obtaining the line with the lowest error of approximation. This error was calculated as the sum of all orthogonal distances (represented in **Figure 4.4A** by the red lines) from the different tracer locations to the line and dividing this value by the number of locations considered. Therefore, an average distance error per tracer location was estimated for a single ejection analysed. **Figure 4.4B** shows a distribution of the averaged distance errors calculated for all the ejections seen. Most of the error values were found to be lower than 2 mm, with the highest concentration seen at values around 1 mm. These error distances fell within the inner tracer error per location as commented in *Chapter 3, section 3.4.1*. The low error values obtained agreed with the assumption of linearity in the water path once it is ejected.

In **Figure 4.5**, a photo taken using a high-speed camera shows the path that a single jet follows inside an ADW. Photos were taken through a Perspex® window replacing one of the sides of a commercially available dishwasher. The linearity in the jet trajectory was again observed.

Figure 4.5. High-speed camera capture from the inside of an ADW.

4.4. EULERIAN ANALYSIS

As spray arms in ADWs rotate around a fixed axis, cylindrical coordinates were used in the following analysis. A symmetry problem is spotted as loading of crockery occurs along a rectangular symmetry while the distribution of water is produced in a cylindrical-rotational way. This issue is commented in more detail in *Chapter 5*.

4.4.1. Velocity profiles

Figure 4.6 illustrates velocity contours for different experimental conditions. Data was grouped as a function of the different steps of the sequential process explained in *section 4.2*. As for a fixed cell location up-flow and down-flow movement might co-exist, plots were divided in two rows to avoid any distortion in data analysis. Contours from tracer locations corresponding to the motion in the spray arm, injection and upward movement are shown in the first row, while contours from tracer down-flow movement and stay in the bulk of the water at the bottom are shown in the second row. Velocity values are given in absolute terms for an easier comparison. In the first row, tracer movement was ascending (ejection step) and followed the positive direction of the height axis. In the second row, tracer movement was the opposite and followed the negative direction of the height axis. Velocity colour map scale was set to be the same for all plots shown, being the upper limit the highest velocity found over all experimental conditions.

In the first row, spray arm area is shown at heights below 30 mm. Above this height, velocity contours represent the tracer ejection movement. The impact of a water jet on surfaces was hard to characterise through these experiments, as the number of points collected for this phenomenon was quite small. For those experiments with 'no load', impact areas were found in dishwasher walls, that is, at high radial distances. However, with presence of load, impacts could happen anywhere, producing high distortions on data results (combination of high velocity values for ejections and low velocity values for impacts). As a consequence, impact data was removed to preserve quality in the analysis. A small gap in coverage at around 100 mm (radial position) can be observed in **Figures 4.6A & 4.6B (first row)**. The specific design of the spray arm was responsible of this. The consequence was that water arriving at those areas did not come directly from a jet but from water being splashed or during the subsequent downfall stage.

Pump speed effect over the ejection velocity can be seen in **Figures 4.6A, 4.6B & 4.6C (first row).** Tracer velocity increased for higher pump speeds as expected. Contours can be considered highly homogeneous over the whole ejection area (above 30 mm) and are not a function of the radial distance. A velocity transition was observed at the vicinity of the ejection points (heights between 30 mm to 50 mm). This effect will be analysed in detail in *section 4.5.2*.

In the second row, water downfall over the wall was found at high radial distances. From the Stokes number analysis, the tracer particle could be considered in this stage as a small soil substance and conclusions still can be made. Low velocity values, corresponding to a dark blue colour, were seen. At lower radial values, two behaviours can be identified depending on the presence of load or not. In Figures 4.6A & 4.6B (second row), and for cases where crockery was not present, tracer downfall inevitably followed a free falling movement driven by gravity from the roof of the dishwasher (pale blue to green colour). The same pattern was obtained independently of the *pump speed*, suggesting that the effect of the pump energy input is negligible over the downfall stages.

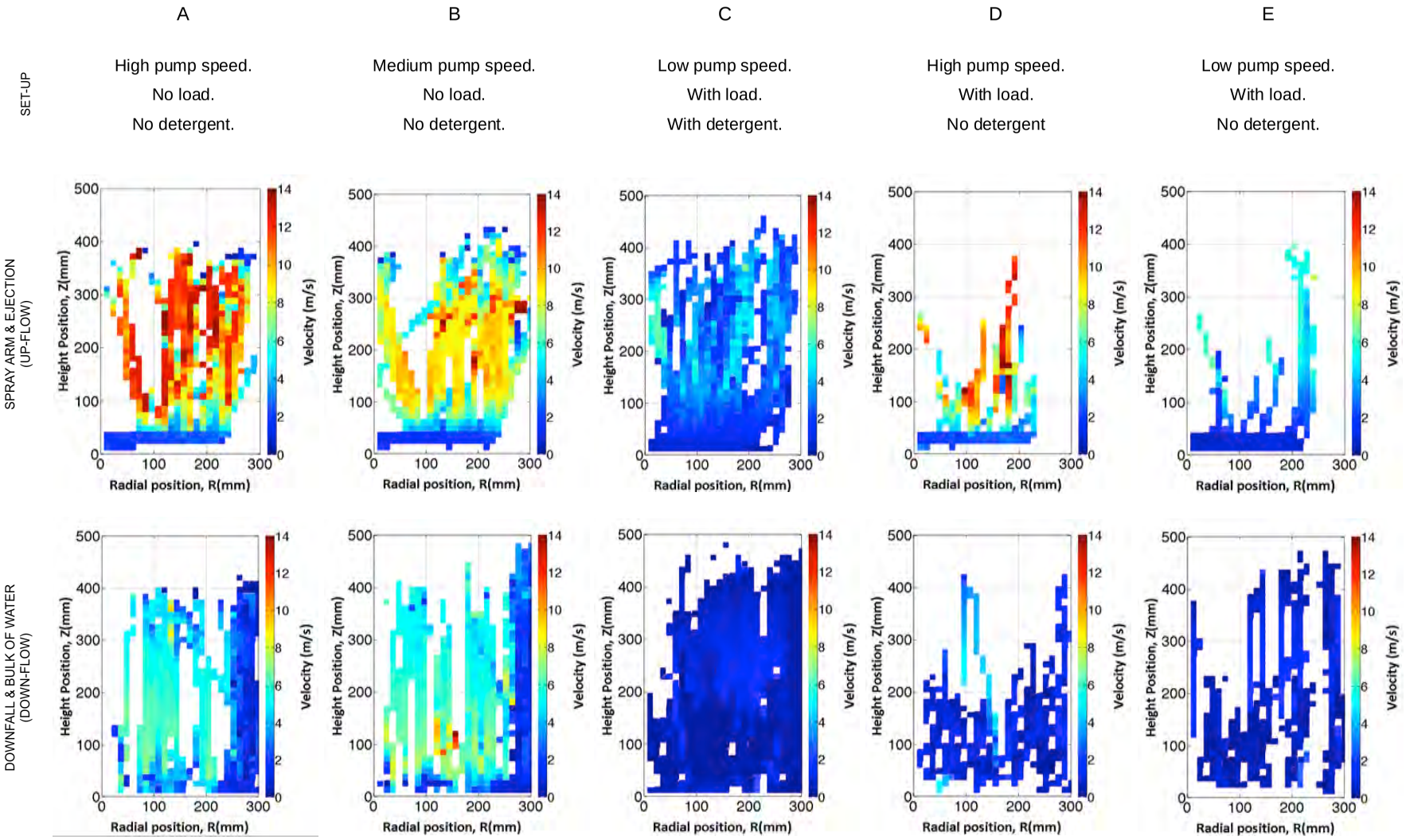

Figure 4.6. Eulerian velocity distributions plots for 5 different experimental set-ups. Impact effect in up-flow movement has not being considered.

When *crockery* was present, tracer downfall velocities were reduced significantly, matching those velocities found at the walls for 'no load' conditions. Therefore, a system 'with load' can be seen as a succession of small walls grouped together. In **Figure 4.7**, the velocity colour map scale was adapted for a typical experiment 'with load'. The upper limit in the scale was re-set to the highest velocity found in that contour plot to allow for a better distinction between areas in the downfall step.

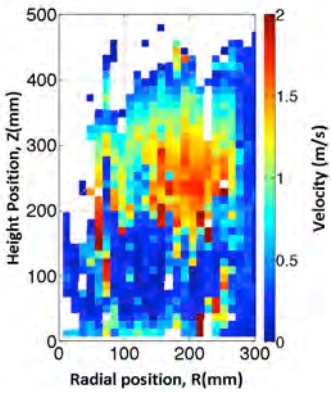

Figure 4.7. Eulerian velocity plot for downfall stage. Experimental conditions: High pump speed, with load & with detergent.

The lowest velocity values were found at a low height, corresponding to the bottom of the plates situated in the lower basket. Low velocity values were also found at the edge of PEPT cameras (~400 mm) where the top basket was located. From top positions, the tracer fell down and increased its velocity (from 400 mm to 200 mm). As it went down the likelihood to impact a plate increased. Once the impact happened, a reduction in velocity occurred (40 mm to 200 mm). A sharp transition in velocity can be seen at heights around 200 mm. In this lower velocity area, the tracer downfall velocity did not seem to change significantly. The high homogeneity found suggests that the distribution of shear stresses (mechanical energy input) over the crockery was low. Tracers were washed down at a very low speed even though they were gravity-aided. High velocity profile areas occurring before the film jump might had been very localised and spaced in time, thus they did not influence averaged results. Other factors affecting the low tracers' velocities could be the inner curvature of plates at their edges, which made the slope smaller; flow resistance forces from tracers; or the higher packing factor at low heights due to the

presence of both dinner plates (D_{cr}=270mm) and dessert plates (D_{cr}=160mm), which made less water reach those areas.

Finally, the *use of detergent* did not seem to affect significantly the flow inside a dishwasher. Comparing **Figure 4.6C & 4.6E**, one would not observe any significant difference on the range of velocity values. Less data was obtained for case E due to a lower radioactivity of the tracers used.

4.4.2. Residence times

Residence time plots indicate the average absolute time the tracers spent in every cell location. These plots aid to highlight those 'dead zones' of the system in which the fluid flow is low in comparison to the average of the system. This time is a function of the tracer velocity but not the number of tracer passes. **Figure 4.8** shows a contour plot of residence time for a typical dishwasher set-up, with load and detergent, and for the down-flow stage.

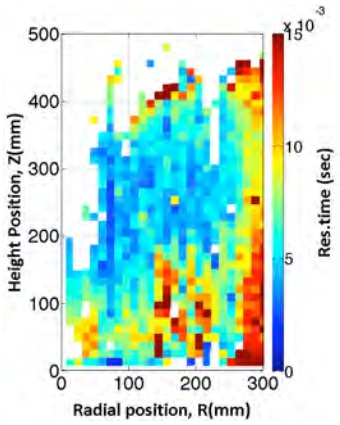

Figure 4.8. Residence time contour for down-flow movement.

Experimental set-up: low pump speed, with load & with detergent.

Regions with higher residence times were found again on walls and crockery areas. The tracer seemed to stay longer at the lower heights of walls (i.e. z < 100 mm) and at the edges of the bulk of water that remained at the bottom of the dishwasher (i.e. R ≈ R_{max}). These zones had very low velocity and were stagnant areas. At heights between 10 mm to 100 mm, corresponding to high packing ratio areas, high residence times were observed as well. These

regions might potentially enhance chemical processes as the contact between soils and chemicals is produced for longer. They also combined low mechanical input from the appliance.

4.5. CFD & PEPT DATA COMPARISON

4.5.1. Eulerian comparison

Figure 4.9 shows Eulerian velocity contours for (A) CFD and (B) PEPT data. Experimental and simulated conditions were: medium pump speed, 'no load' and 'no detergent'. The same division between up-flow and down-flow was also carried out.

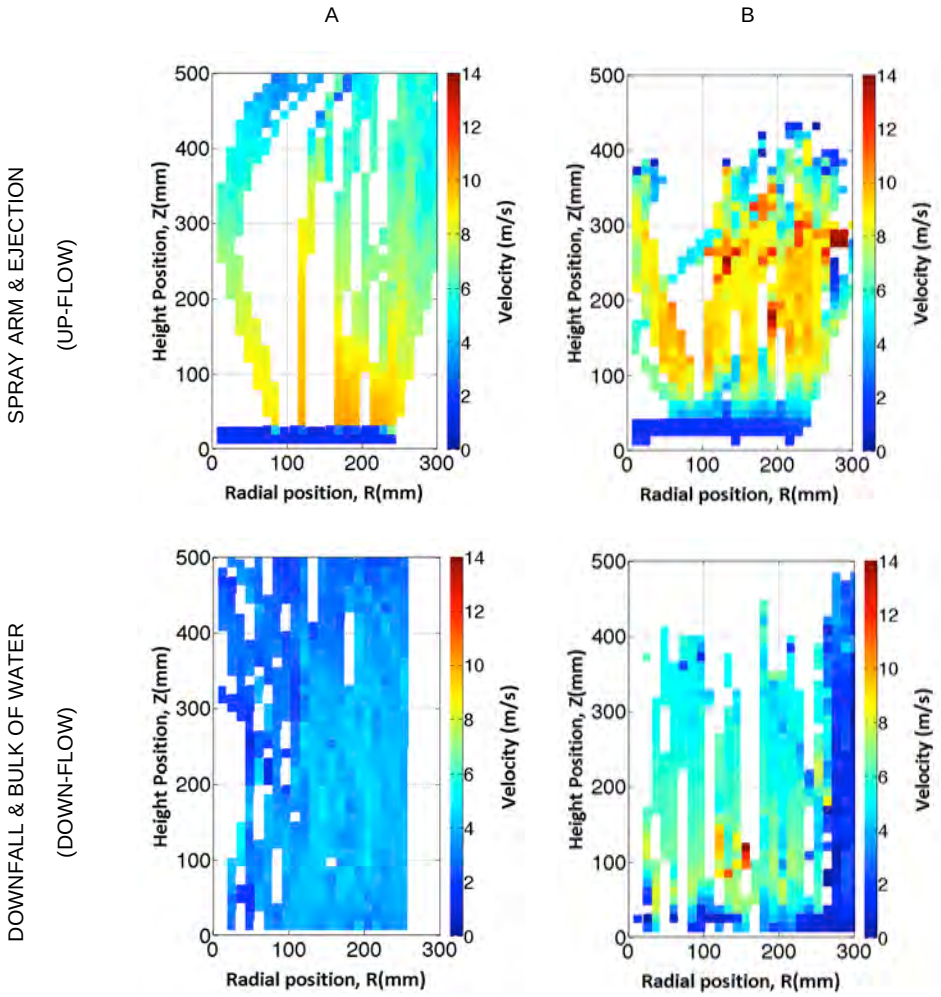

Figure 4.9. Eulerian velocity plots for CFD & PEPT data. A – CFD data. B – PEPT data. Experimental conditions: Medium pump speed, 'no load' and 'no detergent'.

In the first row, which contains the spray arm and ejection steps, a similar distribution of water was observed. PEPT data is noisier than CFD, as a consequence of the variability and perturbations occurring in real-life experiments. The gap in water distribution seen in PEPT data at around 100 mm of radial distance was also observed for CFD data. Also, CFD plot shows another distribution gap at around 150 mm. Slight velocity differences were also observed in the vicinity of spray arm ejections (around 30-40 mm). While CFD data showed a sudden change in velocity as the water exits the spray arm, the velocity profile estimated using PEPT data was not so abrupt. This phenomenon will be discussed in more detail when analysing individual particle paths in the following section.

In the second row of **Figure 4.9**, velocity contours representing the down-flow stage are shown. In CFD simulations (A) it was not possible to distinguish the flow down the sidewalls. An analogy for this flow would be raindrops falling down a window: wide range of velocities depending on the amount of water falling. At low radial distances, free falling movement was captured by CDF. Although a homogeneous range of velocity was obtained over most of the area, higher velocity values were found for PEPT data.

4.5.2. Particle paths comparison

Figure 4.10, first row, represents a velocity comparison for spray arm particle paths locations. Red colour represents PEPT data, while CFD data is shown in blue colour. In column A, all tracer velocities associated to every location were represented in a histogram. The figure shows good initial agreement in terms of velocity distributions. Mean values, represented by both dotted lines, show a slight higher average velocity for PEPT data. In column B, individual particle locations and its associated velocity can be seen. As radial distance increased, PEPT tracer velocity tended to increase as well. CFD data was more uniform, in agreement with a typical Hagen-Poisseuille velocity profile (Bird *et al*. 2007). As a consequence, less overlap between PEPT and CFD data occurred. This slight increase in PEPT tracer velocity suggests that the sudden acceleration effect produced at the nozzle exits might had affected the velocity of the tracer as it passes close to those areas. In column C, a statistical t-test comparison is shown. The bell-shaped curve represents all variability within CFD values. For data not to have

a statistical significant difference, the red line, representing the average PEPT data, should be contained within the curve. This statistical difference is explained by the lack of lower PEPT velocity values at high radial distances. It is in agreement with the data shown in both columns A and B.

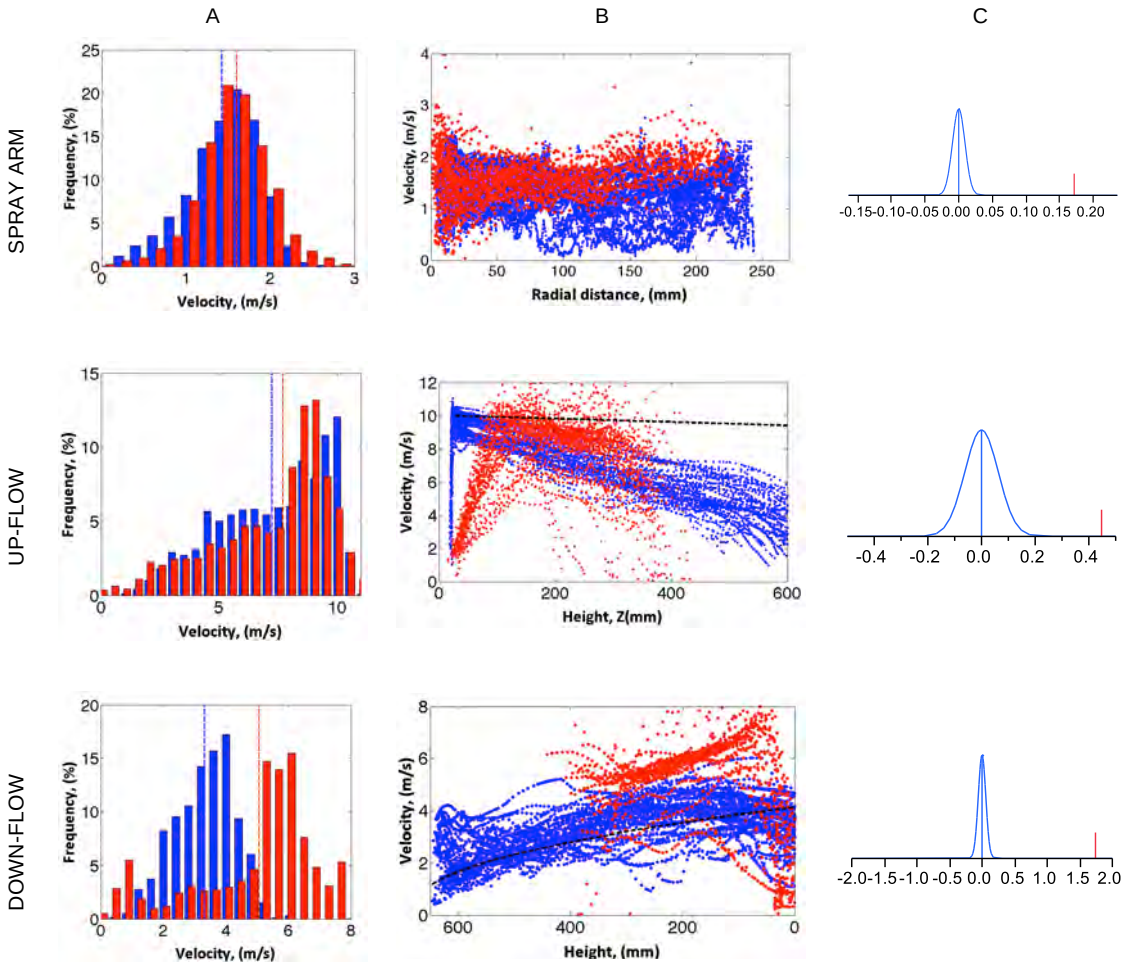

Figure 4.10. Comparison between PEPT & CFD data. First row - spray arm data. Second row – upflow data. Third flow – downflow data. A – Velocity histograms. B – Particle paths. C – Statistical t-test analysis. Red colour – PEPT data; Blue colour – CFD data; Red and blue dotted lines in column A represent average velocity values for PEPT and CFD data respectively. Black dotted line in column B represents gravity deceleration expected.

In **Figure 4.10, second row**, a similar comparison for particle velocities in the up-flow stage can be seen. In column A, velocity distributions obtained during the ejection step were in good agreement, with a slight higher average velocity for PEPT data. In column B, particle velocities as a function of height position are shown. The highest velocity values for PEPT data were

found at higher axial distances than for CFD data. This is a consequence of the fitting routine applied to calculate Lagrangian velocities explained in *Chapter 3, section 3.4.3*. Moving intervals of a defined number of data points were always taken to find the 'best fit' line for a central tracer location. Whenever there was an abrupt change in the tracer velocity or in its direction, as it occurred at the nozzle exits of the spray arm, a delay in the velocity change was introduced. The routine always took low velocity locations from the inside of the spray arm to estimate velocities near the outlet of the nozzles, even though the defined number of data points was small. As a consequence, velocity values were calculated by using low and high velocity tracer locations. Therefore, a lag effect was introduced. The delay in the response from the tracer particle highlighted with the Stokes number was a factor as well of the deviation found in this area. Tracer responded later to an external disturbance when compared to water particles.

The abrupt velocity change seen for CFD data at the water jet exits was due to the application of Bernoulli's equation (Eq. 4.1) in the computer model. As the height difference from the inside of the nozzle to the outside was negligible, the change in velocity given was a function of the pressure difference. Changing the diameter of the nozzles can also change the ejection velocity. The bigger the outlet area, the slower the ejection velocity to maintain a constant flow rate.

$$\frac{v^2}{2g} + \frac{P}{\rho_{ws} g} + h = constant \qquad \text{Eq. 4.1}$$

Outliers from PEPT data can also be seen. These are represented by those locations outside the main cloud of points and are responsible of the variability of PEPT data. They appeared when the tracer travelled at high velocities and PEPT cameras could not collect enough data points or when the radioactivity of the tracer was not high enough. Processing routines were not able to correct entirely the presence of these points. Limitations in the field of view of PEPT cameras were also observed. No locations were collected at height positions above 400 mm.

Gravity deceleration is represented by the black dotted line. It can be seen that for both types of data, the deceleration was higher than the expected by only gravity action. Air resistances for

water simulated particles and tracer movement on the ejection may explain the deceleration observed.

In column C, a statistical t-test to compare both data sets is shown. The bell-shaped curve represents the variability within CFD data. A significant difference was obtained as the red line, representing the average PEPT velocity value, was found at the right side of the curve. The difference was produced by the lack of PEPT data above 400 mm. Lower velocities expected above this height were not found and this increased PEPT tracer velocity average value.

Finally, in **Figure 4.10, third row,** the comparison was done for the down-flow stage. Only free fall data was used. A significant difference was observed in the histogram shown in column A. Although the distribution shape was similar, there was a clear displacement from CFD data to PEPT data. PEPT data showed higher downfall velocities than those predicted by CFD. In column B, representing particle locations and its associated velocities, PEPT cloud of points was found at higher velocities than CFD cloud. No PEPT data was again observed at heights above 400 mm. At height positions lower than 20 mm, the velocity of PEPT tracer decreased as they reached the bottom part of the dishwasher. A smooth velocity transition was again observed, which relates to the constraints of the processing routine used. As the tracer reached the bulk of the water at the bottom, its velocity should have decreased sharply. Gravity acceleration is shown as the black dotted line. The line indicates that an initial velocity from the roof of the dishwasher is necessary to match PEPT data. This suggests some energy carryover of the tracer after the impact on the top. No clear reason was found to explain this phenomenon. Inner elasticity of the tracer might have produced a bouncing off effect at the roof of the dishwasher. In column C, the statistical t-test comparison shows a significant difference between CFD and PEPT data as expected.

In **Table 4.1**, absolute mean values and standard deviations were calculated for every distribution shown before. Results matched well for the spray arm and ejection steps and differences were found in the downfall part.

Table 4.1. Velocity mean and standard deviations values for PEPT and CFD data.

STEP / TYPE OF DATA	PEPT		CFD	
	MEAN	*STD*	*MEAN*	*STD*
Spray Arm	1.60	0.43	1.43	0.45
Ejection	7.69	3.16	7.24	2.30
Downfall	5.05	2.12	3.31	0.97

4.6. ALTERNATIVE ANALYSIS

4.6.1. Velocity characterisation in the spray arm

In **Figure 4.11**, the time the tracers spent inside the spray arm is shown as a function of the radial position from which they were ejected. Data from four different experimental set-ups was represented: (A) High pump speed, no detergent; (B) Medium pump speed, no detergent; (C) Low pump speed, no detergent; (D) Low pump speed, detergent. Each data point shown represents a single pass of a tracer through the spray arm. A linear trend was obtained for each of the experimental conditions. Lines were forced to pass through the origin as time zero was considered the time at which the tracers entered the spray arm (distance travelled equal to zero). By calculating the slopes, the average velocity of the tracer inside the spray arm was estimated.

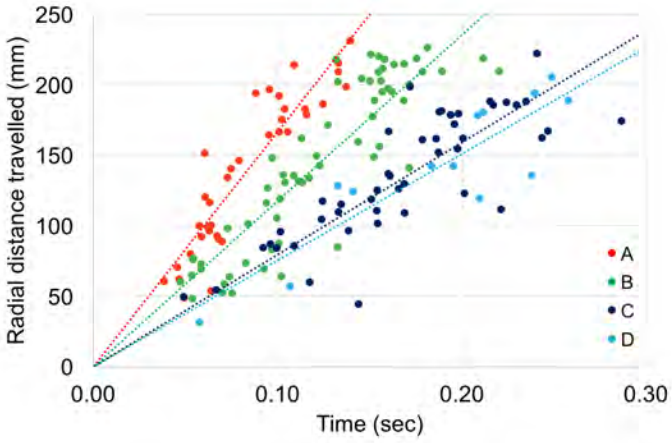

Figure 4.11. Radial distance travelled by the tracers vs. Time in spray arm until ejection. A – High pump speed, no detergent; B – Medium pump speed, no detergent; C – Low pump speed, no detergent; D – Low pump speed, detergent.

Table 4.2 shows a comparison between the averaged velocity estimated using all Lagrangian data available for each case (method A) and the velocity values calculated through this alternative method (method B):

Table 4.2. Average velocity comparison inside the spray arm between the two methods. Standard error deviation and goodness of fit are shown in brackets for Method A and B respectively. Method A – Averaged velocity from all Lagrangian data points for each experimental set-up; Method B – Velocity estimated by dividing the distance travelled by a tracer in the spray arm before ejected and the time taken.

EXPERIMENT / TYPE OF DATA	HIGH PUMP SPEED	MEDIUM PUMP SPEED	LOW PUMP SPEED	LOW PUMP SPEED
	NO DETERGENT			WITH DETERGENT
Method A	1.67 m/s (Std = 0.68)	1.17 m/s (Std = 0.58)	0.71 m/s (Std = 0.35)	0.75 m/s (Std = 0.34)
Method B	1.67 m/s (R^2 = 0.83)	1.18 m/s (R^2 = 0.78)	0.79 m/s (R^2 = 0.66)	0.75 m/s (R^2 = 0.79)

The different pump speeds had a noticeable effect. As pump head increased, the slopes of the trend lines, and therefore, their average velocity values increased as well. The effect of detergent on flow is proved again negligible. Both lines obtained at same pump speed (A & D) did not show variance in the slope given and they overlapped well.

4.6.2. Comparison of Lagrangian and Eulerian data based histograms

Two different sources of data can be used to build velocity histograms: Lagrangian data (particle paths) or Eulerian data (time-average data in a discretised space).

Some characteristics from velocity histograms based on Lagrangian data are:

- *A Higher number of data points* are used compared to Eulerian data histograms, as all individual particle locations are considered.
- *Time* is an important *factor*. The amount of data generated could be higher or lower depending on the resolution of the data collection equipment and the decay on the activity of the tracer.
- *Spatial distribution* of data may result in areas with higher concentration of points. Therefore, the histogram distribution can vary as a function of these specific regions.

Some characteristics from histograms based on Eulerian data are:

- *A lower number of data points* is used. Lagrangian data is time-weighted average and just one value is taken per cell location.
- *Spatial distributions effects* are removed due to the averaged data value in every spatial location.
- *Time effect is removed* as well. The inputted data is time-weighted per cell. Therefore, time error factor is minimised.

Figure 4.12 shows a velocity histogram built from Lagrangian and Eulerian PEPT data. Data corresponds to the ejection step at high pump speed, 'no load' and 'no detergent' conditions. Eulerian data was previously shown in **Figure 4.6B** and Lagrangian data in **Figure 4.10, second row**

.

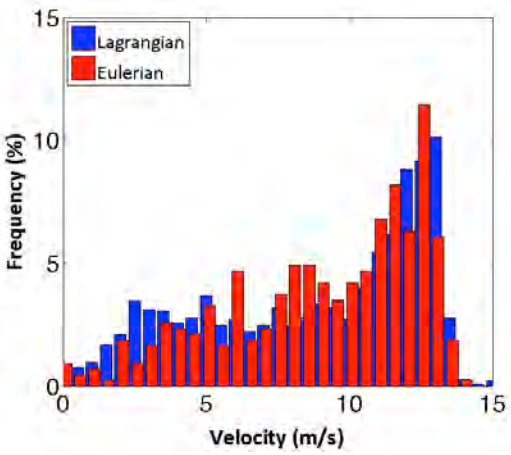

Figure 4.12. Velocity histogram comparison between Lagrangian and Eulerian PEPT data for the up-flow stage. Experimental conditions: High pump, no load and no detergent.

Results did not show significant differences between data sources when velocity distributions were plotted. This indicates that the spatial distribution of data points was highly homogeneous, which increases the reliability on CFD and PEPT data comparisons done and on the histogram velocity analysis explained next.

4.6.3. PEPT data histogram comparison: effect of pump speed

In **Figure 4.13**, a velocity histogram analysis was done to compare velocity distributions for the different pump speeds used experimentally: low, medium and high. Data was divided in three main steps: spray arm movement (A), ejection (B) and downfall (C). As detergent use was proved to not affect flow, it was not considered as an influential factor in the following analysis. Ejection and downfall plots were made by inputting Eulerian data. However, it was not possible to construct Eulerian-based histograms for the spray arm step. As the geometric space was very small in that area, it would have required smaller cell sizes to generate enough Eulerian information. This would have made cells even smaller than the location error associated with PEPT data.

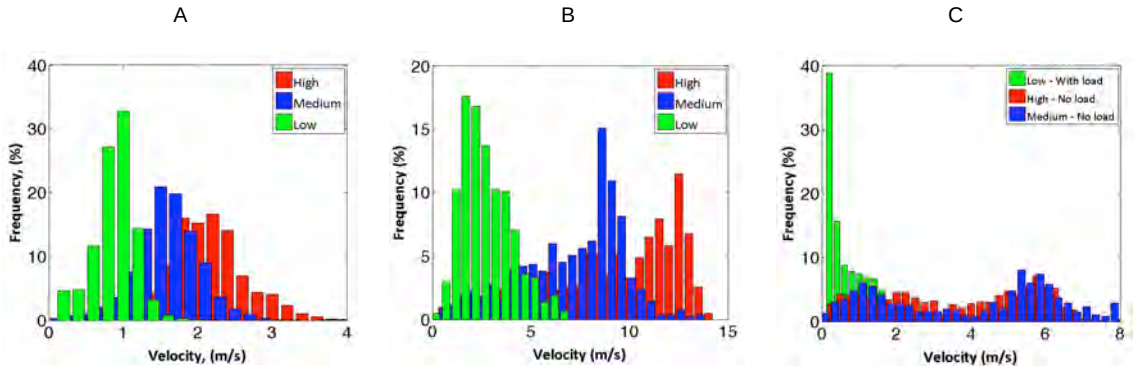

Figure 4.13. Velocity histograms for PEPT experiments. A – Spray Arm. B – Ejection. C – Downfall. Experimental set up: Red: High pump speed, no load & no detergent. Blue: Medium pump speed, no load & no detergent. Green: Low pump speed, with load & with detergent.

Figure 4.13A shows a comparative velocity histogram for the spray arm stage. Pump speed affected the velocity flow and distributions became wider as velocity was increased. This agrees with the application of Navier-Stokes theory for the inner flow in ducts. Either for laminar (linear profile) or turbulent flow (parabolic profile) theory predicts a maximum velocity value at the centre of the pipe and a reduction of it as it moves to the proximities of the pipe wall. Thus, the higher the velocity achieved, the wider the distribution. As histograms have a normal distribution shape, peaks relate to the average velocity estimated.

In **Figure 4.13B**, a comparative histogram for the ejection step can be observed. Again, the effect of pump speed in velocity flow is shown. As mentioned before, the impact stage on the experimental set-up 'with load' was removed to increase the quality of the data. A wider distribution was seen for the case of high pump speed, as velocities reached were higher. In every case, distributions mix the initial acceleration period to reach the maximum velocity and the subsequent deceleration.

Finally, **Figure 4.13C** illustrates a comparative histogram for the down-flow stage. The same bimodal distribution was observed for both high and medium pump speeds with 'no load'. This suggests that pump speed had no effect in this latter stage of the water sequence. The two possible ways for the tracer to fall in an empty dishwasher can be also inferred from data: free falling and downfall along the walls. The bump at lower velocities corresponds to the downfall along the walls while the bump at higher velocities indicates a free falling movement. For data 'with load', the distribution was highly displaced towards values close to zero, suggesting that the effect of load packing slowed the tracers in their move to the bottom. This also indicates the low mechanical input provided by the ADW to haul soil particles. Shear stresses generated by the water must had been low as tracers were washed down very slowly.

4.7. SUMMARY

Water motion inside a household ADW was described via PEPT. Data processing introduced a newly developed algorithm to enhance data quality by including smoothing and interpolation routines.

Analysis of the data showed how a typical water sequence can be divided into the following stages: movement inside pumps and spray arms, ejection, impact, downfall (over walls, crockery or free falling) and residence in the bulk water remaining at the bottom.

Jets paths were determined to follow a straight line for a fixed position and time, so their study can be discretised and analysed as a vector problem. Therefore, a specific dishwasher location is impacted at a frequency rate related to the rotational speed of the spray arms.

The Eulerian velocity analysis showed that the highest velocities over the whole sequence were found on the ejection stage. Energy provided by the pump was the main factor affecting velocities in the spray arm and ejection stages, although its influence was shown to be negligible during the downfall process. At this latter stage, the main difference in flow was found in those areas with high packing density of crockery, where there was little space for the tracer to move. The low velocity profiles seen suggest a low shear distribution over most of the crockery loaded as tracers were washed down very slowly. The homogeneous low velocity profile found in crockery areas also suggested a small coverage from the high velocity water films (before film jump) generated after the impact of jets over different crockery surfaces.

Residence time analysis highlighted lower wall areas and edges of the bottom bulk of water as those areas where tracers stayed for longer, and therefore, that can be considered as stagnant zones. Some high residence values were also found in crockery areas with high packing density. This could benefit chemistry availability and interaction with soils in those zones.

A comparison between PEPT and CFD data was done for a case with an empty dishwasher (no load or basket in the inner volume). Good agreement was achieved for spray arm and ejection steps. However, differences appeared in the downfall free falling profile. A hypothesis is that PEPT tracers bounced off at the roof of the dishwasher creating a higher velocity profile than predicted by CFD. Finally, alternative analyses showed a negligible effect of detergent on the water flow.

Other factors that might be of interest in future work, but not explored in here, are the density and viscosity of the wash solution, which could affect the velocity, residence time and shear stress profiles generated over different items. Results and conclusions made through this chapter are used in the following chapter to develop a mathematical model that describes the effect of different design parameters (dishwasher dimensions, spray arm design or crockery distribution) on the water sprayed in different dishwasher areas, impact frequencies and direct impingement coverage of crockery.

CHAPTER 5

ADWs DESIGN AND ITS INFLUENCE ON WATER DISTRIBUTION

5.1. INTRODUCTION

This chapter develops a mathematical model to describe and predict the distribution of water via coherent jets. The new method is based on geometric and trigonometric principles. The work also aims to understand current ADW design limitations with the analysis of different design parameters that affect the distribution of water. To compare results from multiple design combinations non-dimensionless and dimensionless output parameters are defined. The methodology shows the benefit of being a simple and quick (quicker than CFD) tool to understand design constrains and to predict jet trajectories.

5.2. METHODOLOGY

5.2.1. Assumptions

The methodology developed assumes that the initial distribution of water around the inner volume of the dishwasher occurs via coherent jets formed as the water goes through the different nozzles. Coherent jets were characterised previously (see *Chapter 4*) via Positron Emission Particle Tracking (PEPT) and observed thanks to the high-speed camera Image Analysis (**Figure 4.5**) . Also, this phenomenon is also reported later in Chapter 7, **Figure 7.8**. The subsequent spread of water via breakage of those jets after impacting different surfaces and the waterfall created in some areas is not considered here due to the significant complexity that arises. The methodology attempts to evaluate only the distribution of water until the impact of those jets.

The analysis considers circular plates of different diameters with no shape, that is, completely flat. This is the simplest geometry possible to start formulating the method. These plates are theoretically placed vertically at different locations in the dishwasher. They will be referred to as ‘analysed plate(s)’. Impacts are studied as the intersection projection of a jet over the plane generated by the analysed plate. As coherent jets are assumed (negligible changes on their diameter once ejected and no breakage of them), a single impact point occurs at a defined nozzle position, design and spray arm location in the ADW. As the spray arm rotates, more impact points are defined.

5.2.2. Definition of variables

Initially the system needs to be parameterised. The different design variables comprehend various elements such as dishwasher internal dimensions, spray arm design or plates (crockery) characteristics. **Table 5.1** summarises the design inputs considered.

Table 5.1. Definition of input parameters.

	Type	Name	Symbol
INPUTS	Dishwasher internal dimensions	Width	W_{DW}
		Depth	D_{DW}
		Height	H_{DW}
	Spray arm design	Radial nozzle position	R_{NZ}
		Height nozzle position	z_{NZ}
		Nozzle diameter	D_{NZ}
		Theta angle (x-y angle)	θ_{jet}
		Rho angle (Radius-z angle)	ρ_{jet}
		Spray Arm Rotation Rate	ω
	Plates characterisation	Plate Diameter	D_{PL}
		Width Plate position	x_{PL}
		Depth Plate position	y_{PL}
		Height Plate position	z_{PL}
		Radial Plate Position	R_{PL}
		Separation between plates	**d**
		Nozzle-Plate Relative position $(R_{NZ} – R_{PL})/ R_{PL}$	***R**

The particular design of ADWs arises two different types of symmetries: a Cartesian distribution of crockery and a cylindrical distribution for the spread of water. The origin of any coordinate system is located at the bottom centre of the dishwasher, in line with the rotational axis of the spray arm. To describe the results, a series of non-dimensionless and dimensionless parameters are introduced. They can be divided into ‘time factors’ and ‘spatial factors’. First ones are related only to time and the second ones to geometry parameters. All the variables defined take as a reference one complete rotation of the spray arm. In **Table 5.2**, the outputs considered and their definitions are shown:

Table 5.2. Definition of output variables. *A complete description of the different outputs definitions is given after Figure 5.1.

	Type	Name	Symbol	Definition*
OUTPUTS	Non-dimensionless	Time travelling in vision area	t_{vis}	$(\beta_{in}$- $\beta_{out})$ / ω Appendix A.2
		Time impacting plates	T_{impact}	Appendix A.2
		Impact distance on plates	L_{impact}	Appendix A.2
	Dimensionless	Effective impact time in vision area	τ_{vis}	T_{impact} / t_{vis}
		Effective impact time per lap	τ_{lap}	T_{impact} / t_{lap}
		Effective impact length	δ	L_{impact} / D_{PL}
		Overall efficiency	α	$\tau_{vis} \cdot \delta$

Figure 5.1 illustrates a visual representation of the input and output parameters defined.

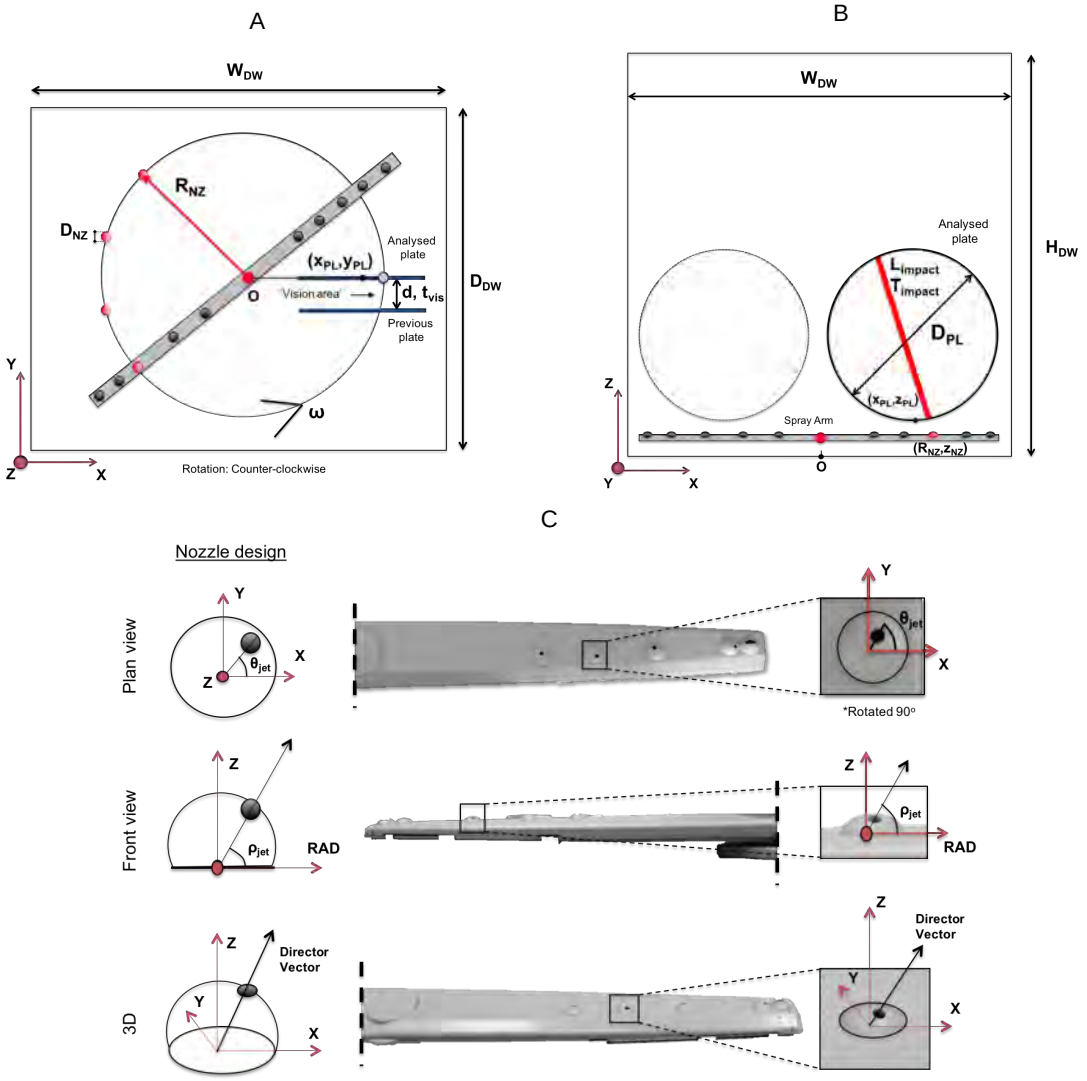

Figure 5.1. Schematic representation of inputs and outputs parameters. Origin (O) is located at the bottom centre of the dishwasher. A – Plan view; B – Front view; C – Nozzle design.

The path of the jets produced from different nozzles is characterised by a direction vector. This indicates the 3D trajectory the coherent jet will follow. It depends on the design of the nozzle and can be expressed in polar coordinates. An angle theta (θ_{jet}) is defined as the angle the jet has in the x-y plane (plan view). Another angle, rho (ρ_{jet}), is defined as the angle between the x-y plane and z-axis (front view). The combination of both gives the 3D projection that describes the trajectory of the jet.

'Vision area' is considered as the space between the analysed plate and the previous plate sitting in front of it (see **Figure 5.1A**). The time a nozzle is travelling within that vision area (t_{vis}) per spray arm rotation represents the maximum time a jet is likely to impact the analysed plate. It is assumed that any jet standing out of the vision area will not hit the analysed plate. As the trajectory of a nozzle travelling within that area is circular, t_{vis} is a function of the angular positions at which the nozzle enters (β_{in}) and exits (β_{out}) the defined 'vision area' and the rotational speed of the spray arm (ω). Two other non-dimensionless parameters are also defined: the total time a jet is directly impacting the plate per rotation (T_{impact}) and the length (L_{impact}) covered by the impact (see mathematical definitions in Appendix A.2).

However, the introduction of dimensionless parameters allows a wider and homogeneous comparison between different cases. The rotational rate (ω) of a spray arm is traditionally linked with its design and flow rate (not considered). Typically, this factor is fixed for a specific ADW model and cycle. It influences by definition the 'time travelling in the vision area (t_{vis})' and also the 'time impacting the plates (T_{impact})'. For a given spray arm design and plate position, the increase in the rotational rate reduces both t_{vis} and T_{impact}. To eliminate the influence of this factor, an effective impact time (in the vision area) is introduced (τ_{vis}) as a dimensionless parameter. It is defined as the ratio between T_{impact} and t_{vis}. The range of τ_{vis} varies from 0 to 1. Overall, ω affects the frequency of impact (how often a new impact happens on the same item), but not the ratio of 'net impact time over maximum impact time per rotation' established by τ_{vis}. Also, an effective impact time per lap can be defined (τ_{lap}) as the ratio between T_{impact} and a lap time (t_{lap}). Due to the impossibility of a jet to impact continuously a specific analysed plate for a

rotation, the value of τ_{lap} will never be as high as one. It represents the ratio of time the jet is impacting the analysed plate per rotation, that is, its frequency.

A similar approach is considered to eliminate the influence of the plate diameter (D_{PL}). An effective impact length (δ) is defined as the ratio of length covered by the impact of the jet (L_{impact}) and the diameter of the analysed plate (D_{PL}). It also ranges from 0 to 1. A value of 1 would indicate that the jet is impacting an equivalent length to the plate diameter.

The introduction of τ_{vis} and δ to characterise the time and geometrical phenomena establishes an easy way to compare information within different ADWs. Cases can occur where τ_{vis} values are high while δ values are low, indicating a continuous impact of a jet over the analysed plate but at a very specific area. The opposite case can also occur: low values for τ_{vis} with high values for δ, indicating a good coverage of the jet but for a minimal impact time. To correlate both phenomena, an overall efficiency (α) is defined as the relationship between τ_{vis} and δ. It again ranges from 0 to 1. A value closer to 1 would indicate the best case scenario, where the jet is both impacting the maximum length possible and for the maximum available time.

5.2.3. Case study: computational experimental design

In order to understand the influence of different input parameters to the outputs already defined, a computational experimental design was conducted. Five input parameters were studied: plate diameter, separation between plates, nozzle-crockery relative position, theta and rho angles (nozzle design). Different levels were assigned and a full factorial design was followed. **Table 5.3** illustrates a summary of the levels studied:

Table 5.3. Levels of the different inputs selected for computational experimental design studied.

VARIABLE TYPE	NAME	SYMBOL	UNITS	LEVELS
Plates Characterisation	Plate Dimension	D_{PL}	mm	100 - 150 - 200 - 250
	Separation between plates	**d**	mm	10 - 20 - 30 - 40 - 50 - 60 - 70 - 80 - 90 - 100
Spray Arm Design	Radial nozzle position	R_{NL}	mm	10 - 40 - 70 - 100 - 125 - 150 - 180 - 210 - 240
	Theta angle	θ_{jet}	Degrees	1 - 20 - 50 - 70 - 80 - 85 - 90 - 95 - 100 - 110 - 130 - 160 - 179
	Rho angle	ρ_{jet}	Degrees	10 - 30 - 45 - 60 - 70 - 75 - 80 - 85 - 89

Inputs not analysed were set to typical design values. **Table 5.4** shows those fixed values used.

Table 5.4. Fixed values for inputs not selected for the computational experimental design.

VARIABLE TYPE	NAME	SYMBOL	VALUE
Dishwasher dimensions	Width	W_{DW}	540 mm
	Depth	D_{DW}	500 mm
	Height	H_{DW}	620 mm
Spray arm design	Nozzle diameter	D_{NZ}	2 mm
	Spray Arm Rotation Rate	ω	30 rpm
Plates	Width plate position	x_{PL}	125mm
	Depth plate position	y_{PL}	0 mm
	Height plate position	z_{PL}	50 mm

Dishwasher dimensions only constrain the number of plates or crockery items that can be loaded and their locations. The analysed plate was located at the mid-right side of the bottom rack (125, 0, 50) as seen in **Figure 5.1A**. This established symmetries between the different positions of the nozzle in the spray arm and plate itself. In **Figure 5.1B** it can be observed how the different nozzles can either be centered related to the plate or shifted to the right or left. The gap between the lower spray arm and the bottom of the plate was 20 mm. The spray arm height

position was 30mm (z_{NZ} = 30 mm). Its rotational speed (30 rpm) was within the values typically found in commercially available ADWs.

A total number of 42,120 design combinations were analysed, obtaining as a result values for the output parameters defined in **Table 5.2**. Information gathered was represented using 'Box Plots', which grouped data for each of the factor levels and indicated the tendency in the variation of the outputs via median and quartile representations. Results are shown in *section 5.4*.

The routine developed can also be used to determine optimum cases and the projection pattern for a fixed set of conditions given.

5.3. PROJECTION PATTERN EXAMPLES

Figure 5.2 illustrates an example of a range of jet patterns that can be produced.

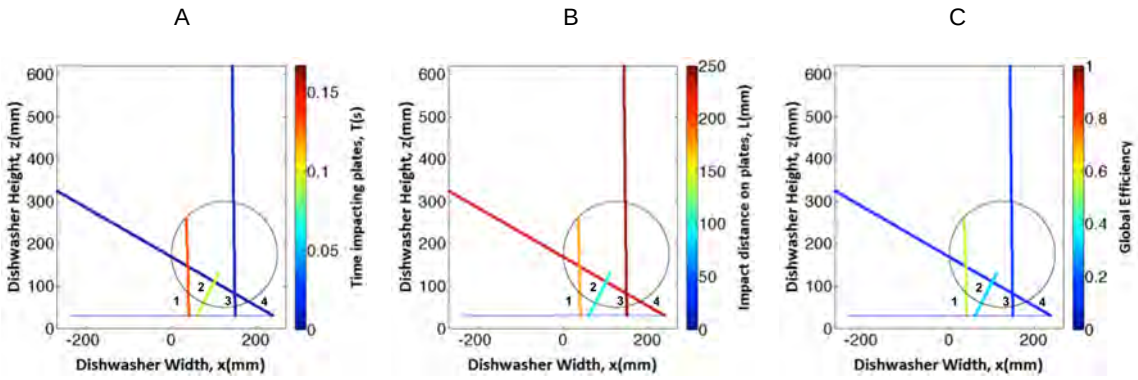

Figure 5.2. Schematic of different projection examples. Each line represents the projection of a jet over the plane formed by the analysed plate. Analysed plate is represented by the circle at the right side of the graph. A – Colormap scale based on time impacting plates, T_{impact}(s); B – Colormap scale based on impact distance on plates, L_{impact}(mm); C – Colormap scale based on global efficiency value (α). Jets are numbered from left to right.

The design information as well as the results are compared in **Table 5.5**. All examples were set for the same separation between plates (d = 20 mm) and different nozzles were placed along the length of the spray arm. Theta and rho angles from nozzle design were varied in a wide

range of values. The diameter of the analysed plate was 250 mm (D_{PL} = 250 mm) and the rotational speed 30 rpm (1 rotation = 2 seconds). Jets are numbered from left to right.

Table 5.5. Example of various designs and their calculated results.

	INPUTS					OUTPUTS					
#	SEPARATION BETWEEN PLATES (d [=] mm)	NOZZLE POSITION (R_{Nz} [=] mm)	NOZZLE –PLATE REL. POS. (*R)	THETA ANGLE (θ_{jet} [=] degrees)	RHO ANGLE (ρ_{jet} [=] degrees)	t_{vis} (s)	T_{impact} (s)	L_{impact} (mm)	τ_{vis}	δ	α
1	20	40	-0.68	90	85	0.1667	0.1303	178.8	0.78	0.72	0.56
2	20	60	-0.52	20	60	0.1082	0.0935	97.7	0.86	0.39	0.34
3	20	150	0.2	130	89	0.0426	0.0069	244.5	0.16	0.98	0.16
4	20	240	0.92	179	30	0.0266	0.0046	227.1	0.17	0.91	0.16

The first jet shows good coverage of the plate (L_{impact} = 178.8 mm / δ = 0.72) and also a fairly high effective impact time (T_{impact} = 0.1303 s / τ_{vis} = 0.78). A theta angle value of 90 degrees makes the jet impact the analysed plate with very little displacement in the x-direction. Also, a rho angle design of 85 degrees lets the jet travel high enough to reach top areas of the analysed plate. For the second jet, a displacement on the impact trajectory to the right is seen as a consequence of a theta angle of 20 degrees. The use of a lower value for rho (60 degrees) does not allow the jet to travel high and therefore less distance is covered (L_{impact} = 97.7 mm / δ = 0.39). However, the jet manages to impact the surface of the analysed plate during most of the time travelling within the vision area (T_{impact} = 0.0935 s / τ_{vis} = 0.78). This represents a case where a jet impacts a very specific area for longer times. For the third jet, the trajectory followed is influenced by a rho angle design value of 89 degrees. This causes the jet to hit a large distance on the analysed plate (L_{impact} = 244.5 mm / δ = 0.98) providing a good coverage. However, the impact occurs for a very short period of time (T_{impact} = 0.0069 s / τ_{vis} = 0.16). It can be seen how the jet manages to reach the ceiling of the dishwasher, meaning that no impact is happening on the analysed plate during that time. Also, a displacement of the jet trajectory to the left could be expected because of a theta design angle of 130 degrees. This is not produced as a consequence of the high value of rho angle. Finally, the influence of theta angle design is shown for jet number four. A value of 179 degrees makes the jet trajectory to travel left on the x-

direction. A similar consequence than the case before is produced: good coverage (L_{impact} = 227.1 mm / δ = 0.91) but for short times (T_{impact} = 0.0046 s / τ_{vis} = 0.17). The jet trajectory is almost parallel to the x-z plane formed by the analysed plate.

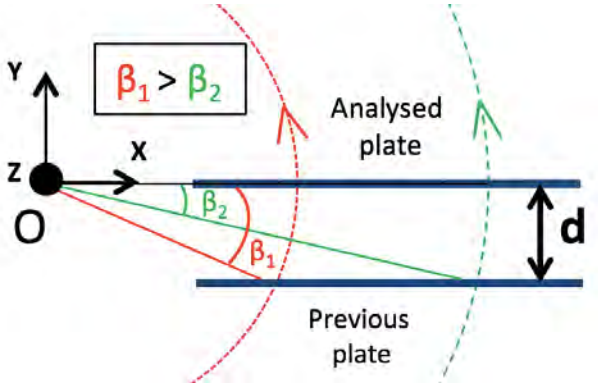

Figure 5.3. Plan view of a schematic of different angles covered by nozzles placed at two different radial distances. Red and green dotted lines show trajectories for two nozzles considered. ß angles represent the angles formed between the position at which a nozzle enters the 'vision area', the origin and the analysed plate.

Different nozzle positions influence the available time a jet is travelling within the vision area (t_{vis}). The closer the nozzle to the axis of rotation the longer the time travelling in that area. This is a consequence of the symmetry between plates placed in parallel and the rotational movement of the spray arm. In **Figure 5.3**, the angle displacement for two nozzles at different radial positions is proved to be different when symmetry between plates exists ($\beta_1 > \beta_2$). As the angular velocity $\left(\omega = {}^{d\beta}/_{dt}\right)$ is the same and the angle covered different, the time is therefore different. Higher separation between plates also provides longer times in the vision area. A displacement of the analysed plate towards the front or back of the dishwasher also changes the radius distance where the plate is located from the origin. Thus, angles and time in vision area also vary.

5.4. COMPUTATIONAL CASE STUDY RESULTS

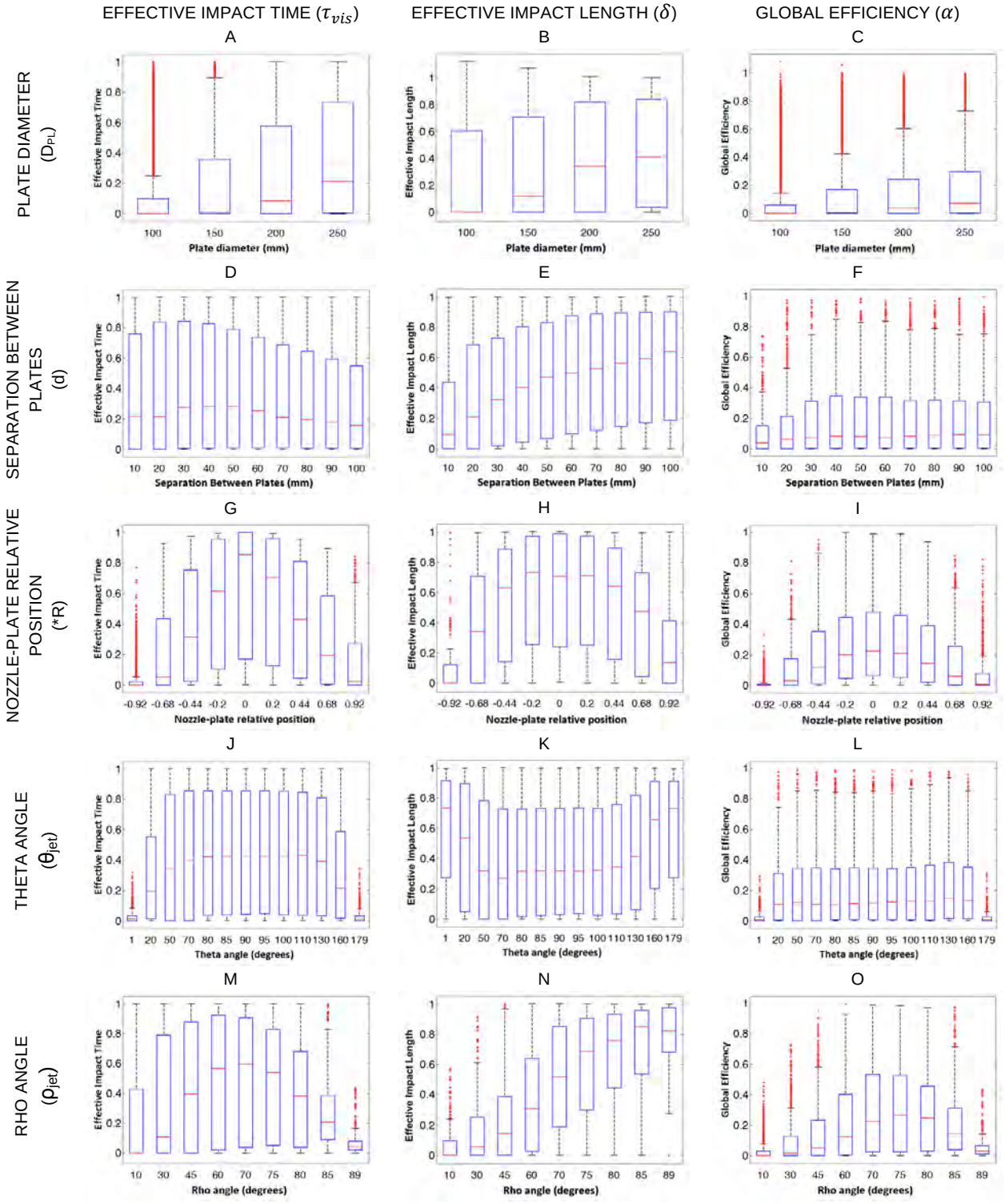

Figure 5.4. Boxplot results for the different input parameters considered. Effective impact time (τ_{vis}), effective impact length (δ) and global efficiency (α) results are distributed in first, second and third column respectively. Plate diameter (D_{PL}), separation between plates (d), nozzle-plate relative position (*R), nozzle's theta angle (θ_{jet}) and nozzle's rho angle (ρ_{jet}) results are shown from first to fifth row. Note: Results from second row on are expressed only for D_{PL} = 250 mm.

5.4.1. Influence of plate diameter (D_{PL})

Figure 5.4 shows the results from the computational experimental design in the form of 'box plots'. They have been separated in different columns showing the effective impact length (δ), effective impact time (τ_{vis}) and global efficiency (α) values as a function of the different levels of the input parameters considered for the analysis. The horizontal red lines represent median values. The edges of the boxes indicate both the 25th and 75th percentile, while data considered as outliers are shown as red dots outside the black edges.

The influence of plate diameter (D_{PL}) clearly shows that the bigger the plate or element of crockery the higher the chances of a jet to impact it for longer while covering also a higher distance. Boxes are displaced towards higher efficiency values as the size of the plate increases.

Effective impact length (δ) values higher than 1 can be achieved for some particular cases. As a nozzle presents a curved trajectory in the vision area, the impact projection can be curved as well. Therefore, the length covered can be higher than the plate diameter.

As the increase in plate diameter improves the quality of the results, further data is only represented for a plate diameter of 250 mm. This allows a clearer representation, as higher sensitivity is found due to a reduction in the size of the boxes. Equivalent box plots can be found for lower plate diameters, but with lower efficiency values.

5.4.2. Influence of separation between crockery elements (d)

In the second row of **Figure 5.4**, the separation between plates (d) shows an optimum value around 20 mm to 30 mm for τ_{vis}. The greater the distance between consecutive plates, the higher the time travelling within the vision area and also the higher the chances to impact different locations outside the analysed plate. Jet projections can cover a wider area. Thus, from an effective use of time, separations higher than 30 mm are likely to reduce its time effectiveness.

The higher coverage that can be produced for higher separations is seen for δ values. More designs will be able to cover a wider area of the analysed plate when the gap between consecutive plates increases. If the space between plates is on the contrary small, less design combinations will be able to efficiently cover a wider area of the analysed plate.

When both parameters, time and length covered, are combined, the resulting global efficiency shows a plateau for separations higher than 20 mm. Also, the smaller the separation the higher number of crockery items that can be loaded in the ADW.

*5.4.3. Influence of nozzle-crockery relative position (*R)*

In the third row of **Figure 5.4**, the influence of nozzle-crockery relative position (*R) on the different outputs considered can be seen. This relative position is calculated for similar y-axes coordinates between the nozzle and the analysed plate (i.e. just below the plate). Negative values indicate that the nozzle is on the left side when compared with the x-axis position of the centre of the analysed plate. Positive values indicate the nozzle is displaced to the right side.

Similar tendencies are found for effective impact time (τ_{vis}) and effective impact length (δ) boxplots. When the nozzle is placed at the same x-axis coordinate than the analysed plate (centered position), the likelihood of longer impacts and longer lengths increases. As the nozzle is displaced towards the edge of the analysed plate, less design combinations produce a good result.

The symmetry is not the same for both positive and negative nozzle-crockery relative positions. The rotation of the spray arm produces slightly better results when the nozzle is on the right side. Within the vision area and for the case considered, the nozzle will be moving from left to right due to the rotational movement (see **Figure 5.3**). Therefore, for an absolute value of i.e. 0.92, a nozzle placed on the left side (-0.92) will start travelling in the vision area at more remote positions than 0.92 and it will move towards that reference. For a nozzle placed at the right side (0.92), the movement will be the opposite: it will go from more centered positions (lower than 0.92) to the edge. Thus, as in this second case the nozzle is ‘seeing’ the plate

better, the likelihood for better results increases. The symmetric distribution of crockery, makes the effect to be the opposite for the backside of the ADW. Jets will be moving from right to left.

5.4.4. Influence of theta angle (θ_{jet})

The forth row of **Figure 5.4** analysed the influence of the nozzle's theta angle (θ_{jet}). This angle is the one seen from the jet when looking at it from above (x-y plane). Results show an inverse effect between τ_{vis} and δ**.** In both cases, a plateau is seen for angles between 70 and 110 degrees. No important trajectory changes are produced when design values are within that range. At the extreme cases is where the inverse effect is highlighted. As commented for **Figure 5.2**, theta angles close to 0 or 180 degrees makes the jet travel almost parallel to the x-z plane where the analysed plate is located. Therefore, impacts at these design extreme values are able to cover most of the length of the analysed plate but for very short periods of time.

No angular positions higher than 180 degrees are considered. A design like that would make the jet impact the back of the analysed plate. The jet trajectory would be moving backwards from its ejection point.

5.4.5. Influence of rho angle (ρ_{jet})

Finally, in the fifth row of **Figure 5.4** the influence of nozzle's rho (ρ_{jet}) value is studied. This angle corresponds to the one formed by the jet when looking at it from the front (radial-z plane). The effective impact time (τ_{vis}) analysis shows an optimum value around 70 degrees with a rapid decrease for higher angles. For the effective impact length (δ), a sigmoidal type increase with an optimum value at around 85 degrees is seen. The higher the angle the higher the jet is able to travel in a smaller space (higher packing). Therefore, a good coverage is almost assured when this angle value is high. However, as indicated previously and showed in **Figure 5.2**, if the rho angle was too high then the jet would travel higher than the analysed plate and an effective use of time would not be reached. This explanation justifies the tendency seen in τ_{vis} after the optimum value. Overall, the global efficiency parameter (α) shows an optimum around 75 degrees. In **Figure 5.5**, the median and 75th percentile values are shown for different plate sizes and for the effective impact time. When smaller plate sizes are analysed a displacement of the

optimum τ_{vis} towards smaller angles is shown. This proves a strong influence of plate size on this parameter for τ_{vis} optimum. The commented decrease in efficiency can be seen for 75th percentile values. This effect is hardly appreciated for median results.

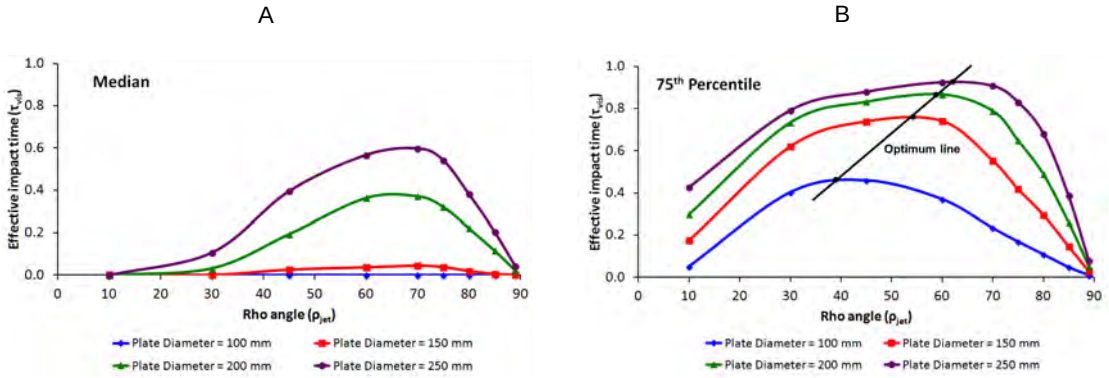

Figure 5.5. Effective impact time (τ_{vis}) as a function of rho angle different levels. Results are expressed for four different plate diameters considered. A – Median values; B – 75th percentile values.

Angles higher than 90 degrees are not considered in the study. A design with those values would hit the back of the analysed plate for the set-up considered. If the analysed plate was presented with some inclination (backwards or forward) the analysis would change. The jet trajectory, nozzle path and plate position defines a triangle. In **Figure 5.6**, a schematic of the problem is seen. If the triangle was 'obtuse' (plate lying backwards), then the impact of the jet would be highly compromised and would be less likely to happen. If the triangle was 'acute' (plate lying forward), the jet could face easily the front of the analysed plate. A better performance is expected with a higher value of γ.

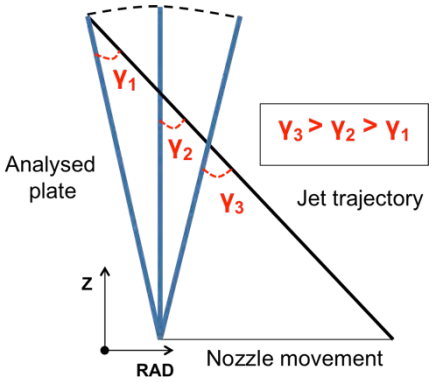

Figure 5.6 Schematic of different 'analysed plate' angle positions for a single jet trajectory.

5.5. OPTIMUM FINDING

The establishment of efficiency parameters (τ_{vis}, δ and α) allows the finding of optimum design values. For the case study considered (see **Table 5.3**) and for a plate diameter (D_{PL}) of 250 mm, the designs with the highest global efficiency coefficients (α) were ordered. **Table 5.6** presents the best 20 theoretical results obtained.

Table 5.6. 20 best design combinations for the computational experimental design considered.

INPUTS				OUTPUTS				
d	*R	θ_{jet}	ρ_{jet}	T (s)	L (mm)	τ_{vis}	δ	α
100	-0.2	50	60	0.497	250.7	0.993	1.003	0.996
90	0	85	70	0.253	249.4	0.991	0.998	0.988
90	0.2	95	70	0.203	249.3	0.991	0.997	0.988
90	0	80	70	0.252	250.2	0.985	1.001	0.986
70	-0.2	50	70	0.243	249.9	0.985	0.999	0.985
50	0	50	75	0.131	245.7	1.000	0.983	0.983
90	0.2	100	70	0.200	250.5	0.978	1.002	0.980
90	0.2	85	70	0.203	247.3	0.990	0.989	0.980
90	0.2	90	70	0.203	247.2	0.990	0.989	0.979
90	0	90	70	0.252	248.3	0.985	0.993	0.978
50	0.2	130	75	0.107	246.3	0.990	0.985	0.975
90	0.2	80	70	0.201	247.9	0.983	0.992	0.975
30	-0.2	20	70	0.095	248.2	0.980	0.993	0.973
20	0	110	85	0.051	243.3	0.999	0.973	0.973
20	0	70	85	0.051	243.2	0.999	0.973	0.972
40	0	110	80	0.104	242.3	1.000	0.969	0.969
80	0	110	70	0.221	241.6	1.000	0.967	0.966
40	0	70	80	0.104	241.6	1.000	0.966	0.966
60	0	110	75	0.159	241.3	1.000	0.965	0.965
50	-0.2	50	75	0.165	242.9	0.990	0.972	0.962

Nozzle-plate relative position (*R) and rho angle (ρ_{jet}) are highlighted as the main factors affecting the results. *R values are contained within a small range (-0.2 to 0.2). This indicates the importance of a centred position of the nozzle (jet) with respect of the crockery item in order to achieve a good coverage of water and for a prolonged time. ρ_{jet} optimum values are found at angles closer to 70º. The narrow range of values given also proves the importance of this

parameter. Wider ranges of values are obtained for d and θ_{jet}, which again suggests the lesser effect of these design variables on the efficient distribution of water and use of time.

5.6. REAL CASE EXAMPLE. EFFECT OF LOADING POSITION.

The methodology developed can also predict the impact projection patterns of a specific ADW design. The theoretical design efficiency of the ADW model used for PEPT experiments (Whirlpool DU750) (*see Chapter 4*) was evaluated. Projection patterns were calculated for the lower spray arm, which is assumed to rotate at 35 rpm. The example also helped the illustration of the effect of different loading positions. Two plane plates with a diameter of 250 mm (D_{PL} = 250 mm) were placed virtually at symmetrical locations on the left and right side of the ADW. Origin was again established at the bottom centre of the ADW in line with the spray arm rotational axis. Coordinates of the base location of both theoretical plates were (-125,0,50) and (125,0,50) for plate 1 (left) and 2 (right) respectively. Different design parameters were measured externally. The spray arm was rotating at a height of 30 mm (Z_{NL} = 30mm) and the separation between plates was 20 mm. **Table 5.7** summarises those design values characterising each of the nozzles present in the spray arm.

Table 5.7. Whirlpool DU750 lower spray arm nozzle's design values.

INPUTS				
#	R_{NZ}	*R	θ_{jet}	ρ_{jet}
1	238	0.904	90	55
2	226	0.808	359	89
3	182	0.456	160	60
4	145	0.160	305	70
5	114	-0.088	90	89
6	89	-0.288	179	89
7	162	0.296	65	70
8	194	0.552	43	62
9	223	0.784	90	89
10	238	0.904	60	55

Those theta angles values higher than 180º indicates an impact occurring on the left plate, while if the angle value is lower than 180º the impact takes place on the right plate. Due to the

rotational movement and the crockery loading symmetry, no jet hitting the front of a plate (either left or right) can hit the front of the other. **Figure 5.7** illustrates the water projection patterns estimated for the case considered.

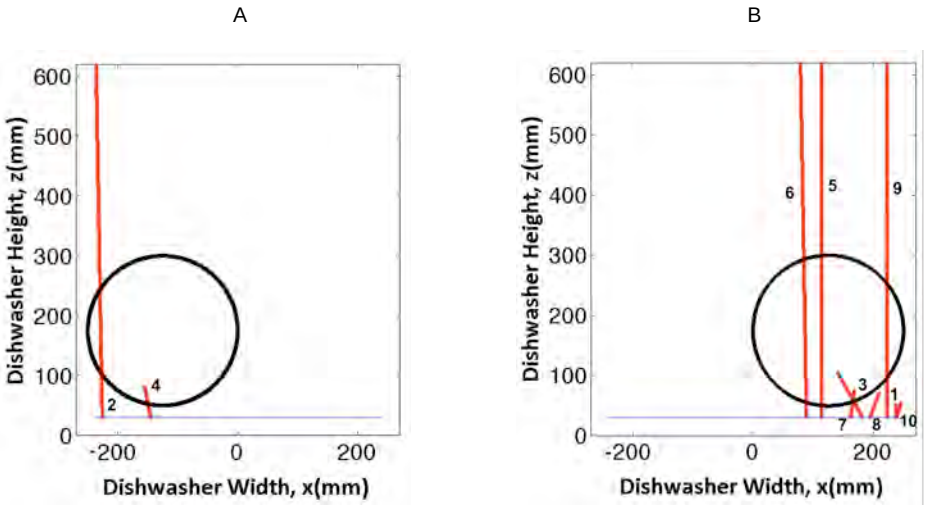

Figure 5.7. Theoretical water impact projections over two plates located symmetrically at left and right side of a Whirlpool DU750 dishwasher. Origin is established at the bottom centre. Plates are placed vertically at coordinates (-125,0,50) and (125,0,50). Spray arm is at a height of 30 mm. Blue line indicates spray arm position; black circles represent analysed plates; and water projections are shown in red. A – Left side projections. B – Right side projections.

A clear inhomogeneous distribution is shown between the left and right plate positions. Spray arm design favours a better coverage on the right side. Only two jets (#2 and #4) manage to impact the left side. On the right side, there are three jets producing a good coverage over the plate surface (#5, #6 and #9), another two producing a small coverage (#3 and #7) and three with no impact on the analysed plate (#1, #8 and #10). **Table 5.8** summarises the output results estimated for each nozzle design while **Figure 5.8** represents the values of the different dimensionless numbers.

Table 5.8. Output values for each nozzle design.

OUTPUTS						
#	t_{vis}	T_{impact} (s)	L_{impact} (mm)	τ_{vis}	δ	α
1	0.017	0.000	0.0	0.000	0.000	0.000
2	0.018	$5.2 \cdot 10^{-5}$	140.2	0.003	0.561	0.002
3	0.023	0.019	74.3	0.857	0.297	0.255
4	0.028	0.027	49.5	0.967	0.198	0.192
5	0.036	0.010	249.0	0.289	0.996	0.288
6	0.046	$2.2 \cdot 10^{-4}$	237.9	0.005	0.951	0.005
7	0.025	0.022	40.0	0.871	0.160	0.139
8	0.021	0.000	0.0	0.000	0.000	0.000
9	0.018	0.003	155.2	0.181	0.621	0.112
10	0.017	0.000	0.0	0.000	0.000	0.000

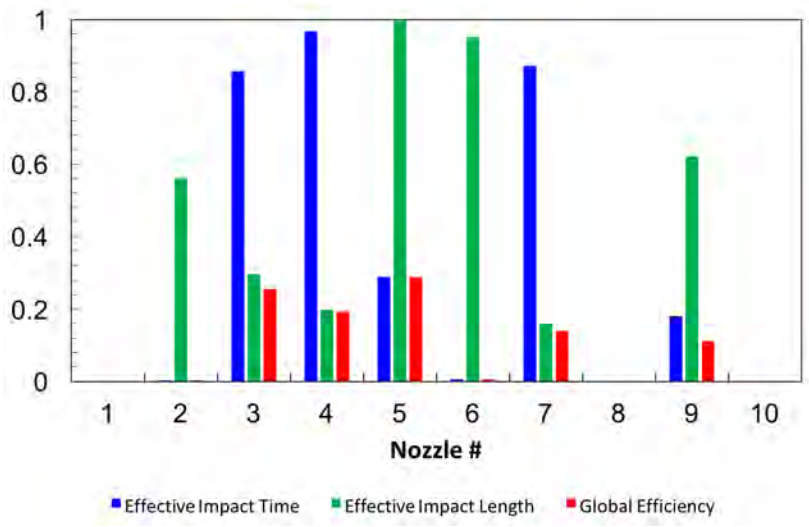

Figure 5.8. Illustration of the values for the different output dimensionless numbers defined for the real case example.

Jets #3, #4 and #7 present high effective impact time values (τ_{vis} > 0.85) with low effective impact lengths coefficients (δ < 0.30). This indicates that the impingement region is very localized but happens during most of the time possible. However, jets #9, #6 and particularly #5 show high coverage (δ > 0.60) but for impacts occurring in a short period of time (τ_{vis} < 0.30). Jet #2 only manages to impact the left plate for a fraction of a second (τ_{vis} < 0.001). Overall, no global efficiency (α) higher than 0.3 is achieved for the two plates locations considered. Most of the jets produced through the different nozzle designs present efficiencies lower than 0.2.

The analysis of different locations would generate slightly different results. However, the trend would be maintained. Important improvements can be achieved to produce a good coverage and an efficient use of time by investigating novel ways of spraying water inside an ADW.

5.7. SUMMARY AND FUTURE MODEL EXTENSIONS

A mathematical approach was considered for the analysis and understanding of ADW design factors and its influence over water distribution. The analysis was based on geometric and trigonometric principles. Main ADW design elements were established as parameters to study and grouped in different categories: dishwasher dimensions, spray arm design and crockery geometry (only plates-type geometry considered).

The method presented is a simplified but intuitive way of understanding ADW design principles. Non-dimensionless and dimensionless parameters were defined as outputs. The use of dimensionless variables established an easy way to compare results from different cases. Output data was normalized in a range between 0 and 1. The introduction of time efficiency (τ_{vis}) and coverage efficiency measurements (δ) separated the understanding of the jet pattern from a time and geometry perspective. The combination of these two parameters in an overall efficiency parameter (α) allowed the interpretation on how well or bad a design was for a particular case.

Five different factors were chosen as the main important parameters to study: plate diameter, separation between consecutive plates, nozzle-plate relative position and nozzle's theta and rho design angles. A wide variety of levels were set for each of them and a virtual full factorial design of experiments run. Results were expressed in box-plots. Data was grouped for each of the different levels considered for every input parameter and separated for the three dimensionless variables established: τ_{vis}, δ and α. Results highlighted the importance of nozzle-plate relative position and rho angles among other factors. The more centred the nozzle with respect of the middle of the crockery element, the better results expected. Also, the more vertical the jet the better coverage, but with a decrease in the effective use of time for angles

higher than 75 degrees. For a specific case considered, the model developed also aided in the finding of optimum designs.

A real case example was presented. Projections estimated for a specific spray arm's design showed low efficiencies values. Important differences in water impact projections from left to right side of the dishwasher were seen as well. Current designs were proved to present room for further improvements.

The study also highlighted the complexity of the problem. Many design factors are interconnected in order to produce efficient results. Understanding the influence of each of them and their interactions is a key step in order to improve future designs. The routine developed presents the benefits of being quicker than CFD analysis and introduces comparable measurements on the quality of a design. Potentially, further expansions could analyse multiple locations in parallel and more complex geometries. An overall ADW efficient coefficient could be introduced as a way to characterise the efficiency across all the inner volume and not just a particular location or crockery element.

In the last two chapters, the design of current ADWs showed important challenges for distributing water efficiently and for creating significant mechanical forces over different locations. Efforts should be focused on the development of new systems to distribute water more homogenously by solving the symmetry problems highlighted here. The information presented in these chapters aims to settle some basics concepts for future research in the field.

CHAPTER 6

SWELLING AND REMOVAL PHENOMENA IN PROTEIN-BASED SAMPLES

6.1. INTRODUCTION

The following chapter studies the typical cleaning evolution occurring on egg-yolk technical stains. Protein-based soils represent one of the most difficult soils to remove in ADWs. Understanding and modelling the removal process can lead to propose optimisation scenarios. If wash conditions established were able to clean dry egg-yolk soils, it could be assumed that other similar less attached soils would be removed as well. Experiments to study typical swelling and removal phenomena via scanning Fluid Dynamic Gauge (sFDG) are presented. Temperature, pH, level of enzyme, net shear stress and frequency of application of shear stress are analysed as factors affecting each of the steps in the removal process. These factors represent a combination of mechanical and chemical parameters typically found in ADWs. They are also considered to influence the cleaning behaviour in these soils.

Initially, dynamic statistical models are developed to study swelling and removal phenomena. Partial Least Squares (PLS) method is the statistical tool used. The importance of the different factors along the process is given. Knowing how and when those factors analysed perform at their best can aid to decide the right way to proceed with this type of soils and to optimise wash cycles and formulations.

Studies on swelling phenomena are further expanded. Temperature and pH effects are analysed in more detail. sFDG data is compared against gravimetric data. Four different diffusional theories are then considered. Firstly, power law model is used to describe the type of transport occurring at different temperatures and alkalinities. Then, Fick's second law and linear and non-linear poroelasticity theories are used to evaluate the dynamics of the diffusion process and their predictions compared.

In the last section, the development of a mathematical swelling-removal model is proposed. A case study is shown as a guideline to understand the steps taken and the decisions made. The different mechanisms involved in a typical protein-based soil cleaning process are identified: swelling and removal via external application of shear stress or soil dissolution. An equation is then proposed as a mathematical approach to visualise the problem. Different phenomena were

initially analysed independently. Uniaxial swelling is described by the non-linear poroelasticity equation. This is a partial differential equation (PDE) that allows to discretise the thickness of the sample and to introduce 'theoretical layers'. Removal is modelled using an empirical approach and removal rates were calculated from experimental data. Finally, the proposed algorithm integrates in parallel swelling and removal mechanisms. The novelty is introduced as the 'theoretical layers' initially defined are removed over time until cleaning is complete.

6.2. DYNAMIC STATISTICAL MODELS

Experimental designs proposed for the development of dynamic statistical models are explained in *Chapter 3, section 3.12.1*. In this case, both types of design chosen allowed the inclusion of single interactions (i.e. Temperature*pH). Squared terms (i.e. Temperature*Temperature) were also included for swelling and removal phenomena model.

6.2.1. Swelling phenomenon (nil enzyme experiments).

For the study of swelling phenomenon, a 3-levels full factorial design was chosen. Temperature and pH range were from 30ºC to 55ºC and 9.5 to 11.5 respectively, in accordance to the values typically seen in an ADW wash cycle. **Figure 6.1** illustrates the thickness profiles obtained for the 9 experimental runs included in the full-factorial DOE. Data is represented by using the data-processing method explained in *Chapter 3, section 3.6.3*.

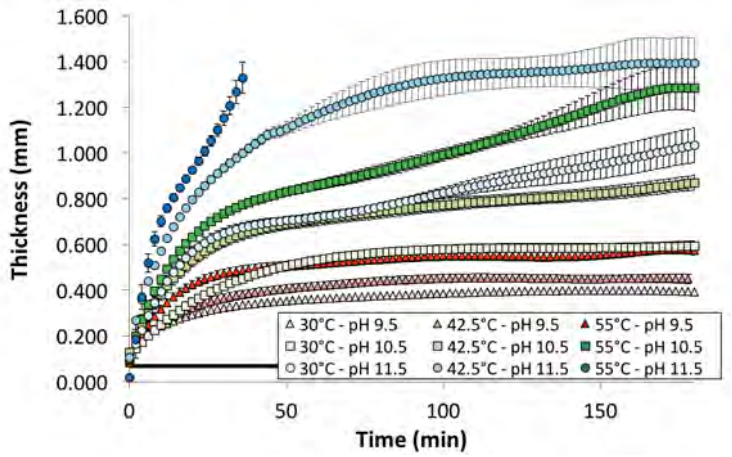

Figure 6.1. Thickness profiles for swelling phenomenon DOE. Red triangles, green squares and blue circles represent pH of 9.5, 10.5 and 11.5 respectively. Temperature range is shown from pale to intense colour gradients. Error bars illustrate the inner variability within a sample. Data is represented for every 2 minutes. Black line indicates the initial thickness of the stains.

Higher degrees of swelling were obtained when temperature and pH increased. pH showed a stronger effect on thickness than temperature. Equilibrium was seen for experimental conditions at pH 9.5 at all temperatures (red triangles) and at pH 10.5 and 30ºC (pale-green squares). The system was considered equilibrated when the swelling or mass-uptake rate was less than 5% of the swelling rate in the first 3 minutes of the experiment. For experimental conditions at pH 10.5 and 42.5ºC and 55ºC (semi-pale and green squares) and at pH 11.5 and 30ºC (pale-blue circles), an increase in the soil thickness was still observed at times above 60 minutes. At pH 11.5 and 55ºC (blue circles), a complete detachment of the soil from the stainless steel substrate occurred between 30 to 40 minutes. At pH 11.5 and 42.5ºC (semi-pale blue circles), a significant increase in the error was observed after 50 minutes despite equilibrium was apparently achieved. When data for single locations were analysed individually, a lift-up effect and the removal of top layers were seen at different locations. These phenomena are explained in more detailed in *section 6.3*, where swelling stage is deeply analysed.

The statistical analysis constructed a full factorial PLS model (temperature, pH and temperature*pH as input factors) for the 181 responses obtained per run (from minute 0 to minute 180). The output result suggested 2 latent factors explaining 60% of the variation in X (input factors) and 96% of the variation in Y (output response). **Table 6.1** summarises the variation explained by each of the factors given.

Table 6.1. Summary of the X and Y variation explained by the factors proposed from PLS model. Swelling phenomenon DOE.

Number of factors	X Effects		Cumulative X
1	32.7663	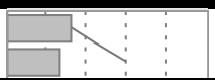	32.766
2	26.9291		59.695

Number of factors	Y Responses		Cumulative Y
1	85.1363	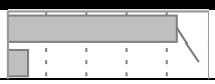	85.1363
2	11.0737		96.2100

Figure 6.2 shows the scores plot for each factor extracted. In this case, no unusual observation was seen in the dataset as a linear tendency was followed. Therefore, data introduced from all experimental runs were considered valid.

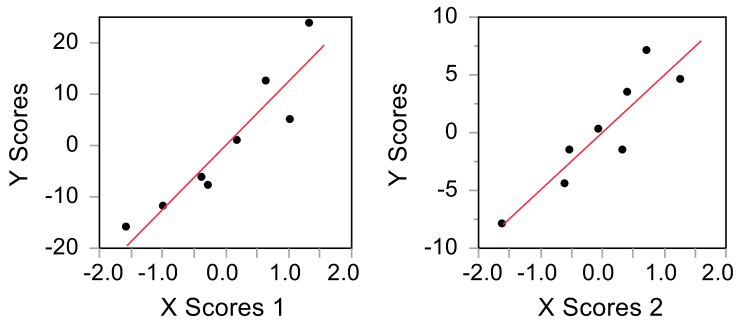

Figure 6.2. Scores plots for the two factors extracted by the PLS method. Swelling phenomenon DOE.

Figure 6.3 illustrates the Variable Importance Plot (VIP) for the case given.

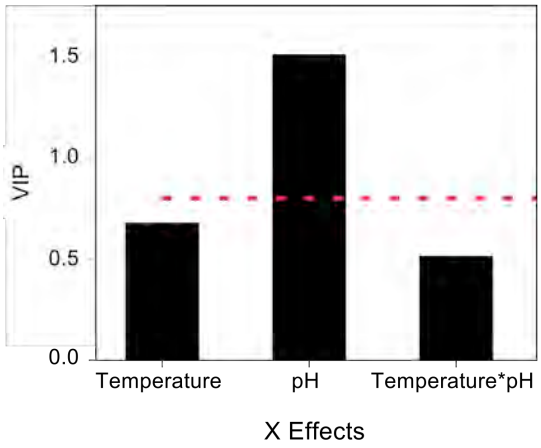

Figure 6.3. Variable Importance Plot (VIP) for the swelling phenomenon DOE.

As commented in **Figure 6.1**, pH was highlighted as the main factor contributing to the increase of thickness. The red dotted line in **Figure 6.3** establishes the limit from which different input parameters can be considered negligible from a statistical perspective. The use of factors below this line in the model could lead to over-fit the predictions. Experimental variability and data-processing errors would not be statistically disregarded, thus the predictive capability of the model would decrease. In this particular case, the number of factors initially considered was low. Also, as the effect of temperature caused important changes in the output response, no

further action was taken and the three model effects initially considered were incorporated to the model. The use of just pH as an input factor could have also lead to a poor predictive model due to a lack of inputted information.

Figure 6.4 shows different examples of the spectral profiler obtained from the analysis of swelling phenomenon.

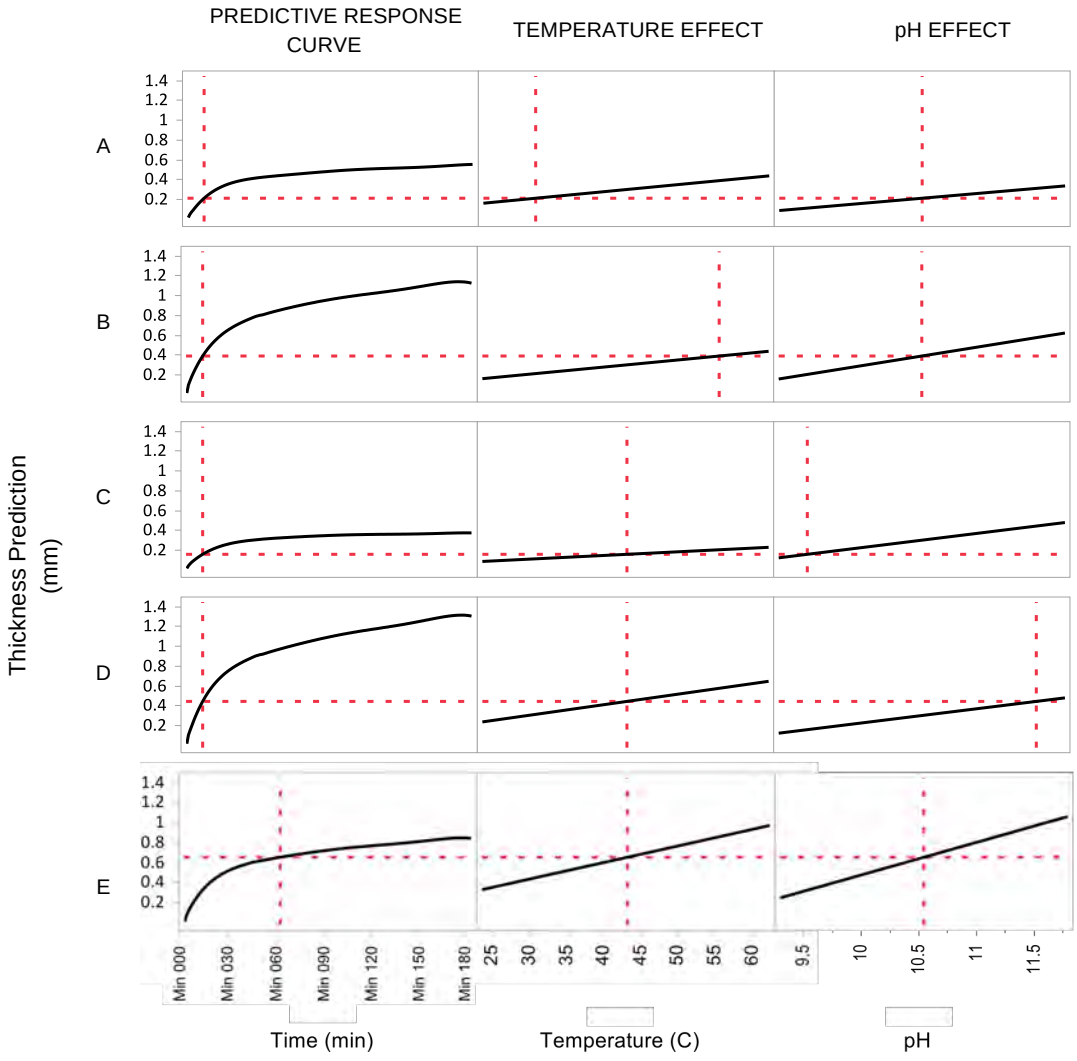

Figure 6.4. Examples of different spectral profiles at different conditions for the swelling phenomenon PLS model. First column plots represent thickness predictions over time. Second column plots represent temperature effect. Third column plots represent pH effect. A – Time located at 10 minutes; T = 30ºC; pH = 10.5; B – Time located at 10 minutes; T = 55ºC; pH = 10.5; C – Time located at 10 minutes; T = 42.5ºC; pH = 9.5; D – Time located at 10 minutes; T = 42.5ºC; pH = 11.5; E – Time located at 60 minutes; T = 42.5ºC; pH = 10.5;

The first row illustrates the thickness prediction curve for experimental conditions at 30ºC and pH 10.5. The graph (first column) shows low degree of swelling as expected. In the second row, the predictive response curve at 55ºC and pH 10.5 shows a considerably higher degree of swelling. The positive effect of temperature on the response matched what was observed experimentally. Plots also show the tendency to equilibrium in the first case and the increase of thickness after 60 minutes in the second case. In rows three and four, the same comparison is done but varying the pH. Again, a significant change in the degree of swelling is observed between pH 9.5 (third row) and pH 11.5 (fourth row), indicating the impact on thickness in the range of pH studied. The effect of the different factors over time can also be explored. The fifth row shows the importance of temperature and pH at a time of 60 minutes for experimental conditions at 42.5ºC and pH 10.5. The slope of the effect lines in the second and third column indicates the intensity of the change to the output response that would occur if these input effects were varied at that time. The steeper the slope, the bigger the change. The comparison of the slopes with previous examples at 10 minutes illustrates the difference of the effect at different times.

6.2.2. Swelling and removal phenomena (experiments with enzymes).

For the study of swelling and removal phenomena, a custom design with 22 runs was chosen. Temperature and pH range were kept from 30ºC to 55ºC and 9.5 to 11.5 respectively. Additionally, enzyme levels were set from 0.02 g/l to 0.10 g/l, shear stresses from 12 Pa to 65 Pa and the frequency factor from 9% to 100%.

Figure 6.5 shows the results for five different experimental runs. Examples selected represent a wide variety of responses obtained.

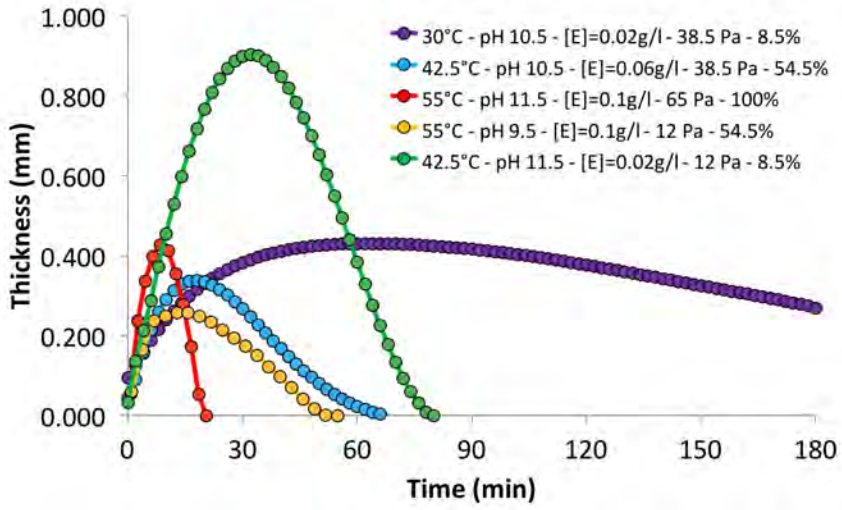

Figure 6.5. 5 different experimental runs from swelling and removal phenomena DOE showing a wide range of thickness profiles. Experimental conditions: Red dots – 55ºC, pH 11.5, [Enzymes] = 0.1 g/l, Shear Stress Frequency = 100%, Net Shear Stress = 65 Pa; Yellow dots – 55ºC, pH 9.5, [Enzymes] = 0.1 g/l, Shear Stress Frequency = 54.5%, Net Shear Stress = 12 Pa; Green dots – 42.5ºC, pH 11.5, [Enzymes] = 0.02 g/l, Shear Stress Frequency = 8.5%, Net Shear Stress = 12 Pa; Blue dots – 42.5ºC, pH 10.5, [Enzymes] = 0.06 g/l, Shear Stress Frequency = 54.5%, Net Shear Stress = 38.5 Pa; Purple dots – 30ºC, pH 10.5, [Enzymes] = 0.02 g/l, Shear Stress Frequency = 8.5%, Net Shear Stress = 38.5 Pa.

The fastest cleaning was achieved when the highest levels of the five factors controlled were tested (i.e. 55ºC, pH 11.5, [Enzymes] = 0.1 g/l, Shear Stress Frequency = 100%, Net Shear Stress = 65 Pa). The case, illustrated as the red circles, showed a quick increase on the thickness during the first 10 minutes followed by a quick decrease of it once removal started. A complete cleaning was observed after 20 minutes approximately.

The yellow circles represent a case with low alkalinity (i.e. 55ºC, pH 9.5, [Enzymes] = 0.1 g/l, Shear Stress Frequency = 54.5%, Net Shear Stress = 12 Pa). As pH is the main driver of the increase on thickness, a low degree of swelling was observed in this case. The high level of protease used and a relatively high frequency factor gave a complete cleaning after 50-55 minutes approximately.

The green circles illustrate the opposite case (42.5ºC, pH 11.5, [Enzymes] = 0.02 g/l, Shear Stress Frequency = 8.5%, Net Shear Stress = 12 Pa). High alkaline conditions were established

with a low level of enzyme and a low frequency factor. As a result, a higher degree of swelling was observed but that did not translate into a shorter cleaning time than the previous case. A complete removal was seen at around 80 minutes. Interactions between different experimental parameters are suggested from these comparisons. Depending on the experimental conditions (i.e. level of enzyme or frequency of application of shear stress) it might be necessary to increase the alkalinity or not in order to speed up the removal process. A high degree of swelling does not guarantee a faster cleaning.

The blue circles represent the thickness profile obtained for the midpoint experimental design run (i.e. 42.5ºC, pH 10.5, [Enzymes] = 0.06 g/l, Shear Stress Frequency = 54.5%, Net Shear Stress = 38.5 Pa). The degree of swelling observed was within the lowest and highest swelling degrees cases. A complete cleaning was achieved at around 65 minutes. Overall, cleaning times were in a range from 20 to 100 minutes.

Exceptions with slower or no complete removal were also found. The purple circles represent a case where no complete removal was observed (i.e. 30ºC, pH 10.5, [Enzymes] = 0.02 g/l, Shear Stress Frequency = 8.5%, Net Shear Stress = 38.5 Pa). The low temperature, enzyme level and frequency factor established made the removal process slow. Soil still remained over the substrate after three hours. The use of a relatively high shear stress did not enhance the removal process, suggesting a small effect on the decrease of thickness from this factor.

The statistical analysis followed the same approach as for the swelling phenomenon model. The model was constructed by inputting a single interaction design (i.e. pH*Enzyme) with individual (i.e. Shear Stress) and quadratic terms for each of the factors studied (i.e. Temperature*Temperature). PLS method initially extracted 14 factors explaining 83% of the variation in X and 99% of the variation in Y. **Table 6.2** summarises the variation explained by each of the new factors constructed.

Table 6.2. Summary of the X and Y variation explained by the factors constructed with PLS method. Swelling and removal phenomena DOE. First iteration.

Number of factors	X Effects	Cumulative X
1	6.1350	6.135
2	6.8421	12.977
3	8.2467	21.224
4	8.2890	29.513
5	5.5589	35.072
6	7.8713	42.943
7	4.5882	47.531
8	4.9601	52.491
9	4.9138	57.405
10	6.1080	63.513
11	6.2953	69.809
12	5.3282	75.137
13	5.5841	80.721
14	3.0317	83.753

Number of factors	Y Responses	Cumulative Y
1	52.1486	52.1486
2	16.7868	68.9353
3	9.8187	78.7541
4	4.8338	83.5879
5	5.2167	88.8046
6	2.1790	90.9837
7	2.5509	93.5346
8	1.9019	95.4365
9	1.3825	96.8190
10	0.6920	97.5110
11	0.5193	98.0303
12	0.3634	98.3936
13	0.2543	98.6479
14	0.3536	99.0015

Table 6.2 shows that only 6 factors explain more than 90% of the variation in Y and 8 factors more than 95%. This suggests that a further reduction in the number of factors considered is possible in order to avoid any over-fitting issue.

Figure 6.6 shows the scores plots for the first three factors extracted by the PLS approach.

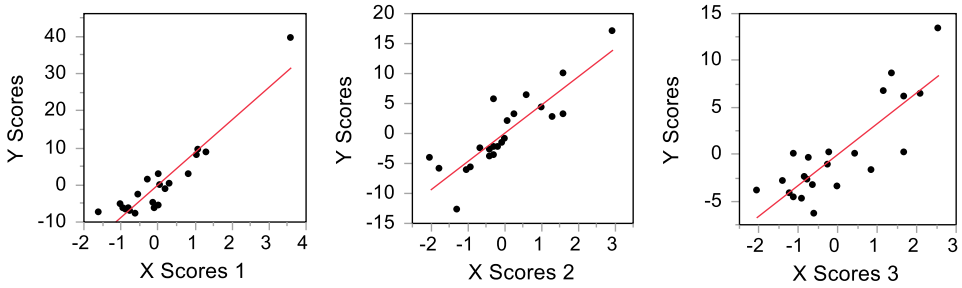

Figure 6.6. Scores plots for the first three factors extracted by the PLS method. First iteration on the swelling and removal phenomena DOE.

An outlier point is seen in the score plot for factor 1 (left). This factor is the most representative as explains more than 52% of the variability found. The outlier corresponds to experimental conditions at 30ºC, pH 10.5, [Enzyme] = 0.02g/l, Shear Stress Frequency = 8.5% and Net Shear Stress = 38.5 Pa. The purple dots in **Figure 6.5** represent its thickness profile. This run illustrates the slowest cleaning process obtained among all experimental cases proposed. The difference between this case and the second slowest one was significant. Thus, the statistical analysis highlighted this case as an outlier. Different analyses were further performed excluding this particular run. However, results obtained did not increase the quality of the model as the subsequent slowest cases were again highlighted as outliers. As a result, the run remained included in the analysis.

Figure 6.7 shows the Variable Importance Plot (VIP) of all the model effects initially inputted in the analysis.

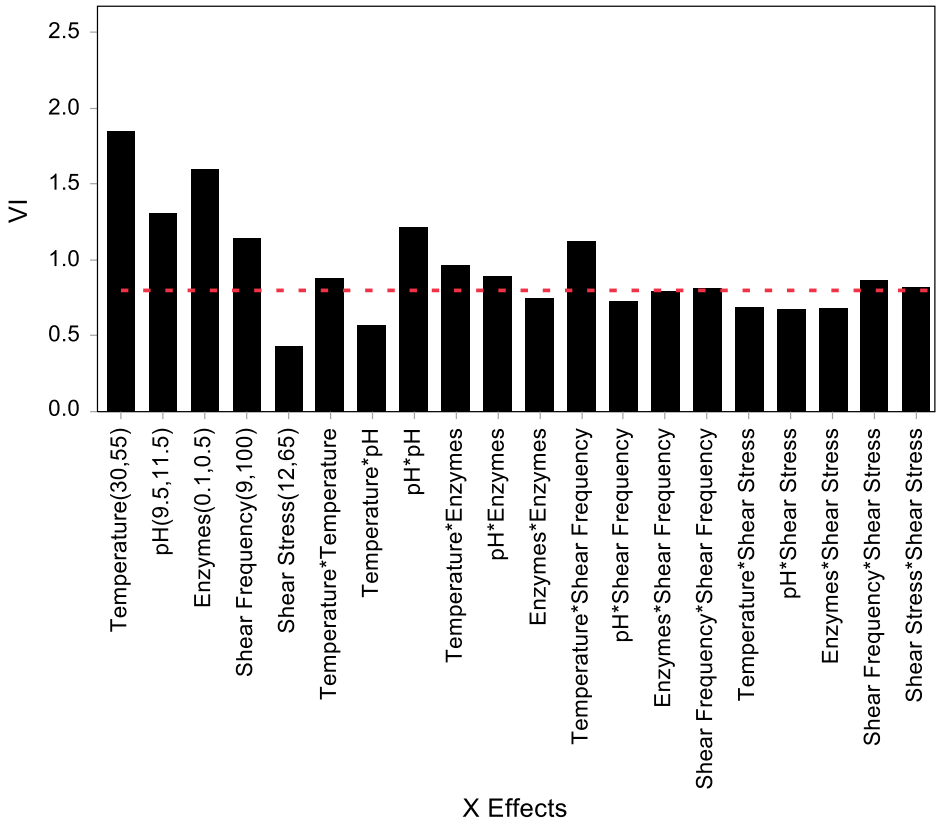

Figure 6.7. Variable Importance Plots (VIP) for swelling and removal phenomena PLS model. Factors inputted in first iteration.

Temperature, pH, level of enzyme and the frequency factor were proved to affect the response (thickness) significantly. However, the net shear stress applied over the sample did not produce a significant impact on thickness change within the range studied (from 12 to 65 Pa). This indicates that the removal of soil layers occurred faster whenever some external energy input was applied (frequency), but that an increase in the external energy imposed (net shear stress) barely changed the rate of removal. The importance of the frequency factor suggests a minimum external mechanical action required to enhance cleaning in this type of protein-based soils. However, once that minimum value is surpassed, the rate of removal remains almost invariant. For the case given, it is suggested the existence of this threshold at shear stress values lower than 12 Pa. This threshold varies with the intrinsic status of the soil at any time. As chemistry affects the soil network (via swelling-stretching or hydrolysis reactions), it moves to lower energy values. **Figure 6.8** summarises the hypothesis proposed:

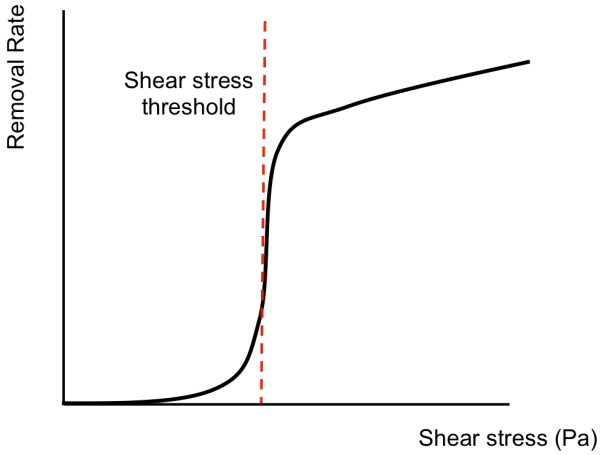

Figure 6.8. Schematics of the shear stress threshold hypothesis.

Among the interactions and quadratic terms, some were also identified as important contributors to the thickness change (i.e. Temperature*Temperature / pH*pH / Temperature*Enzyme / pH*Enzyme / Temperature*Frequency / Frequency*Frequency / Frequency*Shear Stress / Shear Stress*Shear Stress). Some effects are related to already known interactions such as the effect of temperature or alkalinity on enzyme activity (i.e. temperature*enzyme, pH*enzyme).

To avoid any over-fitting issue, JMP software allows rebuilding the model from those factors proved to be significantly important. This simplifies the analysis as a smaller number of effects are considered. This simplification process was repeated twice for the experimental DOE given. As a final result, 5 factors were extracted by the PLS method explaining 73% of the variation in X and 71% of the variation in Y. **Table 6.3** reports the variation explained by each of the final factors constructed.

Table 6.3. Summary of the X and Y variation explained by the factors constructed with PLS method. Third iteration on the swelling and removal phenomena DOE.

Number of factors	X Effects	Cumulative X
1	17.2372	17.237
2	14.3868	31.624
3	12.9935	44.618
4	13.8880	58.506
5	14.9091	73.415

Number of factors	Y Responses	Cumulative Y
1	42.2349	42.2349
2	14.6146	56.8495
3	7.1460	63.9955
4	4.2782	68.2736
5	3.1325	71.4061

Figure 6.9 illustrates the scores plots for the 5 factors extracted. The slowest cleaning process was again highlighted as an outlier. As for the initial iteration, the removal of it in did not enhance the quality of the statistical model. Therefore, the experimental run was again maintained in the analysis.

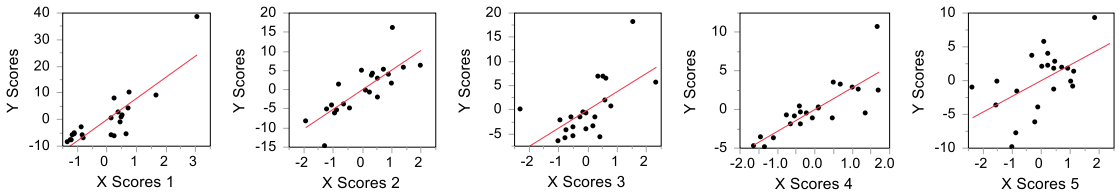

Figure 6.9. Scores plots for the final five factors extracted by the PLS method. Third iteration on the swelling and removal phenomena DOE.

Figure 6.10 represents the VIP for those effects that were established as significant after three iterations in the model building process.

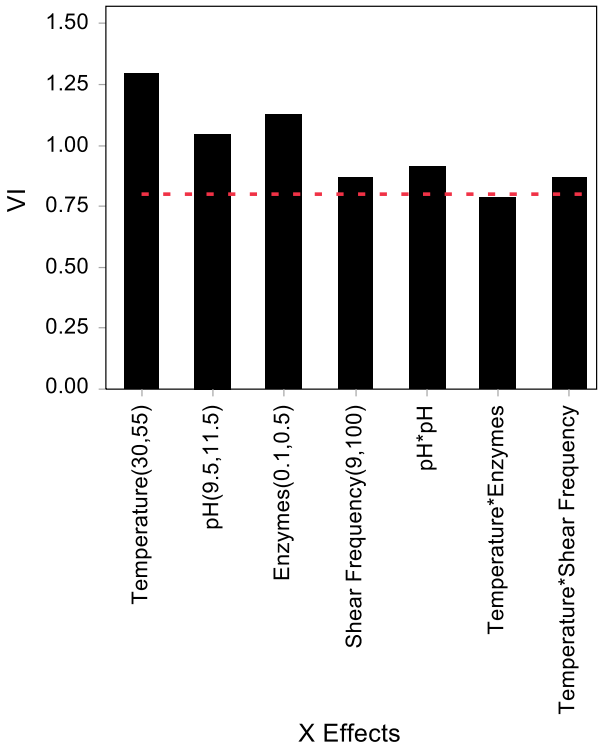

Figure 6.10. Variable Importance Plot (VIP) for swelling and removal phenomena PLS model. Factors shown remained as significant in the third and last iteration.

Temperature, pH, enzyme level and the frequency factor were maintained as significant contributors to the thickness change. As for the interactions and quadratic terms initially established, only the squared term of pH (pH*pH) and the interactions between temperature and enzyme level (Temperature*Enzymes) and temperature and the frequency factor (Temperature*Shear Frequency) were kept as important.

Figure 6.11 shows a normalised effect plot that describes the effect on thickness over time of each of the significant factors remaining. A negative value indicates a negative effect on thickness (removal) while a positive value indicates the opposite (swelling).

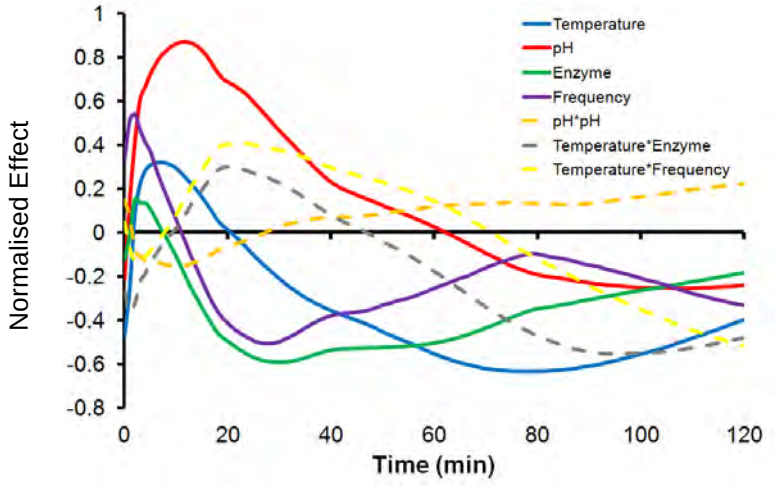

Figure 6.11. Normalised effect over time of the different significant factors remaining. Mechanisms of swelling and removal are later on shown in Figure 6.25.

Temperature (blue line) showed an initial positive contribution to thickness during the first 20 minutes. This corresponds to the swelling stage. As commented for the swelling DOE results, temperature is a factor affecting the degree of swelling at equilibrium. At around 20 minutes, the transition from a net swelling stage (net increase in thickness) to a removal phase (net decrease in thickness) was typically seen. At longer times, temperature contribution shifted from a positive to a negative effect on thickness with an increasing importance over time. The effect was proportionally higher at the removal stage (peak at -0.6) than at the swelling stage (peak at 0.3). Overall, it can be concluded that temperature is a net contributing factor for all the phenomena occurring in a typical protein-based cleaning process, hence its great importance observed in **Figure 6.10**.

pH (red line) was highlighted as a very important factor during the swelling stage of the process, according to what was initially seen with swelling data. The plot shows how pH impacts thickness at early times (i.e. at 10 minutes) with a normalised maximum value around 0.9. Its contribution decreased afterwards in parallel with a reduction of the swelling rate as the stretch of the network approximated towards the equilibrium. At that stage removal mechanisms became predominant. The plot illustrates as well the negligible contributions of pH to removal. Negative values are seen after 60 minutes. At this time most of the experimental conditions

analysed were in the final stages of the cleaning process or completely cleaned. Also, negative values were kept low. This result indicates that high alkalinity is required at the first stages of a protein-based soil cleaning process. However, alkalinity is not an important factor once removal occurs. Boosting alkalinity at the first stages of a wash cycle is therefore recommended when protein-based soils are cleaned. If this were left to a latter stage in the wash cycle, a decrease in the cleaning performance would be expected.

The effect of the enzyme (green line) became significant after an initial lag period of approximately 10 minutes. As a protease promotes the hydrolysis of protein's peptide bonds, its effect on thickness was negative. It required an initial reaction time to induce cleaning. The small positive effect on thickness shown at very early times is probably due to the experimental error and the statistical processing. After that period, the enzyme showed an increased negative effect on thickness until a local minimum was found at around 30 minutes. The enzyme was the main contributor to removal, showing a normalized effect peak at -0.6. Its effect varied slowly once the peak was achieved, remaining almost invariant during most of the removal process (from 20 minutes to 80 minutes).

The frequency of application of shear stress over the soil (purple line) was also an important contributor to removal, following a similar trend as for the enzyme. However, during the initial swelling stage it showed a positive effect on thickness. This suggests that the application of an external shear stress and the water suction produced through the sFDG nozzle could enhance the diffusion process occurring. The convective flow created around the area could promote the diffusion of the wash solution into the soil network. This trend could also be referred to the lift-up effect occurring in the top layers of the soil network. Regardless the real fact, the more frequent the nozzle was over the soil, the faster the thickness increased. After that period, the effect shifted to a negative contribution. Its peak was found at around 30 minutes with a normalised effect value around -0.5. It can be conclude that both the frequency factor and enzyme level were the main contributors to cleaning for this particular soil types.

Interactions showed different behaviours. Overall, their influence was almost negligible during the initial swelling stage. The interaction of temperature with the enzyme (Temperature*Enzyme – discontinuous grey line) and with the frequency factor (Temperature*Frequency – discontinuous yellow line) showed a positive contribution to thickness from 10 to 60 minutes. This contradicts what initially expected from these types of interactions. For example, as commented previously, the activity of the enzyme is highly dependant on temperature. For the range of temperatures given, the protease best performance was at the highest level (55ºC). Therefore, a negative contribution to thickness was expected when temperature and enzyme level were analysed together as an interaction effect. The higher the level of these factors the faster cleaning observed. In **Figure 6.11**, the maximum contribution effect of this interaction (Temperature*Enzyme) was found at 20 minutes approximately. This corresponds to the curve maximum of a typical thickness profile, as seen for the mid-level case in **Figure 6.5** (blue line). Also at that time, temperature contributions were transitioning from positive to negative thickness effect as commented previously. The positive contribution of this interaction suggests that the weakening process given by the action of the enzyme and temperature enhanced a lift-up effect at that stage. Soil network had already lost cohesiveness but still remained strong enough. Thus, a high temperature or high level of the enzyme led to a partial increase on the thickness measured. That partial increase would be higher with the higher the level set for these factors. After overcoming this stage, the influence of this interaction reduced. The soil network became weak enough and the increase of temperature or the frequency factor led to an increase on the removal rates as shown by their individual factors. A similar reasoning could be applied for Temperature*Frequency interaction. Finally, pH interaction squared term did not show a big impact on thickness.

Figure 6.12 illustrates three spectral profiler examples for the swelling and removal phenomena PLS model.

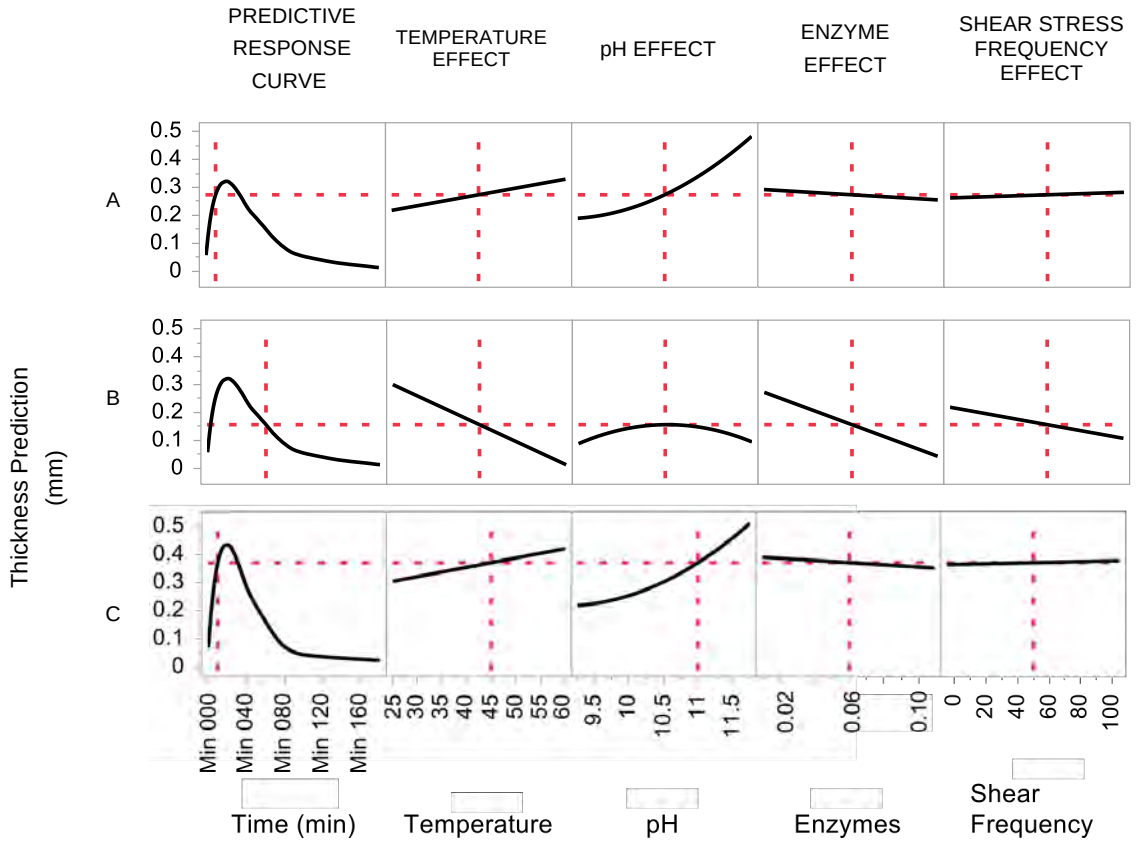

Figure 6.12. Examples of different spectral profiler outputs for the swelling and removal phenomena PLS model. First column plots represent thickness predictions over time. Second column plots represent temperature effect. Third column represent pH effect. Fourth column represent enzyme level effect and fifth column represent frequency factor effect. A – Time located at 10 minutes; T = 42.5ºC; pH =10.5; [Enzyme] = 0.06 g/l; Shear Stress Frequency = 50%; B – Time located at 60 minutes; T = 42.5ºC; pH =10.5; [Enzyme] = 0.06 g/l; Shear Stress Frequency = 50%; C – Time located at 10 minutes; T = 45ºC; pH =11.5; [Enzyme] = 0.06 g/l; Shear Stress Frequency = 50%;

Case A (Temperature 42.5ºC; pH = 10.5; [Enzyme] = 0.06g/l; Shear Stress Frequency = 50%) shows thickness predictions at intermediate levels of the four single factors controlled and established as significantly important by the PLS method. Time position set on the response curve was at 10 minutes, corresponding to the net swelling phase. Temperature effect and mostly pH effect presented a positive and steep slope. Enzyme effect and frequency factor effect remained flat. The positive slope represents a net positive contribution to thickness at that time. This was consistent to what was seen in **Figure 6.11** at that time. Case B set the time

position at 60 minutes at the same experimental conditions as Case A. The response curve did not change as no factors' levels were modified. However, the effect of the different factors did. Temperature effect shifted to a negative steep slope, indicating an important contribution in the removal stage. pH slope turned flat while the enzyme level and frequency factor effects showed significant contributions to the decrease of thickness. Again, this agreed with the information from **Figure 6.11**. Case C (Temperature 45ºC; pH = 11; [Enzyme] = 0.06g/l; Shear Stress Frequency = 50%) shows the effect on the response when the level of the factors were varied. The increase of pH and temperature made the response curve to predict a higher degree of swelling while the total removal time did not vary much (i.e. 80 minutes).

Equations from the statistical model can be retrieved from JMP. The software builds individual equations for every time value considered in the analysis (a minute in this case). The output value is calculated as a function of the different factors remaining. For different equations, the coefficients of the factors vary according to their effect over time. Overall, 180 equations can be extracted from the experimental case analysed. This could be use for the integration of this statistical model into a bigger model containing other attributes from other areas of cleaning (i.e ADW design factors).

6.3. SWELLING STUDIES VIA SCANNING FLUID DYNAMIC GAUGE AND GRAVIMETRIC TESTS

Due to the importance of swelling phenomenon in the cleaning of protein-based soils, further studies were performed to deeply analyse this process. Experimental design selected is explained in *Chapter 3, section 3.12.2*. Temperature and pH were the factors highly affecting swelling, according to the previous statistical analysis. Ranges studied were again from 30ºC to 55ºC for temperature and from 9.5 to 11.5 for pH. The analysis compares sFDG and gravimetric data to prove the existence or not of the hypothesis of lift-up or removal on the top layers of the soil sample due to the application of the external mechanical action from the gauging fluid. 4 different diffusional theories (power law, Fick´s second law, linear and non-linear poroelasticity theory) are used to describe the phenomena occurring. They are explained in *Chapter 2,*

section 2.4. They present an increasing complexity as new theoretical parameters and considerations are introduced in their development.

6.3.1. sFDG and gravimetric results.

Data collected experimentally was processed according to the methodology explained in *Chapter 3, section 3.6.3*. Thickness and mass values were initially represented over time. **Figure 6.13** shows the results for gravimetric (A) and sFDG experiments (B & C).

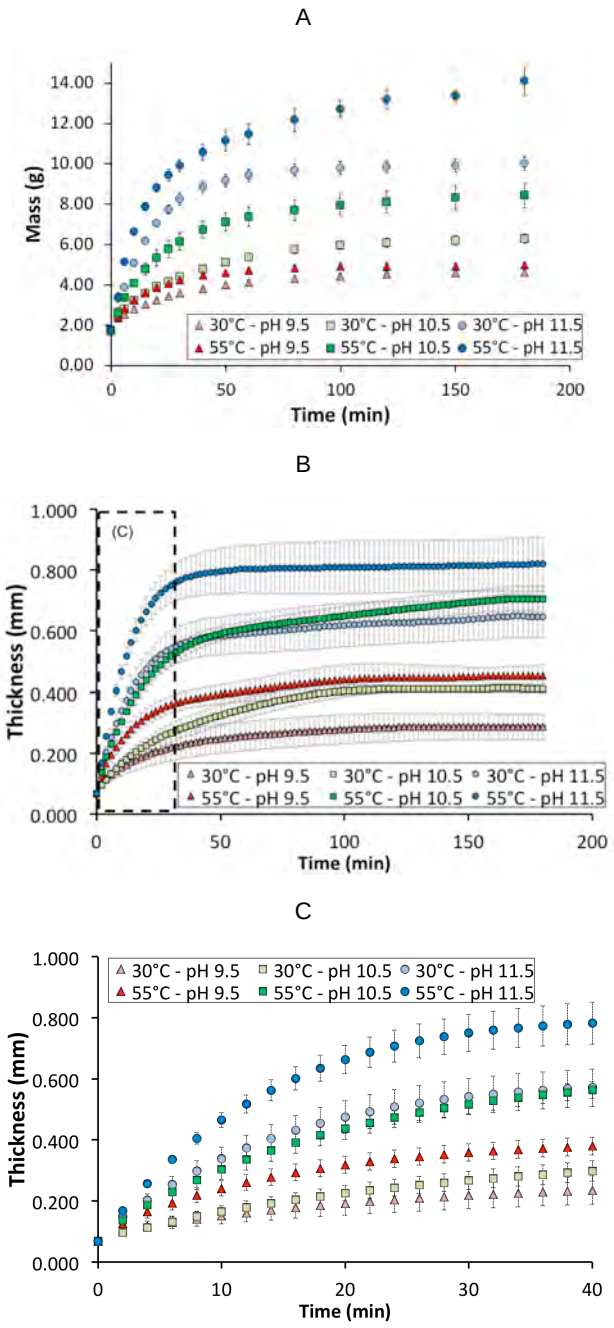

Figure 6.13. Experimental results. A – Gravimetric tests. B – Polynomial fit and averaged sFDG data. C – sFDG data for the first 40 minutes.

The plots show the rapid increase of thickness or mass that occurred during the initial minutes of any experimental run (i.e. 40 min). The rate decreased over time as the samples approached the equilibrium. The end point was different depending on the experimental conditions and equilibrium was reached by the end of the experimental time for all the cases. Again, data demonstrated that by increasing temperature and pH, swelling and water uptake increased. The VIP statistical analysis shown in **Figure 6.14** also confirmed that the effect of pH on the hydration process was more important than temperature within the levels studied. This is clearly seen in **Fig. 6.13A** for gravimetric tests. The difference in behaviour found between the different soil batches used for the swelling phenomenon studies was related to the degree of swelling observed. The initial tests showed a slightly higher swelling than the tests shown in this section, despite the experimental conditions and procedure followed were the same. Regardless of this, the trend and importance of the different factors analysed was maintained.

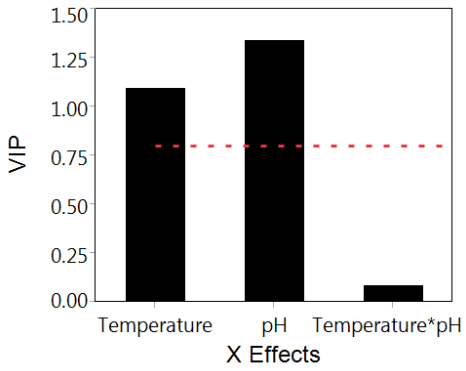

Figure 6.14. Variable Importance Plot (VIP) for sFDG experiments.

For sFDG measurements, the variability between the 4 locations analysed within a sample was found to be about 4% of the measured thickness. The variability increased up to about 10% when different samples were compared. This indicated higher differences between samples than at different locations on a single tile. For gravimetric tests, the variability was lower at around 3% of the measured weight. The higher error seen for sFDG measurements was due to an accumulation of errors from different factors such as the application of a shear stress over the sample, the error related to the movement of the nozzle around different positions, the inner error of the flowmeter, the accuracy of the z-motor and the possible inhomogeneity of the sample at the different locations considered.

At 55ºC and pH 11.5, localised blisters appeared on the surface after 2h as shown in **Figure 6.15**. We believe that these blisters related to hydrolysis reactions occurring at high alkalinity. Peptide bonds broke (cohesive failure) as a consequence of the high concentration of OH^- ions and the network strength weakened (Saikhwan *et al*., 2010). A distortion of the data was thus observed as the presence of big blisters allowed the solvent to penetrate more easily into the network. This would explain the higher weight and variability seen after 150 minutes for the gravimetric tests (**Figure 6.13A**). This weakness in the soil called for extra care when handling the tiles in order to prevent the loss of any soil when measuring their weight.

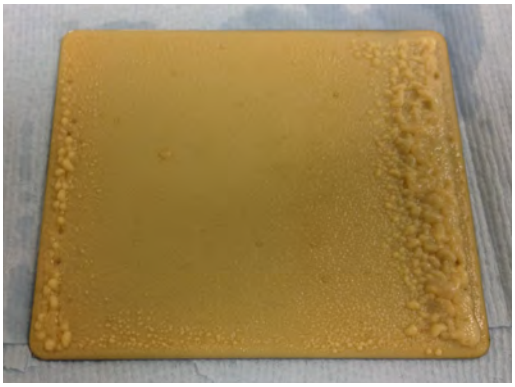

Figure 6.15. Egg yolk tile showing blisters at the edges after being submerged in a solution at 55ºC and pH 11.5 for 180 min.

Similar issues were found for sFDG tests at the same experimental conditions. A lift-up effect or removal of the soil was observed in some of locations studied as for the initial statistical tests performed. Underneath the nozzle a pressure change and a tensile force are generated as a consequence of the fluid moving upwards through the nozzle. The pressure change and pull-force were estimated by applying Bernoulli's equation (Gordon, 2012). With the set-up considered these values were established at 500 Pa and 1.6 mN approximately. The lift-up effect consists of the stretch of the network due to the pull force produced by the liquid suction through the nozzle of the sFDG. The measured thickness increases in consequence. The removal of the sample occurs when the action of the sFDG over the soil surface is high enough to detach some of the top layers. The consequence is that a lower thickness is measured. **Figure 6.16** shows the raw data collected for the three experiments done at 55ºC and pH 11.5 for each of the 4 locations analysed. The graphs illustrate the different behaviours commented. Overall, among the 12 different locations studied, a lift-up effect was observed 5 times followed

by a removal of the soil in 3 occasions. These cases were disregarded when estimating the average thickness profile for that sample. For the locations showing an apparent equilibrium we assumed none of these effects occurred.

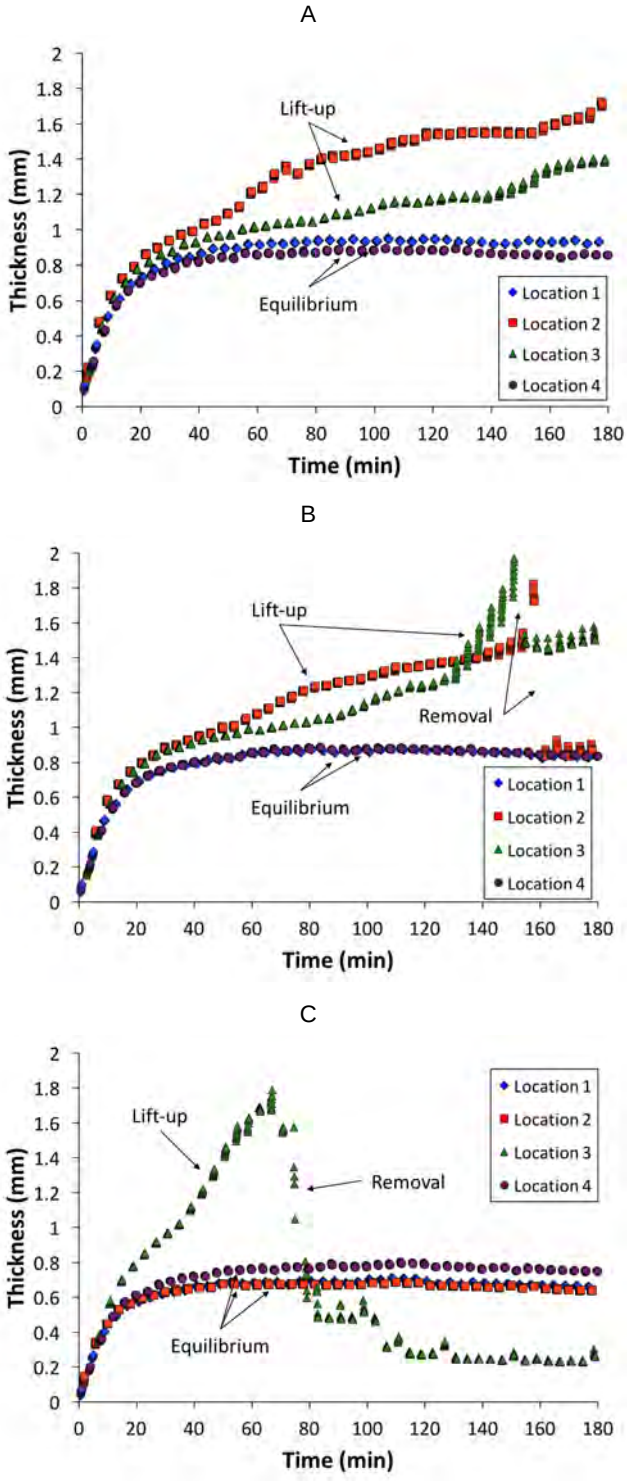

Figure 6.16. sFDG raw experimental data at 55ºC and pH 11.5. A – First test; B – Second test; C – Third test; Blue diamonds, red squares, green triangles and purple circles represent locations from 1 to 4 respectively.

Figure 6.17 summarises the possible scenarios observed for the measurement of thickness using the sFDG.

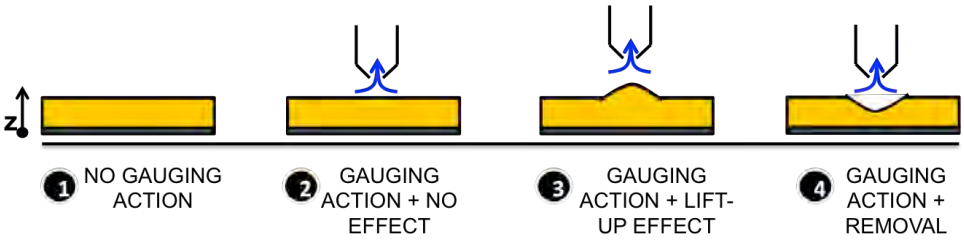

Figure 6.17. Schematic of the different scenarios when using the sFDG to measure the thickness of a sample.

The difference in thickness between lift-up and equilibrium cases within a single replicate represents the stretch occurring in a specific location. **Figure 6.18** represents that difference for the location 3 in the test shown in **Figure 6.16A**. The curve mimics creep profiles observed in plastic or polymeric materials (McKeen, 2015). Creep is defined as the change over time that occurs to a material when subjected to a constant or regular stress. Those locations with a lift-up effect deformed plastically, not elastically, as they did not return to the original shape every time the tensile force was applied. Creep curves typically show three stages: primary, secondary and tertiary. The primary stage is an initial and non-steady deformation on the sample. This is followed by a constant strain rate, which characterises the secondary stage. Finally, when the stretch is high enough, the material starts to fail and the strain accelerates. This last stage precedes the fracture point, where the sample finally breaks. This phenomenon could be identified at a different extent in each of the cases not following an equilibrium trend. These observations arise the suitability of the sFDG in the analysis of creep behaviour of different materials and at different conditions (i.e. temperature, degree of swelling, tensile force applied…).

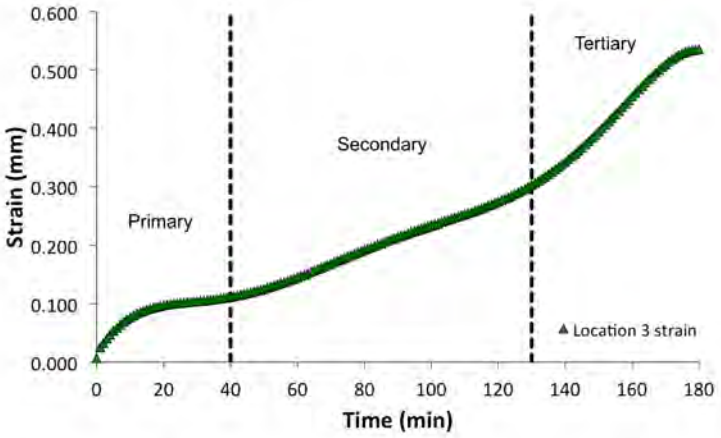

Figure 6.18. Strain profile for location 3 in example shown in Figure 6.16A.

6.3.2. Comparison of sFDG and gravimetric data

In **Figure 6.19** normalised gravimetric, $\overline{M(t)}$ (x-axis), and sFDG, $\overline{h(t)}$ (y-axis), data are shown. Results compare the kinetics of the process. They were separated for every pH level considered. The colour scale indicates the time the measurements were undertaken. Samples started at the beginning of the axis and dimensionless height and mass increased with time as samples reached equilibrium.

A

pH 9.5

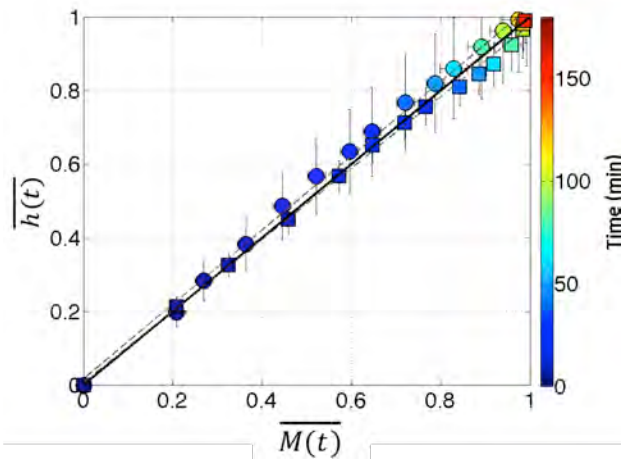

B

pH 10.5

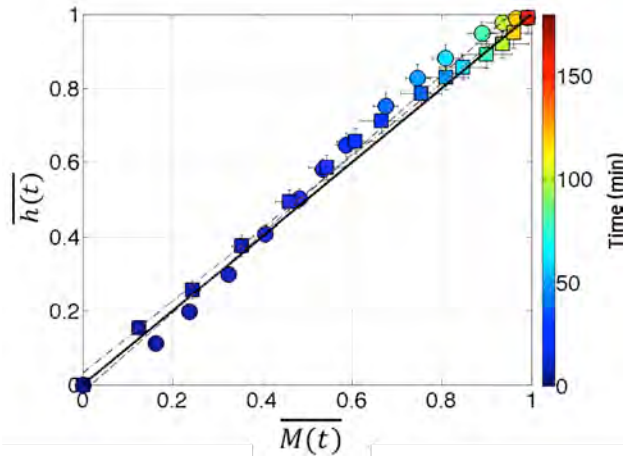

C

pH 11.5

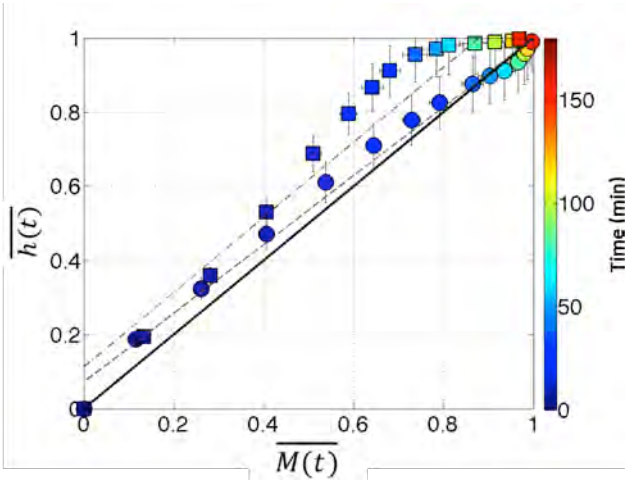

Figure 6.19. Normalised height and weight data to compare sFDG and gravimetric tests. A – pH 9.5; B – pH 10.5; C – pH 11.5. Circles – 30ºC; Squares – 55ºC.

Good agreement between the techniques was observed at pH 9.5 (**Figure 6.19A**), 10.5 (**Figure 6.19B**) and at 30ºC and pH 11.5 (**Figure 6.19C** – circles). 95% of the equilibrium values were reached within 90 min and the kinetics were not significantly affected within the range of temperatures considered (30ºC and 55ºC). At 55ºC and pH 11.5, the maximum value was reached faster in the sFDG than in the gravimetric case. Whilst around 90 minutes were required in the gravimetric experiments to get to 95% of the maximum hydration, this time was significantly reduced to 50 minutes for the sFDG case. As for the analysis shown in **Figure 6.16**, it is likely that the weakest top layers were detached when shear stress was applied from the sFDG, resulting in an underestimation of the swelling time required.

Table 6.4 summarises the parameters obtained by fitting the data from **Figure 6.19**. Overall, a good correlation between the techniques from a kinetics perspective (slope close to 1 and intercept close to zero) was observed for some conditions but not all.

Table 6.4. Linear fitting summary of data from Figure 6.19.

EXPERIMENT		SLOPE	INTERCEPT	R^2
TEMPERATURE	pH			
30ºC	9.5	1.010	0.017	0.997
55ºC	9.5	0.973	0.006	0.998
30ºC	10.5	1.070	0.021	0.989
55ºC	10.5	0.977	0.031	0.996
30ºC	11.5	0.928	0.071	0.991
55ºC	11.5	1.011	0.112	0.930

The comparison was extended by transforming sFDG data into mass using Eq. 2.4. **Figure 6.20** shows sFDG and gravimetric data represented together and expressed in mass units. In **Figure 6.20A** the absolute mass values from the two experimental techniques are shown while **Figure 6.20B** represents the difference over time between gravimetric and sFDG data.

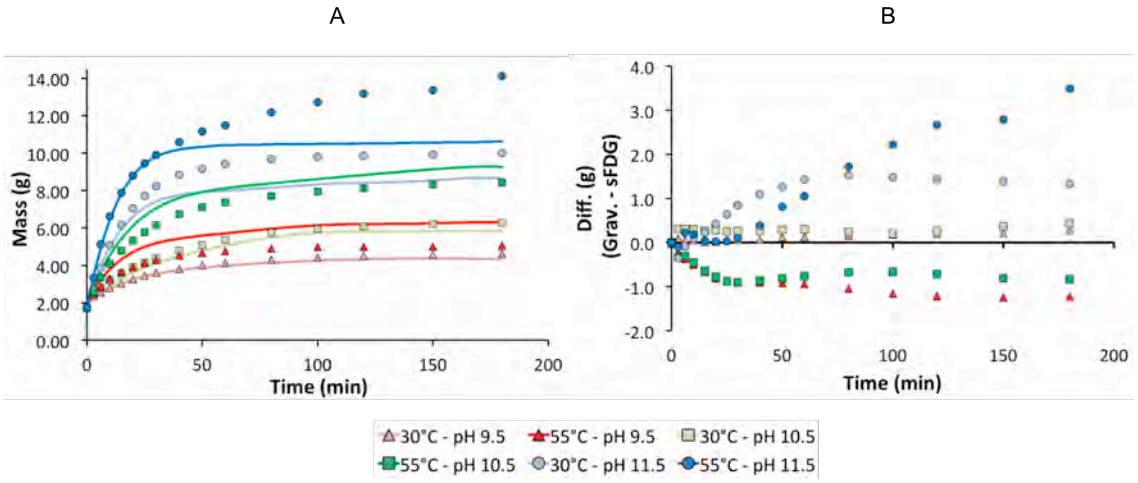

Figure 6.20. Comparison of gravimetric and sFDG data in mass units. A – Total mass over time. Lines and dots with same colour represent sFDG and gravimetric data respectively at the same experimental conditions; B – Difference between gravimetric and sFDG data over time.

Experiments in the milder conditions (30ºC for pH 9.5 and 10.5) showed good agreement as the convergence seen in **Figure 6.20A** was high and the difference showed in **Figure 6.20B** remained flat at values closer to 0.

Experiments at high temperature (55ºC for pH 9.5 and 10.5) showed similar trends for both techniques but the estimated water uptake from sFDG data was systematically higher (1g) when compared to the measured mass uptake given by gravimetric experiments. Two hypotheses were considered to explain this behaviour:

1. A lift-up effect from sFDG measurements that was favoured at higher temperatures. This would indicate higher elasticity of the soil network with the increase of temperature. As the experimental conditions did not result in any removal of material, the lift-up effect occurred and the thickness values measured were higher. A look at the raw data did not allow assuring this hypothesis. Equilibrium trends were similar to those reported in **Figure 6.16**.
2. Higher amount of water could be lost when removing the excess of water in the gravimetric method. At 55ºC, a lower water viscosity and consequent higher water mobility could have led to the removal of larger amounts of liquid. The hypothesis

was tested and disproved by quantifying the amount of water transferred to the drying paper. The difference in weight between the 'wetted' and 'dried' sample was measured and results showed a loss of approximately 0.2 g and 0.16 g for 55ºC and 30ºC respectively. This effect would only explain 4% of the difference seen between sFDG and gravimetric data.

Differences between sFDG and gravimetric data at high pH (i.e. pH 11.5) became obvious after 20-30 minutes. The measured mass uptake from the gravimetric tests was higher than the estimated mass uptake from sFDG experiments. If the assumption of molecular incompressibility is still valid, this indicates a lower volume occupied by the solvent molecules within the soil. Two hypothesis were again considered:

1. The presence of electrostatic screening effects between the Na^+ cations in the water and soil network. This would lead to a decrease in the volume of the network. These effects were studied in a similar work by (Mercadé-Prieto *et al*., 2007b) with protein-based systems. Results reported a significant reduction volume as a consequence of the electrostatic effects. However, these interactions occurred at pH higher than 13.3 when only NaOH was added to the solution.
2. The removal of soil layers in those locations with an equilibrium trend (no lift-up and no removal observed). Highly swelled layers could be detached early in the process thus leading to a lower equilibrium thickness value.

6.3.3. Modelling swelling

Power law equations (Eq. 2.1 and Eq.2.2) were applied to the experimental data obtained via gravimetric and sFDG tests. **Figure 6.21** represents the estimated diffusional exponents, n and n', as a function of temperature and pH. The size of the bubbles is related to the value of the exponent.

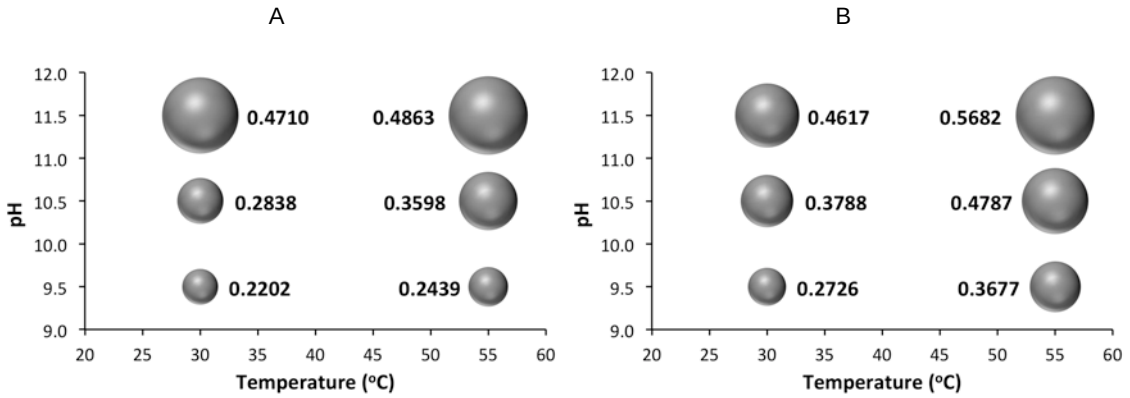

Figure 6.21. Diffusional exponent values. A – From gravimetric data (n). B – From sFDG data (n').

Results for gravimetric data (**Figure 6.21A**) indicated that pH is the main factor affecting the diffusional exponent (n). Results for sFDG data (**Figure 6.21B**) reported slightly higher values of n' for the same experimental conditions and a similar effect of pH. The effect of temperature was more pronounced in this case.

Overall, data suggested a Fickian diffusion (Case I) transport mechanism in all cases ($n < 0.5$). However, as pH increased, there was an increase of 'n' indicating more anomalous or Non-Fickian diffusion (Case II) mechanism. During hydration, as the soil network expanded, the rearrangement became more difficult. Thus, for those cases with higher equilibrium swelling, averaged relaxation times increased and became closer to diffusional times.

The rest of the modelling approach were used to fit gravimetric and sFDG data. **Figure 6.22** illustrates experimental and numerical results for each of the conditions studied.

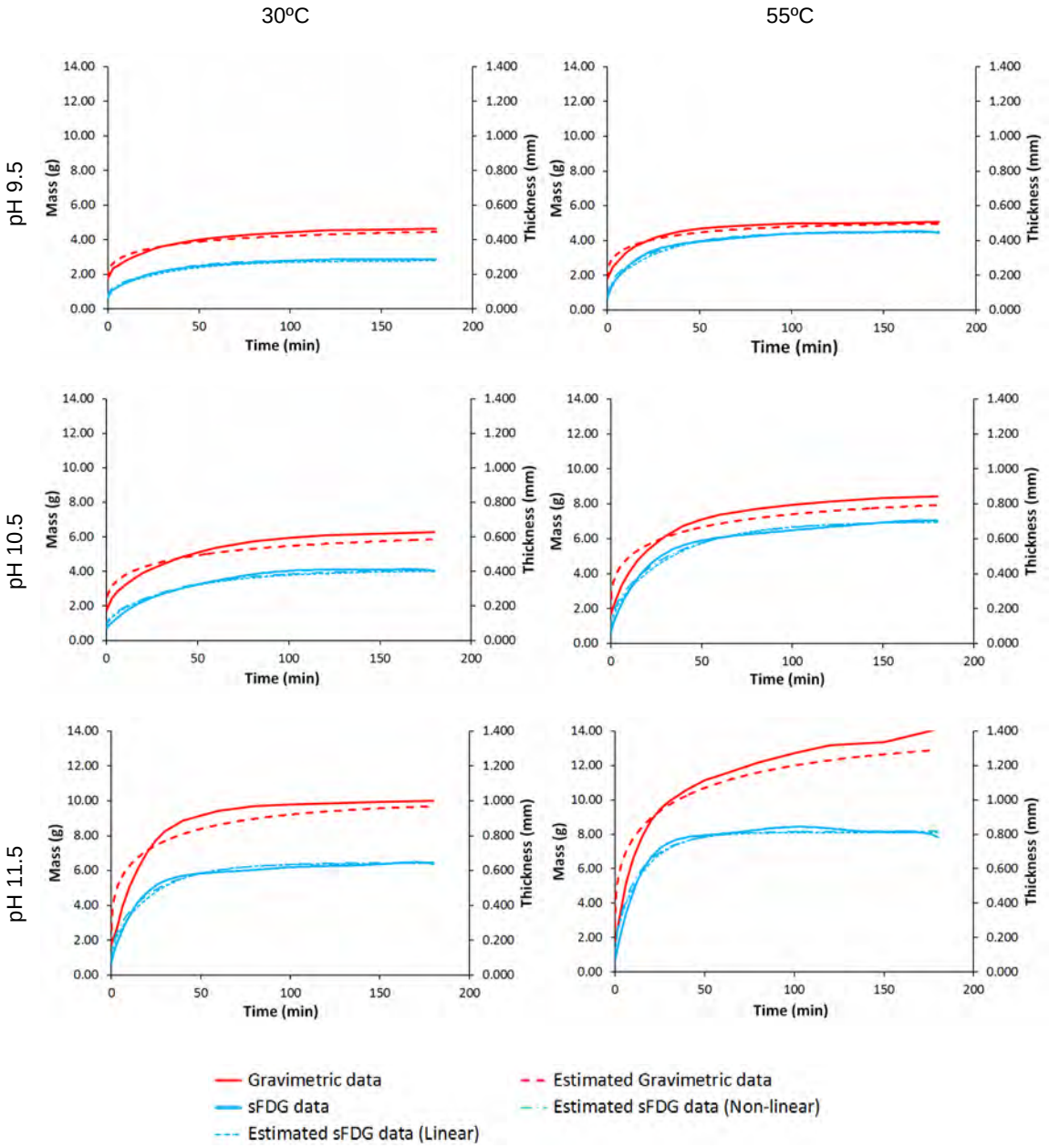

Figure 6.22. Comparative results from experimental and numerical data. Data in red represents values in mass units. Data in blue represents thickness values.

Fick´s second law (Eq. 2.3 and Eq. 2.4) was used to fit gravimetric data. Linear poroelasticity equation (Eq. 2.5) and the non-linear theory approach (Eq. 2.7 and Eq. 2.9) were used to fit thickness results. Overall, Fick´s second law over-predicted results at initial times and under-predicted them at longer times. Numerical estimations from linear and non-linear theories gave more accurate fits in all cases. The higher number of factors considered in the linear and non-linear poroelasticity equations allowed the estimations to be more flexible and precise.

Table 6.5 shows the effective diffusion coefficients (D_F) estimated with Fick´s second law as well as the goodness of fit:

Table 6.5. Fick's second law effective diffusion coefficients (D_F) and goodness of fit for gravimetric experiments.

EXPERIMENT		DIFFUSION COEFFICIENT D_F (m^2/s)	R^2
TEMPERATURE	pH		
30ºC	9.5	$5.5 \cdot 10^{-12}$	0.9477
55ºC	9.5	$1.0 \cdot 10^{-11}$	0.9498
30ºC	10.5	$8.6 \cdot 10^{-12}$	0.9112
55ºC	10.5	$1.9 \cdot 10^{-11}$	0.9498
30ºC	11.5	$4.1 \cdot 10^{-11}$	0.8813
55ºC	11.5	$5.4 \cdot 10^{-11}$	0.9202

Values were in the order of 10^{-11} m^2/s. For the range of pH investigated, the increase from 30ºC to 55ºC showed an increase in the effective diffusion coefficient calculated. This was also observed for increasing pH at the same temperature. Coefficients of determination (R^2) ranged from 0.88 to 0.95.

Table 6.6 shows the results estimated with the linear poroelasticity theory:

Table 6.6. Linear poroelasticity theory effective diffusion coefficients (D_L) and goodness of fit for sFDG experiments.

EXPERIMENT		DIFFUSION COEFFICIENT D_L (m^2/s)	R^2
TEMPERATURE	pH		
30ºC	9.5	$9.60 \cdot 10^{-13}$	0.9971
55ºC	9.5	$1.12 \cdot 10^{-12}$	0.9865
30ºC	10.5	$7.60 \cdot 10^{-13}$	0.9795
55ºC	10.5	$8.90 \cdot 10^{-13}$	0.9785
30ºC	11.5	$1.33 \cdot 10^{-12}$	0.9675
55ºC	11.5	$1.96 \cdot 10^{-12}$	0.9812

Effective diffusion coefficient values (D_L) were in the order of 10^{-12} m^2/s. The increase of temperature from 30ºC to 55ºC showed a slight increase in the effective diffusion coefficient at any pH considered. This tendency was not shown for the increase of pH at a fixed temperature. At pH 11.5, the removal of some of the top layers and its subsequent apparent equilibrium at

shorter times, translated into higher effective diffusion coefficients. Overall, the goodness of fit showed a better agreement than for Fick´s second law in a range between 0.967 to 0.998.

Table 6.7 summarises the results estimated by applying the non-linear theory. The equivalent linear effective diffusion coefficient (D_L) was calculated using Eq. 2.11. The initial swelling ratio (λ_0) and the equilibrium stretch (λ_∞) needed for the calculations were obtained from experimental data. λ_0 was estimated by dividing the initial experimental thickness ($h_0 = 68\mu m$) over the dry thickness ($h_{dry} = 68\mu m - 9\mu m$), giving $\lambda_0(t = 0) = 1.1$. The different λ_∞ were estimated for each case by dividing the maximum thickness reached at equilibrium over the dry thickness (h_{dry}). The volume of a solvent (water) molecule (Ω) was $3 \cdot 10^{-29}$ m^3/molecule.

Table 6.7. Non-linear poroelasticity theory iteration results.

EXPERIMENT		NON-LINEAR DIFFUSION COEFFICIENT D_{NL} (m^2/s)	FLORY-HUGGINGS PARAMETER (χ)	POLYMER CHAINS PER UNIT VOLUME N (m^{-3})	LINEAR DIFFUSION COEFFICIENT D_L (m^2/s)	MARGIN VALUE	R^2
T	pH						
30ºC	9.5	$1.5 \cdot 10^{-10}$	1.00	$9.5 \cdot 10^{26}$	$4.32 \cdot 10^{-13}$	0.1139	0.9935
55ºC	9.5	$2.5 \cdot 10^{-10}$	0.80	$6.0 \cdot 10^{26}$	$8.98 \cdot 10^{-13}$	0.1081	0.9910
30ºC	10.5	$3.0 \cdot 10^{-10}$	0.90	$5.0 \cdot 10^{26}$	$1.50 \cdot 10^{-12}$	0.0832	0.9429
55ºC	10.5	$4.0 \cdot 10^{-10}$	0.80	$4.0 \cdot 10^{26}$	$7.51 \cdot 10^{-13}$	0.1118	0.9828
30ºC	11.5	$4.5 \cdot 10^{-10}$	0.65	$4.5 \cdot 10^{26}$	$1.21 \cdot 10^{-12}$	0.1149	0.9697
55ºC	11.5	$9.0 \cdot 10^{-10}$	0.00	$4.0 \cdot 10^{26}$	$1.95 \cdot 10^{-12}$	0.1018	0.9355

Non-linear diffusion coefficients (D_{NL}) were reported at around 10^{-10} m^2/s. The increase from 30ºC to 55ºC showed slightly higher diffusion coefficients at any pH given. The same correlation was observed for increasing pH at a fixed temperature. Flory-Huggins parameter (χ) showed a slight decrease with the increase of temperature and pH. The low sensitivity observed in the calculations of this intrinsic parameter did not allow any further conclusion to be made. Both, D_{NL} and χ, were likely to change for each experiment as D_{NL} is related to the kinetics of the swelling/diffusion process (temperature dependent) and χ to the interaction between the solvent and the polymer (pH dependent). A decrease in the Flory-Huggins parameter indicates a stronger affinity between the solvent and the polymer (Kuhn *et al*. 2006). Thus, this affinity increased with the increase of pH. N values estimated remained within a range from $4 \cdot 10^{26}$ m^{-3} to $9.5 \cdot 10^{26}$ m^{-3} with an average value of $5.5 \cdot 10^{26}$ ($\pm 2.1 \cdot 10^{26}$) m^{-3}. The variability seen is caused

by the iterative process in the calculations. The estimation of linear effective diffusion coefficients (D_L) from non-linear effective diffusion coefficients (D_{NL}) were similar and of the same order of magnitude as those reported in **Table 6.6**.

The differences on the values of diffusion coefficients represent the difference on the equations. Fick's second law (Eq. 2.3) offered the simplest mode. No intrinsic parameters were considered apart from an effective diffusion coefficient (D_F). The incorporation of moving boundaries into the analysis did not provide sufficient flexibility and predictions had a lower accuracy than for the other two theories. Linear poroelasticity theory (Eq. 2.5) divided the swelling/hydration process in two terms: one related to the stretch of the network (Eq. 2.6) and the other related to the kinetics of the diffusion process. The diffusion coefficient (D_L) was calculated from the characteristic time scale of diffusion (τ) in the second term on the right side of Eq. 2.5. D_L is therefore only characterising the kinetic of the diffusion and not the stretch of the network. As in reality the thickness of the network increased and the diffusion coefficient did not take into account this effect, D_L was lower than diffusion coefficients from other theories. Consequently, the linear poroelasticity theory underestimates the time needed to reach the swelling equilibrium. This issue is highlighted more in cases of large deformations (i.e. data collected in this work). This effect was taken into account in the theories combining swelling and kinetics in one term (i.e. Fick's second law and non-linear theory). Finally, non-linear theory showed the highest effective diffusion coefficient (D_{NL}) values among all theories.

Independently of the theory used, calculated diffusion coefficients were lower than the self-diffusion coefficient of water, estimated to be $2.3 \cdot 10^{-9}$ m^2/s (Métais and Mariette, 2003). This suggests an obstruction effect of the soil network on the diffusion of water molecules. The phenomenon was previously reported (Fukuoka *et al*., 1994). The differences between water self-diffusion coefficient and the ones calculated from these experiments offer an indirect estimation of the resistance offered by the network. The soil network offered the least resistance to diffusion at high pH and high temperature.

The temperature dependence of the different effective diffusion coefficients estimated was also explored. Eq. 2.13 was applied to the results shown in **Tables 6.5 to 6.7**. Despite the lack of rheological information, the soil sample was assumed to behave as a solid as it did not flow in any experimental condition and it was partly detached from its surface when a sufficiently high external force was applied. Maximum effective diffusion coefficients (D_0) and activation energies (E_A) were estimated for pairs of data at the same pH and different temperatures. As only two values were used in the calculations, results only represent an indication of the order of magnitude expected. **Table 6.8** summarises the different values obtained.

Table 6.8. Activation energies and maximum effective diffusion coefficients estimated for each of the theoretical cases previously studied.

THEORY	T	pH	DIFFUSION COEFFICIENT (m^2/s)	E_A (kJ/mol)	D_0 (m^2/s)
Fick's second law	30ºC	9.5	$5.5 \cdot 10^{-12}$	19.8	$1.40 \cdot 10^{-8}$
	55ºC	9.5	$1.0 \cdot 10^{-11}$		
	30ºC	10.5	$8.6 \cdot 10^{-12}$	26.2	$2.83 \cdot 10^{-7}$
	55ºC	10.5	$1.9 \cdot 10^{-11}$		
	30ºC	11.5	$4.1 \cdot 10^{-11}$	9.1	$1.52 \cdot 10^{-9}$
	55ºC	11.5	$5.4 \cdot 10^{-11}$		
	MEAN			18.4 (±9.0)	$9.9 \cdot 10^{-8}$ ($\pm 1.6 \cdot 10^{-7}$)
Linear poroelasticity theory	30ºC	9.5	$9.60 \cdot 10^{-13}$	5.1	$7.3 \cdot 10^{-12}$
	55ºC	9.5	$1.12 \cdot 10^{-12}$		
	30ºC	10.5	$7.60 \cdot 10^{-13}$	5.2	$6.0 \cdot 10^{-12}$
	55ºC	10.5	$8.90 \cdot 10^{-13}$		
	30ºC	11.5	$1.33 \cdot 10^{-12}$	12.8	$2.2 \cdot 10^{-10}$
	55ºC	11.5	$1.96 \cdot 10^{-12}$		
	MEAN			7.7 (±4.4)	$7.6 \cdot 10^{-11}$ ($\pm 1.1 \cdot 10^{-10}$)
Non-linear poroelasticity theory	30ºC	9.5	$1.5 \cdot 10^{-10}$	16.9	$1.2 \cdot 10^{-7}$
	55ºC	9.5	$2.5 \cdot 10^{-10}$		
	30ºC	10.5	$3.0 \cdot 10^{-10}$	9.5	$1.3 \cdot 10^{-8}$
	55ºC	10.5	$4.0 \cdot 10^{-10}$		
	30ºC	11.5	$4.5 \cdot 10^{-10}$	22.9	$4.0 \cdot 10^{-6}$
	55ºC	11.5	$9.0 \cdot 10^{-10}$		
	MEAN			16.4 (±6.7)	$1.4 \cdot 10^{-6}$ ($\pm 2.3 \cdot 10^{-6}$)

Activation energies (E_A) estimated were in the range of 7.7 to 18.4 kJ/mol. The linear theory showed the lowest values while Fick´s second law showed the highest ones. This compares favourably with what was reported previously in literature (Bello *et al*., 2010). Experiments at pH 11.5 showed the biggest displacements to mean values due to the experimental uncertainty introduced in the measurements by the lift-up and hydrolysis processes that occurred.

Maximum effective diffusion coefficient (D_0) showed a wide range of values. They were a function of the theory approach used and should be analysed within those boundaries. Fick's theory showed a maximum effective diffusion coefficient closer to the one previously reported for the self-diffusion of water.

The relationship between N, χ and the equilibrium swelling ratio (λ_∞) was further explored. Different λ_∞ were calculated by applying Eq. 2.9 for a wide range of χ values (-2 to +2) and for 4 representative N values: 10^{25}, 10^{26}, 10^{27} and 10^{28}. **Figure 6.23** illustrates the results obtained.

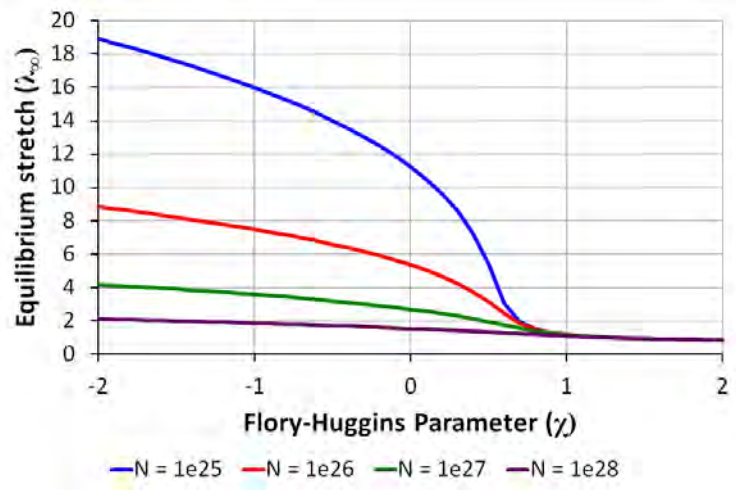

Figure 6.23. Equilibrium stretch as a function of Flory-Huggins parameter (χ) and effective number of polymer chains per unit volume of the polymer (N).

The plot shows an increase in the equilibrium stretch for χ values lower than 0.8 approximately and for N values higher lower than 10^{28}. The higher the value of N, the lower the maximum equilibrium stretch achieved. As the number of polymer chains per unit volume increases, the stretch of the network becomes more difficult as the forces linking the network increase. The

elasticity of the network is reduced as a consequence. For the case studied, the calculated equilibrium stretch ratios were in a range from 3.5 to 10 and N coefficient was in the order of $5 \cdot 10^{-26}$. Given that, the plot indicates that the value of N should be around one order of magnitude higher, that is, $5 \cdot 10^{-25}$. As commented in *Chapter 3, section 3.10* the iteration process and the experimental error introduced made the predictions less sensitive with regard of these parameters.

6.4. DEVELOPMENT OF A SWELLING-REMOVAL MODEL FOR THE SCANNING FLUID DYNAMIC GAUGE

To reinforce the modelling approach, a mathematical swelling-removal model based on a theoretical background is proposed next. As a first objective, the model aims to distinguish between the mechanisms leading to removal, differentiating between the application or not of an external mechanical action. These mechanisms can be further modelled independently as a function of the different factors already highlighted: temperature, pH, enzyme level, shear stress and frequency factor.

It aims to add flexibility by incorporating a simulation schedule. This could include the variation along a typical wash cycle of temperature, pH or enzyme (chemical) levels. These factors have been previously studied as fixed values in the experimental statistical design and output responses calculated also for fixed values across the whole simulation.

It also aims to expand the predictions outside the range studied (i.e. by covering a frequency factor range from 0% to 100%), with no need to run new experiments to correlate and establish new response profiles.

Finally, it aims to provide wider and better information of the soil status at any time of the wash cycle. Discretisation of the soil thickness is proposed as the best approach. The algorithm developed must provide simulated data for thickness profiles, soil remaining, wash solution uptake or total mass in the sample (wash solution + soil) and percentage of cleaning over time.

This information allows a better an easier comparison between different cleaning sequences and supports the decision making process and the finding of an optimum scenario.

6.4.1. Case study

To help the understanding of the model development, experimental conditions seen in **Table 6.9** were considered. These experiments aimed to easily differentiate main cases seen by using the sFDG: no apparent cleaning (test 1), removal by discontinuous (test 2) and continuous (test 3) application of shear stress.

Table 6.9. Experimental conditions considered for illustration purposes.

Test	Temperature	pH	Protease level	Shear Stress	Frequency Shear Stress
1	50ºC	10.5	None	24 Pa	8.5 %
2	50ºC	10.5	Standard formulation	24 Pa	8.5%
3	50ºC	10.5	Standard formulation	24 Pa	100%

Fixed values of temperature (50°C), pH (10.5) and shear stress (24 Pa) were established. Two different levels of protease were also examined: none and standard formulation level. The frequency of application of shear stress over a single location was also considered as a factor affecting the total cleaning time. Two levels were explored: 8.5% and 100%. The above was also expanded in *section 6.4.3.3* to describe the effect of different temperatures (30°C, 40°C and 50°C) in the removal analysis. Triplicates were done for each of the cases considered.

Previous work demonstrated that at these conditions of temperature and pH no decrease in thickness was observed in the absence of enzymes suggesting none or insignificant removal. **Figure 6.24** shows the averaged fitted data from all the locations studied and their triplicates for the three experimental cases considered.

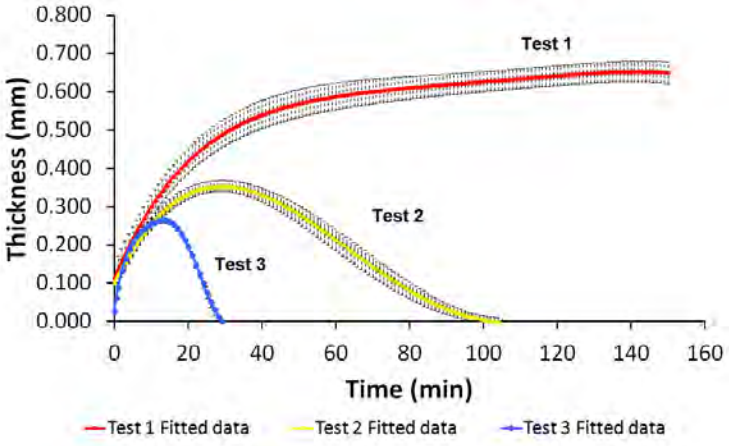

Figure 6.24. Averaged fitted experimental results for the three experimental tests considered. Experimental conditions are included in Table 6.9.

The figure shows a removal stage after an initial net swelling period for cases where protease was present. It also shows a faster cleaning time when a constant application of external shear stress was set (100% frequency). By obtaining thickness values at fixed times, the comparison with the mathematical model is also simplified.

6.4.2. Identification of mechanisms

In **Figure 6.25**, raw data for a single location in test 2 is shown. Similar plots were obtained for other locations under the same experimental conditions.

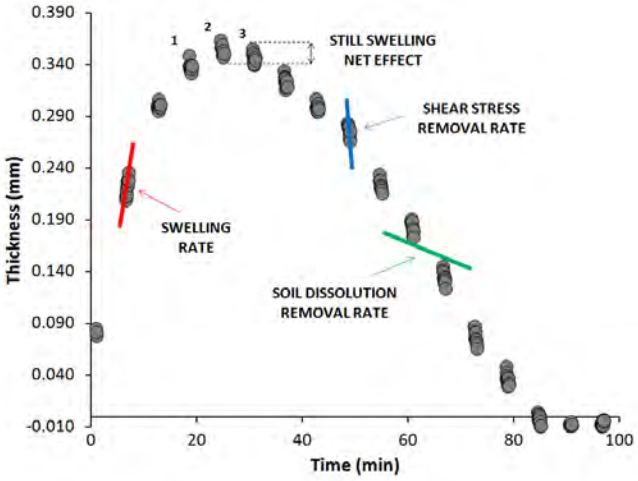

Figure 6.25. Mechanisms identified in a typical protein-based cleaning test in sFDG. Experimental conditions: 50°C; pH = 10.5; [Protease] = Standard formulation level; Shear Stress = 24 Pa; Frequency of application of shear stress = 8.5%.

The figure reveals the three different main mechanisms affecting the thickness change in a soil sample: swelling, removal by shear stress (enzyme-induced disengagement and mechanical action) and removal by soil dissolution (enzyme-induced disengagement and dissolution). As seen in **Figure 6.24**, both types of removal are made possible by the enzymatic action. As there is a lack of bulk fluid movement in these experiments, removal via application of shear stress occurs when the nozzle is positioned on top of a specific location to obtain a height measurement. Removal via soil dissolution occurs when there is no external input of stresses, that is, during the time length where no data is acquired. Soil dissolution mechanism represents the minimum removal rate that can be achieved at the conditions established, with no external disturbances. It corresponds to the mass transfer produced from the soil to the bulk fluid after the chemical action (hydrolysis reactions). The application of an external stress enhances the removal process and soil layers are removed faster. However, the technique does not distinguish the soil disengagement process when an external mechanical input occurs. Molecules to be removed are either already completely disengaged and their transport to the bulk enhanced or the application of the external stress breaks completely the affected areas by the enzymatic action (partially hydrolysed) and produces as well the subsequent transport to the bulk fluid. The origin of disengagement is debatable but has limited effect on modelling results.

The intensity of the different mechanisms is not constant and varies over time. Around the curve maximum, i.e. at approximately 20 to 30 minutes, swelling and removal mechanisms occur at similar rates. Before the maximum thickness (1), the application of an external shear stress produces a net removal effect. The slope of the group of data acquired at that time is negative, indicating a reduction in thickness. Also, as the soil dissolution process is still slower than the swelling rate, an increase in the thickness is seen between consecutive data acquisition periods (1 to 2). Once the maximum is passed, the swelling rate keeps reducing whilst the dissolution increases. There is still a net increase in thickness at the interval period with no measurements, but that increase is lower than the one seen before the curve maximum (2 to 3). Later on, both types of removal mechanisms are able to produce a net decrease on soil thickness. The swelling rate is reduced and the sample is weaker and easier to remove.

Similar plots were reported by Gordon *et al*. (2012b), where cleaning studies were also performed on egg yolk stains. The individual modelling of these three mechanisms forms the basics of the proposed algorithm.

6.4.3. Algorithm development.

6.4.3.1. Proposed equation

The above can be summarised using the following equation (Eq. 6.1):

$$\frac{dh}{dt} = S - f \cdot SS - \left(1 - f\right) \cdot SD \qquad \text{Eq. 6.1}$$

Where:

- h = Thickness.
- t = Time.
- S = Swelling function.
- SS = Shear Stress function.
- SD = Soil Dissolution function (based on enzyme effect).
- f = Frequency function. Step function (0 or 1).

Thickness variation over time is a function of the different mechanisms involved: swelling and removal via shear stress action or soil dissolution. Each of these mechanisms is modelled individually and integrated together over time. The frequency function is used to account for periods with an external application of shear stress imposed by the sFDG. The external mechanical energy input increases the rate of removal when compared to a pure dissolution process as seen in **Figure 6.25**. Thus, a function that describes when an external shear stress is applied is necessary. This frequency function is a step function taking values of 0 and 1. If an external mechanical action is occurring, the function assigns a value of 1 and the soil dissolution term is cancelled. If cleaning is driven by soil dissolution alone, then its value is 0 and the shear stress term is cancelled. Shear stress function could incorporate some soil dissolution (understood as the complete disengagement of soil elements due to chemical reaction). However, the technique does not completely decouple the removal phenomena as commented

previously. For modelling purposes, this approach enables an easier calculation of removal rates.

6.4.3.2. Swelling

To model swelling phenomena, the uniaxial constrained swelling equation (Eq. 2.6) proposed by Bouklas & Huang (2012) is used. The solution of the PDE implies both the discretization of time (Δt) and space (Δz). This allows the introduction of the concept of 'theoretical layers', representing the initial number of layers in which the soil is divided. The concept will be further used to integrate removal mechanisms.

The iterative process required for fitting the experimental data has already been explained in , *Chapter 3, section 3.10*. The difficulty predicting the values for the Flory-Huggins parameter (χ) and the effective number of polymer chains per unit volume (N) does not affect the results from the model proposed. Although better knowledge of the system is required in order to minimise the variability in the prediction of these parameters, the equation shows the flexibility required for accurate fitting the data as well as the discretisation of the layer thickness.

In **Figure 6.26**, predictions results are compared with experimental data. By using the iterative process explained above, the parameters resulting in the best fit were: D_{eff} = $2.5 \cdot 10^{-10}$ m^2/s; χ = 0.9; N = $6 \cdot 10^{26}$ m^{-3}. 50 theoretical layers were initially defined giving a $\Delta z = 1.22\,\mu m$ and a $\Delta t = 0.003\,s$. Overall the model compared favourably with the experimental data (R^2 = 0.98). A slight over prediction is seen at lower times while predicted values at high times shows great accuracy.

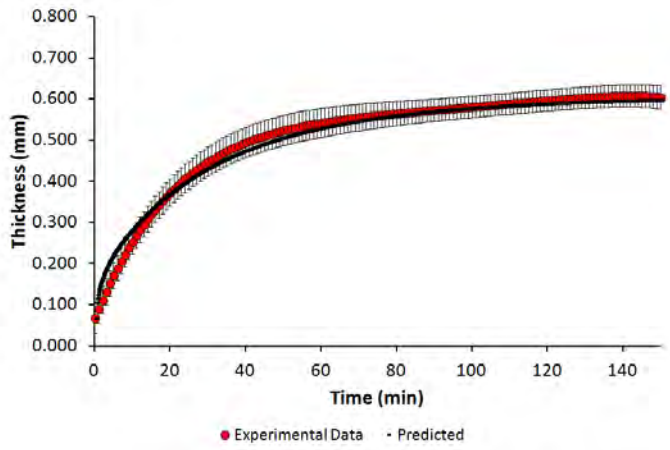

Figure 6.26. Quality of the adjustment for pure swelling experimental data (test 1). Red dots represent averaged fitted experimental data. Black line represents prediction results from model. Experimental conditions: 50°C; pH = 10.5; [Protease] = None; Shear Stress = 24 Pa; Frequency factor = 8.5%.

6.4.3.3. Removal

Removal characterisation was done empirically from experimental data. Removal rates $\left(in\ {}^{\mu m}/_{min}\right)$ for both shear stress and soil dissolution mechanisms were calculated by determining the different experimental removal slopes. Shear stress removal rates were estimated from the groups of thickness data available. For example, for test 2 and as seen in **Figure 6.25**, rates were calculated by linearly fits to those values. The slope (blue line), corresponding to the removal rate at that interval, was assigned to a time value calculated as the average time of the data group analysed. The same procedure was followed to estimate soil dissolution removal rates. The slope from intervals with no data (green line) was calculated and a time value assigned. For cases with a constant application of shear stress (test 3), removal rates were calculated for intervals of 1 minute.

Swelling is incorporated as a positive contributor to thickness. In order to decouple swelling and removal mechanisms, swelling rates from test 1 (at the same temperature and pH conditions) were calculated and used as a base line. Positive swelling contributions to thickness were subtracted for each of the interval times considered (i.e. every minute). This assumes a linear relationship between mechanisms. Swelling rates were obtained from either the groups of data points (shear stress applied) or from periods with no data collection (no shear stress applied). The latter showed typically less noise.

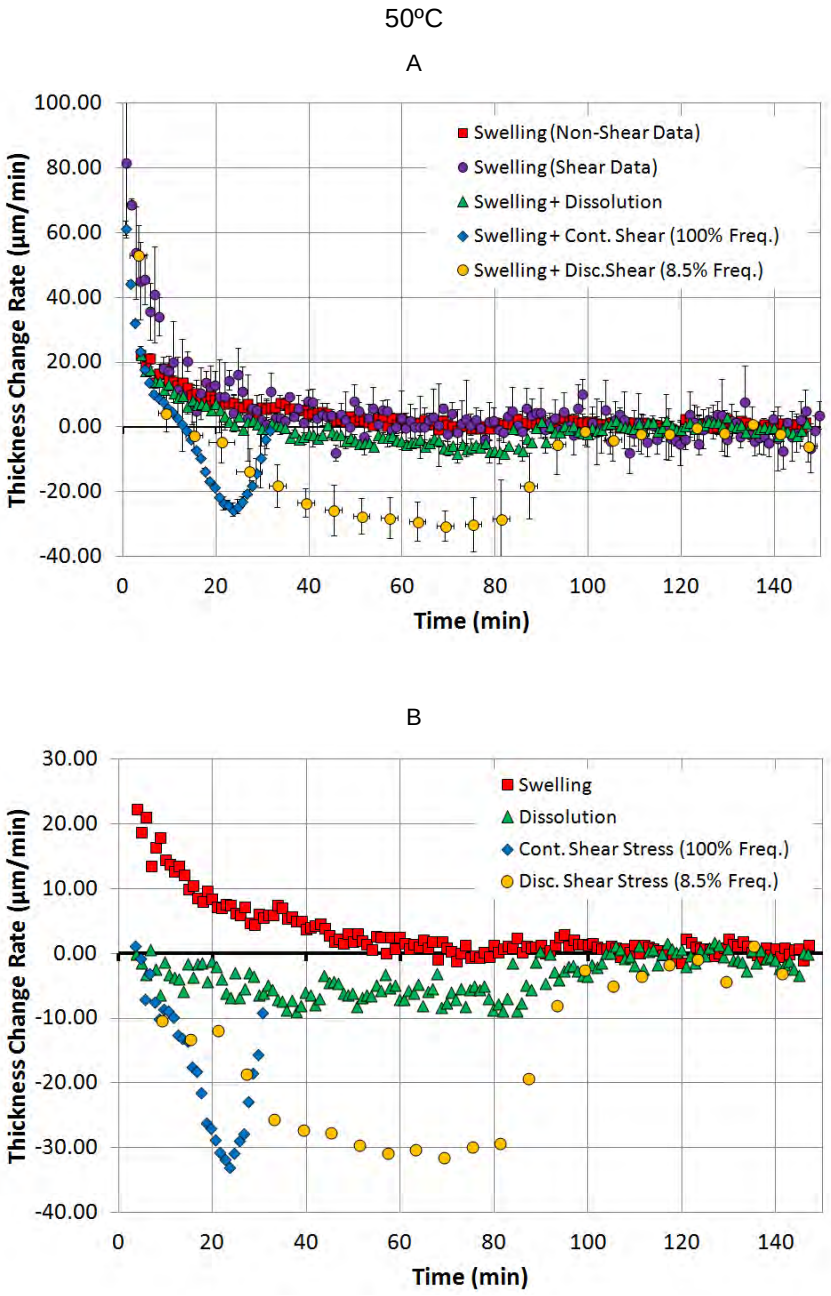

Figure 6.27. Thickness change rate over time for different mechanisms at 50°C, pH =10.5 and shear stress = 24 Pa (processed data from test 1,2 & 3). A – Mechanisms with swelling phenomena not decoupled. B – Mechanisms with swelling phenomena decoupled. Red squares represent swelling rate data calculated through non-measurement periods for pure swelling test (test 1 – [Protease] = none). Purple circles represent swelling rate data calculated through measurement periods for pure swelling test (test 1). Green triangles represent soil dissolution rates obtained from test 2 ([Protease] = Standard formulation level). Blue diamonds represent shear stress removal rates with constant application (100% Frequency) obtained from test 3 ([Protease] = Standard formulation level). Yellow circles represent shear stress removal rates for a discontinuous shear stress (8.5% Frequency) obtained from test 2.

In **Figure 6.27A**, the rate of thickness change over time is shown for each of the key mechanisms investigated. The data indicate that swelling had an important positive contribution to the change of the sample height for the first 15 minutes. At longer times, the application of shear stress resulted in a reduction of the sample height irrespective of the frequency of application (blue and yellow points). A decrease in thickness change rates was also seen as a result of the soil dissolution mechanism (green triangles), but its effect was less strong. The graph also shows higher variability when swelling rates were calculated from the different groups of data points in the experimental readings (purple circles - shear stress applied).

In **Figure 6.27B**, the contribution of swelling to thickness was subtracted from removal mechanisms by using the swelling curve (red squares) as a base line. At initial times, removal action showed very little negative effect to the thickness. This negative contribution increased over time and constant removal rates were obtained for soil dissolution (green triangles) and removal via discontinuous application of shear stress (yellow circles) cases, with thickness change rates values of approximately -6 μm/min and -30 μm/min. However, continuous application of shear stress (blue diamonds) did not produce a constant removal rate. The maximum value was reached at approximately 20 minutes (-32 μm/min) and its subsequent decrease in rate is an indication that cleaning was in its final decay stage. Complete removal was achieved soon after 30 minutes. The fact that the removal rate was higher between 10 to 30 minutes for a continuous exposure to shear stress (100%) than for 8.5% frequency suggests a weakening of the soil network at these conditions (50ºC, pH 10.5, 24 Pa). The continuous application of shear is able to produce extra mechanical removal. The graph also illustrates the important difference in removal rates between removal by soil dissolution alone (only enzymatic-induced removal) and shear stress removal (mechanical + enzymatic-induced removal).

The same approach was applied to data collected at 30°C and 40°C to determine the effect of lower temperatures. **Figure 6.28** shows the thickness change rate for each of the mechanisms studied. Swelling effect was also subtracted by applying the same approach as for the case at 50°C.

A

40 ºC

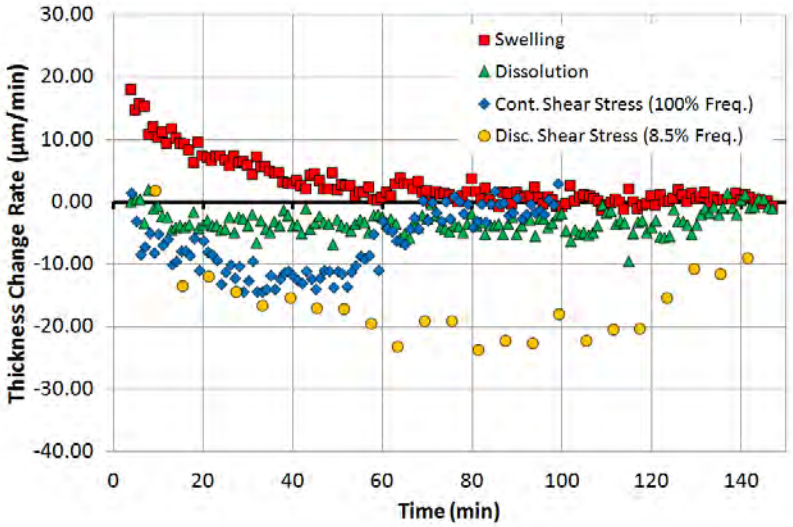

B

30 ºC

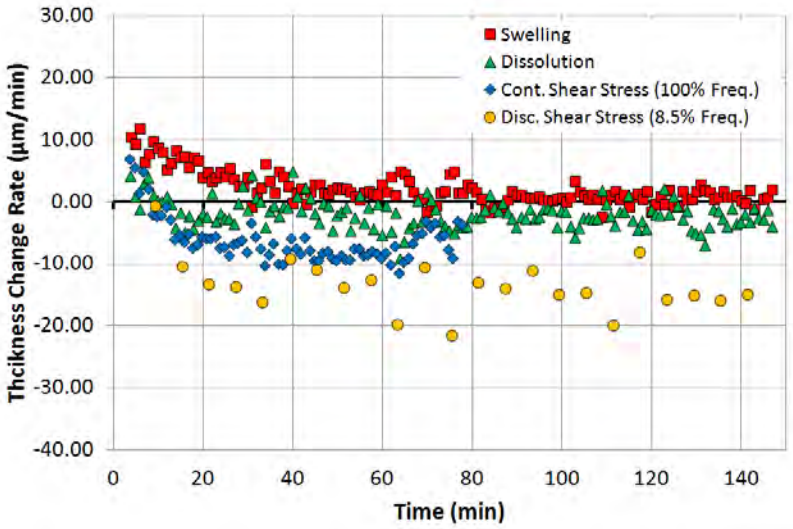

Figure 6.28. Thickness change rate over time for different mechanisms at 40°C (A) and at 30°C (B) for pH = 10.5 and shear stress = 24 Pa. Mechanisms with swelling process decoupled. Meaning of the symbols is the same as for Figure 6.27.

In **Figures 6.28A and 6.28B**, removal rates seemed to be constant over time after the initial non-steady period. This includes the case of a constant application of shear stress (blue diamonds). A decrease in the removal rate was also seen after the constant rate period, indicating the final decay stage. Cleaning times were extended as a consequence of the reduction of temperature. In these two cases, higher instantaneous removal rates were obtained

when the frequency of application of shear stress was lower (yellow dots versus blue diamonds). This suggests an enzyme reaction rate limiting stage. As the function of the enzyme function is to help and promote the breakage of peptide bonds (Aehle, 2007), the number of bonds hydrolysed at a certain time is limited. The longer the period without application of shear (lower frequency), the higher the number of bonds affected. As soil dissolution removal (mass transfer process) is slower, when shear stress is reapplied, the amount of soil 'ready to be removed' will be higher. Therefore, higher removal rates will be obtained. For continuous application of shear stress (100% Frequency), the instantaneous removal rate achieved will never be higher than a discontinuous application unless the amount of external energy applied (net shear stress value) is able to break mechanically a higher number of inner bonds of the soil network (cohesive failure). An example of this behaviour was commented previously for the case of 50°C. In any case, the continuous application of shear stress over the soil typically leads to reduced cleaning times as there is no soil dissolution alone.

This enzyme reaction rate also complements the shear stress threshold proposed in *section 6.2.2* (see **Figure 6.8**). The shear stress threshold indicates the minimum energy required to produce the removal of the soil at a *specific time* while the enzyme reaction rate mechanism explains the *removal rate* limit over time. However, it is important to state that the data in this work do not absolutely precise the hypotheses given.

Thickness change rates shown previously were integrated over time. In **Figure 6.29**, the resulting cumulative effect on thickness over the cumulative integrated time is seen for cases of continuous and discontinuous application of shear stress and for soil dissolution mechanisms.

A

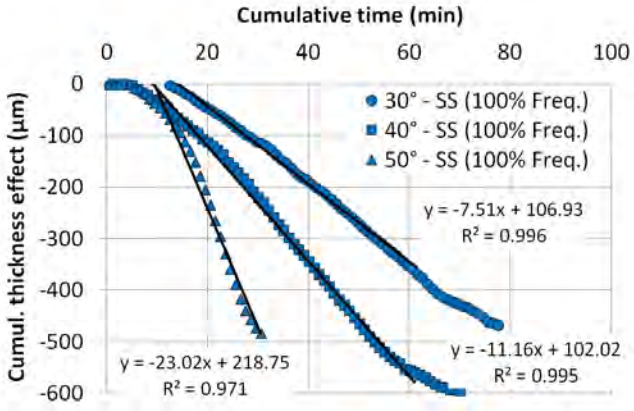

B

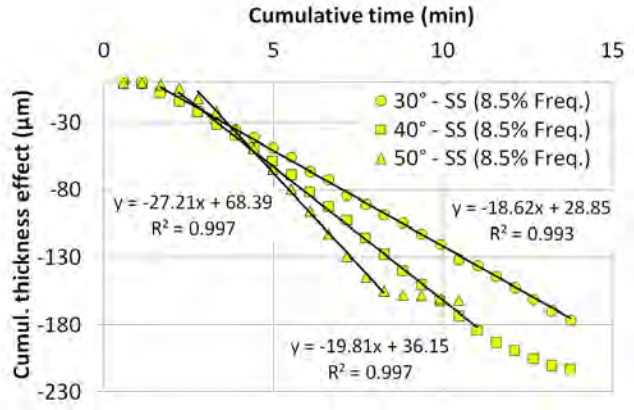

C

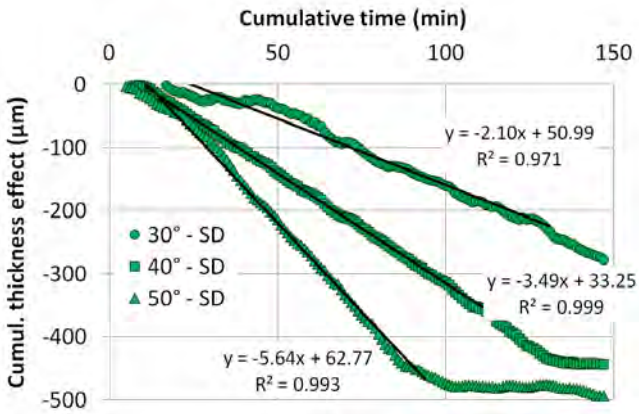

Figure 6.29. Cumulative thickness effect over time at different temperatures and for different cleaning mechanisms. A – Continuous application of shear stress (100% Frequency). B – Discontinuous application of shear stress (8.5% Frequency). C – Soil dissolution. Circles, squares and triangles represent data for 30°C, 40°C and 50°C respectively. Experimental conditions: pH = 10.5; [Protease] = Standard formulation level; Shear Stress = 24 Pa.

Their different effects are also seen for the three different temperatures previously shown (30°C, 40°C and 50°C). Given the linear tendency observed, the data were fitted to a linear correlation. The gradient was an estimate of a constant removal rate for each of the cases considered. A lag time was also calculated as the initial time with no cleaning. Its value was established as the intercept on the time axis (x-axis).

In **Figure 6.30**, estimated removal rates are compared for all mechanisms at the temperatures studied.

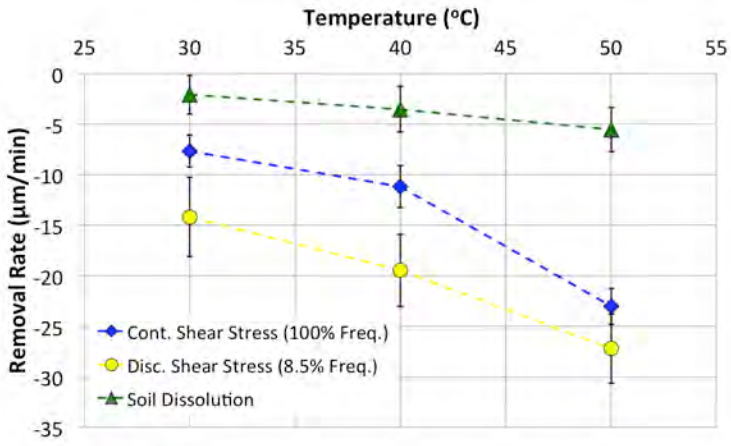

Figure 6.30. Constant removal rates calculated for different mechanisms at different temperatures. Green triangles represent removal rates for soil dissolution. Blue diamonds and yellow dots represent removal rates for a continuous (100% freq.) and discontinuous (8.5% freq.) application of shear stress over the soil. Experimental conditions: pH = 10.5; [Protease] = Standard formulation level; Shear Stress = 24 Pa.

The soil dissolution values represent the maximum amount of soil removed if cleaning occurs without any external mechanical action. The highest removal rates were observed for a discontinuous application of shear. This is believed to be a consequence of the enzyme reaction rate limit explained before. The increase in temperature led to the increase in removal rates, regardless the mechanism. Thus, it is supposed that the energy requirement needed to break cohesively the soil network was reduced at higher temperatures. At 50°C, an approximation between rates from frequencies of 100% and 8.5% is seen. The hypothesis given previously suggested an extra mechanical breakage of some inner bonds of the soil network when a continuous shear is applied, as the shear stress threshold was overcome.

An Arrhenius analysis was performed on the soil dissolution data as described by Mercadé-Prieto and Chen (2008). **Figure 6.31** illustrates the results obtained.

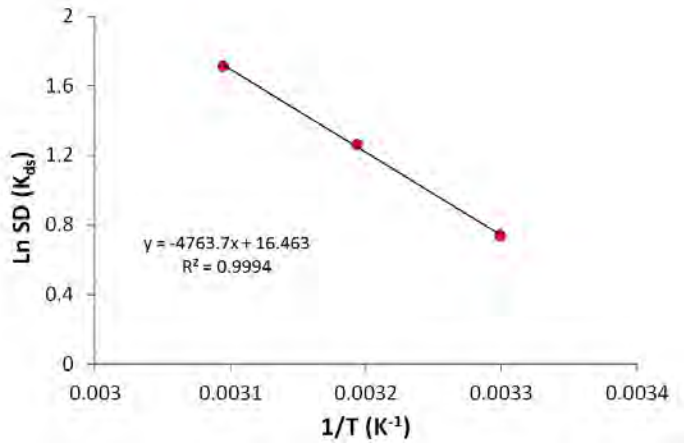

Figure 6.31. Arrhenius analysis on soil dissolution data from Figure 6.30.

Despite only three points were analysed (three temperatures considered), a linear correlation was seen when representing removal rates (ln SD) as a function of temperature (1/T). The coefficient of determination estimated was high (R^2 = 0.999). This gave an activation energy (E_a) of approximately 4.8 kJ/mol, slightly lower but in the same order of magnitude than for a non-catalysed breakage of peptide bonds (8-10 kJ/mol) (Martin, 1998). This enhances the hypothesis already given of a reaction rate limiting stage and suggests that the rate limiting stage is the same independently of temperature. A deeper analysis on this phenomenon will require the study of the dissolution behaviour at different pH, enzyme levels or sample processing conditions.

The empirical approach followed in this section was used to calculate removal rates. Different cleaning mechanisms can be modelled statistically as a function of the parameters controlled. The examples given have shown the effect of temperature and frequency of application of shear stress. Two phases of the cleaning process are distinguished: an initial stage with no removal defined by a lag time and a subsequent constant removal phase. To compensate for the sudden increase in removal rates that this approach would produce, a transition period was also defined. A linear increase in the removal rate was established after the initial lag time for an

extra half of the lag time estimated. The use of this transition period is used to provide smoother simulated curves around the curve maximum. An opportunity for further development is possible. The application of a stronger theoretical background to characterise enzyme kinetics (i.e. Michaelis-Menten approach) would lead to a removal model that would be less empirical.

Concerns about a change over time (decrease) of the N parameter (the effective number of polymer chains per unit volume of the polymer) can also arise when analysing the definition of the parameter in detail. Hydrolysis reactions breaking protein network bonds reduce the number of crosslinks and long chains. Therefore, the value of N reduces. However, removal occurs from top to bottom layers and experimental data suggests an enzyme reaction rate limiting stage. This indicates that only top layers are affected by the enzymatic action at a given time. Those layers are removed as soon as an external mechanical action is applied or through a dissolution process. Deeper layers remain unreacted and therefore with the same 'N' value initially established. Thus, the integrated swelling process can still be applied without any changes over time. For further developments, the decrease of N in top layers could be used as limit criteria to establish the point from which removal is going to occur.

6.4.3.4. Frequency function

The frequency function is a step function that distinguishes when an external mechanical action is being applied over the soil. Whenever this occurs, the function assigns a value of 1. If cleaning is driven by a pure soil dissolution mechanism, then the value given is 0.

Typically, cleaning patterns are repeated periodically (i.e. automatic dishwashing). In order to define these repetitions, the following terms need to be defined:

- t = Experimental time.
- t_s = Start time of application of shear within an interval.
- t_e = End time of application of shear within an interval.
- υ_i = Time length of the interval.
- i = Counter. Defines the number of pattern repetition it is occurring.

- $Nt_s = {}^{t_s}/_{\upsilon_i}$ = Normalised start time of application of shear within an interval.
- $Nt_e = {}^{t_e}/_{\upsilon_i}$ = Normalised end time of application of shear within an interval.

Therefore, the frequency function establishes:

$$f = 1 \;\; if \;\; \frac{t_s}{\upsilon_i} \leq \frac{[t-(i-1)\cdot\upsilon_i]}{\upsilon_i} \leq \frac{t_e}{\upsilon_i} \qquad \text{Eq. 6.2}$$

$$f = 0 \;\; if \;\; \frac{t_s}{\upsilon_i} \geq \frac{[t-(i-1)\cdot\upsilon_i]}{\upsilon_i} \; or \; \frac{[t-(i-1)\cdot\upsilon_i]}{\upsilon_i} \geq \frac{t_e}{\upsilon_i} \qquad \text{Eq. 6.3}$$

Figure 6.32 shows different pattern examples.

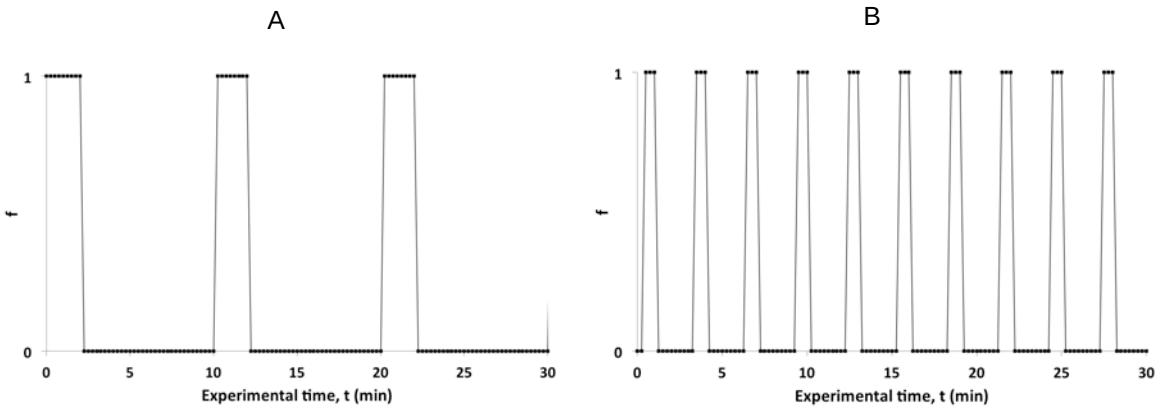

Figure 6.32. Frequency function pattern examples. A – ts = 0 min.; te = 2 min.; υ_i = 10 min.; B - ts = 0.5 min.; te = 1 min.; υ_i = 3 min.

If the pattern does not occurs periodically the sequence needs to be inputted manually.

6.4.3.5. Developed algorithm

A computer routine developed in MATLAB™ allowed the integration of the different mechanisms studied. In **Figure 6.33**, a schematic of the algorithm used is shown:

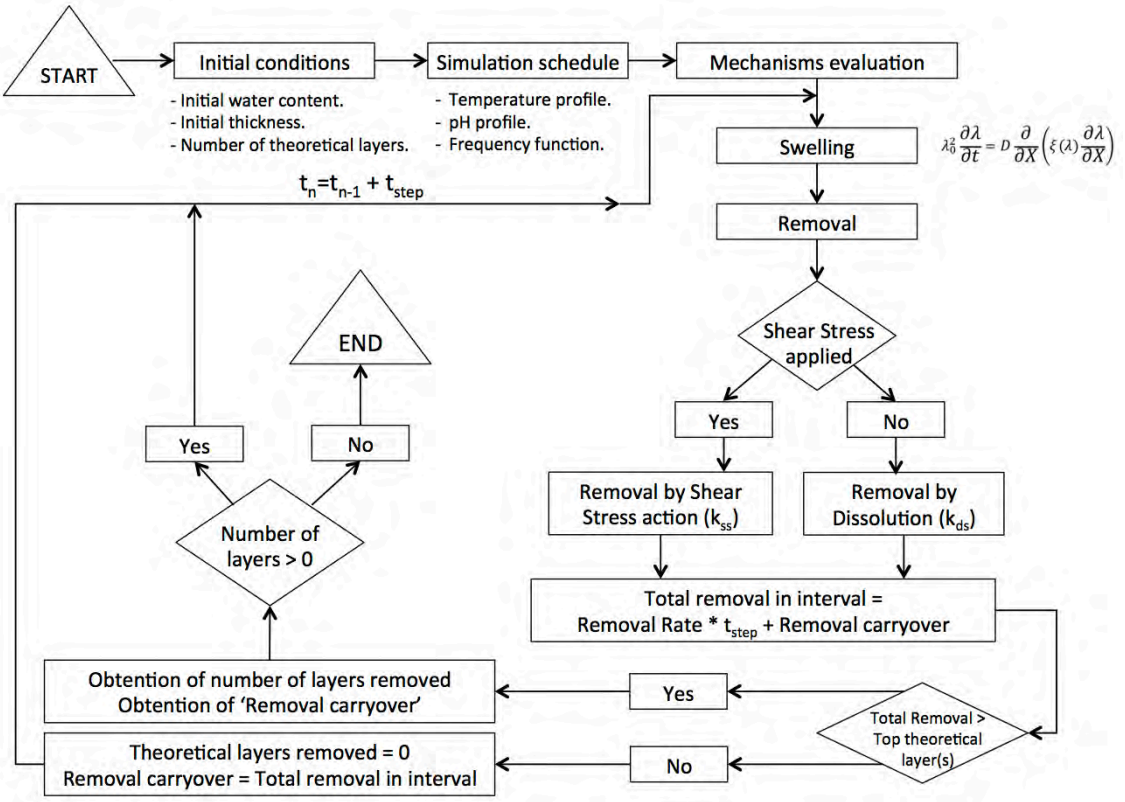

Figure 6.33. Schematic of the algorithm developed.

Initially, starting conditions for the different experimental variables (temperature, pH, [Enzyme], shear stress, frequency of shear stress) and their profiles along the simulation must be established. These factors are linked (if previously modelled) with the parameters defining both the swelling and removal mechanisms. The initial thickness of the sample is discretised into a number of *theoretical layers* and a *time step* established to comply with the convergence in the solution of the swelling non-linear partial differential equation (PDE). The model evaluates and combines each of the mechanisms (swelling and removal) for every time step. Cleaning happens either by shear stress removal or soil dissolution depending on whether some external mechanical input is applied or not (frequency function). The net removal rate at any stage is given by the approach explained in *section 6.4.3.3*. The integration over the time step gives a net thickness swelling/removal value. To compute for swelling and removal in parallel, the algorithm developed introduces a novel consideration: a deletion of theoretical layers occurs

when the integrated rate of removal over a time step is higher than the thickness of the top layer(s) considered. A 'removal carryover' is also calculated as the difference between the net removal in that step time and the net thickness of the layers removed (if there is any layer removed). The routine keeps on calculating the thickness profile over time until no theoretical layers remain. **Figure 6.34** shows a schematic on the modelling approach taken.

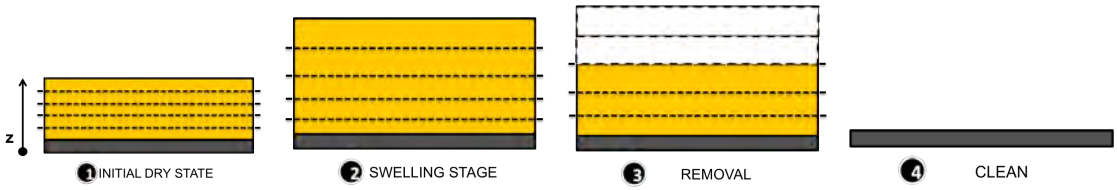

Figure 6.34. Schematic of the cleaning process. Removal of the layers occurs when the net removal calculated is higher than the thickness of one or more of the layers above. Yellow tone simulates the colour of egg yolk.

6.4.3.6. Simulation example

In **Figure 6.35**, a simulation performed by the developed algorithm is compared to averaged fitted experimental data.

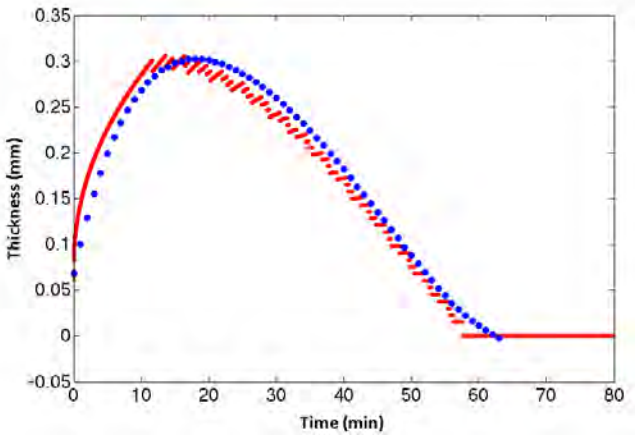

Figure 6.35. Simulation results versus real data. Blue colour represents experimental averaged fitted data. Red colour represents simulated data. Experimental conditions: 50°C, pH 10.5, [Enzyme] = standard, Shear Stress = 24Pa, Frequency = 17%. 50 theoretical layers considered.

The conditions of the test were the following: 50°C, pH 10.5, [Enzyme] = standard, Shear Stress = 24 Pa and Frequency of application of shear = 17%. This frequency corresponded to the analysis of three different points over the soil at intervals of a minute with a repetition pattern

every 3 minutes. Experimental data was acquired approximately during 30 seconds per point as the rest of the time is spent on moving and placing the nozzle in the defined location. **Table 6.10** summarises the parameters under which the simulation was run:

Table 6.10. Values of the parameters used for simulation example.

MECHANISMS	PARAMETER	VALUE
General specifications	Theoretical layers	50
	Time step, Δt	3 ms.
Swelling	Effective diffusion coefficient, D_{eff}	$2.5 \cdot 10^{-10}$ m^2/s.
	Flory-Huggins parameter, χ	0.9
	Polymer chains per unit volume, N	$6 \cdot 10^{26}$ chains/m^3.
Removal	Shear Stress Removal Rate, k_{ss}	25.10 μm/min.
	Soil Dissolution Removal Rate, k_{ds}	5.55 μm/min.
	Lag time	9 min.

The plot shows how the algorithm is able to compute the observed swelling and removal. The removal of the layers is represented by each of the small 'jumps' that can be seen in the graph. Accordingly to what is seen in experimental data (see **Figure 6.25**), swelling and removal mechanisms acting at similar rates are shown around the curve maximum. Anytime a layer is removed a decrease in thickness is seen. If no layer removal happens, the algorithm still computes for swelling and thickness increases.

Figure 6.36 represents the relationship between the quality of the simulation and the computational time as a function of the number of theoretical layers defined.

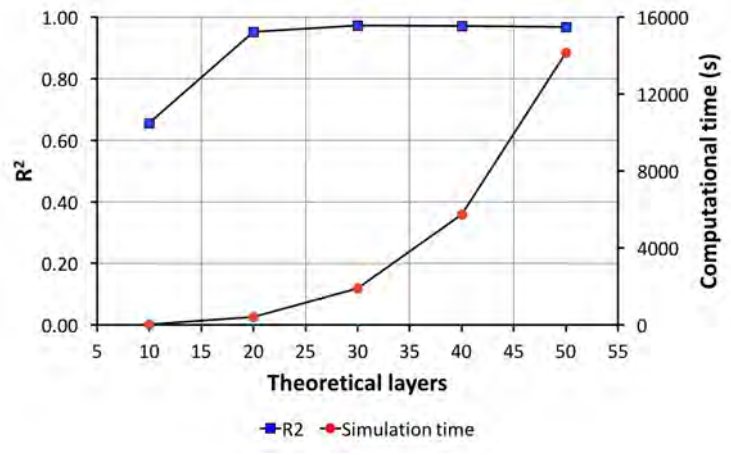

Figure 6.36. Computational cost (s) in CPU time, and quality of the analysis (R^2) as a function of number of theoretical layers defined.

Simulations with less than 10 theoretical layers would under predict the removal occurring, leading to poor results (low R^2 values). Each of the layers defined would be thicker and therefore, anytime one of them would be removed, it would be equivalent to the removal of a relative high amount of soil. This would contradict what was observed experimentally where small quantities of soil were removed progressively. Also, as swelling is computed in parallel, the longer the layer remains the thicker it would get with no removal occurring. The accuracy of the simulation could be improved by using a higher number of theoretical layers. This would lead to smoother curves and therefore higher sensitivity. However, the computational cost would be compromised. The higher the number of theoretical layers, the lower the time step and so, more calculations would be required to reach the solution. Above 20 theoretical layers it was observed that the computational time required to simulate the process increases exponentially while the quality of the prediction did not enhanced very much.

6.4.3.7. Other outputs

The algorithm also allows different information to be estimated. In **Figure 6.37**, a series of possible outputs is shown.

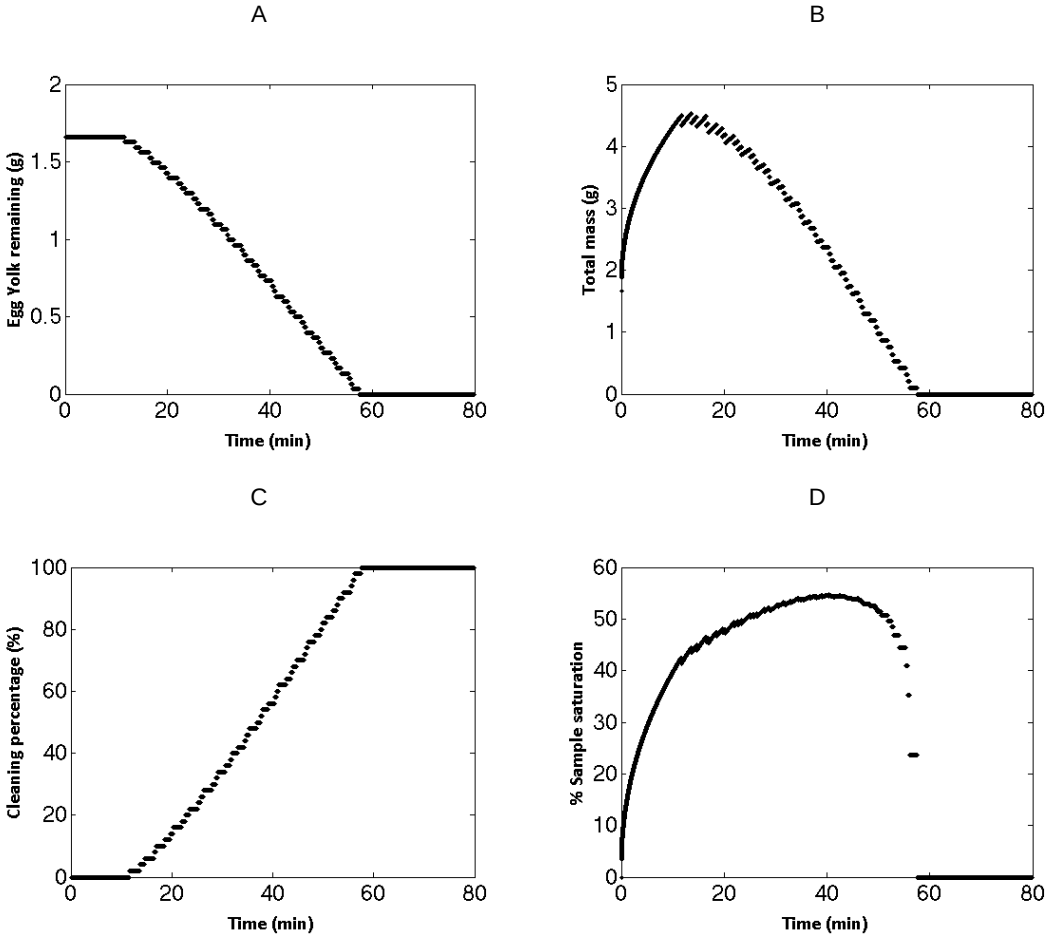

Figure 6.37. Other outputs that can be obtained with the algorithm developed. A – Soil remaining over time; B – Total mass (soil + solvent) over time; C – Cleaning percentage over time; D – Sample saturation over time.

If the initial soil dry mass is known, a soil mass content can be assigned to each layer and the amount of soil remaining can be estimated as seen in **Figure 6.37A**. The net amount of mass in the system (soil + solvent) can also be calculated when increase in thickness is correlated with the amount of solvent (water) uptake via a density relationship. This is seen in **Figure 6.37B**. A cleaning percentage profile can be calculated if cleaning rate is normalised as a function of the layers remaining. This approach can lead to better comparison between cleaning rates for different systems. It establishes a common cleaning scale for different procedures and soil

types as cleaning is evaluated in a scale from 0 to 100. The graph is shown in **Figure 6.37C**. Finally, the increase of layers' thickness can be correlated with the equilibrium thickness and their 'saturation' calculated. 'Saturation' tells whether the soil network has 'room' for further swelling (or solvent uptake). Data calculated can be analysed for different numbers of layers (i.e. individual layers, group of bottom/top layers, all layers, etc.) depending on the information required. In **Figure 6.37D**, the saturation of the soil is represented considering all the layers available at each time of the process. Maximum saturation is estimated around 50-60%. This indicates that if no removal happens, the soil still has the potential to hydrate by another 40%. At the end of the process, the routine predicts a decrease in the saturation of the remaining soil. This corresponds to the bottom layers, which are calculated theoretically to be low hydrated, as the liquid penetration is low. Once all layers are removed the curve drops to a 0% value.

6.5. SUMMARY

Swelling and removal phenomena occurring in protein-based soils were studied via scanning Fluid Dynamic Gauge (sFDG). Factors such as temperature, pH, enzyme level, net shear stress and the frequency of application of shear stress were investigated.

The dynamic statistical study built predictive curve responses as well as highlighted those parameters significantly impacting thickness variations. Initially, temperature and pH were evaluated as factors affecting swelling. Results showed pH as the most contributing factor to the degree of swelling. Swelling ratio increased with the increase of alkalinity. Temperature also played an important role. At high alkaline and temperature conditions (i.e. pH 11.5 and 55ºC), hydrolysis effects weakened the structure and the soil was detached from the surface.

The addition of enzymes to the wash solution led to a decrease in thickness after an initial swelling period. A second experimental design incorporated the effect of the enzyme level, the net shear stress and its frequency (frequency factor) into the analysis. Results established temperature, pH, enzyme level and the frequency factor as significant contributors to the thickness change. The effect of the net shear stress applied was disregarded in the statistical analysis. This indicated that at the range of shear stresses studied (12 Pa to 65 Pa), an

increase on the net shear stress applied did not produce a significant thickness change. However, the importance of the frequency factor suggested that the quick removal of a protein-based sample requires the application of an external force as frequently as possible. This further suggested the existence of a shear stress threshold below which an external mechanical action does not impact the removal process. If this threshold value is achieved, removal is suddenly enhanced though the removal rate does not vary much with a further increase on the shear stress applied. This threshold would vary with the change of the status of the sample (more or less hydration, hydrolysis reactions…).

The effect over time of each of the significant factors showed the importance of pH in the first stages of the process as a positive contributor to thickness (swelling) only. Temperature showed an important effect on both swelling and removal stages, presenting the overall biggest importance. Enzyme level and the frequency factor were negative contributors to thickness (removal) and their effect was noticeable once the removal stage started (typically after 15 to 20 minutes). The pH square term (pH*pH) and the interaction effect between temperature and enzyme level (temperature*enzyme) and temperature and frequency factor (temperature*frequency) were also reported as significant contributors to thickness changes.

The analysis of swelling phenomena was expanded by comparing hydration studies performed via sFDG and gravimetric methods. At high alkalinity (pH 11.5), some of the material was removed when an external surface shear stress was applied. The formation of blisters was also observed in these conditions. The soil network was weaker due to the increase of moisture content and hydrolysis reactions that occurred. The kinetics of the diffusion process did not shown significant differences within the range of conditions studied. 95% of the maximum swelling was reached approximately after 90 min.

The use of the power-law model suggested a Fickian diffusion transport model. The adaptation of the equation to fit sFDG data produced comparable results. The increase of temperature and pH led the mass transfer process towards an anomalous scenario. The sample network needed

to accommodate higher volumes of liquid over the same time period as the maximum swelling was reached at the same time. Therefore, the network rearrangement became more difficult.

Three different theoretical approaches were used to fit the experimental data and to estimate effective diffusion coefficients. Fick's second law (with moving boundaries) showed the lowest accuracy in predictions. Linear poroelasticity theory allowed good fits on the experimental data. However, this mathematical approach led to lower effective diffusion coefficients than the other theories. The non-linear approach also reported accurate predictions. The use of these theories allowed the estimation of activation energies in the analysis of the temperature dependence of the diffusion coefficient.

Finally, a novel algorithm based on theoretical background was developed to describe and model swelling and removal. The use of sFDG allowed the identification of the different mechanisms leading to removal: either via application of an external shear stress (mechanical and enzymatic-induced cleaning) or soil dissolution (pure enzymatic-induced cleaning). The process was mathematically expressed in Eq. 6.1.

Swelling was described by applying the non-linear poroelasticity theory. The second order non-linear partial differential equation given allowed the introduction of 'theoretical layers'. These theoretical layers correspond to the number of parts into which the initial dry thickness of the soil is divided. A mathematical requirement to comply with the convergence in the solution of the PDE included as well the introduction of a time step. This was used further on to integrate the removal mechanisms.

Cleaning phenomena was modelled empirically. For each of the removal mechanisms identified (shear stress removal and soil dissolution), removal rates over time were calculated by subtracting the positive contribution to thickness from swelling. Results showed constant removal rates after an initial induction period with increasing removal rates. Different temperatures and frequencies of application of shear stress were explored. An increase in temperature increased the removal rates observed for any of the cleaning mechanism involved.

The constant application of shear stress over a fixed location promoted a reduction in the instantaneous cleaning rate observed. The hypothesis suggested an enzyme reaction rate limiting stage. Long intervals without the application of an external mechanical cleaning action allowed higher quantities of soil to be removed when mechanical action was applied. At 50°C and with a continuous application of shear stress, results also indicated a stronger mechanical removal. In the first stages of the cleaning process (induction period), removal rates were higher than for a discontinuous application of shear. This agreed with the shear stress threshold hypothesis commented before.

The algorithm developed was able to integrate all phenomena occurring. By using ‘theoretical layers’ and its associated time step, overall cleaning process was modelled. Theoretical layers were removed over time until a complete cleaning was achieved. The deletion of layer occurs if the accumulated removal thickness over a time step exceeds the thickness of the layer(s) above. The approach used also allows different ways of presenting the results. Cleaning can be expressed as thickness evolution over time, as a percentage, as the amount of soil left or total mass (soil + solvent) of the system at any time. A saturation analysis, expressed as the potential for further swelling, can also be performed.

Statistical and mathematical models for the cleanibility of protein-based soils will be used in the following chapter to predict and compare results in cleaning processes occuring in full scale ADWs.

CHAPTER 7

CLEANING ON FULL SCALE ADWs.

7.1. INTRODUCTION

The assessment of cleaning in commercial ADWs has always represented a challenge. Multiple soils attached to different surfaces with different shapes can be found at different status during a wash cycle. Therefore, describing their cleaning process is always complex. This chapter introduces the results of a novel system to constantly evaluate cleaning of technical soils inside an ADW. The technique improves the current assessment used in these appliances as the kinetics of the process can be measured. Current technical analyses are done via visual grading or through external image analysis systems (EN 50242). Thus, only the end result is measured.

Also, the mathematical model for water distribution inside an ADW (*Chapter 5*) is combined with the statistical and fundamental models developed in *Chapter 6* to predict and compare cleaning profiles in ADWs. This modelling effort concludes the integration of the learning made during this work and provides a tool to optimise experimental scenarios and speed-up knowledge gain.

7.2. IMAGE ANALYSIS STUDIES

The technical principles as well as the experimental procedure are explained in *Chapter 3, section 3.11*. Also, a schematic representation of the different vectors into which colour is divided (L*a*b) was previously shown in **Figure 3.10**. Temperature, pH and enzyme level effects were evaluated on egg yolk technical stains. Levels selected were kept in the same range as studied previously: 30ºC to 55ºC for temperature, 9.5 to 11.5 for pH and 0.02 g/l to 0.1 g/l for the enzyme level. Triplicates were measured for each experimental case considered. Cleaning profiles represented the stain removal index (SRI) achieved at any time of the wash.

7.2.1. Typical tile cleaning evolution

Figure 7.1 illustrates a typical tile cleaning evolution.

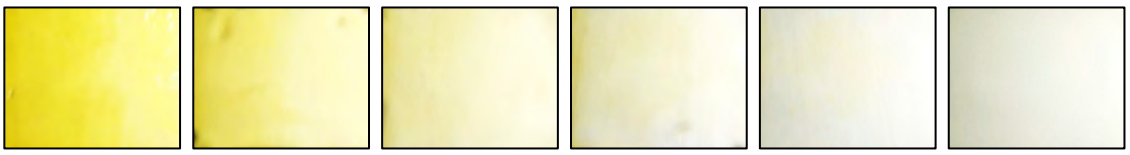

t = 0 min. t = 15 min. t = 30 min. t = 45 min. t = 60 min. White Reference

Figure 7.1. Typical cleaning evolution path. Wash conditions were T = 55ºC, pH = 10.5 and 0.06 g/l of enzyme.

The figure shows the changes in colour through the wash cycle from the initially soiled tile. The difference in colour to the white reference decreases over time as cleaning occurs. A ‘white reference tile’ is always considered as the best cleaning output possible and establishes the upper limit in the scale (SRI = 100%). Cleaning processes observed experimentally showed a homogeneous removal across the tile area. This suggests a diffusion-reaction mechanism where the enzyme helps breaking the network and the soil washes out continuously as the water reaches the tile. It also suggests a small effect of the external shear stress generated by the direct impact of water as no areas were cleaned faster.

Water droplets on the images can be observed eventually at different locations (i.e. t = 15 min. at upper and bottom left side) due to the splashing of water occurring internally in the dishwasher. This obscures the images by creating darker spots, thus increasing the noise in the readings. Sometimes, a water film is developed as well at the front of the camera distorting some of the images. The placement of the light torch also makes the right side of the tile to be more illuminated. This produces a gradient in L vector across the width of the sample and distortions on ‘a’ and ‘b’ vectors.

Figure 7.2 illustrates L*a*b values obtained over time for a row of pixels (350 pixels height) across the width of the soil from the cleaning example shown.

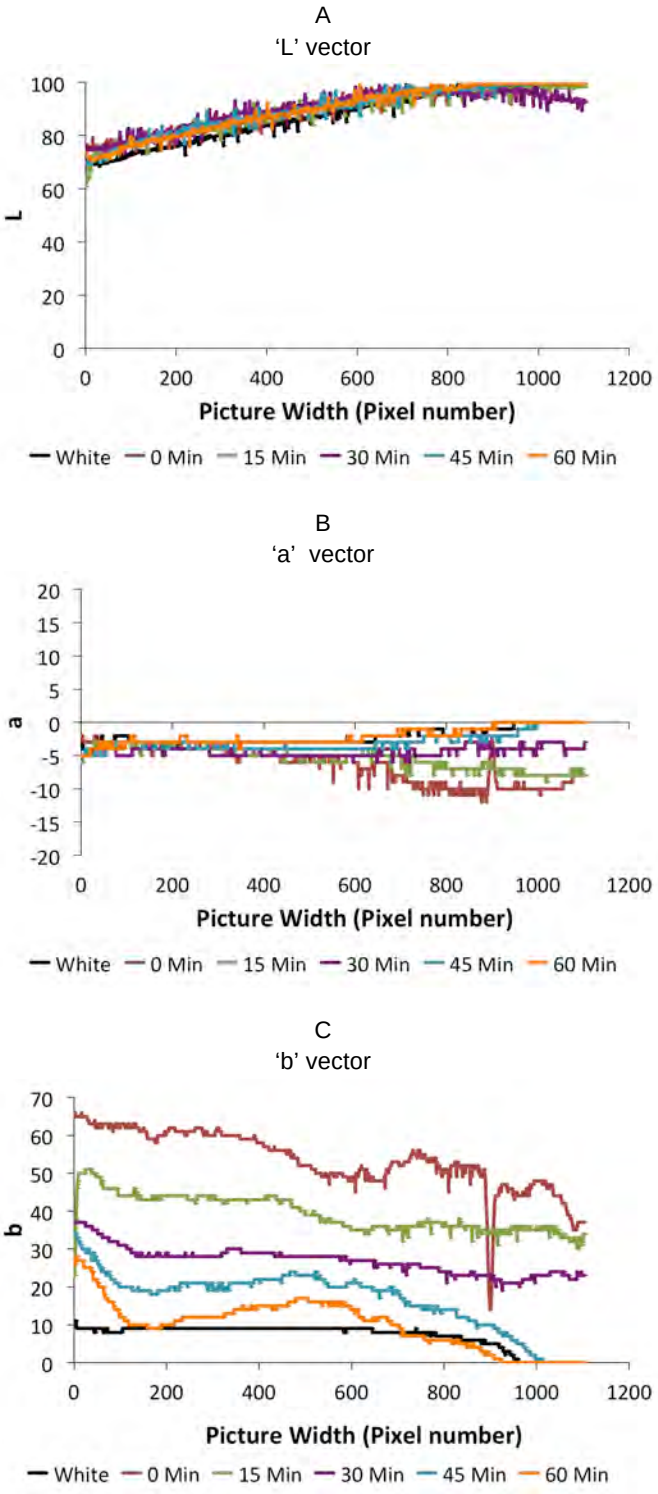

Figure 7.2. L*a*b values of a row of pixels across the width of the soil. A – 'L' vector; B- 'a' vector; C – 'b' vector.

Figure 7.2A shows the linear gradient previously commented for 'L' vector. At the right side of the image the luminosity reached its maximum (L = 100). No differences in the 'L' value would be spotted from picture to picture if the luminance of the sample varied during the cleaning

process. As a consequence, pictures were re-cropped to a width not higher than 700 pixels for further analyses. The plot also shows no changes in L over time, indicating that the luminance did not vary when these soils were cleaned. **Figure 7.2B** shows the results of the chromatic component 'a' (red-greeness). A small distortion was produced again at the right side as a consequence of the inhomogeneous illumination. In that area, the system evolved from values around -10 to values close to 0 at the end of the wash cycle, in agreement with the profile given by the white reference. The area not distorted directly by the illumination shows no differences over time. **Figure 7.2C** analyses the chromatic component 'b' (blue-yellowness). It shows a clear evolution from high values (b = 70), corresponding to the 'yellowness' of the picture, to low values (b = 10), in accordance to the white reference. Therefore, this vector was the main contributor in the measurement of the colour change. The profile shows as well the decrease of 'b' component from left to right as a consequence of the inhomogeneous illumination. At 45 and 60 minutes a sharp decrease in the 'b' value was also seen on the left side of the picture. This was related to the accumulation of water in this area. Overall, L*a*b values were averaged across the cropped area considered. Therefore, only a single 'L', 'a' and 'b' value was given at a specific time (one 'L','a' and 'b' value per picture). This reduced all the illumination and homogenised the results.

Figure 7.3 illustrates the SRI profile obtained from the example given. Data was processed according to the method explained in *Chapter 3, section 3.11.4*.

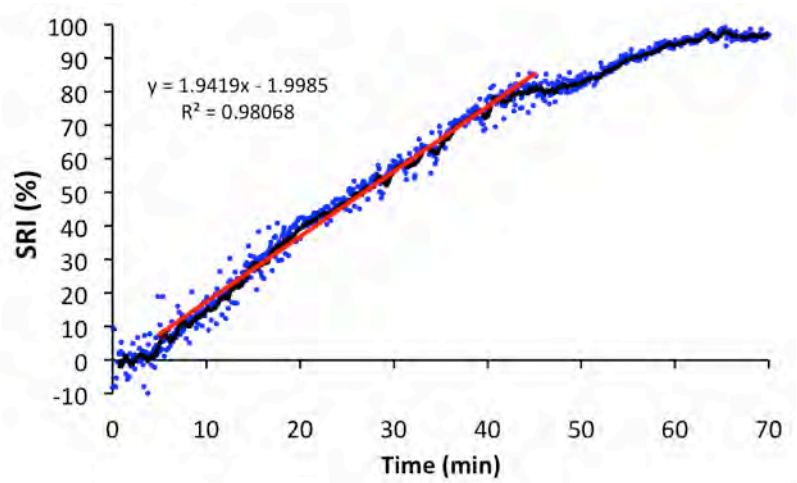

Figure 7.3. Stain Removal Index profile for the example given. Blue dots represent SRI values calculated for each picture taken. Black line represents a moving average line with a period of 10. Red line represents the linear fitting on the constant removal period.

The plot identified three different stages in the cleaning process. Firstly, an initial period with no removal was observed for the first 5 minutes. This related to the time required for cleaning to start and was in agreement with the swelling phenomenon explained in the previous chapter. No colour changes were therefore associated with swelling. Then, cleaning occurred at a constant rate during most of the wash cycle. Again, the phenomenon agreed with the removal rates profiles calculated in *Chapter 6, section 6.4.3.3,* (**Figure 6.29**). Finally, removal was reduced gradually as the process moved to the decay stage and the tile was completely clean.

Due to the inherent error in a single L*a*b picture measurement, the initial reference contrast [$(Contrast)_{t=0}$] was calculated as the average result for images taken during the first three minutes of the experimental procedure. As no cleaning occurred within that period, this aimed to reduce the overall error in the calculations.

The fitting of a line during the constant removal stage allowed the calculation of an averaged cleaning rate. For the example given, this stage was found between 5 to 45 minutes approximately. The linear fitting estimated a removal rate of 1.94 %SRI/min (R^2 = 0.9807). This methodology will be used further as a quantitative comparison for different washing conditions considered.

Despite the issues highlighted previously on data acquisition and image processing, the method was able to represent clear cleaning profiles. Deviations from consecutive points were very small and the presence of outliers scarce. The effect of temperature, pH and enzyme level on the cleaning of protein-based soils is shown next.

7.2.2. Effect of temperature

Figure 7.4 shows the results from experiments at 30ºC and 55ºC. They were initially set-up with an enzyme level of 0.06 g/l and a pH of 10.5.

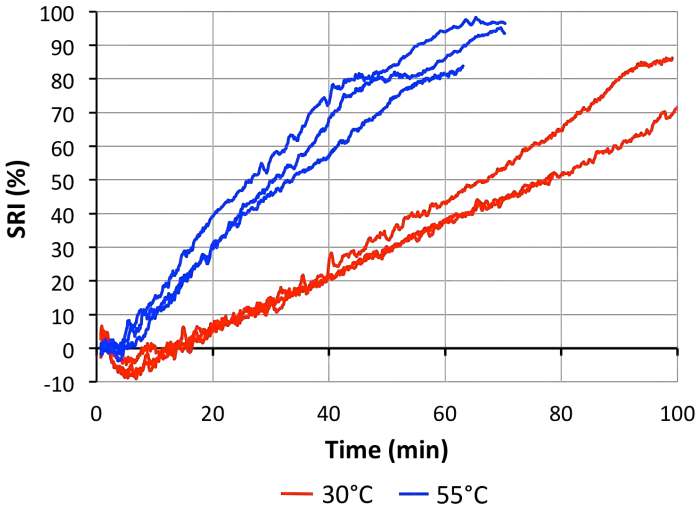

Figure 7.4. Temperature effect on cleaning performance. Red and blue lines represent the moving average fit with a period of 10 at 30ºC and 55ºC respectively. Experimental conditions were set at pH 10.5 and 0.06 g/l of enzyme. Individual data points are not shown to preserve the clarity of the figure.

The graph clearly shows how the cleaning rate increased with the increase of temperature. A reduction in the initial lag period was also observed at 55ºC. As explained in the previous chapter, these differences were due to the following phenomena:

1. The absorption of higher quantities of liquid is faster at higher temperatures. This phenomenon leads to a faster weakening of the soil structure. Therefore the subsequent cleaning process occurs at an early stage.

2. The use of a protease is favoured at 55ºC. According to literature (Aehle, 2007), this type of enzyme finds their optimum performance at a range of temperatures between 50ºC to 60ºC. By making the enzyme work at its best, hydrolysis kinetics was faster and therefore removal occurred faster as observed.

Table 7.1 compares the averaged cleaning rates estimated for each of the cases studied:

Table 7.1. Cleaning rate values for experiments at 30ºC and 55ºC.

CASE	CLEANING RATE	STD
30ºC	0.85 %/min	0.12 %/min
55ºC	1.75 %/min	0.29 %/min

Results show how the cleaning rate was twice as fast at 55ºC when compared to 30ºC runs.

7.2.3. Effect of enzyme level

Figure 7.5 illustrates three different cleaning profiles for three enzyme levels considered: 0.02 g/l, 0.06 g/l and 0.10 g/l. These experiments were run at 55ºC and at initial pH of 10.5.

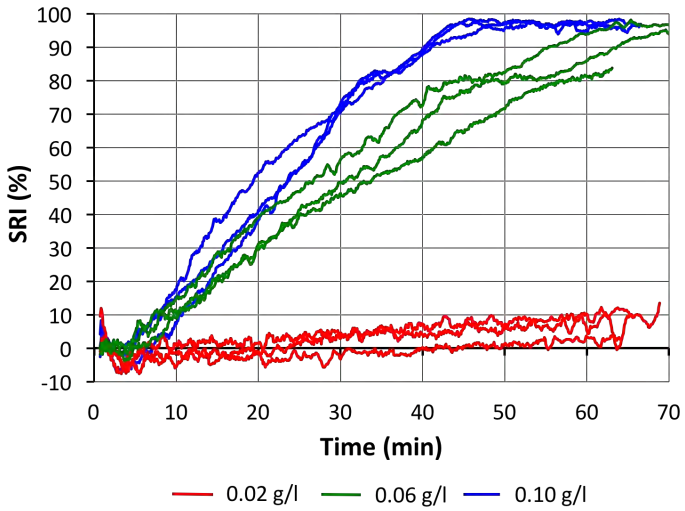

Figure 7.5. Enzyme level effect on cleaning performance. Red, green and blue lines represent the moving average fit with a period of 10 at 0.02, 0.06 and 0.10 g/l of protease respectively. Experimental conditions were 55ºC and pH 10.5.

The plot shows how the lowest level of enzyme (0.02 g/l) hardly produced any removal on the soil. A significant difference was observed when compared to higher levels. For the highest level considered (0.10 g/l) a complete cleaning was achieved at around 45 minutes. The medium level results (0.06 g/l - seen as well in **Figure 7.4**) suggested a completed removal at around 65 minutes. The difference in performance, apart from the obvious increase in protease concentration, could also be influenced by a lower impact on the replenishment effect produced by the water action. The spread of water on a particular location is a periodic movement as commented in *Chapters 4 and 5.* For the rotation rate given of 35 rpm a jet would impact the same spot every 1.7 seconds approximately. Enzymes deposited at the surface at the moment of the impact could either be reacting or remain unreacted. Those not reacting at that particular moment are more likely to be wash out from the soil surface. It could also be assumed that the higher the concentration the more molecules reacting until the saturation of the soil surface is achieved. Given that case, a higher concentration would lead to more molecules remaining at the surface and for longer which in the latter case would increase the removal rate.

Table 7.2 summarises the averaged cleaning rates calculated:

Table 7.2. Cleaning rate values for experiments at 0.02, 0.06 and 0.10 g/l levels of enzyme.

CASE	CLEANING RATE	STD
0.02 g/l	0.17 %/min	0.05 %/min
0.06 g/l	1.75 %/min	0.29 %/min
0.10 g/l	2.59 %/min	0.22 %/min

A significant difference in the cleaning performance was observed between the three levels considered. The rate increase from 0.02 g/l to 0.06 g/l was much higher than from 0.06 g/l to 0.10 g/l (increment of 1.58 %/min versus 0.84 %/min), indicating an exponential variation. This suggests that potential savings or optimization scenarios can be explored in order to correlate the usage of enzyme and its associated cost with the performance expected in a typical wash cycle.

7.2.4. Effect of pH

Figure 7.6 shows the effect of pH on the removal of egg yolk technical samples. These experiments were run at 55ºC with 0.06 g/l of protease.

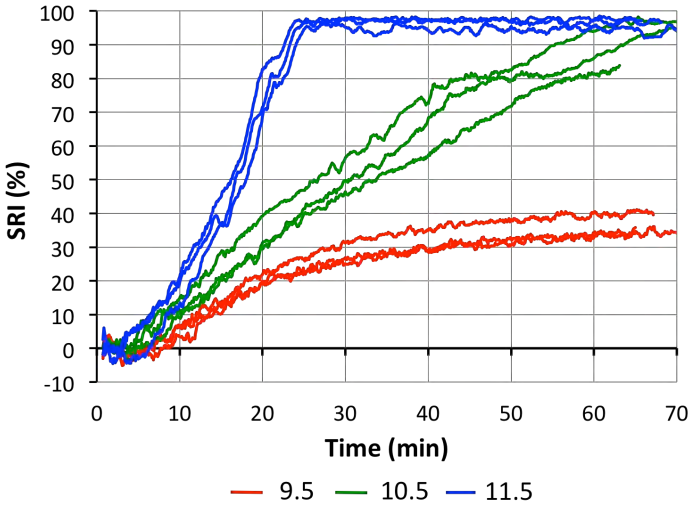

Figure 7.6. pH effect on cleaning performance. Red, green and blue lines represent the moving average fit with a period of 10 at pH 9.5, 10.5 and 11.5 respectively. Experimental conditions were 55ºC and 0.06 g/l of protease.

Results indicated that the increase of alkalinity led to a faster removal within the range studied. This was favoured by both the weakening of the soil network as the swelling-ratio increased and by the hydrolysis reactions occurring at high pH (Mercadé-Prieto *et al.*, 2008, 2007a). These phenomena were commented in detailed in the previous chapter.

The different cleaning rates calculated were summarised in **Table 7.3**:

Table 7.3. Cleaning rate values for experiments at pH 9.5, 10.5 and 11.5.

CASE	CLEANING RATE	STD
9.5	0.69 %/min	0.16 %/min
10.5	1.75 %/min	0.29 %/min
11.5	4.66 %/min	0.38 %/min

The experiment at pH 11.5 showed the highest removal rate among all the experimental conditions analysed. For this case, a complete cleaning was achieved at around 25 minutes. The increase of pH from 10.5 to 11.5 led to an increase in the cleaning rate by a factor higher

than 2.5. At pH 9.5, a reduction on the removal rate was observed after 20 minutes and a complete cleaning was far from being achieved. The curvature given in the cleaning profiles also reduced the accuracy to calculate the removal rate values. The estimation for each of the triplicates showed higher error. The coefficients of determination (R^2) calculated were within 0.78-0.81, while for the rest of the experimental cases were typically around 0.95-0.99.

Apart from the effect of the enzyme on the soil surface, the mechanism of removal could incorporate some penetration of the enzyme into the soil network. As the swelling-ratio achieved increases, the diffusion of bigger molecules becomes easier. The increase of alkalinity, leading to more hydration, could enhance the penetration of enzyme molecules to some layers underneath the surface. Therefore, the breakage of peptide bonds would occur both at the surface and inside the soil. If the swelling-ratio achieved was not high enough, the enzyme would not diffuse and the hydrolysis would only occur at the surface. This would decrease the cleaning rate observed.

The different experiments analysed showed no change in colour during the initial swelling stage as commented previously. Therefore it can be concluded that colour changes are only related to the cleaning process occurring in this type of soils. This makes the technique suitable for the analysis of cleaning inside an ADW.

7.2.5. Peculiar cases

Two different and uncommon cleaning patterns were seen only once: the formation of a cleaning moving front and the pattern created by the direct impact of a jet.

a) Creation of a cleaning moving front

Figure 7.7 illustrates the evolution of a cleaning front starting at the bottom left of the tile and expanding upwards and to the right. Experimental conditions were 55ºC, pH 10.5 and 0.02 g/l of protease.

Figure 7.7. Cleaning moving front seen for experimental conditions at 55ºC, pH 10.5 and 0.02 g/l of protease.

Previously reported values at these conditions showed almost no cleaning. This pattern was also different to the typical homogeneous cleaning observed across the area of the tile. Two hypothesis were suggested for the creation of this moving front:

1. A higher deposition of the enzyme at the bottom left side where cleaning started. This could be caused either by a poor dissolution of the enzyme in the wash solution and/or by a progressive accumulation of the enzyme at that area. The way the tile was placed could have created a dead space where enzyme molecules were accumulated. In that area the replenishment of chemistry caused by the action of the water jets was more difficult. Therefore, even a low level of enzyme could have started the cleaning process, as the contact between the enzyme and the soil was extended in time. Once this occurred, the removal action expanded to the vicinities. This dead spot can be seen as a ‘cleaning seeding point’.
2. The characteristics of the tile used. The use of a defective tile could also explain this phenomenon. Low amounts of soil at the bottom left side of the tile could have eased the start the cleaning process. Liu *et al*. (2006) reported that less mechanical or chemical energy input is required to completely clean areas with lower quantities of soil. Therefore, those particular areas could have acted as starting points of the cleaning process.

b) Jet impact pattern

Figure 7.8 shows the cleaning pattern created as a consequence of the direct impact of water in an experiment at 55ºC, pH 9.5 and 0.06 g/l of protease.

A B

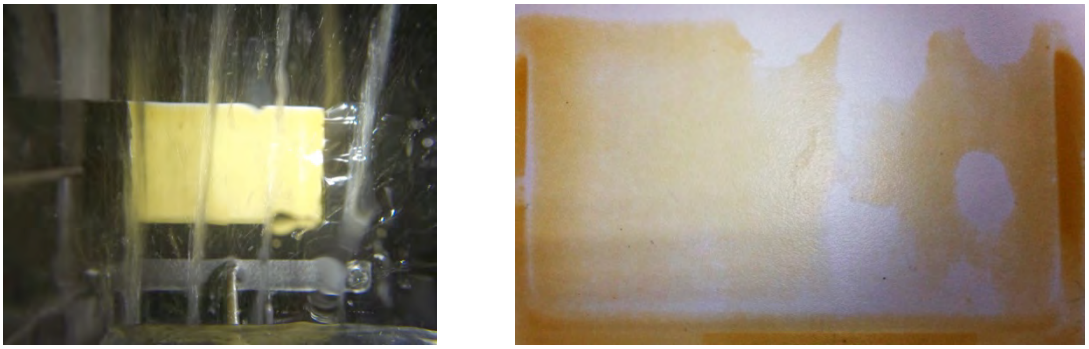

Figure 7.8. Jet impact pattern on the tile surface. A – Multiple water jets on their way to impact the tile. B – Straight cleaning pattern observed at right side of the tile. Picture was taken after drying the tile at room temperature during 24h. Experimental conditions were 55ºC, pH 9.5 and 0.06 g/l of protease.

Figure 7.8A illustrates different water jets heading to the soil tile. As explained in *Chapter 5*, only those jets with the right combination of nozzle position and angles would be able to directly impact the tile. A deeper study on this particular experimental set-up is explained in the following *section 7.3.1*. **Figure 7.8B** shows the vertical pattern created by the water. These types of cleaning patterns were not seen in any other run at any experimental condition. Two hypotheses were again suggested to explain this behaviour:

1. The tile was not placed steadily and in the same position as the rest of the experiments. The tile could have been inclined and the impact pattern been changed. An initial visual approach suggested that, given the set-up considered, only 2 of the 10 jets from the spray arm were facing towards the front of the tile. This is confirmed in *section 7.3.1*.
2. A non-homogeneous distribution of the soil. As explained before, areas with low amounts of soil require less energy for cleaning to occur.

7.3. PREDICTIONS FROM DEVELOPED MODELS

To close up the different pieces of work done during this research, full-scale experimental data were compared to predictions built directly from models described in previous chapters. Firstly, the water distribution pattern, impact locations over the soil tile and its frequency factor were calculated for the set-up considered in full-scale tests by applying the model developed in

Chapter 5. Then, using the data from the statistical studies in *Chapter 6, section 6.2.2*, removal rates were modelled for each of the cleaning mechanisms previously identified (shear stress and soil dissolution removal). Finally, this information was input into the mathematical swelling-removal model and full-scale cleaning profiles were estimated and compared against experimental data. **Figure 7.9** illustrates a schematic of the integrated model built.

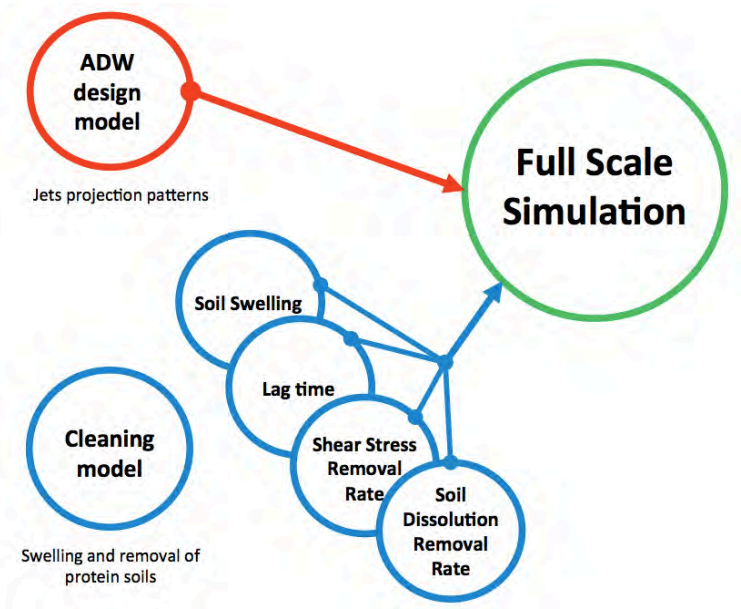

Figure 7.9. Schematic of the integrated model built to simulate full scale cleaning profiles.

7.3.1. Building predictions

7.3.1.1. Jets impact patterns and frequency

The input parameters required to establish the water impact patterns and frequency factor involve knowing the coordinates of the area occupied by the tile, the 'vision area' distance, the spray arm rotation rate and the design parameters of the different nozzles in the lower spray arm. The characteristics of the spray arm were shown in *Chapter 5, section 5.6, table 5.7* and the spray arm rotation rate was measured at 35 rpm (1.71 seconds per revolution) as commented previously.

Figure 7.10 illustrates a schematic of the experimental set-up used for full-scale tests. The different corners defining the area of the tile are numbered as shown above. The coordinates of them are summarised in **Table 7.4**.

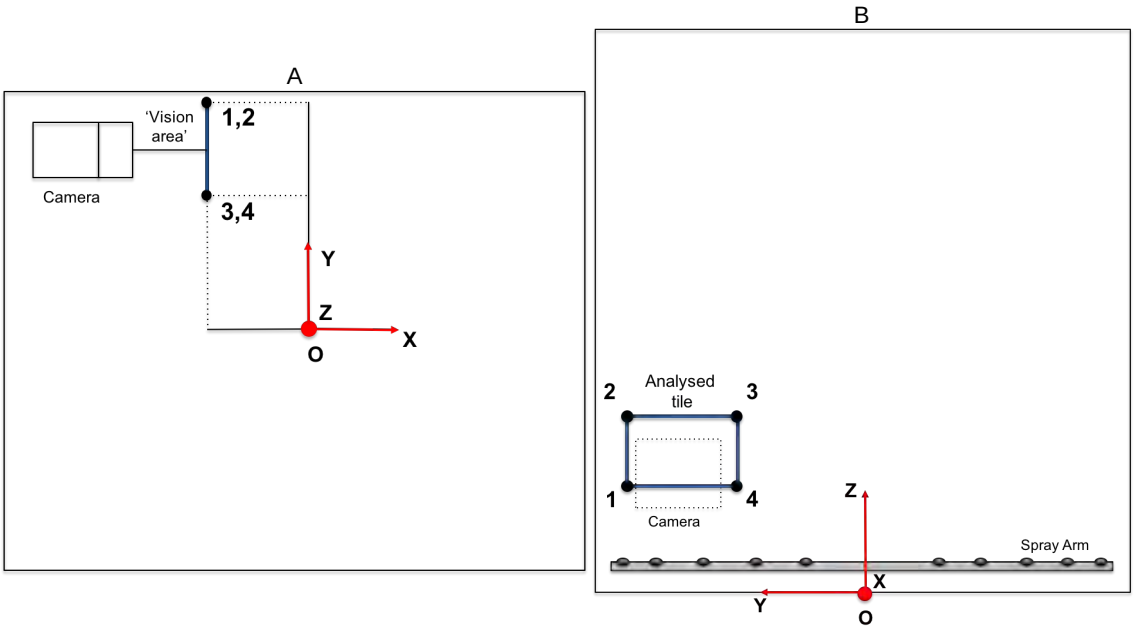

Figure 7.10. Schematic of the experimental set-up for full-scale tests. A – Plan view. B – Side view.

Table 7.4. Coordinates of the 4 corners defining the area occupied by the soil tile.

POINTS	X	Y	Z
1	-35	245	180
2	-35	245	240
3	-35	155	240
4	-35	155	180

The vision area distance was set at 75 mm. With this information, the routine predicted only two jets (#2 and #4) able to directly impact the soil. **Figure 7.11** illustrates the water impact pattern simulated for those jets.

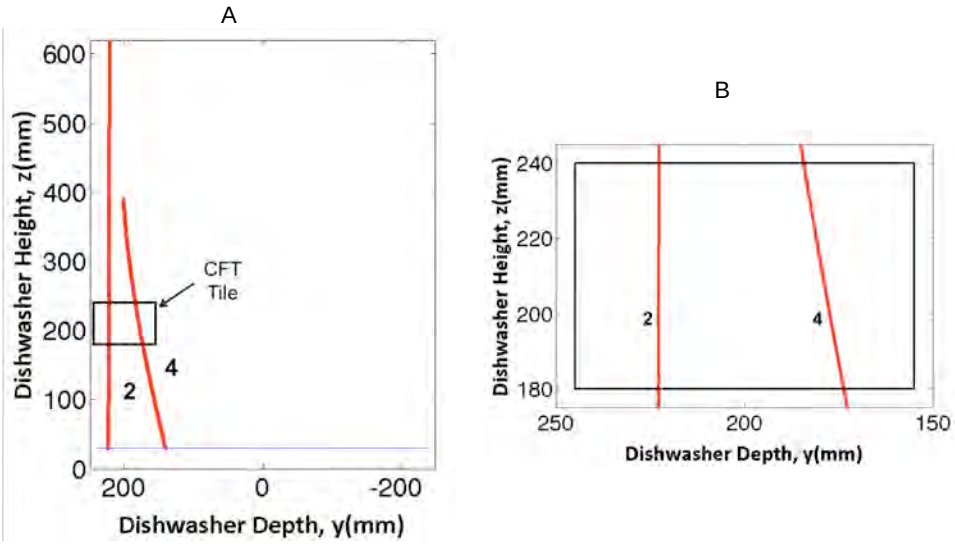

Figure 7.11. Water jets projections. A – Side Elevation at x = -35 mm. B – Detailed water projection pattern over soil tile.

Table 7.5 summarises the input and output values obtained from the simulation.

Table 7.5. Input and output values for the full-scale set-up.

	INPUT				OUTPUT						
#	NOZZLE POSITION (R_{NZ} [=] mm)	NOZZLE –PLATE REL. POS. (*R)	THETA ANGLE (θ_{jet} [=] degrees)	RHO ANGLE (ρ_{jet} [=] degrees)	t_{vis} (s)	T_{impact} (s)	L_{impact} (mm)	τ_{vis}	τ_{lap}	δ	α
2	226	0.2262	359	89	0.0963	0.0013	59.86	0.0133	0.0007	0.998	0.0133
4	145	-0.5717	305	70	0.1685	0.0272	60.93	0.1617	0.0159	1.015	0.1642

For jet #2, the impact time over the soil was estimated at 0.0013 seconds per revolution of the spray arm. This corresponds to only 0.07% of the total rotational time ($\tau_{lap} = 0.0007$). This is a consequence of the rho angle design value (ρ_{jet} = 89 degrees), which projects the jet almost vertically in the dishwasher. For jet #4, the impact time was higher and estimated to be 0.0272 seconds. This led to a frequency of impact of 1.59% of the total rotational time ($\tau_{lap} = 0.0159$). The rho angle design (ρ_{jet} = 70 degrees) projected this jet less vertically in the dishwasher, thus allowing it to impact the soil tile for longer. For the full-scale simulations, the frequency of

application of an external shear stress over the soil tile was assigned a value of 1.59%, representing the best-case scenario estimated.

Both jets impacted the tile across its height as seen in **Figure 7.11**, therefore producing a good coverage ($\delta \approx 1$). Given that, for the full-scale simulations, it was assumed that the water shear stress generated was homogeneous across the soil area at any time the impact of the jets occurred.

7.3.1.2. Swelling and removal rate predictions

Four different pieces of information were required in order to estimate swelling and removal rates at any experimental conditions considered in full-scale tests: swelling profiles, cleaning lag times, shear stress removal rates (k_{ss}) and soil dissolution removal rates (k_{ds}).

Swelling profiles were obtained directly from experiments shown in *Chapter 6, section 6.3.1*. Cleaning lag times, shear stress removal rates and soil dissolution removal rates were estimated by building Response Surface (RS) statistical models from data from the swelling and removal phenomena study in *Chapter 6, section 6.2.2.*

Table 7.6 summarises the different cleaning lag times, shear stress and soil dissolution removal rates calculated for each experimental case considered in the experimental design proposed for the sFDG tests. Extra information was calculated in those experiments at a frequency of 54.5 %. In these cases, as the sFDG nozzle moved from one position to another to set the desired frequency, alternative data (out of the original design) was collected at a frequency of 17%. This data was incorporated for the modelling of shear stress and soil dissolution removal rates as it enhanced the quality of the predictions. It is shown at the bottom of the table.

Table 7.6. Summary of cleaning lag times, shear stress removal rates and soil dissolution removal rates estimated from swelling and removal phenomena studies over protein-based soils by using the sFDG.

T (ºC)	pH	ENZYME (g/l)	SHEAR STRESS FREQUENCY (%)	SHEAR STRESS (Pa)	t_{lag} (min)	k_{ds} (µm/min)	k_{ss} (µm/min)
55	9.5	0.10	9	65	0.38	-11.72	-26.29
30	9.5	0.06	54.5	65		-3.30	-9.43
30	10.5	0.02	9	38.5	10.94	-5.31	-16.46
55	11.5	0.02	100	12	5.03		-53.20
30	9.5	0.10	9	12	18.77	-4.64	-16.73
42.5	10.5	0.06	54.5	38.5		-8.29	-16.91
30	11.5	0.06	54.5	38.5		-9.66	-15.62
55	9.5	0.06	9	12	4.52	-9.16	-25.56
42.5	9.5	0.02	54.5	38.5		-6.40	-9.09
30	9.5	0.10	100	38.5	0.80		-7.25
55	9.5	0.02	100	65	6.19		-16.99
42.5	11.5	0.10	100	12	8.37		-42.56
30	10.5	0.10	54.5	65		-7.08	-13.34
42.5	10.5	0.06	100	38.5	16.83		-18.97
30	10.5	0.02	100	12	25.30		-10.18
55	11.5	0.10	9	38.5	10.54	-60.87	-93.54
55	10.5	0.02	54.5	65		-7.43	-13.39
55	11.5	0.10	100	65	3.55		-77.21
42.5	11.5	0.06	9	65	20.29	-37.30	-133.74
55	9.5	0.10	54.5	12		-10.82	-20.27
30	11.5	0.02	100	65	16.86		-12.94
42.5	11.5	0.02	9	12	33.23	-23.57	-66.83
30	9.5	0.06	17	65		-5.35	-12.87
42.5	10.5	0.06	17	38.5		-10.23	-21.84
30	11.5	0.06	17	38.5		-11.45	-19.96
42.5	9.5	0.02	17	38.5		-5.73	-10.21
30	10.5	0.10	17	65		-7.56	-21.71
55	10.5	0.02	17	65		-8.90	-11.28
55	9.5	0.10	17	12		-14.03	-14.51

The lag time model used as input factors the individual temperature, pH, level of enzyme and frequency factor response surfaces (e.g. temperature*RS). No interactions were considered as the amount of data was low and therefore there were less degrees of freedom. For the soil dissolution removal rate model, input factors considered were the individual response surfaces of temperature, pH and enzyme level, their interactions (eg. pH*enzyme) and square terms (e.g.

pH*pH). As this removal phenomenon is not related to the application of any external mechanical action, the frequency factor and shear stress applied were not incorporated as inputs. Finally, the shear stress removal rate model built used as input factors the individual response surfaces of temperature, pH, enzyme level and frequency factor, and their second polynomial to degree interactions (i.e. temperature*temperature, temperature*pH, temperature*enzyme, temperature*frequency for temperature factor). Shear stress was not incorporated as a factor as the statistical analysis in *Chapter 6, section 6.2.2*, did not highlight this parameter as significant in the swelling-removal process. **Figure 7.12** illustrates the actual by predicted plots obtained for every case as well as the R^2 and R^2 adjusted calculated.

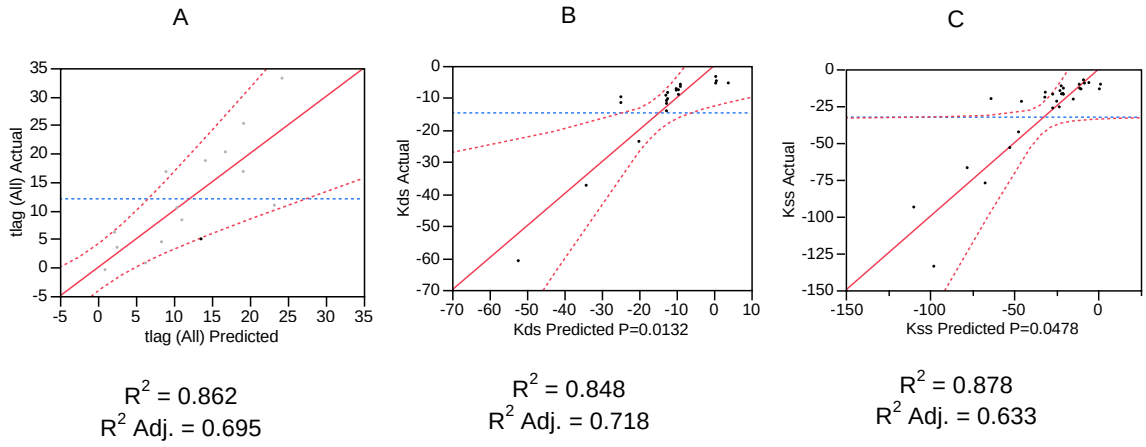

Figure 7.12. Actual by predicted plots for lag time (A), soil dissolution removal rate (B) and shear stress removal rate (C) response surface models. Dotted red lines represent the confidence interval.

Overall, models built showed relatively high agreement with real data (R^2 > 0.84). Bigger deviations were expected at the extreme values (i.e. large lag times or high soil dissolution or shear stress removal rates), as the number of data points was lower. As the experiments were not originally designed for the purpose of using them in full-scale predictions, the Response Surface models built were not fully symmetrical. This introduced some uncertainty in the predictions and also reduced the accuracy of the models.

With all these tools and data, it was already possible to estimate full-scale cleaning profiles at the different experimental conditions tested. In the following section, and for each experimental condition considered, the simulations parameters inputted in the mathematical swelling-removal

model are detailed. A representation comparing directly the experimental and simulated removal profiles, the total thickness, the total mass (soil + water), the egg yolk remaining and the soil saturation over time are also given.

7.3.2. Results comparison

EXPERIMENTAL CONDITIONS	
Temperature	30ºC
pH	10.5
Enzyme	0.06 g/l
Shear Stress Frequency	1.58%
Shear Stress	N/A
SIMULATION PARAMETERS	
Diffusion Coefficient, D	$3.0 \cdot 10^{-10}$ m^2/s
Flory-Huggins Parameter, X	0.9
Polymer Chains Per Unit Volume, N	$5.5 \cdot 10^{26}$ m^{-3}
Volume Per Solvent Molecule, Ω	$3 \cdot 10^{-29}$ m^3
Equilibrium Thickness, h_∞	0.410 mm
Lag Time, t_{lag}	13.05 min
Shear Stress Removal Rate, k_{ss}	-24.28 μm/min
Dissolution Removal Rate, k_{ds}	-2.84 μm/min

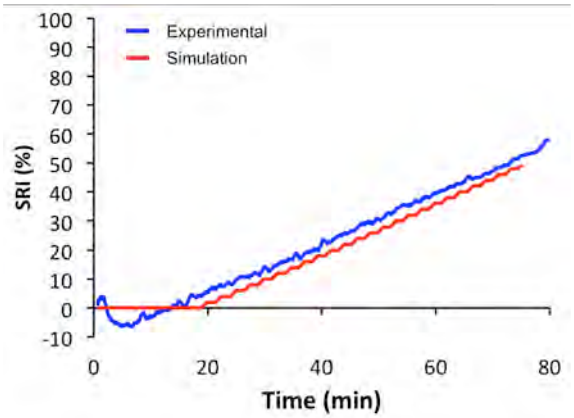

Other outputs from simulation

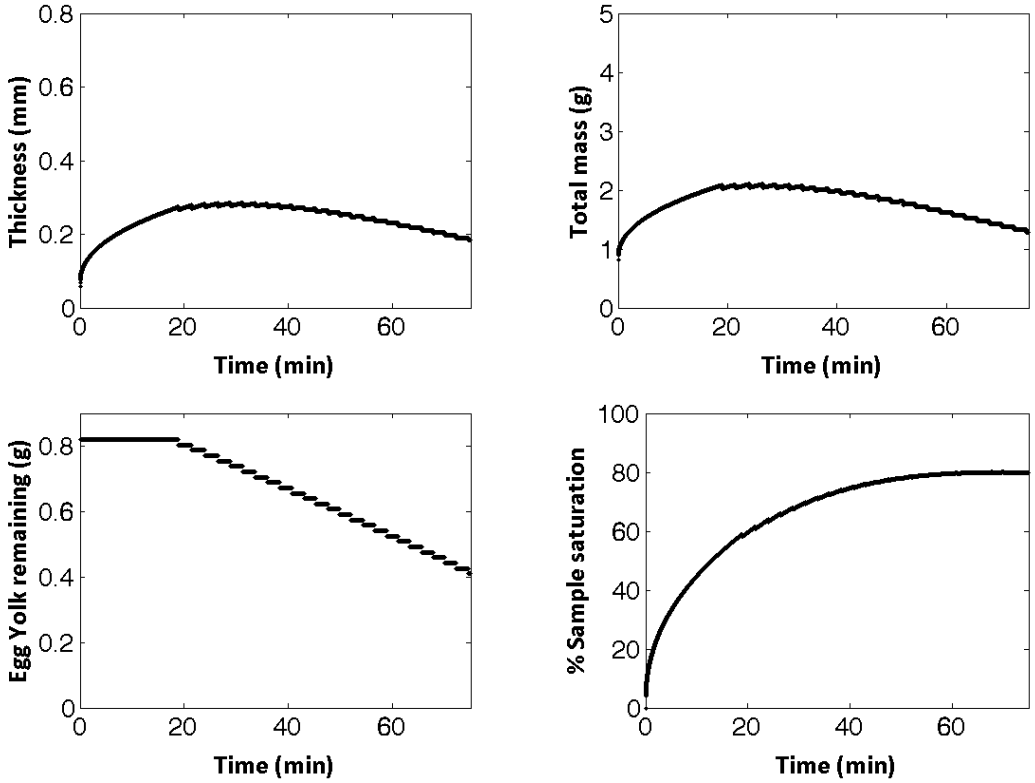

Figure 7.13. Simulation results for the experimental case at 30ºC, pH 10.5, 0.06 g/l of enzyme.

EXPERIMENTAL CONDITIONS	
Temperature	55ºC
pH	10.5
Enzyme	0.06 g/l
Shear Stress Frequency	1.58%
Shear Stress	N/A
SIMULATION PARAMETERS	
Diffusion Coefficient, D	$4.0 \cdot 10^{-10}$ m^2/s
Flory-Huggins Parameter, X	0.8
Polymer Chains Per Unit Volume, N	$5.5 \cdot 10^{26}$ m^{-3}
Volume Per Solvent Molecule, Ω	$3 \cdot 10^{-29}$ m^3
Equilibrium Thickness, h_∞	0.703 mm
Lag Time, t_{lag}	3.14 min
Shear Stress Removal Rate, k_{ss}	-69.42 µm/min
Dissolution Removal Rate, k_{ds}	-9.63 µm/min

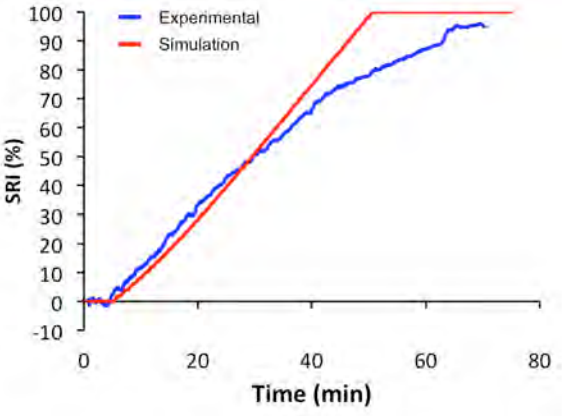

Other outputs from simulation

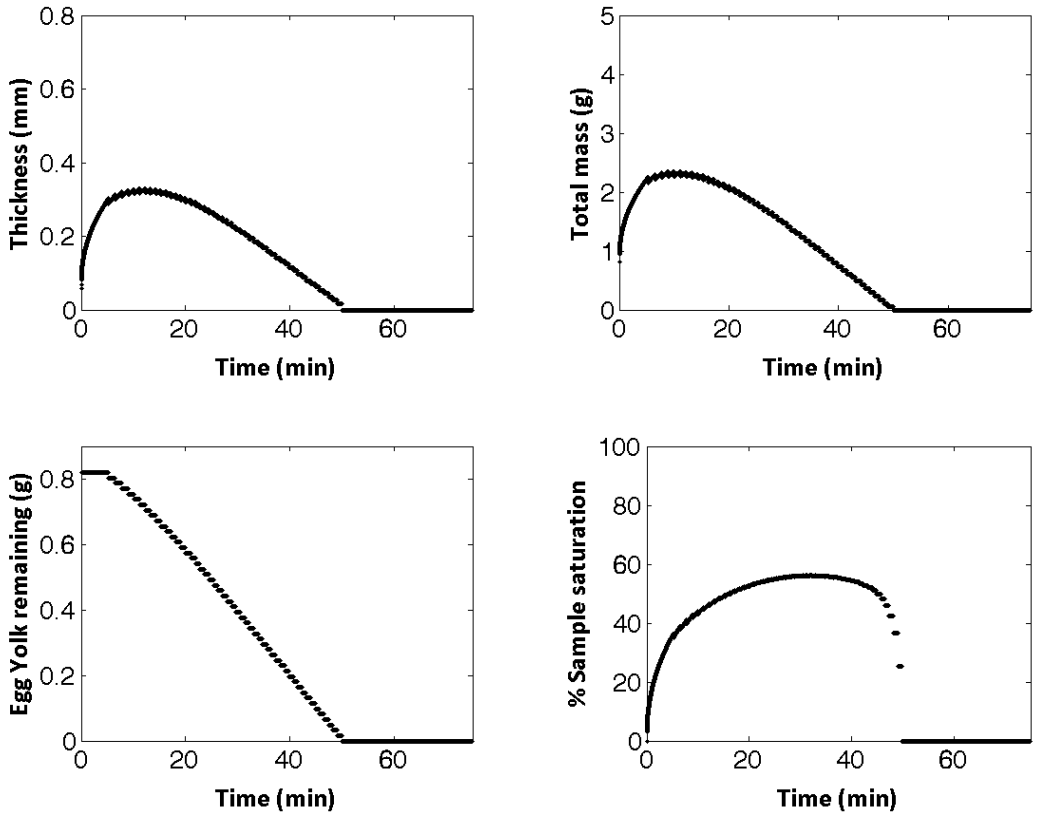

Figure 7.14. Simulation results for the experimental case at 55ºC, pH 10.5, 0.06 g/l of enzyme.

EXPERIMENTAL CONDITIONS	
Temperature	55ºC
pH	10.5
Enzyme	0.02 g/l
Shear Stress Frequency	1.58%
Shear Stress	N/A
SIMULATION PARAMETERS	
Diffusion Coefficient, D	$4.0 \cdot 10^{-10}$ m^2/s
Flory-Huggins Parameter, X	0.8
Polymer Chains Per Unit Volume, N	$5.5 \cdot 10^{26}$ m^{-3}
Volume Per Solvent Molecule, Ω	$3 \cdot 10^{-29}$ m^3
Equilibrium Thickness, h_∞	0.703 mm
Lag Time, t_{lag}	8.45 min
Shear Stress Removal Rate, k_{ss}	-31.06 μm/min
Dissolution Removal Rate, k_{ds}	-7.82 μm/min

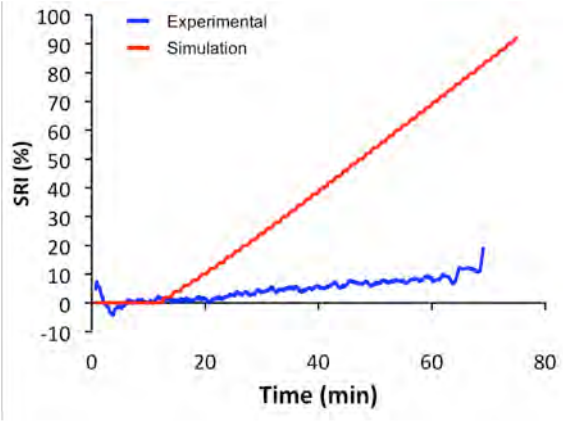

Other outputs from simulation

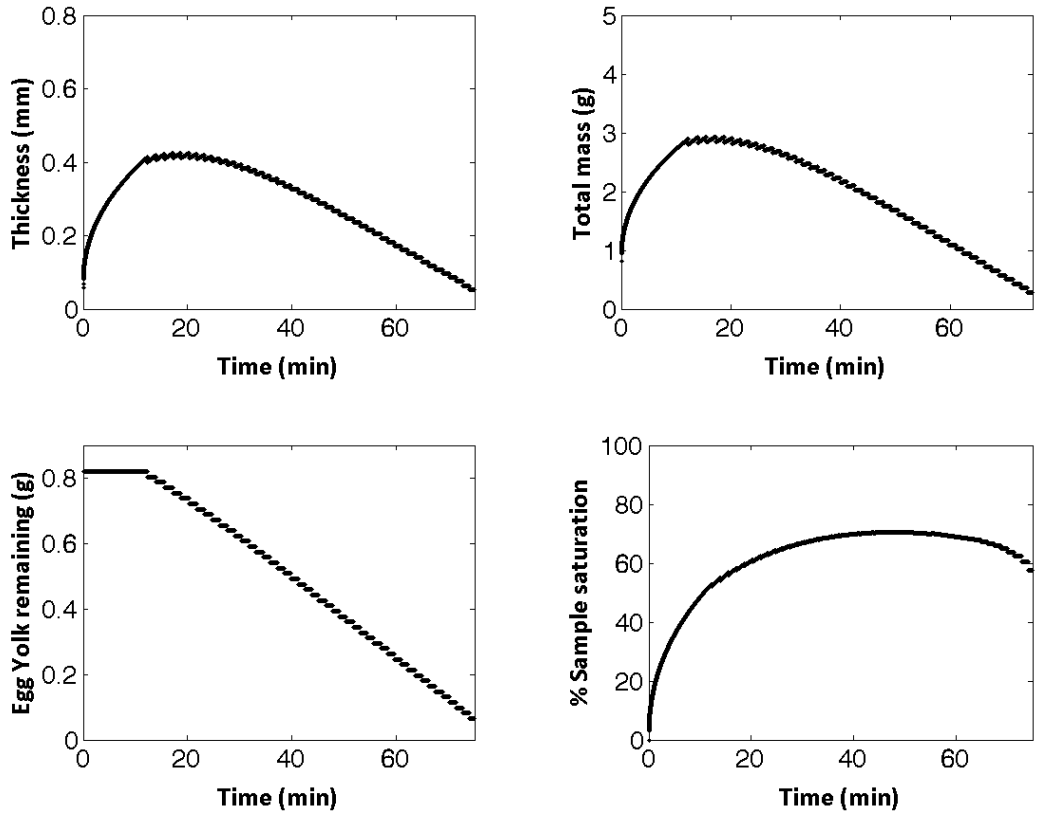

Figure 7.15. Simulation results for the experimental case at 55ºC, pH 10.5, 0.02 g/l of enzyme.

EXPERIMENTAL CONDITIONS	
Temperature	55ºC
pH	10.5
Enzyme	0.10 g/l
Shear Stress Frequency	1.58%
Shear Stress	N/A
SIMULATION PARAMETERS	
Diffusion Coefficient, D	$4.0 \cdot 10^{-10}$ m^2/s
Flory-Huggins Parameter, X	0.8
Polymer Chains Per Unit Volume, N	$5.5 \cdot 10^{26}$ m^{-3}
Volume Per Solvent Molecule, Ω	$3 \cdot 10^{-29}$ m^3
Equilibrium Thickness, h_∞	0.703 mm
Lag Time, t_{lag}	0.41 min
Shear Stress Removal Rate, k_{ss}	-95.66 µm/min
Dissolution Removal Rate, k_{ds}	-12.19 µm/min

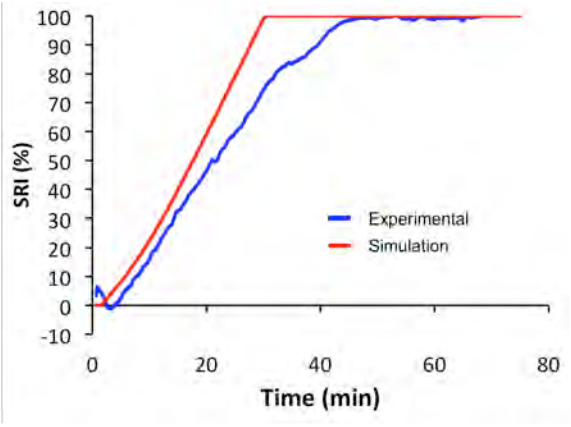

Other outputs from simulation

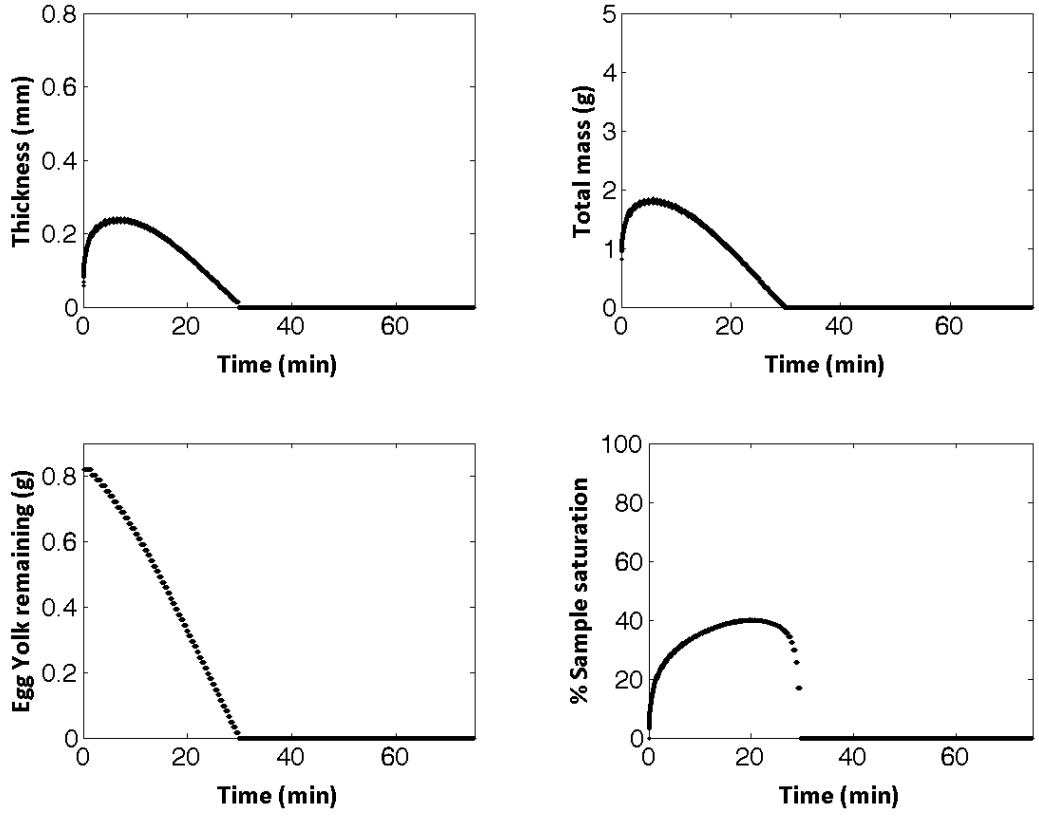

Figure 7.16. Simulation results for the experimental case at 55ºC, pH 10.5, 0.10 g/l of enzyme.

EXPERIMENTAL CONDITIONS	
Temperature	55ºC
pH	9.5
Enzyme	0.06 g/l
Shear Stress Frequency	1.58%
Shear Stress	N/A
SIMULATION PARAMETERS	
Diffusion Coefficient, D	$2.5 \cdot 10^{-10}$ m^2/s
Flory-Huggins Parameter, X	0.8
Polymer Chains Per Unit Volume, N	$5.5 \cdot 10^{26}$ m^{-3}
Volume Per Solvent Molecule, Ω	$3 \cdot 10^{-29}$ m^3
Equilibrium Thickness, h_∞	0.445 mm
Lag Time, t_{lag}	0.93 min
Shear Stress Removal Rate, k_{ss}	-19.20 μm/min
Dissolution Removal Rate, k_{ds}	-7.69 μm/min

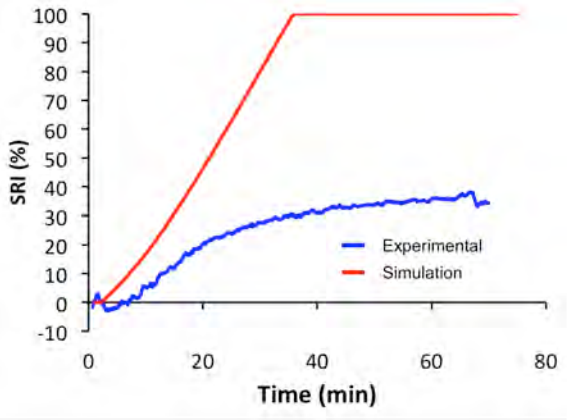

Other outputs from simulation

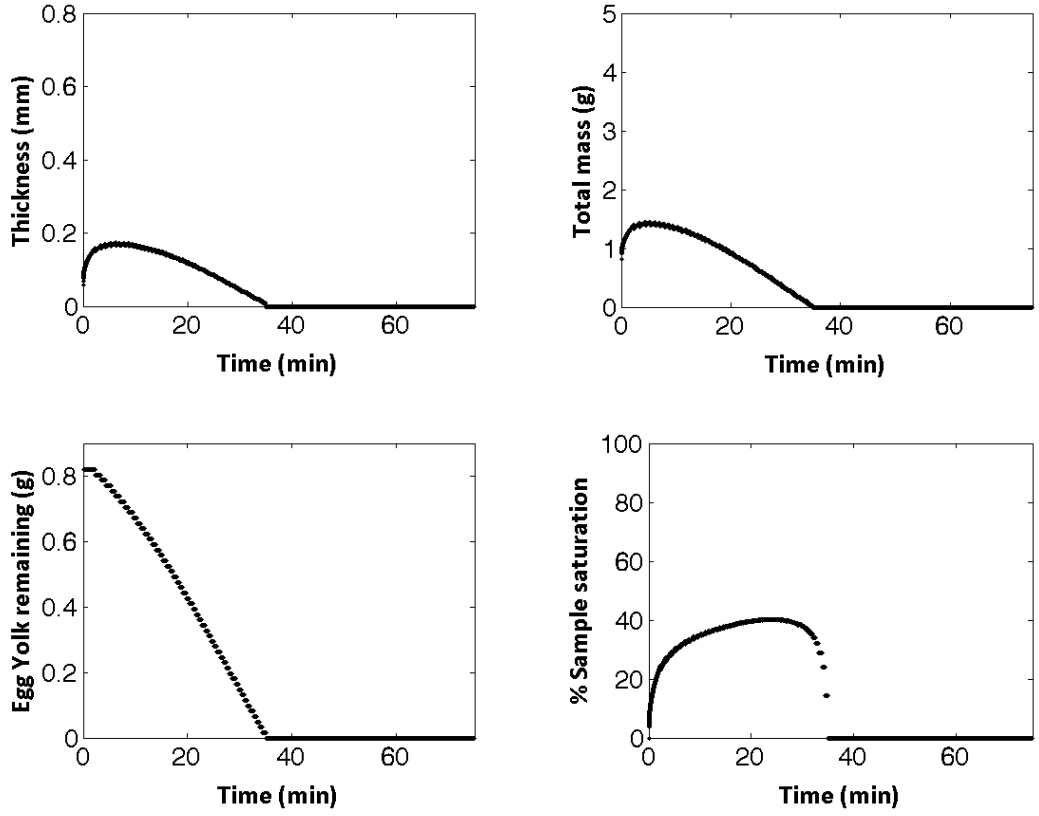

Figure 7.17. Simulation results for the experimental case at 55ºC, pH 9.5, 0.06 g/l of enzyme.

EXPERIMENTAL CONDITIONS	
Temperature	55ºC
pH	11.5
Enzyme	0.06 g/l
Shear Stress Frequency	1.58%
Shear Stress	N/A
SIMULATION PARAMETERS	
Diffusion Coefficient, D	$9.0 \cdot 10^{-10}$ m^2/s
Flory-Huggins Parameter, X	0.0
Polymer Chains Per Unit Volume, N	$5.5 \cdot 10^{26}$ m^{-3}
Volume Per Solvent Molecule, Ω	$3 \cdot 10^{-29}$ m^3
Equilibrium Thickness, h_∞	0.822 mm
Lag Time, t_{lag}	5.92 min
Shear Stress Removal Rate, k_{ss}	-154.65 µm/min
Dissolution Removal Rate, k_{ds}	-22.93 µm/min

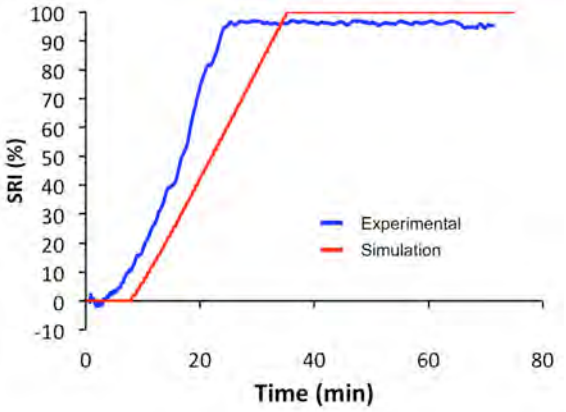

Other outputs from simulation

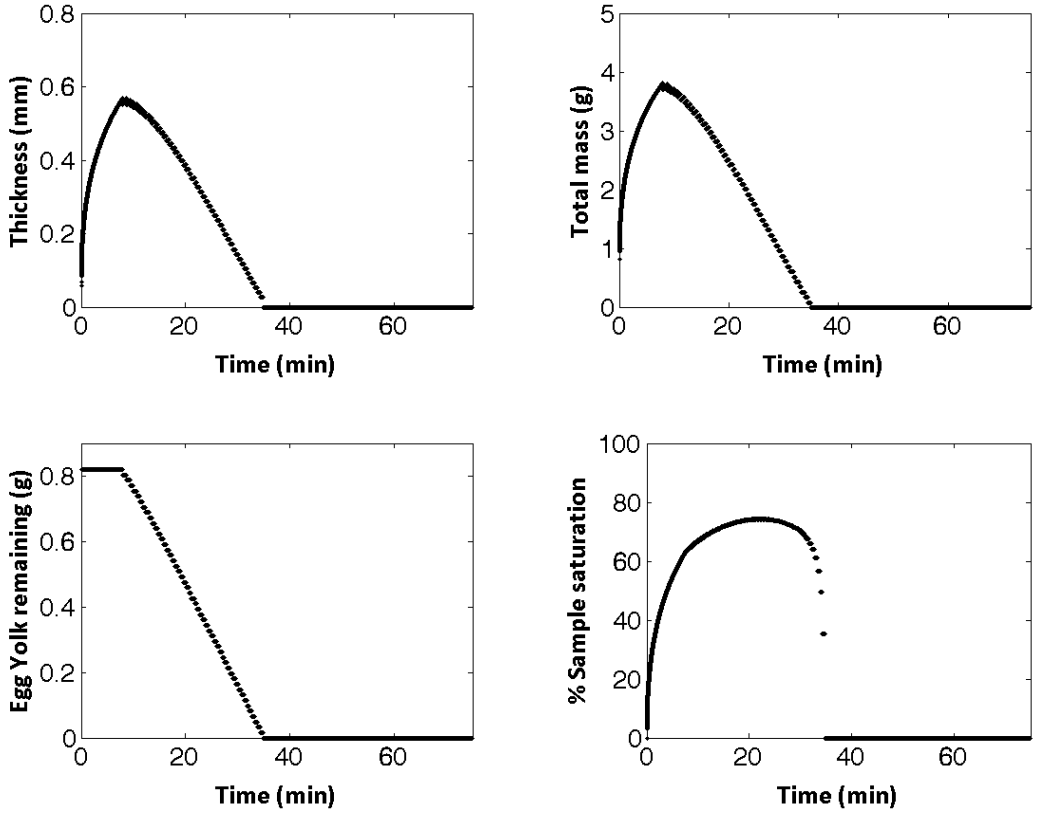

Figure 7.18. Simulation results for the experimental case at 55ºC, pH 11.5, 0.06 g/l of enzyme.

Simulations showed good agreement with real data in 4 of the 6 cases. The algorithm was able to make close predictions under circumstances where cleaning conditions in reality were relatively strong, that is, mid or high levels of enzymes, temperature and pH. The other two cases not showing an accurate prediction belonged to scenarios where the cleaning rates were the lowest ones observed. Main distortions to predictions were introduced by the soil dissolution removal rate (k_{ds}) term. As the frequency factor was established at 1.58%, the main mechanism for cleaning was soil dissolution. In order to get similar profiles between real and simulated data, soil dissolution rates should have been established in the range of -0.90 μm/min and -2.00 μm/min for the cases shown in **Figure 7.15** and **Figure 7.17** respectively. By looking at **Table 7.6** -which shows the data inputted for the lag time, soil dissolution and shear stress removal rate models- it can be seen that the slowest removal rate observed in the soil dissolution (k_{ds}) column was -3.90 μm/min. This corresponded to the experimental case at low temperature (30ºC), low pH (9.5) and low level of enzyme (0.02 g/l). Therefore, the statistical model built for the soil dissolution removal rate will never be able to predict such low removal rates within the levels studied.

Data suggest different enzyme deposition levels over the soil at low enzyme concentrations for the two experimental set-up considered. Main differences between them are summarised in **Table 7.7**. In full-scale and at low concentrations, the enzyme molecules could struggle to bind to the soil surface. The low availability of enzyme combined with the vertical placement of the tile plus a fast solution renewal means that less enzyme molecules are deposited and the hydrolysis of the sample is reduced. In sFDG tests, the horizontal placement of the soil immersed in the wash solution with a slow renewal of it offers advantages for this enzyme deposition. At higher concentrations, the higher number of enzyme molecules could compensate the disadvantages previously observed in full-scale and more molecules could bind the soil surface per unit time thus increasing the soil dissolution as observed. In the sFDG, the increase in the number of enzyme molecules could increase the soil dissolution rate as well, however, due to the poor solution renewal the transport of hydrolysed soil material to the bulk solution could be done much slower therefore reducing or making the previous divergences negligible.

Table 7.7. Main differences between sFDG and Full-Scale experimental set-ups.

	sFDG	FULL-SCALE
Position of the tile	Horizontal	Vertical
Tile completely sunk	Yes	No
Wash solution renewal	Slow	Fast

Apart from the discrepancies previously mentioned, the integrated model also misses the final decay stage of the cleaning process. This can be observed in **Figures 7.14** and **7.16**. The model replicates the real data with high accuracy until the SRI reaches 70% approximately. From this point on, the removal rate decreases for real data (indicating the decay stage of the cleaning process), while for simulated data the removal rate remains invariant.

Figure 7.19 illustrates a comparison between the real and estimated removal rates at the constant cleaning stage.

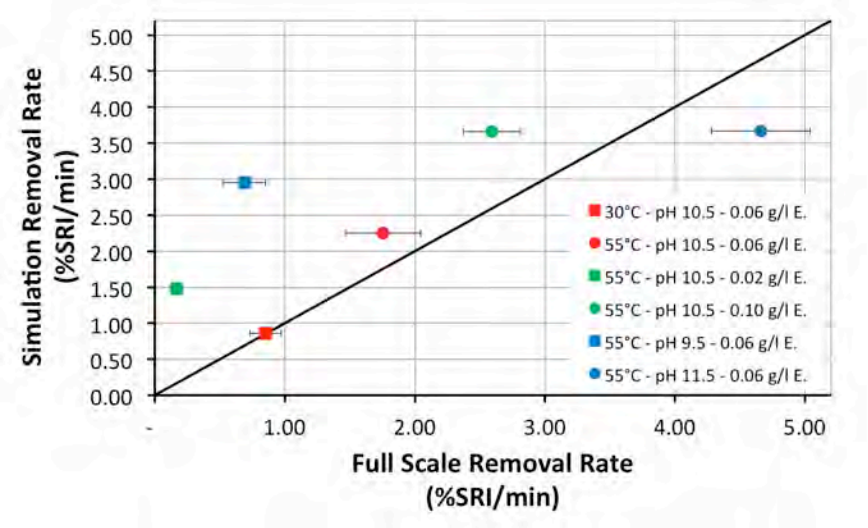

Figure 7.19. Comparison between simulated and full scale removal rates at the constant cleaning stage. Black line represents equal removal rates for both cases.

Overall, the integrated model over-predicts slightly the removal rate at the constant cleaning stage. This is particularly seen in the two cases already commented, represented by the green and blue squares.

In order to reduce the errors shown, it would be recommended to expand the initial test design to gather more information and balance the design. This would reduce the statistical errors shown, therefore increasing the accuracy of the predictions.

7.4. SUMMARY

The first part of this chapter shows the applicability of a waterproof camera used on the online measurement of cleaning inside ADWs. Images obtained were processed using the CIELAB colour space. To compare data from different experimental conditions, a homogeneous scale from 0 to 100 was used to describe cleaning. It indicates the Stain Removal Index (SRI), that is, the percentage of cleaning achieved at any time. The technique was proved successful despite the non-homogeneous distribution of light along the width of the sample. This effect was corrected by averaging L*a*b values of the area of study as cleaning occurred homogeneously on the tile.

Different cleaning experiments were carried out using egg yolk technical samples. The three different stages reported in literature were observed: (1) an initial lag phase, (2) a constant cleaning removal stage and (3) a final decay stage in which the cleaning rate reduces progressively. No colour change was observed during the initial lag phase. This phase relates to the swelling phenomenon as explained in *Chapter 6*. Cleaning during the constant cleaning rate stage occurred homogeneously across the soil area. This suggested a removal mechanism mainly driven by soil dissolution with little effect from the shear stress created by the direct impact of the water jets. The final decay stage was typically observed after SRI values were higher than 70%. The influence of temperature, pH and enzyme levels on cleaning was studied. Increasing cleaning rates were observed for higher levels of these factors. Triplicates for each experimental condition showed good reproducibility and sensitivity.

Two uncommon cleaning mechanisms were also reported. A cleaning moving front was observed in one occasion for the case of low level of enzyme. Higher protease concentration at the starting cleaning point was suggested as the trigger of the process. The second case, also observed once, showed higher cleaning on a specific area of the soil where the direct impact of

a jet occurred. The introduction of this novel technique aims to normalise the cleaning evaluation in full-scale ADW testing and to increase the information gathered.

The second part of this chapter presented the integration of the different modelling efforts made throughout this work. Simulated data were compared against full-scale profiles previously obtained through experimentation. Initially, water distribution patterns were estimated using the mathematical model from *Chapter 5*. Two jets were determined to directly impact the soil according to the set-up proposed. The frequency factor was established at 1.59%. Then, removal rate data from work shown in *Chapter 6, section 6.2.2* were used to build statistical models based on the response surface (RS) methodology. This allowed the estimation of lag times, shear stress and soil dissolution removal rates. This information was further inputted in the mathematical swelling-removal model developed in *Chapter 6, section 6.4* to finally obtain full-scale cleaning predictions.

Simulated results compared favourably with real data in 4 of the 6 scenarios proposed. Differences were observed in those cases showing the lowest removal rates. The divergences arose as a consequence of scaling-up the information obtained through the sFDG. The different set-ups and phenomena occurring between the two cleaning techniques (full-scale and sFDG) led to these deviations.

This integrated model represents the first modelling effort that combines the mechanical action from the ADW and the different removal mechanisms to predict cleaning profiles in full-scale testing.

CHAPTER 8

CONCLUSIONS

8.1. PROJECT CONCLUSIONS

8.1.1. Key findings

The analysis of a complex cleaning system such as an Automatic Dishwasher (ADW) has provided interesting and useful insights that have led to a better understanding of some of the on-going phenomena.

Water distributed via coherent jets.

Particularly, the study of the water distribution patterns by using Positron Emission Particle Tracking (PEPT) technique proved the initial distribution of water via straight water jets. From a specific location, a jet shows a defined trajectory that can be easily calculated by applying trigonometric principles.

Little and localized areas of direct impingement. Low shear areas are predominant in consequence.

As the number of jets is typically low in current ADW appliances (no more than 10-12 nozzles per spray arm), the area of direct impingement is very small and very localised. Data from PEPT also demonstrated the low energy profile occurring during the downfall stage of the water by showing a homogeneous low velocity pattern across the radial distance. Thus, most of the wetting of the soils occurs at low shear stress (i.e. falling films with shear stresses between 0 Pa to 2 Pa). Despite the efforts from manufactures to increase the mechanical action (shear stresses between 5 Pa to 50 Pa), most common appliances lack an optimum design to properly distribute water. The room for improvement and future innovations therefore exists.

Importance of frequency factor.

The mathematical model developed with the insights provided by PEPT experimentation also introduced another important element for the analysis: the frequency factor. The frequency factor stands for the time a specific crockery item (i.e. plate) is being hit directly by an impingement jet. This definition was adapted for the sFDG tests as the ratio of time the gauging fluid is imposing a shear stress action over a particular location of the soil analysed. The simulations undertaken with the mathematical model for ADWs suggested that this frequency

factor was very low (less than 10% in most cases) and a direct impact of an impingement jet occurs for a very limited time period.

Introduction of dimensionless parameters to cross compare ADWs performance.

New dimensionless parameters were also introduced to facilitate the comparison between different appliances and to standardise the results obtained (range from 0 to 1). The coverage was assessed by the effective impact length (δ) coefficient and the frequency factor by the effective impact time (τ_{vis}). A global factor measured the overall efficiency (α). The two main design factors highlighted as important for the water distribution were the nozzle-plate relative position (how centred the nozzle is with respect of the crockery element) and the nozzle's rho angle value (vertical projection of the jet). The study also showed a problem of symmetry in the design of current commercial dishwashers: while the ejection of water is produced in a circular movement, the distribution of the items follows a rectangular pattern. This automatically produces that low radial locations are impacted for longer.

Swelling affected by pH and temperature; Removal by temperature, enzyme level and frequency factor; Net shear stress negligible as a factor.

Technical egg yolk stains were selected as a typical hard-to-remove soil in auto-dishwashing. The study of swelling and removal phenomena in these soils highlighted the importance of pH at the beginning. The increase of pH led to an increase of the degree of swelling observed. No removal action was observed unless the enzyme was present, except for the case of high alkalinity (pH 11.5) and high temperature (55ºC) where top layers were partially detached when an external shear stress was applied. Enzyme level and the frequency factor were estimated as the two main factors leading to removal. Interestingly though, net shear stress applied over the soil was statistically disregarded as a significant factor. Results suggested the existence of a shear stress threshold among the levels studied (12 to 65 Pa) below which no cleaning occurs. Once that threshold value is surpassed, the removal of soil material takes place but the rate of removal increases slowly with the increase of the shear stress applied. Temperature also was highlighted as a significant factor over the whole process. It aided both the initial swelling

phenomenon and the subsequent removal process. Overall, the cleaning process was faster with the increase of temperature.

Development of a mathematical model with the novelty of the introduction of 'theoretical layers'.

A new mathematical swelling-removal model was also introduced. It presented as a novelty the concept of 'theoretical layers'. They represent the number of layers in which the soil is divided. The model illustrates cleaning in a simple equation that summarises the different phenomena occurring: swelling and removal via direct application of shear stress or via soil dissolution. Experiments performed using the sFDG were able to separate and characterise each of these mechanisms. Swelling was modelled by using the non-linear poroelasticity theory approach, which showed good accuracy in the fitting of the data. The Partial Differential Equation (PDE) describing swelling allowed the use of the theoretical layers concept. To model cleaning, the algorithm removed one by one each of the theoretical layers considered anytime the integrated removal rate was higher than the thickness of one or more of the top layers of the soil. The integration over time of two opposite phenomena, swelling (increase of thickness) and removal (decrease of thickness) was successful and described in detail the phenomena observed. The model is also able to provide complementary information apart from a thickness profile: cleaning percentage, soil remaining, total mass or the saturation (understood as percentage of maximum swelling) of the soil over time.

Design of an online cleaning evaluation system in ADWs

The need of a better understanding of cleaning phenomena in current full-scale testing was solved with the introduction of a waterproof camera to be used inside an ADW. The different tests performed showed good sensitivity of the camera and reproducibility of the results. More importantly, it introduced 'time' as a factor in the measurement of cleaning performance for different formulations, as nowadays this is evaluated only by comparing the end result.

First full scale model in ADW.

To close up the work undertaken during this project, full-scale simulations were performed by integrating the mathematical model describing the distribution of water together with the

swelling and removal information from tests done with the sFDG. Statistical models were built to estimate lag times, shear stress and soil dissolution removal rates for a range of experimental conditions. The information initially generated with these smaller models was inputted to the mathematical swelling-removal model to simulate full-scale results. Good agreement was observed between real and simulated data in most cases (removal rates over 1.00 %SRI/min). Poor agreement was observed for the cases showing low removal rates in full-scale tests (less than 0.75 %SRI/min), where the integrated model overestimated the cleaning rate.

8.1.2. Application on product development

As an industrially sponsored project, the aim of a company such as Procter & Gamble was to create value to their products with the information provided through this research. The deeper understanding on the mechanical action provided by the appliance has sparked the thoughts on the integration of chemical and physical forces in the search of an optimum performance. The analysis of the different effects of each of the main formulation ingredients over time has led to the idea of providing optimum amounts of chemistry at specific times of the wash cycle. This can potentially lead to benefits to the company (i.e. cost savings as no chemistry will be lost or misused at the different stages of the wash cycles) or to the consumer (i.e. by reducing cycle lengths and/or by buying products at a cheaper cost).

The use of dynamic models is also a tool with high potential in the understanding and the analysis of the performance of different formulations. The inclusion of time as a factor multiplies the information gathered and allows better and faster decisions to be made. By evaluating not only the end cleaning point of an specific formulation, but also the evolution of the soil over time, it is possible to know where the formulation performs at its best (i.e. reduced lag times, faster constant cleaning stage, etcetera… for the case of protein-based soils). This information could be also used for consumer claims and to establish competitive advantages. In this scenario, the use and introduction of new tools, such as the scanning fluid dynamic gauge or the waterproof camera, represents a clear benefit for these purposes. These new tools also represent a cost saving opportunity in experimentation, as less information/testing is required to make the right decision.

Finally, the identification of the different mechanisms involved in the cleaning of different soils is important in order to determine new ways to evaluate the performance of individual ingredients. For example, different enzymes can be tested by comparing the soil dissolution rates observed at different experimental conditions using the sFDG.

8.2. LOOKING FORWARD

8.2.1. Studies on different soil samples.

This research focused on technical egg yolk stains as a representative hard-to-remove soil within automatic dishwashing. However, there are also other challenging soils that can be commonly found. Typically, they do not follow the same cleaning pattern observed for protein-based soils and therefore, their way to study how the get cleaned might vary slightly.

Particularly, another soil of interest nowadays are the commonly known as 'burnt-on/ baked-on'. These stains are formed, as seen in *Chapter 2*, by strongly adhere layers formed on the oxidative polymerisation of unsaturated components. They typically show an adhesive failure when cleaned, that is, they are completely detached from the surface. The techniques showed throughout this work could also be applied to study their cleaning mechanisms. Thus, for example, and due to the different behaviour when cleaned, sFDG might not be suitable to study the thickness evolution of the system but the moment at which the 'baked-on' layer detaches at different chemical conditions and mechanical stresses. Although the information provided might be less, the technique could still determine the limiting criteria required to clean these soils. Statistical models could be built based on the different treatments that the samples might have received (i.e. baking temperatures and times, layer thickness, composition…) and the conditions at which the cleaning process will take place (i.e. chemistry, temperature, shear stress and frequency). With this information it would be possible to determine the main factors affecting the cleaning process, the interactions between them and the existence or not of some limiting criteria for cleaning to occur. Full-scale studies could also be performed by using the waterproof camera. The real visualisation of the cleaning process could help the understanding of the mechanisms leading to cleaning and the establishment of similarities or differences observed between small-scale and full-scale techniques.

Finally, the use of the waterproof camera could help the understanding of different issues also observed in automatic dishwashing and not related to cleaning. Another common problem of interest is the formation of spots or films after the cleaning sequence, which creates the feeling of dirtiness or incomplete removal. By using this camera it could be possible to observe this phenomenon during the final drying stage and identify which are the factors leading to this.

8.2.2. Improvements on existing models.

All different models presented throughout this work can be expanded or upgraded by incorporating other elements to make them more accurate or flexible. Overall, and due to the complexity of some of the models built, it is highly recommended the development of user interfaces to allow non-familiarised people to perform their estimations easily.

It is also recommended to quantify in more detail the agreement between the CFD model developed by the appliance manufacturer and PEPT data generated experimentally. A further analysis should give numbers in terms of the percentage of correlation by looking into different unitary phenomena (i.e. ejections through an specific nozzle) and also via the realisation of simpler individual tests that can be performed externally (i.e. trajectories of jets at different pump speeds). The idea would be to characterise the system through smaller subsystems and validate them individually.

The mathematical model describing the water distribution inside an ADW can be improved by adding the following:

- Analysis of water distribution on crockery items loaded at a certain angle (not only vertically).
- Incorporation of different geometries, such as cylinders or rounded areas to mimic glasses, bowls or other common elements.
- Determination of shear stress profiles generated by direct impingement of jets.

With regard to the different removal mechanisms models (shear stress and soil dissolution), next steps to improve their quality should be:

- Incorporation of enzyme kinetics (as commented in *Chapter 6, section 6.4.3.3.*) to expand the theoretical background and make the soil dissolution model rely less on empirical data.
- Perform extra experiments to augment the initial design in order to make it balanced and to reduce the error in the estimations.

Finally, the integrated mathematical swelling-removal model used to estimate full-scale cleaning profiles should incorporate the following features:

- Profiles over time of the cleaning factors used as inputs. This feature is essential to mimic temperature, pH or enzyme level changes during a typical wash cycle (as seen in *Chapter 2, section 2.1*). As the integration occurs in small time steps, removal rates can be estimated at any time as a function of the specific temperature, pH, enzyme level or other factor at that particular time.
- Reduce computational times by using an optimised programming code.

8.2.3. Energy requirements on cleaning

The final aim of any research focused on cleaning must be the understanding of the energy needed to remove any soil attached to any surface and at any condition. In order to take a step forward, the elaboration of a dynamic cleaning scale based on this energy requirement is of particular interest. Throughout this work it has been shown, for example, how the use of a higher level of enzyme reduces the total cleaning time by increasing the rate of removal, or how this effect is also produced by increasing the frequency factor. In a basic level, this means that the amount of energy inputted to the system per unit time is higher and therefore removal occurs faster. This energy requirement is also related to the status of the soil. At a dry state, higher energy is required to fully remove any protein-based soil. However, if the sample is partially hydrated this energy requirement is lower. Swelling and hydration phenomena are produced by a chemical potential gradient established between the liquid and the soil. As a consequence, the hydration process implies an energy input into the system. Baking the sample produces the opposite effect. It increases the strength of the soil-to-soil bonds due to secondary reactions (e.g. Maillard reaction) and of the soil-to-substrate bonds and, therefore, more energy

is required to fully remove the soil material. **Figure 8.1** represents a schematic of the concept here commented.

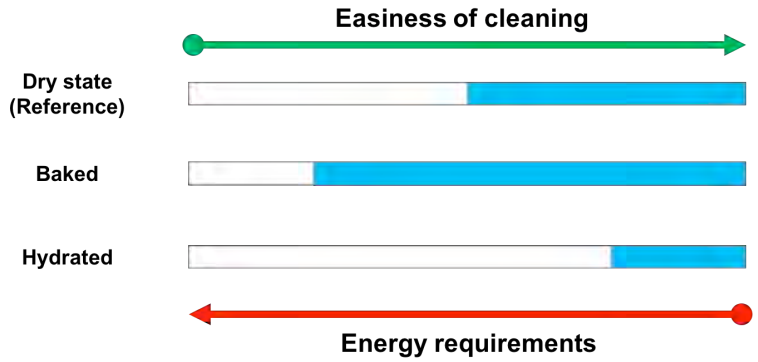

Figure 8.1. Schematic of the energy requirements in cleaning process.

During the past decade, some analytical instruments have been developed to analyse the energy required to remove a soil from a surface. This is the case of micromanipulation (Liu *et al*., 2006a, 2006b, 2006c, 2005, 2002) and more recently millimanipulation (Ali *et al*., 2015). A t-shaped blade is used to sweep soil samples at different conditions and at different thicknesses while constantly measuring the force applied. By integrating the curve obtained, total energy required is calculated. The information obtained is related to the cohesive and adhesive strength of the soils sample analysed. These techniques represent a powerful source of information that can be used to map different factor effects on cleaning (i.e. temperature, pH, enzyme level, surfactant level…). By establishing an adequate approach, it is possible to start building models to predict the energy requirements needed to remove any soil from any surface at any condition and then correlate the results with bigger scale experiments.

8.2.4. The dishwasher as a unit operation

In chemical engineering or other related fields, a unit operation is defined as one basic step (in a major transformative process) that is always based on the same scientific principles and that always share a similar final objective (McCabe *et al*., 1993). Considering the life cycle of any food material, cleaning of any residue left over a substrate can be considered as a unit operation itself. Particularly in ADW, the process involves the use of an automated and

independent machine that always based its performance on the same physical and chemical principles.

This research has shown the broad knowledge of the chemical engineering profession and the direct applicability of chemical engineering concepts in a non-common studied field. Throughout this work, mathematical, physical and chemical approaches have been followed to explain the fundamentals of the removal of protein-based soils in a specific environment. However, the principles applied here as well as the models developed can be used in other similar areas (i.e. pipe cleaning). This agrees with the unit operation concept, where the systematic study of a particular operation can cross industries.

8.3. CLOSING THOUGHTS

This research work has met the original objectives established *(Chapter 1, section 1.2)*:

1. Water motion has been characterised via PEPT. The study showed the water patterns followed in a typical sequence and how the water is ejected through the various nozzles in a spray arm.
2. The information provided in the initial PEPT experiments was further used to develop a mathematical model that showed the constraints in current ADW design. This model is also a tool really useful to predict water distribution patterns quickly.
3. New and existing techniques were fully developed for the analysis of cleaning of protein-based soils. sFDG and a camera kit were used to gather data and understanding the mechanisms underlying in the swelling and removal process occurring in technical egg yolk soils.
4. New theoretical and statistical models have been built to predict cleaning. The insights gathered have allowed to establish the limiting factors at each time of the cleaning sequence and to spark the thoughts on a more efficient cleaning approach.

It is desired that all the information provided in this dissertation aids the development of more efficient and sustainable automatic dishwashing units and detergents. Ideally, new appliances designs should focus on distributing the water more efficiently, paying attention into a more

homogeneous and more frequent water action onto the different items loaded. It is therefore encouraged to investigate new spray water systems aiming to fill the gap currently existing. New designs however should preserve an easy way to load and unload the dishes. From the detergent perspective, efforts should be put into a more intelligent use of the different ingredients, making them only to act at the specific moment where they are required. This could lead into savings for both consumers and detergents manufactures as an optimal and more efficient use of chemistry is achieved.

BIBLIOGRAPHY

Aehle, W., 2007. Enzymes in Industry: Production and Applications, Third Ed. ed. Wiley-VCH Verlag GmbH & Co. KGaA, Weinheim, Germany. doi:10.1002/9783527617098

AHAM, 1992. AHAM DW-1: Household Electric Dishwashers by Association of Home Appliance Manufacturers. United States of America.

Alexander, L.A., 1865. Machine for washing dishes. US 51000.

Alfrey, T., Gurnee, E.F., Lloyd, W.G., 1966. Diffusion in glassy polymers. J. Polym. Sci. Part C 12, 249–261. doi:10.1002/polc.5070120119

Ali, A., de'Ath, D., Gibson, D., Parkin, J., Alam, Z., Ward, G., Wilson, D.I., 2015. Development of a "millimanipulation" device to study the removal of soft solid fouling layers from solid substrates and its application to cooked lard deposits. Food Bioprod. Process. 93, 256–268. doi:10.1016/j.fbp.2014.09.001

Arnoldi, A., 2001. Thermal processing and food quality: analysis and control, in: Richardson, P. (Ed.), Thermal Technologies in Food Processing. Woodhead Publishing. doi:10.1533/9781855736610.2.138

Asteasu, C., Astiazaran, J., Besga, J., 1993. A dishwasher design system: An application of tailor-made CAD systems versus commercial systems. Comput. Graph. 16, 395–399. doi:10.1016/0097-8493(92)90026-R

Bakalis, S., Fryer, P.J., Parker, D.J., 2004. Measuring velocity distributions of viscous fluids using positron emission particle tracking (PEPT). AIChE J. 50, 1606–1613. doi:10.1002/aic.10153

Bakalis, S., Kyritsi, A., Karathanos, V.T., Yanniotis, S., 2009. Modeling of rice hydration using finite elements. J. Food Eng. 94, 321–325. doi:10.1016/j.jfoodeng.2009.03.023

Barigou, M., 2004. Particle Tracking in opaque mixing systems: An overview of the capabilities of PEP and PEPT. Chem. Eng. Res. Des. 82, 1258–1267. doi:10.1205/cerd.82.9.1258.44160

BBC, 2005. Homes in the UK [WWW Document]. URL http://news.bbc.co.uk/1/shared/spl/hi/guides/456900/456991/html/default.stm

Bbosa, L.S., Govender, I., Mainza, A.N., Powell, M.S., 2011. Power draw estimations in experimental tumbling mills using PEPT. Miner. Eng. 24, 319–324. doi:10.1016/j.mineng.2010.10.005

Bello, M., Tolaba, M.P., Aguerre, R.J., Suarez, C., 2010. Modeling water uptake in a cereal grain during soaking. J. Food Eng. 97, 95–100. doi:10.1016/j.jfoodeng.2009.09.020

Berkholz, P., Stamminger, R., Wnuk, G., Owens, J., Bernarde, S., 2010. Manual dishwashing habits: an empirical analysis of UK consumers. Int. J. Consum. Stud. 34, 235–242. doi:10.1111/j.1470-6431.2009.00840.x

Bezerra, M.A., Santelli, R.E., Oliveira, E.P., Villar, L.S., Escaleira, L. a., 2008. Response surface methodology (RSM) as a tool for optimization in analytical chemistry. Talanta 76, 965–977. doi:10.1016/j.talanta.2008.05.019

Biot, M.A., 1941. General theory of three dimensional consolidation. J. Appl. Phys. 12, 155–164.

Bird, M.R., Fryer, P.J., 1991. An experimental study of the cleaning of surfaces fouled by whey proteins. Food Bioprod. Process. Trans. Inst. Chem. Eng. Part C 69, 13–21.

Bird, R.B., Stewart, W.E., Lightfoot, E.N., 2007. Transport phenomena, John Wiley & Sons.

Booth, D.T., 2003. Composition and energy density of eggs from two species of freshwater turtle with twofold ranges in egg size. Comp. Biochem. Physiol. A. Mol. Integr. Physiol. 134, 129–37. doi:10.1016/S1095-6433(02)00216-7

Bouklas, N., Huang, R., 2012. Swelling kinetics of polymer gels: comparison of linear and nonlinear theories. Soft Matter 8, 8194. doi:10.1039/c2sm25467k

Briffaz, A., Bohuon, P., Méot, J.M., Dornier, M., Mestres, C., 2014. Modelling of water transport and swelling associated with starch gelatinization during rice cooking. J. Food Eng. 121, 143–151. doi:10.1016/j.jfoodeng.2013.06.013

Broze, G., 1999. Handbook of Detergents: Properties, Surfactant Science. Taylor & Francis.

Carnali, J.O., Zhou, Y., 1997. Role of Hydration via Alkaline Wash Liquor in the Removal of Starchy Soil during Machine Dishwashing. Ind. Eng. Chem. Res. 36, 667–674. doi:10.1021/ie960420q

Chapwanya, M., Misra, N.N., 2015. A soft condensed matter approach towards mathematical modelling of mass transport and swelling in food grains. J. Food Eng. 145, 37–44. doi:10.1016/j.jfoodeng.2014.08.010

Chen, G., Campanella, O.H., Purkayastha, S., 2007. A dynamic model of crosslinked corn starch granules swelling during thermal processing. J. Food Eng. 81, 500–507. doi:10.1016/j.jfoodeng.2006.12.001

Chew, J.Y.M., Paterson, W.R., Wilson, D.I., Höufling, V., Augustin, W., 2005. A Method for Measuring the Strength of Scale Deposits on Heat Transfer Surfaces. Dev. Chem. Eng. Miner. Process. 13, 21–30. doi:10.1002/apj.5500130103

Chiti, F., Bakalis, S., Bujalski, W., Barigou, M., Eaglesham, A., Nienow, A.W., 2011. Using positron emission particle tracking (PEPT) to study the turbulent flow in a baffled vessel agitated by a Rushton turbine: Improving data treatment and validation. Chem. Eng. Res. Des. 89, 1947–1960. doi:10.1016/j.cherd.2011.01.015

CIE, 2014. International Commission on Illumunation [WWW Document]. URL http://www.cie.co.at/

D'Ambrosio, B., 2011. From Football to Fig Newtons: 76 American Inventors and The Inventions You Know By Heart.

Daintith, J., Martin, E., 2010. Dictionary of Science (6th Edition), Oxford University Press. Oxford University Press.

Davey, M.J., Landman, K.A., McGuinness, M.J., Jin, H.N., 2002. Mathematical modeling of rice cooking and dissolution in beer production. AIChE J. 48, 1811–1826. doi:10.1002/aic.690480821

De Paepe, M., Theuns, E., Lenaers, S., Van Loon, J., 2003. Heat recovery system for dishwashers. Appl. Therm. Eng. 23, 743–756. doi:10.1016/s1359-4311(03)00016-4

Denmat, M., Anton, M., Gandemer, G., 1999. Protein Denaturation and Emulsifying Properties of Plasma and Granules of Egg Yolk as Related to Heat Treatment. J. Food Sci. 64, 194–197. doi:10.1111/j.1365-2621.1999.tb15863.x

Ding, Y.L., Forster, R., Seville, J.P.K., Parker, D.J., 2002. Segregation of granular flow in the transverse plane of a rolling mode rotating drum. Int. J. Multiph. Flow 28, 635–663. doi:10.1016/S0301-9322(01)00081-7

Dixon, G., 2009. Dishwasher Manual, 4th Editio. ed. Haynes Publishing.

DuPont, 2012. US consumer dishwashing study [WWW Document]. URL http://fhc.biosciences.dupont.com/consumer-trends/consumer-studies/us-consumer-dishwashing-study/ (accessed 12.5.14).

Dürr, H., Graßhoff, A., 1999. Milk Heat Exchanger Cleaning: Modelling Of Deposit Removal. Food Bioprod. Process. 77, 114–118. doi:10.1205/096030899532402

Dürr, H., 2002. Milk Heat Exchanger Cleaning: Modelling of Deposit Removal II. Food Bioprod. Process. 80, 253–259. doi:10.1205/096030802321154745

Eriksson, L., Johansson, E., Kettaneh-Wold, N., Trygg, J., Wikström, C., Wold, S., 2006. Multi- and Megavariate Data Analysis, Part 1, Basic Principles and Applications. Umetrics AB.Title. Umetrics AB.

Europan Committee for Electrotechnical Standardization, 2012. EN 50242. Electric dishwashers for household use - Methods for measuring the performance.

Flory, P.J., Rehner Jr., J., 1943. Statistical mechanics of cross-linked polymer networks II. Swelling. J. Chem. Phys. 11, 521–526.

Frigidaire, 2014. The Frigidaire Gallery® Dishwasher [WWW Document]. URL http://www.frigidaire.com/Kitchen-Appliances/Dishwashers/

Fryer, P.J., Christian, G.K., Liu, W., 2006. How hygiene happens: physics and chemistry of cleaning. Soc. Dairy Technol. 59, 76–84. doi:10.1111/j.1471-0307.2006.00249.x

Fryer, P.J., K.Asteriadou, 2009. A prototype cleaning map: A classification of industrial cleaning processes. Trends Food Sci. Technol. 20 (2009), 255–262. doi:10.1016/j.tifs.2009.03.005

Fuchs, R.J., 1981. Formulation of household automatic dishwasher detergents. J. Am. Oil Chem. Soc. 58, 366A–370A. doi:10.1007/BF02541583

Fukuoka, M., Watanabe, H., Mihori, T., Shimada, S., 1994. Moisture diffusion in a dry soybean seed measured using pulsed-field-gradient NMR. J. Food Eng. 23, 533–541. doi:10.1016/0260-8774(94)90110-4

Ganji, F., 2010. Theoretical Description of Hydrogel Swelling: A Review. Iran. Polym. … 19, 375–398.

Geladi, P., Kowalski, B., 1986. Partial least-squares regression: a tutorial. Anal. Chim. Acta.

Gibbs, J.W., 1906. The Scientific Papers of Willian Gibbs [WWW Document]. URL http://books.google.com/books?id=-neYVEbAm4oC&oe=UTF-8 (accessed 12.9.13).

Goode, K.R., Asteriadou, K., Fryer, P.J., Picksley, M., Robbins, P.T., 2010. Characterising the cleaning mechanisms of yeast and the implications for Cleaning in Place (CIP). Food Bioprod. Process. 88, 365–374. doi:10.1016/j.fbp.2010.08.005

Gordon, P.W., Brooker, A.D.M., Chew, Y.M.J., Wilson, D.I., York, D.W., 2010. Studies into the swelling of gelatine films using a scanning fluid dynamic gauge. Food Bioprod. Process. 88, 357–364. doi:10.1016/j.fbp.2010.08.012

Gordon, P.W., 2012a. Development of a Scanning Fluid Dynamic Gauge for Cleaning Studies. Thesis. University of Cambridge.

Gordon, P.W., Brooker, A.D.M., Chew, Y.M.J., Letzelter, N., York, D.W., Wilson, D.I., 2012b. Elucidating enzyme-based cleaning of protein soils (gelatine and egg yolk) using a scanning fluid dynamic gauge. Chem. Eng. Res. Des. 90, 162–171. doi:10.1016/j.cherd.2011.07.007

Hong, W., Zhao, X., Zhou, J., Suo, Z., 2008. A theory of coupled diffusion and large deformation in polymeric gels. J. Mech. Phys. Solids 56, 1779–1793. doi:10.1016/j.jmps.2007.11.010

Hong, W., Liu, Z., Suo, Z., 2009. Inhomogeneous swelling of a gel in equilibrium with a solvent and mechanical load. Int. J. Solids Struct. 46, 3282–3289. doi:10.1016/j.ijsolstr.2009.04.022

Hong, W., Zhao, X., Suo, Z., 2010. Large deformation and electrochemistry of polyelectrolyte gels. J. Mech. Phys. Solids 58, 558–577. doi:10.1016/j.jmps.2010.01.005

Howard, L.W., 1924. Improvements in apparatus for washing household crockery and the like. FRD579765 19240403.

IFIS, 2009. Dictionary of Food Science and Technology (2nd Edition), International Food Information Service (IFIS Publishing).

Ingram, A., Seville, J.P.K., Parker, D.J., Fan, X., Forster, R.G., 2005. Axial and radial dispersion in rolling mode rotating drums. Powder Technol. 158, 76–91. doi:10.1016/j.powtec.2005.04.030

Jensen, B.B.B., 2011. Tank cleaning technology : Innovative application to improve clean-in-place (CIP).

Jin, L., Li, D., 2007. A switching vector median filter based on the CIELAB color space for color image restoration. Signal Processing 87, 1345–1354. doi:10.1016/j.sigpro.2006.11.008

Kruif, C.G.K. De, Anema, S.G., Zhu, C., Havea, P., Coker, C., 2015. Food Hydrocolloids Water holding capacity and swelling of casein hydrogels. Food Hydrocoll. 44, 372–379. doi:10.1016/j.foodhyd.2014.10.007

Kuhn, C.R., Soares, G.J.D., Kuhn, P.S., 2006. Electrostatic contribution to polymer gels. Colloids Surfaces A Physicochem. Eng. Asp. 281, 184–189. doi:10.1016/j.colsurfa.2006.02.037

Labuza, T.., Hyman, C.., 1998. Moisture migration and control in multi-domain foods. Trends Food Sci. Technol. 9, 47–55. doi:10.1016/S0924-2244(98)00005-3

Liu, X., Lienhard, J.H., 1993. The hydraulic jump in circular jet impingement and in other thin liquid films. Exp. Fluids 116, 108–116. doi:10.1007/BF00190950

Liu, W., Christian, G.K., Zhang, Z., Fryer, P.J., 2002. Development and use of a micromanipulation technique for measuring the force required to disrupt and remove fouling deposits. Inst. Chem. Eng. 80 Part C.

Liu, W., Aziz, N., Zhang, Z., Fryer, P., 2005. Quantification of the cleaning of egg albumin deposits using micromanipulation and direct observation techniques. J. Food Eng. 78, 217–224. doi:10.1016/j.jfoodeng.2005.09.019

Liu, W., Christian, G.K., Zhang, Z., Fryer, P.J., 2006a. Direct measurement of the force required to disrupt and remove fouling deposits of whey protein concentrate. Int. Dairy J. 16, 164–172. doi:10.1016/j.idairyj.2005.02.008

Liu, W., Fryer, P.J., Zhang, Z., Zhao, Q., Liu, Y., 2006b. Identification of cohesive and adhesive effects in the cleaning of food fouling deposits. Innov. Food Sci. Emerg. Technol. 7, 263–269. doi:10.1016/j.ifset.2006.02.006

Liu, W., Zhang, Z., Fryer, P., 2006c. Identification and modelling of different removal modes in the cleaning of a model food deposit. Chem. Eng. Sci. 61, 7528–7534. doi:10.1016/j.ces.2006.08.045

Mac Namara, C., Gabriele, a., Amador, C., Bakalis, S., 2012. Dynamics of textile motion in a front-loading domestic washing machine. Chem. Eng. Sci. 75, 14–27. doi:10.1016/j.ces.2012.03.009

Malumba, P., Jacquet, N., Delimme, G., Lefebvre, F., Béra, F., 2013. The swelling behaviour of wheat starch granules during isothermal and non-isothermal treatments. J. Food Eng. 114, 199–206. doi:10.1016/j.jfoodeng.2012.08.010

Martin, R.B., 1998. Free energies and equilibria of peptide bond hydrolysis and formation. Biopolymers 45, 351–353. doi:10.1002/(SICI)1097-0282(19980415)45:5<351::AID-BIP3>3.0.CO;2-K

McCabe, W.L., Smith, J.C., Harriott, P., 1993. Unit operations of chemical engineering., 5th ed, Chemical Engineering Science. doi:10.1016/0009-2509(57)85034-9

McKeen, L.W., 2015. Introduction to Creep, Polymers, Plastics and Elastomers, in: The Effect of Creep and Other Time Related Factors on Plastics and Elastomers. Elsevier Inc. doi:10.1016/B978-0-323-35313-7.00001-8

Mehrer, H., 2007. Diffusion in Solids: Fundamentals, Methods, Materials, Diffusion-Controlled Processes, Springer Series in Solid-State Sciences. Springer.

Mercadé-Prieto, R., Falconer, R.J., Paterson, W.R., Wilson, D.I., 2006. Probing The Mechanisms Limiting Dissolution of Whey Protein Gels During Cleaning. Food Bioprod. Process. 84, 311–319. doi:10.1205/fbp06021

Mercadé-Prieto, R., Falconer, R.J., Paterson, W.R., Wilson, D.I., 2007a. Swelling and dissolution of beta-lactoglobulin gels in alkali. Biomacromolecules 8, 469–76. doi:10.1021/bm060553n

Mercadé-Prieto, R., Paterson, W.R., Wilson, D.I., 2007b. The pH threshold in the dissolution of beta-lactoglobulin gels and aggregates in alkali. Biomacromolecules 8, 1162–70. doi:10.1021/bm061100l

Mercadé-Prieto, R., Paterson, W.R., Dong Chen, X., Ian Wilson, D., 2008. Diffusion of NaOH into a protein gel. Chem. Eng. Sci. 63, 2763–2772. doi:10.1016/j.ces.2008.02.029

Mercadé-Prieto, R., Paterson, W.R., Wilson, D.I., 2009. Effect of salts on the alkaline degradation of β-lactoglobulin gels and aggregates: Existence of a dissolution threshold. Food Hydrocoll. 23, 1587–1595. doi:10.1016/j.foodhyd.2008.11.007

Mercadé-Prieto, R., Sahoo, P.K., Falconer, R.J., Paterson, W.R., Ian Wilson, D., 2007c. Polyelectrolyte screening effects on the dissolution of whey protein gels at high pH conditions. Food Hydrocoll. 21, 1275–1284. doi:10.1016/j.foodhyd.2006.09.015

Métais, A., Mariette, F., 2003. Determination of water self-diffusion coefficient in complex food products by low field 1H PFG-NMR: comparison between the standard spin-echo sequence and the T1-weighted spin-echo sequence. J. Magn. Reson. 165, 265–275. doi:10.1016/j.jmr.2003.09.001

Mezzenga, R., Schurtenberger, P., Burbidge, A., Michel, M., 2005. Understanding foods as soft materials. Nat. Mater. 4, 729–740. doi:10.1038/nmat1496

Miele, 2011. Operating instructions for dishwashers.

Mine, Y., Zhang, H., 2013. Biochemistry of Foods, Third Ed. ed, Biochemistry of Foods. Elsevier. doi:10.1016/B978-0-08-091809-9.00005-4

Mintel, 2011. Dishwashing Detergents - UK.

Mitchell, S.L., O'Brien, S.B.G., 2012. Asymptotic, numerical and approximate techniques for a free boundary problem arising in the diffusion of glassy polymers, in: Applied Mathematics and Computation. pp. 376–388. doi:10.1016/j.amc.2012.06.026

Morison, K., Thorpe, R., 2002. Liquid distribution from cleaning-in-place sprayballs. Food Bioprod. Process. 80, 2–7.

Neiditch, O.W., Mills, K.L., Gladstone, G., Brothers, L., 1980. Technical The Stain Removal Index (SRI): A New Reflectometer Method for Measuring and Reporting Stain Removal Effectiveness. J. Am. Oil Chem. Soc. 57, 426–429. doi:10.1007/BF02678931

Olsen, H.S., Falholt, P., 1998. The role of enzymes in modern detergency. J. Surfactants Deterg. 1, 555–567. doi:10.1007/s11743-998-0058-7

Oztop, M.H., McCarthy, K.L., 2011. Mathematical modeling of swelling in high moisture whey protein gels. J. Food Eng. 106, 53–59. doi:10.1016/j.jfoodeng.2011.04.007

Parker, D.J., Broadbent, C.J., Fowles, P., Hawkesworth, M.R., McNeil, P., 1993. Positron emission particle tracking - a technique for studying flow within engineering equipment. Nucl. Instruments Methods Phys. Res. Sect. A Accel. Spectrometers, Detect. Assoc. Equip. 326, 592–607. doi:10.1016/0168-9002(93)90864-E

Parker, D.J., Dijkstra, a. E., Martin, T.W., Seville, J.P.K., 1997. Positron emission particle tracking studies of spherical particle motion in rotating drums. Chem. Eng. Sci. 52, 2011–2022. doi:10.1016/S0009-2509(97)00030-4

Parker, D.J., Fan, X., 2008. Positron emission particle tracking—Application and labelling techniques. Particuology 6, 16–23. doi:10.1016/j.cpart.2007.10.004

Peppas, N.A., Brannon-Peppas, L., 1994. Water diffusion and sorption in amorphous macromolecular systems and foods. J. Food Eng. 22, 189–210. doi:10.1016/0260-8774(94)90030-2

Peppas, N.A., Sinclair, J.L., 1983. Anomalous Transport of Penetrants in Glassy Polymers. Colloid Polym. Sci. 261, 404–409.

Petsko, G.A., Ringe, D., 2004. Protein Structure and Function. New Science Press.

Phillips, G.O., Williams, P.A., 2011. Handbook of Food Proteins, Woodhead Publishing. Woodhead Publishing.

Procter&Gamble, 2014. Cascade [WWW Document]. URL http://www.pg.com/en_US/brands/global_fabric_home_care/cascade.shtml

Rahman, M.S., 2006. State diagram of foods: Its potential use in food processing and product stability. Trends Food Sci. Technol. 17, 129–141. doi:10.1016/j.tifs.2005.09.009

Riley, D., Carbonell, R., 1993. Mechanisms of particle deposition from ultrapure chemicals onto semiconductor wafers: deposition from bulk liquid during wafer submersion. J. Colloid Interface Sci.

Saikhwan, P., Mercadé-Prieto, R., Chew, Y.M.J., Gunasekaran, S., Paterson, W.R., Wilson, D.I., 2010. Swelling and dissolution in cleaning of whey protein gels. Food Bioprod. Process. 88, 375–383. doi:10.1016/j.fbp.2010.09.006

Sam Saguy, I., Marabi, A., Wallach, R., 2005. New approach to model rehydration of dry food particulates utilizing principles of liquid transport in porous media. Trends Food Sci. Technol. 16, 495–506. doi:10.1016/j.tifs.2005.07.006

Samsung, 2014. Samsung's Chef Collection Dishwasher with Water Wall Technology [WWW Document]. URL http://www.samsung.com/us/appliances/dishwashers/DW80H9970US/AA

Schetz, J.A., Fuhs, A.E. (Eds.), 1996. Handbook of Fluid Dynamics and Fluid Machinery: Fundamentals of Fluid Dynamics. John Wiley & Sons, Inc. doi:10.1002/9780470172636

Schubert, E.F., 2006. Light-Emitting Diodes, Proceedings of SPIE - The International Society for Optical Engineering. Cambridge University Press.

Sen, S., Venkata Dasu, V., Mandal, B., Rajendran, K., 2014. Enzymatic removal of burnt-on protein residues from solid surface: A potential food equipment cleanser. Food Control 40, 314–319. doi:10.1016/j.foodcont.2013.12.013

Sharifzadeh, S., Clemmensen, L., 2014. Supervised feature selection for linear and non-linear regression of L a b color from multispectral images of meat. Eng. Appl. Artif. Intell. 27, 211–227.

Tavano, O.L., 2013. Protein hydrolysis using proteases: An important tool for food biotechnology. J. Mol. Catal. B Enzym. doi:10.1016/j.molcatb.2013.01.011

Thomas, N., Windle, A., 1982. A theory of case II diffusion. Polymer (Guildf). 23, 529–542.

Thomas, N.L., Windle, A.H., 1980. A deformation model for case II diffusion. Polymer (Guildf). 21, 613–619.

Tkalcic, M., Tasic, J.F., 2003. Colour spaces - perceptual, historical and applicational background. EUROCON 304–308.

Tomlinson, A., Carnali, J., 2007. A Review of Key Ingredients Used in Past and Present Auto-Dishwashing Formulations and the Physico-Chemical Processes They Facilitate, in: Johansson, I., Somasundaran, P. (Eds.), Handbook for Cleaning/Decontamination of Surfaces. Elsevier B.V, pp. 197–255.

Tsutsui, T., 1988. Functional Properties of Heat-Treated Egg Yolk Low Density Lipoprotein. J. Food Sci. 53, 1103–1106.

Tuladhar, T.., Paterson, W.R., Macleod, N., Wilson, D.I., 2000. Development of a novel non-contact proximity gauge for thickness measurement of soft deposits and its application in fouling studies. Can. J. Chem. Eng. 78, 935–947. doi:10.1002/cjce.5450780511

Tuladhar, T.R., Paterson, W.R., Wilson, D.I., 2002. Thermal Conductivity of Whey Protein Films Undergoing Swelling. Food Bioprod. Process. 80, 332–339. doi:10.1205/096030802321154862

Van Der Sman, R.G.M., 2012. Soft matter approaches to food structuring. Adv. Colloid Interface Sci. 176-177, 18–30. doi:10.1016/j.cis.2012.04.002

Van Der Sman, R.G.M., 2014. Moisture transport in swelling media modelled with a Lattice Boltzmann scheme having a deforming lattice. J. Food Eng. 124, 54–63. doi:10.1016/j.jfoodeng.2013.09.033

van der Sman, R.G.M., van der Goot, A.J., 2009. The science of food structuring. Soft Matter 5, 501–510. doi:10.1039/b718952b

Wang, T., Davidson, J.F., Wilson, D.I., 2013a. Effect of surfactant on flow patterns and draining films created by a static horizontal liquid jet impinging on a vertical surface at low flow rates. Chem. Eng. Sci. 88, 79–94. doi:10.1016/j.ces.2012.11.009

Wang, T., Davidson, J.F., Wilson, D.I., 2014. Flow patterns and cleaning behaviour of horizontal liquid jets impinging on angled walls. Food Bioprod. Process. 93, 333–342. doi:10.1016/j.fbp.2014.09.006

Wang, T., Faria, D., Stevens, L.J., Tan, J.S.C., Davidson, J.F., Wilson, D.I., 2013b. Flow patterns and draining films created by horizontal and inclined coherent water jets impinging on vertical walls. Chem. Eng. Sci. 102, 585–601. doi:10.1016/j.ces.2013.08.054

Weiss, M., Patel, M., Junginger, M., Blok, K., 2010. Analyzing price and efficiency dynamics of large appliances with the experience curve approach. Energy Policy 38, 770–783. doi:10.1016/j.enpol.2009.10.022

Wilson, D.I., 2005. Challenges in Cleaning: Recent Developments and Future Prospects. Heat Transf. Eng. 26, 51–59. doi:10.1080/01457630590890175

Wilson, D.I., Atkinson, P., Köhler, H., Mauermann, M., Stoye, H., Suddaby, K., Wang, T., Davidson, J.F., Majschak, J.-P., 2014. Cleaning of soft-solid soil layers on vertical and horizontal surfaces by stationary coherent impinging liquid jets. Chem. Eng. Sci. 109, 183–196. doi:10.1016/j.ces.2014.01.034

Wilson, D.I., Köhler, H., Cai, L., Majschak, J.-P., Davidson, J.F., 2015. Cleaning of a model food soil from horizontal plates by a moving vertical water jet. Chem. Eng. Sci. 123, 450–459. doi:10.1016/j.ces.2014.11.006

Wilson, D.I., Le, B.L., Dao, H.D. a., Lai, K.Y., Morison, K.R., Davidson, J.F., 2012. Surface flow and drainage films created by horizontal impinging liquid jets. Chem. Eng. Sci. 68, 449–460. doi:10.1016/j.ces.2011.10.003

Wold, H., 1985. Partial least squares. Encycl. Stat. Sci. 1–10.

Xin, H., Chen, X.D., Özkan, N., 2004. Removal of a model protein foulant from metal surfaces. AIChE J. 50, 1961–1973. doi:10.1002/aic.10149

Yoon, J., Cai, S., Suo, Z., Hayward, R.C., 2010. Poroelastic swelling kinetics of thin hydrogel layers: comparison of theory and experiment. Soft Matter 6, 6004. doi:10.1039/c0sm00434k

APPENDICES

A.1. Appendix

The following appendix shows the routines used for the processing of PEPT data (see *Chapter 3)*. Routines are shown in the order they were used according to *Chapter 3, section 3.3*.

Pre-processing

```
function [data1,data2]=PEPTloadtransfil(data)

    % Routine that loads the data, translate the origin and filters out high
    % error values.

    clc
    clearvars -except data

    % 1.1.- Add time column in seconds
    data(:,1)=data(:,1)/1000;


%% 1.- Translation of the origin and axis change.
    % The origin will be set centered at the bottom of the dishwasher and axis will
change in the following way:
        % Raw x - changes to new y.
        % Raw y - changes to new z.
        % Raw z - changes to new x.

    % Creation of the new matrix.
        % Column 1.- time (s).
        % Column 2.- x(mm).
        % Column 3.- y(mm).
        % Column 4.- z(mm).
        % Column 5.- Error.


data1(:,2) = data(:,4)-340;       % New x
data1(:,3) = data(:,2)-260;       % New y
data1(:,4) = data(:,3)-130;       % New z
data1(:,1) = data(:,1)/1000;      % New time(s)
data1(:,5) = data(:,5);           % New error


%% 2.- Data filtering.

data2 = data1;

temp            = find(data2(:,5)>3);       % Find data with error > 3 mm.
data2(temp,:)   = [];

meandata    = mean(data2(:,5));
stddata     = std (data2(:,5));
error       = meandata+(2*stddata);

temp1           = find(data2(:,5) > error);
data2(temp,:)   = [];
```

Smoothing

```
function [data1,meanvalue,standdev] = PEPTsmooth1(data)

%% Routine to smooth PEPT data.
clc
clearvars -except data
close all


%% Definitions
n = 5;                % Minimum Number of Points in Fitting
m = 25;               % Maximum Number of Points in Fitting

step=1;               % Step is created to cut the number of data, if (step=1)
                      % all the data is calculated.

n_el = size(data,1);
T    = data(:,1);        % [s]
X    = data(:,2);        % [mm]
Y    = data(:,3);        % [mm]
Z    = data(:,4);        % [mm]

time = 0.1               % [s]. Time limit for smoothing process.

meanvalue = zeros (1000,6);
standdev  = zeros (1000,7);


%% Creating the smooth matrix
l=1;      % Counter.

for o = 1:1:3         % Loop for different fitting orders
    for k = n:2:m     % Loop for different intervals

        % Initial values
        j     = floor(k/2);
        data1 = zeros(n_el,7);

         % Add missing data - Beggining of the matrix
        for q = 1:4
            for i = 1:j
                data1(i,q)  = data(i,q);
                data1(i,q+3)= data(i,q);
            end
        end


        % Creation of the fitted matrix
        for i = ceil(k/2):step:(n_el-(floor(k/2)))
            range = (i-(floor(k/2))):(i+(floor(k/2)));    % Creates a range of the size
(pnt-1).
            Tran  = T(range);
            Xran  = X(range);
            Yran  = Y(range);
            Zran  = Z(range);

            j=j+1;
            [Xfit,Yfit,Zfit]= PEPTsmooth2(Tran,Xran,Yran,Zran,o,time);
            data1(j,1)      = T(i);              %[s]
            data1(j,2)      = X(i);              %[mm]
            data1(j,3)      = Y(i);              %[mm]
            data1(j,4)      = Z(i);              %[mm]
            data1(j,5)      = Xfit;              %[mm]
            data1(j,6)      = Yfit;              %[mm]
            data1(j,7)      = Zfit;              %[mm]

        end

        % Add missing data - End of the matrix.
        for q = 1:4
            for i = (j:n_el)
            data1(i,q)  = data(i,q);
            data1(i,q+3)= data(i,q);
            end
        end
```

```
        % Obtention of mean value and standard deviation.
        difference = diff(data1);       % Row differences.

        for p=1:3
        meanvalue(l,p)= mean(difference(:,p+4));    % New x,y & z.
        standdev(l,p) = std(difference(:,p+4));     % New x,y & z.
        end

        standdev(l,5) = o;         % Fitting order.
        standdev(l,6) = k;         % Number of points in fitting.

        % Preparation for next loop stage.
      l=l+1;
    end
end


 %% Finding best smoothing value and obtention of new smoothed matrix
meanvalue (l+1,:) = [];
standdev  (l+1,:) = [];

for r = 1:size(standdev,1)
    standdev(r,4) = sqrt(standdev(r,1)^2 + standdev(r,2)^2 + standdev(r,3)^2);
end

[a1,a2] = min(standdev(:,4));   % Find best smoothing process.
o = standdev(a2,5);             % Best fitting value - Fitting order.
m = standdev(a2,6);             % Number of points in fitting.

j    = floor(m/2);
data1= zeros(n_el,7);


 % Add missing data - Beggining of the matrix
for k = 1:4
    for i=1:j
        data1(i,k)  = data(i,k);
        data1(i,k+3)= data(i,k);
    end
end


 % Smooth calculations
for i = ceil(m/2):step:(n_el-(floor(m/2)))
    range = (i-(floor(m/2))):(i+(floor(m/2)));  % Creates a range of the size (pnt-1).
    Tran  = T(range);
    Xran  = X(range);
    Yran  = Y(range);
    Zran  = Z(range);

        j=j+1;
        [Xfit,Yfit,Zfit] = smooth2(Tran,Xran,Yran,Zran,o,time);
        data1(j,1)       = T(i);              %[s]
        data1(j,2)       = X(i);              %[mm]
        data1(j,3)       = Y(i);              %[mm]
        data1(j,4)       = Z(i);              %[mm]
        data1(j,5)       = Xfit;              %[mm]
        data1(j,6)       = Yfit;              %[mm]
        data1(j,7)       = Zfit;              %[mm]

 end


 % Add missing data
for k=1:4
    for i=(j:n_el)
        data1(i,k)  = data(i,k);
        data1(i,k+3)= data(i,k);
    end
end



%%  Plots comparison

% X-axis
figure(1)
axes('FontSize',20,'FontName','Calibri')
plot(data1(:,1),data1(:,2),'MarkerFaceColor',[0 0
```

```
1],'MarkerSize',4,'Marker','o','LineStyle','none',...
    'Color',[0 0 1])
hold on
plot(data1(:,1),data1(:,5),'MarkerFaceColor',[1 0
0],'MarkerSize',4,'Marker','o','LineStyle','none',...
    'Color',[1 0 0])
% plot(data1(:,1),data1(:,2),'r.',data1(:,1),data1(:,5),'b-')
set(gcf,'Color',[1,1,1])
ylabel('Height Position,
Z(mm)','FontWeight','bold','FontSize',20,'FontName','Calibri',...
    'FontAngle','normal')
xlabel('Time, t (seconds)','FontWeight','bold','FontSize',20,'FontName','Calibri',...
    'FontAngle','normal')
box('on');
hold on


% Y-axis
figure(2)
plot(data1(:,1),data1(:,3),'r.',data1(:,1),data1(:,6),'b-')
set(gcf,'Color',[1,1,1])
title('Y-axe comparison','interpreter','Latex','FontSize',24)
ylabel('Y(mm)','interpreter','Latex','FontSize',18)
xlabel('time(sec)','interpreter','Latex','FontSize',18)
box('on');
grid('on');


% Z-axis
figure(3)
plot(data1(:,1),data1(:,4),'r.',data1(:,1),data1(:,7),'b-')
set(gcf,'Color',[1,1,1])
title('Z-axe comparison','interpreter','Latex','FontSize',24)
ylabel('Z(mm)','interpreter','Latex','FontSize',18)
xlabel('time(sec)','interpreter','Latex','FontSize',18)
box('on');
grid('on');


% 3D
figure(4)
axis equal
xlim([-270 270]);     % Axis X limit. Front
set(gca,'XDir','reverse');
set(gcf,'Color',[1,1,1])
zlim([0 600]);        % Axis Z limit
ylim([-250 250]);     % Axis Y limit. Side
set(gca,'YDir','reverse');
hold on
plot3(data1(:,2),data1(:,3),data1(:,4),'MarkerFaceColor',[1 0
0],'MarkerSize',4,'Marker','o',...
    'LineStyle','none',...
    'Color',[1 0 0])
title('3D view','interpreter','Latex','FontSize',26)
xlabel('x(mm)','interpreter','Latex','FontSize',18)
ylabel('y(mm)','interpreter','Latex','FontSize',18)
zlabel('z(mm)','interpreter','Latex','FontSize',18)
view([-37.5 30]);
box('on');
grid('on');
hold on
plot3(data1(:,5),data1(:,6),data1(:,7),'MarkerFaceColor',[0 0
1],'MarkerSize',4,'Marker','o',...
    'LineStyle','none',...
    'Color',[0 0 1])
```

```
function [Xfit,Yfit,Zfit] = PEPTsmooth2(Tran,Xran,Yran,Zran,o,time)

%% Regression Analysis

    d = distcar(Xran,Yran,Zran);  %Interval distance

if (Tran(end)-Tran(1))>=0 && (Tran(end)-Tran(1))<=time
    if d < 200  %% Do not fit if the points distance is higher than 200 mm.
   %% Calculate Velocities, Error & Accelerations
    %Vx
[Xfit] = PEPTsmooth3(Tran,Xran,o);

    %Vy
[Yfit] = PEPTsmooth3(Tran,Yran,o);

    %Vz
[Zfit] = PEPTsmooth3(Tran,Zran,o);


    elseif (Tran(end)-Tran(1))<=0
        j=ceil(size(Tran,1)/2);

        Xfit = Xran(j);
        Yfit = Yran(j);
        Zfit = Zran(j);
    else
        j=ceil(size(Tran,1)/2);

        Xfit = Xran(j);
        Yfit = Yran(j);
        Zfit = Zran(j);
    end
end

[Xfit] = Xfit(ceil(length(Xfit)/2));
[Yfit] = Yfit(ceil(length(Xfit)/2));
[Zfit] = Zfit(ceil(length(Xfit)/2));

%% Subfunction to calculate cartesian distance

function d=distcar(Xran,Yran,Zran)
d=((Xran(end)-Xran(1))^2 + ...
    (Yran(end)-Yran(1))^2 + ...
    (Zran(end)-Zran(1))^2)^.5;
```

```
function [yfit] = PEPTsmooth3(xdat,ydat,o)

 Coeffs = polyfit(xdat,ydat,o);     % Getting the coefficients.

 yfit = polyval(Coeffs,xdat);       % Fitted data.

 yfit = yfit(ceil(length(yfit)/2)); % Value taken.
```

Selective linear interpolation

```
function [mat2] = PEPTintrpselective(data)
    %% Interpolating data where points are missing

        %% Input
            % Column 1 - Time [s].
            % Column 2 - x-axis [mm].
            % Column 3 - y-axis [mm].
            % Column 4 - z-axis [mm].

dmin = 5;       % Minimum distance to interpolate. [mm]
dmax = 20;      % Maximum distance to interpolate. [mm]

mat2        = zeros(length(data),4);
mat2(1,:)   = data(1,:);
k = 2;


for i=2:length(data)
    p1 = data(i-1,:);
    p2 = data(i,:);
    d  = distcar(p1,p2);
    if (d>dmin & d<dmax)
        Nint= floor(d/dmin);
        t   = linspace(p1(1),p2(1),Nint+2);
        k   = k-1;
        mat2(k:k+Nint+1,1) = t;
        mat2(k:k+Nint+1,2) = intfab([p1(1) p2(1)],[p1(2) p2(2)],t); %X-axis
        mat2(k:k+Nint+1,3) = intfab([p1(1) p2(1)],[p1(3) p2(3)],t); %Y-axis
        mat2(k:k+Nint+1,4) = intfab([p1(1) p2(1)],[p1(4) p2(4)],t); %Z-axis
        k   = k+Nint+2;
    else
        mat2(k,:) = data(i,:);
        k   = k+1;
    end
end
mat2(k:end,:) = [];
toc

%% ======================================================================%%
%% Subfunction to calculate cartesian distance                           %%
%% ======================================================================%%
function d = distcar(p1,p2)
d = ((p1(4)-p2(4))^2 + ...
    (p1(2)-p2(2))^2 + ...
    (p1(3)-p2(3))^2)^.5;

%% ===================================================================== %%
%% Interpolation first order                                             %%
%% xdat is time, whilst ydat is the coordinate                           %%
%% ======================================================================%%
function int = intfab (xdat,ydat,t)
a  = (ydat(2)-ydat(1))/(xdat(2)-xdat(1));
b  = ydat(1)-a*xdat(1);
int= a*t+b;
```

Lagrangian analysis

```
function [data1] = PEPTlagrangian1(data)
    %% Routine to calculate Lagrangian velocities
clc
close all

%% Initial definitions

n=7;        % Minimum number of points in fitting.
pnt=17;     % Maximum number of points in fitting.

step=1;            %step is create to cut the number of data, if (step=1)
                   %all the data are calculated.
n_el = size(data,1);
T    = data(:,1);   %Time       [=] s.
X    = data(:,2);   %X-axe      [=] mm.
Y    = data(:,3);   %Y-axe      [=] mm.
Z    = data(:,4);   %Z-axe      [=] mm.
R    = data(:,6);   %Radius-axe [=] mm.


%% Creating the velocity matrix
j     = 0;
data1 = zeros(n_el,15); % OUTPUT MATRIX
err   = 1;

for i = ceil(pnt/2):step:(n_el-(floor(pnt/2)))
    range = (i-((pnt-1)/2)):(i+((pnt-1)/2));  % Creates a range of the size pnt.
    Tran  = T(range);
    Xran  = X(range);
    Yran  = Y(range);
    Zran  = Z(range);
    Rran  = R(range);


        j=j+1;
        [Vt,Vx,Vy,Vz,Vrad,At,Ax,Ay,Az,Arad] =
PEPTlagrangian2(Tran,Xran,Yran,Zran,Rran,n,pnt);
        data1(j,1)  = T(i);   %Time       [=] s.
        data1(j,2)  = X(i);   %X-axe      [=] mm.
        data1(j,3)  = Y(i);   %Y-axe      [=] mm.
        data1(j,4)  = Z(i);   %Z-axe      [=] mm.
        data1(j,5)  = R(i);   %Radius-axe [=] mm.
        data1(j,6)  = Vx;     %X-axe Velocity [=] m/s.
        data1(j,7)  = Vy;     %Y-axe Velocity [=] m/s.
        data1(j,8)  = Vz;     %Z-axe Velocity [=] m/s.
        data1(j,9)  = Vt;     %3D Velocity    [=] m/s.
        data1(j,10) = Vrad;   %Radial-axe Velocity [=] m/s.
        data1(j,11) = Ax;     %X-axe Acceleration  [=] m/s2.
        data1(j,12) = Ay;     %Y-axe Acceleration  [=] m/s2.
        data1(j,13) = Az;     %Z-axe Acceleration  [=] m/s2.
        data1(j,14) = At;     %3D Acceleration     [=] m/s2.
        data1(j,15) = Arad;   %Radial-axe Acceleration [=] m/s.
end

data1(j+1:end,:) = [];


    %% Stablish decelerations
        % Cartesian accelerations
for i = 1:(size(data1(:,9),1)-4)
    posneg(i,1) = data1(i+4,9)-data1(i,9);
end

for i = 1:size(posneg,1)
    if posneg(i,1)<0
    data1(i,14) = -data1(i,14);
    end
end


        % Radius accelerations
for i = 1:(size(data1(:,10),1)-4)
    posneg(i,1) = data1(i+4,10)-data1(i,10);
end

for i = 1:size(posneg,1)
```

```
    if posneg(i,1)<0
    data1(i,15) = -data1(i,15);
    end
end


    %% Input of new columns for final matrix
for i=7:21
    data(:,i)=zeros;    % Expand initial matrix. Increase columns.
end


for i=12:1:21
    for q=1:size(data1,1)
    data(q+floor(pnt/2),i) = data1(q,i-6);  % Incorporate velocities and accelerations.
    end
end
```

```
function [vt,vx,vy,vz,vrad,acct,accx,accy,accz,accr] =
PEPTlagrangian2(Tran,Xran,Yran,Zran,Rran,n,pnt)

%% Regression Analysis
l = 1;
d = distcar(Xran,Yran,Zran);


for m=n:2:pnt

    if (Tran(end)-Tran(1))>=0
        if d < 25

%% Calculate Velocities, Error & Accelerations
%Vx
[vx(l,1),errx(l,1),accx(l,1)]   = PEPTlagrangian3(Tran((ceil(pnt/2)-
floor(m/2)):(ceil(pnt/2)+floor(m/2))),Xran((ceil(pnt/2)-
floor(m/2)):(ceil(pnt/2)+floor(m/2))));
%Vy
[vy(l,1),erry(l,1),accy(l,1)]   = PEPTlagrangian3(Tran((ceil(pnt/2)-
floor(m/2)):(ceil(pnt/2)+floor(m/2))),Yran((ceil(pnt/2)-
floor(m/2)):(ceil(pnt/2)+floor(m/2))));
%Vz
[vz(l,1),errz(l,1),accz(l,1)]   = PEPTlagrangian3(Tran((ceil(pnt/2)-
floor(m/2)):(ceil(pnt/2)+floor(m/2))),Zran((ceil(pnt/2)-
floor(m/2)):(ceil(pnt/2)+floor(m/2))));
%Vrad
[vrad(l,1),errr(l,1),accr(l,1)] = PEPTlagrangian3(Tran((ceil(pnt/2)-
floor(m/2)):(ceil(pnt/2)+floor(m/2))),Rran((ceil(pnt/2)-
floor(m/2)):(ceil(pnt/2)+floor(m/2))));


errt(l,1) = errx(l,1)+erry(l,1)+errz(l,1);
vt(l,1)   = ((vx(l,1).^2)+(vy(l,1).^2)+(vz(l,1).^2)).^.5;
acct(l,1) = ((accx(l,1).^2)+(accy(l,1).^2)+(accz(l,1).^2)).^.5;
l = l+1;

    else

    vt=0; vx=0; vy=0; vz=0; vrad=0;
    acct=0; accx=0; accy=0; accz=0; accr=0;

        end
    end
end

if exist('errt')
m=n+((find(errt(:,1)==min(errt(:,1)))-1)*(2));

vt(1,1)       = vt(((m-n)/2)+1,1);
vx(1,1)       = vx(((m-n)/2)+1,1);
vy(1,1)       = vy(((m-n)/2)+1,1);
vz(1,1)       = vz(((m-n)/2)+1,1);
vrad(1,1)     = vrad(((m-n)/2)+1,1);
vt(2:end,:)   = [];
vx(2:end,:)   = [];
vy(2:end,:)   = [];
```

```
vz(2:end,:)   = [];
vrad(2:end,:) = [];
acct(1,1)     = acct(((m-n)/2)+1,1);
accx(1,1)     = accx(((m-n)/2)+1,1);
accy(1,1)     = accy(((m-n)/2)+1,1);
accz(1,1)     = accz(((m-n)/2)+1,1);
accr(1,1)     = accr(((m-n)/2)+1,1);
acct(2:end,:) = [];
accx(2:end,:) = [];
accy(2:end,:) = [];
accz(2:end,:) = [];
accr(2:end,:) = [];
else
vt=NaN; vx=NaN; vy=NaN; vz=NaN; vrad=NaN;
acct=NaN; accx=NaN; accy=NaN; accz=NaN; accr=NaN;
end


   %% Subfunction to calculate cartesian distance

function d=distcar(Xran,Yran,Zran)
d=((Xran(end)-Xran(1))^2 + ...
    (Yran(end)-Yran(1))^2 + ...
    (Zran(end)-Zran(1))^2)^.5;
```

```
function [vel,err,acc,yfit] = PEPTlagrangian3(xdat,ydat)
%% Least square polynomial dx/dt interpolation using m points to find velocities
%xdat is time, whilst ydat is the coordinate
%xdats=rangesc(xdat);

xdats      = xdat(:,1)-xdat(1,1); % Substract the first value of time
xdats(:,2) = xdats(:,1);
xdats(:,1) = 1;
xdats(:,3) = xdats(:,2).^2;       % Squared second column.

a = inv(transpose(xdats)*(xdats))*(transpose(xdats))*(ydat); % Velocity units.

for j=1:length(ydat)
    yfit(j,1) = a(1,1)+(a(2,1)*xdats(j,2))+(a(3,1)*(xdats(j,2)^2)); % Second grade fit.
end

err = mean((ydat-yfit).^2);

%% Velocity
vel = ((2*(a(3,1)*(xdats(ceil(length(xdat)/2),2))))+a(2,1))/1000; %[m/s]

%% Acceleration
acc = (2*a(3,1))/1000;  % [m/s2]
```

Eulerian analysis

```
function [E,ZI,RI] = PEPTeulerian1(data)
%% Routine for the creation of velocity distribution and occupancies plots. Eulerian
analysis.
 clc
 close all


% Data Handling
t    = data(:,1);       %Time        [=] s.
x    = data(:,2);       %X-axis      [=] mm.
y    = data(:,3);       %Y-axis      [=] mm.
z    = data(:,4);       %Z-axis      [=] mm.
rad  = data(:,6);       %Radial-axis [=] mm.

Vx   = data(:,12);      %X-axis Velocity [=] m/s.
Vy   = data(:,13);      %Y-axis Velocity [=] m/s.
Vz   = data(:,14);      %Y-axis Velocity [=] m/s.
V    = data(:,15);      %3D Velocity     [=] m/s.
Vrad = data(:,16);      %Radial-axis Velocity [=] m/s.

Ax   = data(:,17);      %X-axis Acceleration  [=] m/s2.
Ay   = data(:,18);      %Y-axis Acceleration  [=] m/s2.
Az   = data(:,19);      %Z-axis Acceleration  [=] m/s2.
A    = data(:,20);      %3D Acceleration      [=] m/s2.
Arad = data(:,21);      %Radial-axis Acceleration  [=] m/s2.

data2   = [t,x,y,z,rad]; %Creation of the data matrix

% Non-dimensionless
MaxZ    = 600;           % Dishwasher dimensions [=] mm.
MaxY    = 500;           % Dishwasher dimensions [=] mm.
MaxX    = 540;           % Dishwasher dimensions [=] mm.
MaxRad  = max(rad);

cellsize = 10;        % Cellsize [=] mm.


x_bins  = floor(MaxX/cellsize);
y_bins  = floor(MaxY/cellsize);
z_bins  = floor(MaxZ/cellsize);
rad_bins= ceil(MaxRad/cellsize);


[E] =
PEPTeulerian2([data2],Vx,Vz,Vy,V,Vrad,Ax,Ay,Az,A,Arad,MaxZ,MaxY,MaxX,MaxRad,y_bins,x_bin
s,z_bins,rad_bins,cellsize);

%% Plots
PEPTeulerian3
```

```
function [EulerianC] =
PEPTeulerian2(data1,Vx,Vz,Vy,V,Vrad,Ax,Ay,Az,A,Arad,MaxZ,MaxY,MaxX,MaxRad,y_bins,x_bins,
z_bins,rad_bins,cellsize);

%% Nodes & Centers
%X-axis
x_nodes     = [-(MaxX/2):cellsize:(MaxX/2)];
x_centers   = (x_nodes(1:length(x_nodes)-1)+x_nodes(2:length(x_nodes)))/2;

%Y-axis
y_nodes     = [-(MaxY/2):cellsize:(MaxY/2)];
y_centers   = (y_nodes(1:length(y_nodes)-1)+y_nodes(2:length(y_nodes)))/2;

%Z-axis
z_nodes     = [(0:cellsize:MaxZ)];
z_centers   = (z_nodes(1:length(z_nodes)-1)+z_nodes(2:length(z_nodes)))/2;

%Radial-axis
rad_nodes   = [(0:cellsize:MaxRad)];
rad_centers = (rad_nodes(1:length(rad_nodes)-1)+rad_nodes(2:length(rad_nodes)))/2;
```

```
%% Hipermatrix
EulerianC = zeros(rad_bins-1,z_bins,16);

[EulerianC(:,:,15),EulerianC(:,:,16)] = meshgrid(z_centers,rad_centers);

    % Loop
for i_lag=1:length(Vz)-1

    x_act  = data1(i_lag,2);
    y_act  = data1(i_lag,3);
    z_act  = data1(i_lag,4);
    rad_act= data1(i_lag,5);

    %dt=(data1(i_lag+1,1)-data1(i_lag,1));

    ix  = find(x_centers<=x_act,1,'last');
    iy  = find(y_centers<=y_act,1,'last');
    iz  = find(z_centers<=z_act,1,'last');
    irad= find(rad_centers<=rad_act,1,'last');


    if ix > x_bins
        ix=x_bins;
    end

    if iy > y_bins
        iy=y_bins;
    end

    if iz > z_bins
        iz=z_bins;
    end

    if irad > rad_bins
        irad=rad_bins;
    end


    dt=(data1(i_lag+1,1)-data1(i_lag,1));

    if dt>=0 && dt<=1
        dt=dt;
    else
        dt=0;
    end



     %clear irad
     %irad=ix;

    EulerianC(irad,iz,1) = EulerianC(irad,iz,1) + Vx(i_lag);     %Vx
    EulerianC(irad,iz,2) = EulerianC(irad,iz,2) + Vy(i_lag);     %Vy
    EulerianC(irad,iz,3) = EulerianC(irad,iz,3) + Vz(i_lag);     %Vz
    EulerianC(irad,iz,4) = EulerianC(irad,iz,4) + V(i_lag);      %V
    EulerianC(irad,iz,5) = EulerianC(irad,iz,5) + Vrad(i_lag);   %Vrad

    EulerianC(irad,iz,6) = EulerianC(irad,iz,6) + Ax(i_lag);     %Ax
    EulerianC(irad,iz,7) = EulerianC(irad,iz,7) + Ay(i_lag);     %Ay
    EulerianC(irad,iz,8) = EulerianC(irad,iz,8) + Az(i_lag);     %Az
    EulerianC(irad,iz,9) = EulerianC(irad,iz,9) + A(i_lag);      %A
    EulerianC(irad,iz,10)= EulerianC(irad,iz,10)+ Arad(i_lag);   %Arad

    EulerianC(irad,iz,11)= EulerianC(irad,iz,11)+dt;    %TIME IN EACH CELL
    EulerianC(irad,iz,12)= EulerianC(irad,iz,12)+1;     %PASS count

end

    exptime  = sum(EulerianC(:,:,11));
    exptime2 = sum(exptime);            % Total experimental time


    %%AVERAGES
    EulerianC(:,:,1) = (EulerianC(:,:,1)./EulerianC(:,:,12));    %FINAL Vx
    EulerianC(:,:,2) = (EulerianC(:,:,2)./EulerianC(:,:,12));    %FINAL Vy
    EulerianC(:,:,3) = (EulerianC(:,:,3)./EulerianC(:,:,12));    %FINAL Vz
    EulerianC(:,:,4) = (EulerianC(:,:,4)./EulerianC(:,:,12));    %FINAL V
    EulerianC(:,:,5) = (EulerianC(:,:,5)./EulerianC(:,:,12));    %FINAL Vrad
```

```
    EulerianC(:,:,6) = (EulerianC(:,:,6)./EulerianC(:,:,12));    %FINAL Ax
    EulerianC(:,:,7) = (EulerianC(:,:,7)./EulerianC(:,:,12));    %FINAL Ay
    EulerianC(:,:,8) = (EulerianC(:,:,8)./EulerianC(:,:,12));    %FINAL Az
    EulerianC(:,:,9) = (EulerianC(:,:,9)./EulerianC(:,:,12));    %FINAL A
    EulerianC(:,:,10) = (EulerianC(:,:,10)./EulerianC(:,:,12));  %FINAL Arad

    EulerianC(:,:,13) =
sqrt(EulerianC(:,:,1).^2+EulerianC(:,:,2).^2+EulerianC(:,:,3).^2);  % Avg. Velocity
    EulerianC(:,:,14) =
sqrt(EulerianC(:,:,5).^2+EulerianC(:,:,6).^2+EulerianC(:,:,7).^2);  % Avg. Acceleration
    EulerianC(:,:,15) = EulerianC(:,:,11)./EulerianC(:,:,12); %Avg. Residence Time
    EulerianC(:,:,16) = EulerianC(:,:,11)/exptime2;     %Occupancy
```

```
%% Routine to plot the results from Eulerian analysis


%% Nodes & Centers
   %X
x_nodes=[-(MaxX/2):cellsize:(MaxX/2)];
x_centers=(x_nodes(1:length(x_nodes)-1)+x_nodes(2:length(x_nodes)))/2;

   %Y
y_nodes=[-(MaxY/2):cellsize:(MaxY/2)];
y_centers=(y_nodes(1:length(y_nodes)-1)+y_nodes(2:length(y_nodes)))/2;

   %Z
z_nodes=[(0:cellsize:MaxZ)];
z_centers=(z_nodes(1:length(z_nodes)-1)+z_nodes(2:length(z_nodes)))/2;

   %Rad
rad_nodes=[(0:cellsize:MaxRad)];
rad_centers=(rad_nodes(1:length(rad_nodes)-1)+rad_nodes(2:length(rad_nodes)))/2;


[ZI,RI]=meshgrid(z_centers,rad_centers);    %Meshgrid


%% Matrices

%Velocities
a1=find(E(:,:,4)>=0); b1=find(E(:,:,4)<=0); C1=zeros(size(RI,1),size(RI,2));
C=E(:,:,4); C1(a1)=C(a1); C1(b1)=C(b1);

%Accelerations
a2=find(E(:,:,9)>=0); b2=find(E(:,:,9)<=0); C2=zeros(size(RI,1),size(RI,2));
C=E(:,:,9); C2(a2)=C(a2); C2(b2)=C(b2);

%Residence times
a3=find(E(:,:,15)>=0); b3=find(E(:,:,15)<=0); C3=zeros(size(RI,1),size(RI,2));
C=E(:,:,15); C3(a3)=C(a3); C3(b3)=C(b3);

%Occupancy
a4=find(E(:,:,16)>=0); b4=find(E(:,:,12)<=0); C4=zeros(size(RI,1),size(RI,2));
C=E(:,:,16); C4(a4)=C(a4); C4(b4)=C(b4);


%% Plots

% Velocity
figure(1)
axes('FontSize',34)
ph=surf(RI,ZI,C1,'Edgecolor','None');
hold on
xlabel('Radial position,
R(mm)','FontWeight','bold','FontSize',34,'FontName','Calibri',...
    'FontAngle','normal');
set(gcf,'Color',[1,1,1])
ylabel('Height Position,
Z(mm)','FontWeight','bold','FontSize',34,'FontName','Calibri',...
    'FontAngle','normal');
view(0,90)
axis tight
axis equal
```

```
cd=get(ph,'cdata');
cd(C1==0)=NaN;
set(ph,'cdata',cd)
cb=colorbar('FontSize',30);
set(get(cb,'ylabel'),'string','Velocity
(m/s)','FontWeight','bold','FontSize',34,'FontName','Calibri',...
    'FontAngle','normal')
caxis([0 14])
box('on')
ylim([0 500]);
xlim([0 300]);
hold off


% Acceleration
figure(2)
axes('FontSize',34)
ph=surf(RI,ZI,C2,'Edgecolor','None');
hold on
xlabel('Radial position,
R(mm)','FontWeight','bold','FontSize',34,'FontName','Calibri',...
    'FontAngle','normal');
set(gcf,'Color',[1,1,1])
ylabel('Height Position,
Z(mm)','FontWeight','bold','FontSize',34,'FontName','Calibri',...
    'FontAngle','normal');
view(0,90)
axis tight
axis equal
cd=get(ph,'cdata');
cd(C2==0)=NaN;
set(ph,'cdata',cd)
cb=colorbar('FontSize',30);
set(get(cb,'ylabel'),'string','Acceleration
(m/s2)','FontWeight','bold','FontSize',34,'FontName','Calibri',...
    'FontAngle','normal')
caxis([-500 500])
box('on')
ylim([0 500]);
xlim([0 300]);
hold off


% Residence time
figure(3)
axes('FontSize',34)
ph=surf(RI,ZI,C3,'Edgecolor','None');
hold on
xlabel('Radial position,
R(mm)','FontWeight','bold','FontSize',34,'FontName','Calibri',...
    'FontAngle','normal');
set(gcf,'Color',[1,1,1])
ylabel('Height Position,
Z(mm)','FontWeight','bold','FontSize',34,'FontName','Calibri',...
    'FontAngle','normal');
view(0,90)
axis tight
axis equal
cd=get(ph,'cdata');
cd(C3==0)=NaN;
set(ph,'cdata',cd)
cb=colorbar('FontSize',30);
set(get(cb,'ylabel'),'string','Res.time
(sec)','FontWeight','bold','FontSize',34,'FontName','Calibri',...
    'FontAngle','normal')
caxis([0 0.015])
box('on')
ylim([0 500]);
xlim([0 300]);
hold off


%Occupancy
figure(4)
axes('FontSize',34)
ph=surf(RI,ZI,C4,'Edgecolor','None');
hold on
xlabel('Radial position,
R(mm)','FontWeight','bold','FontSize',34,'FontName','Calibri',...
```

```
    'FontAngle','normal');
set(gcf,'Color',[1,1,1])
ylabel('Height Position,
Z(mm)','FontWeight','bold','FontSize',34,'FontName','Calibri',...
    'FontAngle','normal');
view(0,90)
axis tight
axis equal
cd=get(ph,'cdata');
cd(C4==0)=NaN;
set(ph,'cdata',cd)
cb=colorbar('FontSize',30);
set(get(cb,'ylabel'),'string','Fraction of total
time','FontWeight','bold','FontSize',34,'FontName','Calibri',...
    'FontAngle','normal')
caxis([0 0.005])
box('on')
ylim([0 500]);
xlim([0 300]);
hold off
```

A.2. Appendix

Time travelling in 'vision area' (t_{vis}), Time impacting plates (T_{impact}) and Impact Length (L_{impact}) per spray arm rotation.

Let there be a plate located vertically at coordinates (x_{PL},y_{PL},z_{PL}) with a separation from the front plate d. Let there be also a nozzle located at a radial distance R_{NZ}, a height z_{NL} and rotating from an axis of rotation at (0,0,z_{NL}) coordinates. The angles at which the nozzle enters (β_{in}) and exits (β_{out}) the defined vision area can be calculated as follow:

$$\beta_{in} = arc\sin\left(\frac{y_{PL}-d}{R_{NZ}}\right) \quad (1)$$

$$\beta_{out} = arc\sin\left(\frac{y_{PL}}{R_{NZ}}\right) \quad (2)$$

Given a rotational speed of the spray arm ω ($\omega = {}^{d\beta}/_{dt}$), the time the nozzle (jet) is travelling in the 'vision area' is given by:

$$t_{vis} = \frac{(\beta_{out} - \beta_{in})}{\omega} \quad (3)$$

In between those angles, the path followed by the nozzle is given by:

$$x_{NZ} = R_{NZ} \cdot \cos(\beta) \quad (4)$$

$$y_{NZ} = R_{NZ} \cdot \sin(\beta) \quad (5)$$

Where: $\beta_{in} > \beta > \beta_{out}$

A time value can also be assigned for each of the nozzle locations if the rotational speed ω is known.

The Cartesian components of the direction vector characterising the jet path are calculated as follow:

x-direction: $(dir)_x = 1$ (6)

y-direction: $(dir)_y = (dir)_x \cdot tg(\theta_{jet})$ (7)

z-direction: $(dir)_z = \sqrt{(dir)_x{}^2 + (dir)_y{}^2} \cdot tg(\rho_{jet})$ (8)

With those parameters, the impact locations on the x-z plane formed by the analysed plate are given by:

$$x_{PL} - \frac{D_{PL}}{2} < x_{impact}(t) = \frac{(y_{PL} - y_{NZ}(t))}{(dir)_y} \cdot (dir)_x + x_{NZ}(t) < x_{PL} + \frac{D_{PL}}{2} \quad (9)$$

$$z_{PL} - D_{PL} < z_{impact}(t) = \frac{(y_{PL} - y_{NZ}(t))}{(dir)_y} \cdot (dir)_z + z_{NZ}(t) < z_{PL} \quad (10)$$

The times at which the first and last impact locations within the boundaries of the analysed plate occur indicate the total impact time (T_{impact}). The sum of the distance between consecutive impact locations within the analysed plate edges gives the length coverage by the jet (L_{impact}).

MATLAB routine

The following routine illustrates the mathematical approach used to obtain the results for the case study shown in section 4.3.2.

```
function [table,P] = jets(A);
%% Routine for calculating the impact areas of water jets into plates.
    %Example given.

        % Input matrix A:
            % A (:,1) = Separation between plates. [=] mm.
            % A (:,2) = Nozzle position. [mm].
            % A (:,3) = Theta angle. [Degrees].
            % A (:,4) = Rho angle. [Degrees].


clc
close all
table = zeros(size(A,1),13);      % OUTPUT MATRIX.


for j=1:size(A,1)

%% 1-Design Data
% Plates characteristics.
dpl = 250;                              %Plate diameter. (mm)
rpl = 125;                              %Plate width position (mm).
d   = A(j,1);                           %Distance between plates (mm). Separation.
ylimi(2) = 0;                           %Plate 2 position.
ylimi(1) = ylimi(2)-d;                  %Plate 1 position.


% Jet characteristics.
nd  = 2e-3;                             % Nozzle diameter. [=] m.
radius = A(j,2);                        % Nozzle position. [=] mm.
w   = 30;                               % Spray Arm rotational velocity. [=] rpm.
w   = w*2*pi/60;                        % Spray Arm rotational velocity. [=] rad/seg.
turningtime = 2*pi/w;                   % Time to complete a rotation.   [=] s.

thetajet = A(j,3);                      % Theta angle. [=] Degrees.
rhojet   = A(j,4);                      % Rho angle.   [=] Degrees.
thetajet = (thetajet*pi/180);           % Theta angle. [=] Radians.
rhojet   = (rhojet*pi/180);             % Rho angle.   [=] Radians.

veljet = 9;                                 % Velocity of the jet. [=] m/s.
vz     = veljet*sin(rhojet);                % x-axis velocity of the jet. [=] m/s.
vy     = veljet*cos(rhojet)*sin(thetajet);  % y-axis velocity of the jet. [=] m/s.
vx     = veljet*cos(rhojet)*cos(thetajet);  % z-axis velocity of the jet. [=] m/s.


%% 2 - Finding angles for areas seen by the plate.
for i=1:2
    thetalim(i) = asin(ylimi(i)/radius);            % Defines the start and the end of
the areas where the plate sees the jet in the rotation.
    xlimi(i)    = sqrt((radius^2)-(ylimi(i)^2));
end


% Time the plate sees the jet
timeexposed     = abs((thetalim(2)-thetalim(1))/w);  % Time - Used for mass flow hitting
the plate.


%% 3 - Obtention of nozzle trajectories inside the "vision area".

Theta = (0:0.0001:2*pi)';        % Whole NOZZLE rotation movement.

for i = 1:size(theta,1)
x1(i) = radius*cos(theta(i));    % NOZZLE circle - XAXE -
y1(i) = radius*sin(theta(i));    % NOZZLE circle - YAXE -
end
```

```
platetheta=(thetalim(1):0.0001:thetalim(2))';    % Vision area.

for i = 1:size(platetheta,1)
x2(i) = radius*cos(platetheta(i));       % NOZZLE trajectory inside Vision Area - XAXE -
y2(i) = radius*sin(platetheta(i));       % NOZZLE trajectory inside Vision Area - YAXE -
z2(i) = 30;                              % Height of the SPRAY ARM.
end


deltat=timeexposed/size(x2,2);

for i = 1:size(x2,2)
time(i) = (i-1)*deltat;
end

x2=x2'; y2=y2'; z2=z2'; time=time';

sprayarm = zeros(size(x2,1),4);
sprayarm(:,1) = x2;
sprayarm(:,2) = y2;
sprayarm(:,3) = z2;
sprayarm(:,4) = time; %DATA FROM SPRAY ARM.



%% 4 - Projection of the jet onto the plate surface.
% Obtention of the JET DIRECTION VECTOR
dir(1) = 1;                                          % x-direction
dir(2) = dir(1)*tan(thetajet);                       % y-direction
dir(3) = (sqrt((dir(1)^2)+(dir(2)^2)))*tan(rhojet);  % z-direction


% Points in the projection - Impact of water.
for i = 1:size(platetheta,1)
xplate(i) = ((ylimi(2)-y2(i))/dir(2))*dir(1)+x2(i);      % y2-y1=m(x2-x1) - Looking for
x2
zplate(i) = (abs((ylimi(2)-y2(i))/dir(2))*dir(3))+z2(i);
end

xplate = xplate';
zplate = zplate';



%% 5 - Obtention of distance covered by jet.

plate = zeros(size(xplate,1),3);
plate(:,1) = xplate;      %Impact on X-AXE
plate(:,2) = zplate;      %Impact on Z-AXE

% Circular plates
platecentre = [rpl (30+(dpl/2))];  %Coordinates where the plate sits (x-axe,z-axe).

for i = 1:size(plate,1)
    plate(i,3) = sqrt(((plate(i,1)-platecentre(1,1))^2)+((plate(i,2)-
    platecentre(1,2))^2)); %Obtention of the distance from plate centre.
end

a1 = find(plate(:,3)>(dpl/2));     % If impact distance to the plate centre is higher
that dpl/2, it means it does not touch the plate. Circular plates
plate(a1,:) = [];


if size(plate,1)>1
dplate = diff(plate);

for i = 1:size(dplate,1)
dplate(i,3) = sqrt((dplate(i,1)^2) + ((dplate(i,2))^2));
end

    dist1 = sum(dplate(:,3));

elseif size(plate,1)<=1
    dist1 = 0;
end
```

```
if size(plate,1)>1

%% 6 - Time water is impacting the plate.
ytime(1) = ylimi(2)-((plate(1,2)-z2(1))/(dir(3)/dir(2)));    % y1=y2-(z2-z1)/m
ytime(2) = ylimi(2)-((plate(end,2)-z2(1))/(dir(3)/dir(2)));

thetaimpactlimit(1) = asin(ytime(1)/radius);
thetaimpactlimit(2) = asin(ytime(2)/radius);

impacttime = (abs(thetaimpactlimit(2)-thetaimpactlimit(1)))/w;

vwater = veljet*((pi/4)*nd^2)*impacttime*1e3;  % Volume of water hitting a plate
(litres).


%% 7 - Dimensionless number calculations.

tauvis = impacttime/timeexposed;    %Effective impact time in vision area;
taulap = impacttime/turningtime;    %Effective impact lap time;

effimpactarea = dist1/dpl;  %Effective impact area;


%% 8 - Creation of output table

                                    %INPUTS
table(j,1) = ylimi(2);              % Plate position.
table(j,2) = rpl;                   % Plate width position.
table(j,3) = d;                     % Distance between plates.
table(j,4) = radius;                % Nozzle rotation radius. Nozzle position
table(j,5) = thetajet*180/pi;       % Theta jet angle.
table(j,6) = rhojet*180/pi;         % Rho jet angle.
table(j,7) = (A(j,2)-rpl)/(dpl/2);  % Nozzle-plate relative position.

                                    %OUTPUTS
table(j,8) = timeexposed;           % Time in vision area;
table(j,9) = impacttime;            % Time impacting the plate (sec);
table(j,10)= dist1;                 % Distance covered
table(j,11)= vwater;                % Total water input on plate (mm3);
table(j,12)= tauvis;                % Effective impact time in vision area;
DIMENSIONLESS.
table(j,13)= taulap;                % Effective impact time per lap; DIMENSIONLESS.
table(j,14)= effimpactarea;         % Effective impact area; DIMENSIONLESS.
table(j,15)= table(j,12)*table(j,14);   % Global efficiency.


elseif size(plate,1)<=1

                                    %INPUTS
table(j,1) = ylimi(2);              %Plate position.
table(j,2) = rpl;                   %Plate width position.
table(j,3) = d;                     %Distance between plates.
table(j,4) = radius;                %Nozzle rotation radius. Nozzle position
table(j,5) = thetajet*180/pi;       %Theta jet angle.
table(j,6) = rhojet*180/pi;         %Rho jet angle.
table(j,7) = (A(j,2)-rpl)/(dpl/2);  %Nozzle-plate relative position.

                                    %OUTPUTS
table(j,8) = timeexposed;           %Time in vision area;
table(j,9) = 0;                     %Time impacting the plate (sec);
table(j,10)= 0;                     %Distance covered. [mm]
table(j,11)= 0;                     %Total water input on plate (mm3);
table(j,12)= 0;                     %Effective impact time in vision area;
DIMENSIONLESS.
table(j,13)= 0;                     %Effective impact time per lap; DIMENSIONLESS.
table(j,14)= 0;                     %Effective impact area; DIMENSIONLESS.
table(j,15)= 0;                     %Global efficiency;

end

   clear x2; clear y2; clear z2; clear time


   %For plotting all impact points for an Spray Arm design

P1=[xplate zplate];
```

```
P1(:,3) = table(j,9);                % Time impacting plate. [s].
   P1(:,4) = table(j,10);               % Distance covered. [mm].
   P1(:,5) = table(j,15);               % Global Efficiency.

   if j==1
   P=[xplate zplate];
   P(:,3) = table(j,9);                % Time impacting plate. [s].
   P(:,4) = table(j,10);               % Distance covered. [mm].
   P(:,5) = table(j,15);               % Global Efficiency.
   end

   if j>1
   P=[P;P1];
   end


   clear xplate
   clear zplate


end
```

A.3. Appendix

The following appendix shows the different MATLAB routines used for the evaluation of the diffusional theories in *Chapter 6, section 6.3*.

Fick´s second law with moving boundaries

```
function [D,thickness,thickness_layer,total_mass,mass_layer,error_matrix,w_s,r2] = FDGfitdiffusion
(data);

%% Routine for the estimation of diffusion values for Gravimetric experiments.
    % FICK'S SECOND LAW.
    % Asumptions:
            % - Diffusion coefficient does not depend on thickness change or water concentration
(constant).
            % - Moving boundary conditions considered.


         % Input matrix (data).
            % Column1: time (min);
            % Column2: Total mass (g);

clc
clearvars -except data
close all


%% Input data transformations
E(:,1)  = data(:,1)*60;                  % Experimental time [s].
E(:,2)  = data(:,2)/1000;                % Experimental mass [kg].

m0      = E(1,2);                        % Initial mass. [kg]
mh2o0   = 0.11/1000;                     % Initial water content. [kg]
mdry    = m0 - mh2o0;                    % Dry mass. [kg]
h0      = 0.068/1000;                    % Initial layer thickness. [m]
hh2o0   = mh2o0 / (0.12*0.10*1000);      % Initial thickness of water layer. [m]
hdry    = h0-hh2o0;                      % Dry thickness. [m].


    % Obtention of equilibrium mass.
        a = size(E,1);
        mmax1 = zeros(size(E,1),1);
            for j= (a-1):1:a
                mmax1(j,1) = E(j,2);
            end
        mmax1(1:(a-2)) = [];
        mmax = mean (mmax1);
        mmax = mmax - mdry;  % Total water uptake at equilibrium


    % Obtention of water mass fraction.
        for i = 1:size(E,1)
         E(i,3) = (E(i,2)-mdry)/mdry;        % [kg.H2O/kg.dry]
        end


    % Obtention of water mass fraction equilibrium.
        a = size(E,1);
        wmax1 = zeros(size(E,1),1);
            for j= (a-1):1:a
                wmax1(j,1) = E(j,3);
            end
        wmax1(1:(a-2)) = [];
        wmax = mean (wmax1);                    % [kg.H2O/kg.dry]


    % Obtention of maximum stretch obtained.
        hmax = hdry + ((mdry*wmax)/(1000*0.10*0.12));   % [m].


    % Simulation time
        t    = data(end,1)*60;                % Total experimental time (s).
```

```
%% Initial evaluation.

    % Effective diffusion coefficient (DF)
     D1 = [1e-13:0.1e-13:9e-13];
     D2 = [1e-12:0.1e-12:9e-12];
     D3 = [1e-11:0.1e-11:9e-11];
     D4 = [1e-10:0.1e-10:9e-10];
     D  = [D1 D2 D3 D4]';


    loops = length(D)   % Number of loops in simulation.
    error_matrix = zeros(length(D),2);


    % Number or layers
        pointsz = 50;   % Establish the number of layers available.


    % Thickness matrices
        thickness       = zeros (300000,2);          % [s m].
        thickness(1,1)  = 0;                         % [s].
        thickness(1,2)  = h0;                        % [m].

        thickness_layer = zeros (300000,pointsz);    % [m].
        thickness_layer(1,:) = h0/pointsz;           % [m].


    % Water mass fraction matrix
        w_0      = E(1,3);               % Initial water mass fraction of the layers.[kg.H2O/kg.dry]
        w_inf    = wmax;                 % Water mass fraction at equilibrium. [kg.H2O/kg.dry]
        w_s      = zeros(300000,pointsz); % Layer thickness vector. [kg.H2O/kg.dry]

        w_s(1,:) = w_0;          % Initial condition - Initial water mass fraction of the layers.
        w_s(2:size(w_s,1),pointsz) = w_inf;       % BC 2: Top layer in equilibrium instantly.


    % Total mass and mass per layer matrices
        total_mass  = zeros(300000,2);               % Total Mass. [kg].
        total_mass(1,1) = 0;                         % Initial time. [s].
        total_mass(1,2) = m0;                        % Initial total mass. [kg].

        mass_layer  = zeros(300000,pointsz);         % Mass per layer. [kg].
        mass_layer(1,:) = m0/pointsz;                % Mass per layer. [kg].


%% Loop for solving the equation.
for k = 1:length(D);

    % PDE simulation
    tic
    h = 1; %counter

    while thickness(h,1) <= t

    delta_z = thickness(h,2)/pointsz;        % [m].
    delta_t = (0.5/D(k))*delta_z^2;          % [s].


        for j = 2:pointsz-1
        w_s(h,1) = w_s(h,2);                   % Boundary condition 1: no flux at the bottom layer.

        % Discretisation of the dif. equation
        w_s(h+1,j) =  w_s(h,j) + (D(k)*delta_t/delta_z^2)*(w_s(h,j+1)-2*w_s(h,j)+w_s(h,j-1));
        end

        w_s(h+1,1) = w_s(h,1);


        % Mass
        for j = 1:pointsz
        mass_layer(h+1,j)  =   mdry*(1+w_s(h+1,j))/pointsz;   % Mass per layer. [kg].
        end

        total_mass(h+1,1)  =   total_mass(h) + delta_t;       % [s].
        total_mass(h+1,2)  =   sum(mass_layer(h+1,:));        % [kg].



        % Thickness
        for j = 1:pointsz
        thickness_layer(h+1,j) = (((mdry*w_s(h+1,j))/(1000*0.10*0.12)) + hdry)/pointsz;     % [m].
        end

        thickness(h+1,1)  = thickness(h,1) + delta_t;      % [s].
        thickness(h+1,2)  = sum(thickness_layer(h+1,:));   % [m].

        h = h+1; % Counter
  end
    %Removal of extra rows
```

```
    thickness (h+1:end,:)       = [];
    thickness_layer (h+1:end,:) = [];
    total_mass (h+1:end,:)      = [];
    w_s (h+1:end,:)             = [];
    mass_layer (h+1:end,:)      = [];



    % Comparison between real and simulated data
    thickness(:,2) = thickness(:,2)*1e6;                    % [µm].

    closest = zeros(size(E,1),1);
    for i=1:size(E,1)
        val = E(i,1);                                       % Value to find [s].
        tmp = abs(total_mass(:,1)-val);
        [idx idx] = min(tmp);                               % Index of the closest value.
        closest(i,1) = idx;
    end

    B = zeros (size(E,1),2);                        % Simulation results matrix.
    B(:,1) = total_mass(closest,1);                 % Column 1: Time [s].
    B(:,2) = total_mass(closest,2);                 % Column 2: Mass [kg].



    % Calculate R2 for fitting.
    yresid = E(:,2) - B(:,2);
    SSresid = sum(yresid.^2);
    SStotal = (length(E(:,2))-1) * var(E(:,2));
    rsq = 1 - SSresid/SStotal;                          % R2.

    error_matrix(k,1) = D(k);
    error_matrix(k,2) = rsq;



    % Re-start simulation matrices
        % Thickness matrices
        thickness       = zeros (300000,2);             % [s m].
        thickness(1,1)  = 0;                            % [s].
        thickness(1,2)  = h0;                           % [m].

        thickness_layer = zeros (300000,pointsz);
        thickness_layer(1,:) = h0/pointsz;              % [m].


        % Water mass fraction matrix
        w_0      = E(1,3);                              % Initial water mass fraction of the layers.
        w_inf    = wmax;                                % Water mass fraction at equilibrium.
        w_s      = zeros(300000,pointsz);               % Layer thickness vector.

        w_s(1,:) = w_0;           % Initial condition - Initial water mass fraction of the layers.
        w_s(2:size(w_s,1),pointsz) = w_inf;           % BC2: Top layer in equilibrium inmediatly.


        % Total mass, mass per layer matrices
        total_mass  = zeros(300000,2);                  % Total Mass. [kg].
        total_mass(1,1) = 0;                            % Initial time. [s].
        total_mass(1,2) = m0;                           % Initial total mass. [kg].

        mass_layer  = zeros(300000,pointsz);            % Mass per layer. [kg].
        mass_layer(1,:) = m0/pointsz;                   % Mass per layer. [kg].



        toc

        % Evolution of the fitting.
        if k == ceil(loops/10)
            disp('10% COMPLETE')
        elseif k == ceil(2*loops/10)
            disp('20% COMPLETE')
        elseif k == ceil(3*loops/10)
            disp('30% COMPLETE')
        elseif k == ceil(4*loops/10)
            disp('40% COMPLETE')
        elseif k == ceil(5*loops/10)
            disp('50% COMPLETE')
        elseif k == ceil(6*loops/10)
            disp('60% COMPLETE')
        elseif k == ceil(7*loops/10)
            disp('70% COMPLETE')
        elseif k == ceil(8*loops/10)
            disp('80% COMPLETE')
        elseif k == ceil(9*loops/10)
            disp('90% COMPLETE')
        end

end
```

```
    %% Choose lowest error aproximation.
tic

r2  = max (error_matrix(:,2));          % Find maximum R2 value.
d   = find (error_matrix(:,2)==r2);     % Find row with highest R2.

clear D, clear B, clear delta_t, clear delta_z, clear i, clear j, clear k

D = error_matrix(d,1);                  % Effective diffusion coefficient with highest R2.


    h = 1; %counter

    while thickness(h,1) <= t

    delta_z = thickness(h,2)/pointsz;   % [m].
    delta_t = (0.5/D)*delta_z^2;        % [s].


        for j = 2:pointsz-1
        w_s(h,1) = w_s(h,2);            % BC 1: no flux at the bottom layer.

            % Discretisation of the dif. equation
        w_s(h+1,j) =  w_s(h,j) + (D*delta_t/delta_z^2)*(w_s(h,j+1)-2*w_s(h,j)+w_s(h,j-1));
        end

        w_s(h+1,1) = w_s(h,1);


        % Mass
        for j = 1:pointsz
        mass_layer(h+1,j)  =   mdry*(1+w_s(h+1,j))/pointsz;   % Mass per layer. [kg].
        end

        total_mass(h+1,1)  =   total_mass(h) + delta_t;       % [s].
        total_mass(h+1,2)  =   sum(mass_layer(h+1,:));        % [kg].



        % Thickness
        for j = 1:pointsz
        thickness_layer(h+1,j) = (((mdry*w_s(h+1,j))/(1000*0.10*0.12)) + hdry)/pointsz;     % [m].
        end

        thickness(h+1,1)  = thickness(h,1) + delta_t;      % [s].
        thickness(h+1,2)  = sum(thickness_layer(h+1,:));   % [m].

        h = h+1; % Counter

    end


    %Removal of extra rows
    thickness (h+1:end,:)       = [];
    thickness_layer (h+1:end,:) = [];
    total_mass (h+1:end,:)      = [];
    w_s (h+1:end,:)             = [];
    mass_layer (h+1:end,:)      = [];


    % Comparison between real and simulated data
    thickness(:,1) = thickness(:,1)/60;                     % [min].
    thickness(:,2) = thickness(:,2)*1e6;                    % [µm].

    total_mass(:,1)= total_mass(:,1)/60;                    % [min].
    total_mass(:,2)= total_mass(:,2)*1000;                  % [g].
```

Linear poroelasticity theory

```
function [D,error_matrix,r2] = FDGswellinglintheory (data);

%% Routine for the estimation of diffusion values for sFDG experiments.
    % LINEAR POROELASTICITY THEORY.
        % Input matrix
            % Column1: time (min);
            % Column2: height (mm);

clc
close all

%% INITIAL MODIFICATIONS
    % Matrix E
            % Column 1: Time. [s].
            % Column 2: Thickness. [m].
            % Column 3: Thickness increase. [m].

    % Unit transformations.
E      = data;
E(:,1) = E(:,1)*60;       % Time. [s].
E(:,2) = E(:,2)/1000;     % Height. [m].


    % Initial thickness.
%h0=E(1,2);               % Initial Thickness from data (m). NOT CONSTANT.
h0=0.075/1000;            % Initial Thickness. [m]. CONSTANT.


    % Thickness increase.
E(:,3)=E(:,2)-h0;         % h(t)-h(0). [m].


    % Thickness at equilibrium.
a   = size(E,1);
delta_inf1 = zeros (a,1);
    for j  = (a-10):1:a
         delta_inf1(j) = E(j,3);
    end
delta_inf1(1:(a-11)) = [];
delta_inf            = mean (delta_inf1);  %[m].
clear a; clear delta_inf1;

% delta_inf = ((1 - 2*poisson_ratio)*(mu - mu_0) * H) / (2 * (1-poisson_ratio) * G * omega)


    % Other variables.
exp_time = E(end,1);          % Experimental time. [s].
time     = (0:1:exp_time)';   % Time vector. [s].



%% LINEAR THEORY EQUATION
    % Effective diffusion coefficient.
    D1 = [1e-17:0.1e-17:9e-17];
    D2 = [1e-16:0.1e-16:9e-16];
    D3 = [1e-15:0.1e-15:9e-15];
    D4 = [1e-14:0.1e-14:9e-14];
    D5 = [1e-13:0.1e-13:9e-13];
    D6 = [1e-12:0.1e-12:9e-12];
    D  = [D1 D2 D3 D4 D5 D6]';  % [m2/s].


    loops = length(D)   % Number of loops in simulation.
    h = 1; %counter

    error_matrix = zeros(length(D),2);


% Loop for obtaining results.
for i = 1:length(D);
    tic

    tau = (h0^2)./D;        % Characteristic time scale. [s].

    % Seconds term
    for j=1:size(time,1)
        A=zeros(15,1);

        for k=1:size(A,1);
        A(k)=(1/((2*(k-1)+1)^2)) * exp(-(((2*(k-1)+1)^2)*(time(j)*(pi^2)/(4*tau(i)))));
        end

        a(j,1)=sum(A);
        clear A

    end
```

```
    second_term = zeros(length(time),1);
    second_term = (1-((8/pi^2)*a));


B = zeros (length(time), 2);        % Simulation results matrix.
B(:,1) = time;                      % Column 1: Time. [s].
B(:,2) = delta_inf * second_term;   % Column 2: Thickness increase. [m].


    % Comparison
    clear a
    for m=1:size(E,1)
    b(m)=find(B(:,1)==E(m,1));      % Find same time values in both Real and Simulation matrices.
    end

    b=b';
    B1=B(b,:);                      % Simulation matrix with just 'Same time' values.


    % Calculate R2 for fitting.
     yresid = E(:,3) - B1(:,2);
     SSresid = sum(yresid.^2);
     SStotal = (length(E(:,3))-1) * var(E(:,3));
     rsq = 1 - SSresid/SStotal;

     error_matrix(i,1) = D(i);
     error_matrix(i,2) = rsq;



     % Evolution of the fitting.
        if h == ceil(loops/10)
            disp('10% COMPLETE')
        elseif h == ceil(2*loops/10)
            disp('20% COMPLETE')
        elseif h == ceil(3*loops/10)
            disp('30% COMPLETE')
        elseif h == ceil(4*loops/10)
            disp('40% COMPLETE')
        elseif h == ceil(5*loops/10)
            disp('50% COMPLETE')
        elseif h == ceil(6*loops/10)
            disp('60% COMPLETE')
        elseif h == ceil(7*loops/10)
            disp('70% COMPLETE')
        elseif h == ceil(8*loops/10)
            disp('80% COMPLETE')
        elseif h == ceil(9*loops/10)
            disp('90% COMPLETE')
        end


     h = h+1; % Counter
     toc
end



%% Choose lowest error aproximation.

r2 = max(error_matrix(:,2));          % Find maximum R2 value.
d  = find (error_matrix(:,2)==r2);    % Find row with maximum R2 value.

clear D
D = error_matrix(d,1);

clear tau; clear a; clear second_term; clear B;

    tau = (h0^2)/D;         % Characteristic time scale. [s].

    % Second term
    for j=1:size(time,1)
        A=zeros(15,1);

        for k=1:size(A,1);
        A(k)=(1/((2*(k-1)+1)^2)) * exp(-(((2*(k-1)+1)^2)*(time(j)*(pi^2)/(4*tau))));
        end

        a(j,1)=sum(A);
        clear A
    end

    second_term = zeros(length(time),1);
    second_term = (1-((8/pi^2)*a));


B = zeros (length(time), 2);        % Simulation results matrix.
B(:,1) = time;                      % Column 1: Time (seconds).
B(:,2) = delta_inf * second_term;   % Column 2: Thickness increase (m).
```

```
%% Plot results.

B(:,1) = B(:,1)/60; B(:,2) = B(:,2)*1000;                        % Time into min / Thickness into mm.
E(:,1) = E(:,1)/60; E(:,2) = E(:,2)*1000; E(:,3) = E(:,3)*1000;  % Time into min / Thickness into mm.


% Real vs simulated swelling.
figure(1)
axes('FontSize',24,'FontName','Calibri')
set(gcf,'Color',[1,1,1])
plot(B(:,1),B(:,2),'.g','markersize',8)
hold on
plot(E(:,1),E(:,3),'.r','markersize',8)
hold on
%xlim([0 10000])
%ylim([0 1])
%set(gca,'XDir','reverse');
title('SWELLING OVER TIME','FontWeight','bold','FontSize',20,'FontName','Calibri',...
    'FontAngle','normal')
xlabel('Time, (min)','FontWeight','bold','FontSize',20,'FontName','Calibri',...
    'FontAngle','normal')
ylabel('Thickness increase, (mm)','FontWeight','bold','FontSize',20,'FontName','Calibri',...
    'FontAngle','normal')
h=legend('Fitted data','Experimental data', 'Location', 'Southeast')
    set(h,'FontSize',22,'FontName','Calibri','FontAngle','normal')
hold on


% R2 profile
figure(2)
axes('FontSize',24,'FontName','Calibri')
set(gcf,'Color',[1,1,1])
semilogx (error_matrix(:,1),error_matrix(:,2),'.b','markersize',8)
xlabel('Effective Diffusion, (m2/s)','FontWeight','bold','FontSize',20,'FontName','Calibri',...
    'FontAngle','normal')
ylabel('R-squared','FontWeight','bold','FontSize',20,'FontName','Calibri',...
    'FontAngle','normal')
hold on
```

Non-linear poroelasticity theory

```
function
[thickness,lambda_s,lambda_lin,lambda_0,lambda_inf,error_matrix,error_matrix2,D,D_linear,chi,n,omega,
r2,d,loops,rsq_matrix] = FDGnonlinear3(data);

%% Routine to solve Bouklas(2010) non-linear equation for swelling samples.
    %% Iteration to obtain D, chi and n*omega parameters.

        % Input matrix
            % Column1: Time (min).
            % Column2: Thickness (mm).

        % Forward difference in time and second order central difference for X
        % domain. Explicit algorithm.

        % BOUNDARY CONDITIONS

            % IC: at any X; t = 0; lambda = lambda_0;
            % BC1: at any t; X = 0; dlambda/dX = 0;        ** No flux at the bottom **
            % BC2: at any t; X = H; lambda = lambda_inf    ** Instantaneous equilibrium at the upper
surface **



clearvars -except data
close all;
clc;



%% 1. INITIAL DEFINITIONS
E      = data;
E(:,1) = E(:,1)*60;             % Time in seconds [s].


%Thickness
    hh2o0 = 0.009/1000;         % Initial water thickness. [m].
    h_0   = E(1,2)/1000;        % Initial experimental sample thickness. [m].
    h     = h_0-hh2o0;          % Dry sample thickness [m].

% Flory-Huggins parameter.
    chi   = [0:0.05:1.2];

% Effective number of polymer chains per unit volume
    n1    = [1e25:1e25:9e25];
    n2    = [1e26:1e26:9e26];
    n3    = [1e27:1e27:9e27];
    n     = [n1 n2 n3];         % [chains/m3].

% Volume per solvent molecule
    omega = 3e-29;              % [m3/water.molecule].

% Diffusion coefficient
   D1 = [1e-13:1e-13:9e-13];
   D2 = [1e-12:1e-12:9e-12];
   D3 = [1e-11:1e-11:9e-11];
   D4 = [1e-10:1e-10:9e-10];
   D  = [D1 D2 D3 D4]';

% Simulation time
   t     = 180;                 % Simulation time [min].
   t     = t * 60;              % Simulation time [sec].

% Obtention of equilibrium thickness.
   a = size(E,1);
   for j= (a-10):1:a
    hmax(j) = E(j,2);
   end
   hmax(1:(a-11)) = [];
   hmax1 = mean (hmax)/1000;  % Thickness equilibrium value [m].


   % Stretch
   lambda_0   = h_0/h;          % Initial stretch.
   lambda_inf = hmax1/h;        % Equilibrium stretch.


   % Loops & Error Matrix
   loops        = length(D)*length(chi)*length(n)  % Number of loops in simulation.
   error_matrix = zeros(loops,6);
```

```
%%  2. SOLUTION OF PDE
counter = 1;                    % Counter

 for k = 1:length(D);
     for l = 1:length(n);
         for v = 1:length(chi);
    tic

    % Initial iteration for Deltas. Optimising computational cost.
    t1 = [1 0.5 0.2 0.1 0.05 0.02 0.01 0.005 0.002 0.001 0.0005 0.0002 0.0001 0.00005 0.00002];
    t2 = [1 2 5 10 20 30 60 120 300 600];

    delta_t   = t1(1);                    % Size of time step to match stability criteria
    delta_X   = sqrt(D(k)*delta_t/0.5);   % Size of position step to match stability criteria
    pointsX   = h./delta_X;
    i1=2; i2=2;


    while pointsX < 20        % Cases where diffusion values are high. (E-7; E-8; E-9).
    delta_t   = t1(i1);
    delta_X   = sqrt(D(k)*delta_t/0.5);
    pointsX   = h/delta_X;
    i1=i1+1;
    end

    while pointsX > 60        % Cases where diffusion values are low. (E-13; E-14).
    delta_t   = t2(i2);
    delta_X   = sqrt(D(k)*delta_t/0.5);
    pointsX   = h/delta_X;
    i2=i2+1;
    end

    t_d       = [0:delta_t:t];     % Discretised time domain. Time vector.
    X_d       = [0:delta_X:h];     % Discretised spatial domain


    % Stretch at equilibrium value.
    lambda_s      = zeros(length(t_d),length(X_d));     % STRETCH VECTOR.
    lambda_s(1,:) = lambda_0;                           % INITIAL BOUNDARY CONDITION. t=0

    thickness = zeros(length(t_d),1);                   % THICKNESS.[m].


    lambda_s(2:length(t_d),length(X_d)) = lambda_inf;   % BC1: Instantaneous equilibrium swelling
ratio at the upper surface.


    % Non-linear equation solver.
    for i = 1:length(t_d)-1
       for j = 2:length(X_d)-1
       lambda_s(i,1) = lambda_s(i,2);   % BC2: No flux at the bottom layer.

       lambda_A = (lambda_s(i,j+1)+lambda_s(i,j))/2;
       lambda_B = (lambda_s(i,j)+lambda_s(i,j-1))/2;

       xiA = (1/(lambda_0^2 * lambda_A^4)) - ((2*chi(v)*((lambda_0^2 * lambda_A)-1))/(lambda_0^4 *
lambda_A^5)) + (n(l)*omega*((lambda_0^2 * lambda_A)-1)*((lambda_A^2)+1))/(lambda_0^2 * lambda_A^4);
       xiB = (1/(lambda_0^2 * lambda_B^4)) - ((2*chi(v)*((lambda_0^2 * lambda_B)-1))/(lambda_0^4 *
lambda_B^5)) + (n(l)*omega*((lambda_0^2 * lambda_B)-1)*((lambda_B^2)+1))/(lambda_0^2 * lambda_B^4);
       lambda_s(i+1,j) = lambda_s(i,j) +
((D(k)*(lambda_0^2)*delta_t)/delta_X^2)*((xiA*(lambda_s(i,j+1)-lambda_s(i,j))) - xiB*(lambda_s(i,j)-
lambda_s(i,j-1)));

       end
    end

    lambda_s(end,1) = lambda_s(end-1,1);      % Final value. Close loop.


    % Obtention of total thickness
    for i = 1:length(t_d)
         thickness(i,1) = t_d(i);                                          % Time. [s].
         thickness(i,2) = ((sum(lambda_s(i,:))*h)/length(X_d))*1000;       % Thickness. [mm].
    end


    % Comparison with experimental data
    B = thickness;

    clear a
    for m = 1:size(E,1)
    b(m) = find(B(:,1)==E(m,1));      % Find same time values in both Real and Simulation matrices.
    end

    b  = b';
    B1 = B(b,:);


    % Calculate R2.
     yresid = E(:,2) - B1(:,2);
```

```
     SSresid = sum(yresid.^2);
     SStotal = (length(E(:,2))-1) * var(E(:,2));
     rsq = 1 - SSresid/SStotal;

     error_matrix(counter,1) = D(k);
     error_matrix(counter,2) = n(l);
     error_matrix(counter,3) = chi(v);
     error_matrix(counter,4) = omega;
     error_matrix(counter,5) = rsq;
     counter=counter+1;

     clear yresid, clear SSresid, clear SStotal, clear rsq


    % Calculation of lambda_inf condition.
    A_inf = log((((lambda_0^2)*lambda_inf)-1)/((lambda_0^2)*lambda_inf));
    B_inf = 1/((lambda_0^2)*lambda_inf);
    C_inf = chi(v)/((lambda_0^4)*(lambda_inf^2));
    D_inf = ((n(l)*omega)/(lambda_0^2))*(lambda_inf - (1/lambda_inf));

    result = A_inf + B_inf + C_inf + D_inf;
    error_matrix(counter,6) = result;


    clear a; clear b; clear c; clear d; clear A_inf; clear B_inf; clear C_inf; clear D_inf;

    toc


    % Evolution of the fitting.
        if counter == ceil(loops/10)
            disp('10% COMPLETE')
        elseif counter == ceil(2*loops/10)
            disp('20% COMPLETE')
        elseif counter == ceil(3*loops/10)
            disp('30% COMPLETE')
        elseif counter == ceil(4*loops/10)
            disp('40% COMPLETE')
        elseif counter == ceil(5*loops/10)
            disp('50% COMPLETE')
        elseif counter == ceil(6*loops/10)
            disp('60% COMPLETE')
        elseif counter == ceil(7*loops/10)
            disp('70% COMPLETE')
        elseif counter == ceil(8*loops/10)
            disp('80% COMPLETE')
        elseif counter == ceil(9*loops/10)
            disp('90% COMPLETE')
        end


         end
     end
 end


%% 3. FINAL ESTIMATION. LOWEST ERROR VALUE.

    % Lambda_inf Condition.
    error_matrix2 = error_matrix;

    a = find (error_matrix2(:,6)<0.12);
    clear error_matrix
    error_matrix = error_matrix2(a,:);


    % Searching for best fit.
    r2 = max(error_matrix(:,5));
    d  = find (error_matrix(:,5)==r2);

    clear D

    D = error_matrix(d,1);      % [m2/s].
    D(2:end,:) = [];

    n = error_matrix(d,2);      % [m-3].
    n(2:end,:) = [];

    chi = error_matrix(d,3);
    chi(2:end,:) = [];

    clear tau; clear a; clear B;


    t1 = [1 0.5 0.2 0.1 0.05 0.02 0.01 0.005 0.002 0.001 0.0005 0.0002 0.0001 0.00005];
    t2 = [1 2 5 10 20 30 60 120 300];

    delta_t   = t1(1);                % Size of time step to match stability criteria
    delta_X   = sqrt(D*delta_t/0.5);  % Size of position step to match stability criteria
```

```
    pointsX   = h./delta_X;
    i1=2; i2=2;


    while pointsX < 20        % Cases where diffusion values are high. (E-7; E-8; E-9).
    delta_t   = t1(i1);
    delta_X   = sqrt(D*delta_t/0.5);
    pointsX   = h/delta_X;
    i1=i1+1;
    end

    while pointsX > 60        % Cases where diffusion values are low. (E-13; E-14).
    delta_t   = t2(i2);
    delta_X   = sqrt(D*delta_t/0.5);
    pointsX   = h/delta_X;
    i2=i2+1;
    end

    t_d       = [0:delta_t:t];       % Discretised time domain. Time vector.
    X_d       = [0:delta_X:h];     % Discretised spatial domain


    % Stretch at equilibrium value.
    lambda_s  = zeros(length(t_d),length(X_d));         % STRETCH VECTOR.
    lambda_s(1,:) = lambda_0;                           % INITIAL BOUNDARY CONDITION. t=0

    thickness = zeros(length(t_d),1);                   % THICKNESS. [m].

    lambda_s(2:length(t_d),length(X_d)) = lambda_inf;   % BC 1: Instantaneous equilibrium swelling
ratio at the upper surface.


    % Non-linear equation solver.
    for i = 1:length(t_d)-1
       for j = 2:length(X_d)-1
       lambda_s(i,1) = lambda_s(i,2);    % BC2: No flux at bottom layer.

       lambda_A = (lambda_s(i,j+1)+lambda_s(i,j))/2;
       lambda_B = (lambda_s(i,j)+lambda_s(i,j-1))/2;

       xiA = (1/(lambda_0^2 * lambda_A^4)) - ((2*chi*((lambda_0^2 * lambda_A)-1))/(lambda_0^4 *
lambda_A^5)) + (n*omega*((lambda_0^2 * lambda_A)-1)*((lambda_A^2)+1))/(lambda_0^2 * lambda_A^4);
       xiB = (1/(lambda_0^2 * lambda_B^4)) - ((2*chi*((lambda_0^2 * lambda_B)-1))/(lambda_0^4 *
lambda_B^5)) + (n*omega*((lambda_0^2 * lambda_B)-1)*((lambda_B^2)+1))/(lambda_0^2 * lambda_B^4);
       lambda_s(i+1,j) = lambda_s(i,j) + ((D*(lambda_0^2)*delta_t)/delta_X^2)*((xiA*(lambda_s(i,j+1)-
lambda_s(i,j))) - xiB*(lambda_s(i,j)-lambda_s(i,j-1)));
       end
    end

    lambda_s(end,1)=lambda_s(end-1,1);      % Final value. Close loop.


    for i = 1:length(t_d)
         thickness(i,1)= t_d(i);                                        % Time. [s].
         thickness(i,2)= ((sum(lambda_s(i,:))*h)/length(X_d))*1000;     % Thickness. [mm].
    end

    B = thickness;


%% 4. ERROR VARIATION MATRIX

a = find (error_matrix (:,5) > 0);

rsq_matrix      = zeros(length(a),5);
rsq_matrix(:,1) = error_matrix(a,5);                % R2
rsq_matrix(:,2) = error_matrix(a,1);                % D. [m2/s].
rsq_matrix(:,3) = error_matrix(a,3);                % Chi.
rsq_matrix(:,4) = error_matrix(a,2);                % n. [m2].
rsq_matrix(:,5) = error_matrix(a,6);                % Lambda_inf condition.


%% 5. D_linear vs. D_nonlinear

lambda_lin  = (lambda_0+lambda_inf)/2;
xi_lin      = (1/(lambda_0^2 * lambda_lin^4)) - ((2*chi*((lambda_0^2 * lambda_lin)-1))/(lambda_0^4 *
lambda_lin^5)) + (n*omega*((lambda_0^2 * lambda_lin)-1)*((lambda_lin^2)+1))/(lambda_0^2 *
lambda_lin^4);

D_linear = D * xi_lin;
```

```
%% 6. PLOTS
thickness(:,1)=thickness(:,1)/60;                    % Time into minutes. [min].


%   Swelling over time
figure(1)
axes('FontSize',24,'FontName','Calibri')
set(gcf,'Color',[1,1,1])
plot(thickness(:,1),thickness(:,2),'.g','markersize',8)
hold on
plot(data(:,1),data(:,2),'.r','markersize',8)
hold on
% xlim([0 10000])
% ylim([0 1])
title('THICKNESS OVER TIME','FontWeight','bold','FontSize',20,'FontName','Calibri',...
    'FontAngle','normal')
xlabel('Time, (min)','FontWeight','bold','FontSize',20,'FontName','Calibri',...
    'FontAngle','normal')
ylabel('Thickness, (mm)','FontWeight','bold','FontSize',20,'FontName','Calibri',...
    'FontAngle','normal')
ylim([0 0.8])
h=legend('Model prediction','Experimental data');
    set(h,'FontSize',22,'FontName','Calibri','FontAngle','normal')
hold on


%   R2 vs D
figure(2)
axes('FontSize',24,'FontName','Calibri')
set(gcf,'Color',[1,1,1])
semilogx (rsq_matrix(:,2),rsq_matrix(:,1),'.b','markersize',8)
xlabel('Effective Diffusion, D(m2/s)','FontWeight','bold','FontSize',20,'FontName','Calibri',...
    'FontAngle','normal')
ylabel('R-squared','FontWeight','bold','FontSize',20,'FontName','Calibri',...
    'FontAngle','normal')
ylim([0 1])
hold on


%   R2 vs Chi
figure(3)
axes('FontSize',24,'FontName','Calibri')
set(gcf,'Color',[1,1,1])
plot (rsq_matrix(:,3),rsq_matrix(:,1),'.b','markersize',8)
xlabel('Flory-Huggins Parameter','FontWeight','bold','FontSize',20,'FontName','Calibri',...
    'FontAngle','normal')
ylabel('R-squared','FontWeight','bold','FontSize',20,'FontName','Calibri',...
    'FontAngle','normal')
hold on


%   R2 vs n
figure(4)
axes('FontSize',24,'FontName','Calibri')
set(gcf,'Color',[1,1,1])
semilogx (rsq_matrix(:,4),rsq_matrix(:,1),'.b','markersize',8)
xlabel('Polymer Chains Per Unit Volume (m-
3)','FontWeight','bold','FontSize',20,'FontName','Calibri',...
    'FontAngle','normal')
ylabel('R-squared','FontWeight','bold','FontSize',20,'FontName','Calibri',...
    'FontAngle','normal')
hold on



%   Lambda Inf. Constraint vs n
figure(5)
axes('FontSize',24,'FontName','Calibri')
set(gcf,'Color',[1,1,1])
plot(rsq_matrix(:,5),rsq_matrix(:,1),'.b','markersize',8)
xlabel('Lambda Inf. Constraint','FontWeight','bold','FontSize',20,'FontName','Calibri',...
    'FontAngle','normal')
ylabel('R-squared','FontWeight','bold','FontSize',20,'FontName','Calibri',...
    'FontAngle','normal')
hold on



%   R2 vs D
figure(6)
axes('FontSize',24,'FontName','Calibri','XScale','log','XMinorTick','on','XGrid','on')
set(gcf,'Color',[1,1,1])
hold on
semilogx (error_matrix2(:,1),error_matrix2(:,5),'MarkerSize',8,'LineWidth',3,'Color',[0 0 0])
xlabel('Effective Diffusion, D(m2/s)','FontWeight','bold','FontSize',20,'FontName','Calibri',...
    'FontAngle','normal')
ylabel('R-squared','FontWeight','bold','FontSize',20,'FontName','Calibri',...
    'FontAngle','normal')
ylim([0 1])
xlim([1e-10 1e-9])
```

```
hold on
box on


%   R2 vs Chi
figure(7)
axes('FontSize',24,'FontName','Calibri')
set(gcf,'Color',[1,1,1])
hold on
plot(error_matrix2(:,3),error_matrix2(:,5),'MarkerSize',8,'LineWidth',3,'Color',[0 0 0])
xlabel('Flory-Huggins Parameter','FontWeight','bold','FontSize',20,'FontName','Calibri',...
    'FontAngle','normal')
ylabel('R-squared','FontWeight','bold','FontSize',20,'FontName','Calibri',...
    'FontAngle','normal')
ylim([0 1])
xlim([0 2.5])
hold on
box on


%   R2 vs n
figure(8)
axes('FontSize',24,'FontName','Calibri','XScale','log','XMinorTick','on','XGrid','on')
set(gcf,'Color',[1,1,1])
hold on
semilogx(error_matrix2(:,2),error_matrix2(:,5),'MarkerSize',8,'LineWidth',3,'Color',[0 0 0])
xlabel('Polymer Chains Per Unit Volume (m-
3)','FontWeight','bold','FontSize',20,'FontName','Calibri',...
    'FontAngle','normal')
ylabel('R-squared','FontWeight','bold','FontSize',20,'FontName','Calibri',...
    'FontAngle','normal')
ylim([0 1])
xlim([1e25 1e29])
hold on
box on


disp ('100% COMPLETE')
```

A.4. Appendix

The following appendix shows the MATLAB routine used for the swelling-removal model developed in *Chapter 6, section 6.4*.

```
%% Script to estimate swelling-removal model predictions.
    %% Version 2.0 - Raul Perez Mohedano

     % Input data:
            % Data1:    Removal matrix.
                    % Column 1: Time [=] min.
                    % Column 2: Thickness [=] mm.
            % exptime:  Simulation time considered [=] min.
            % hmax1:    Equilibrium thickness [=] mm.
            % nz:       Number of theoretical layers considered.
            % k1:       Shear stress removal rate [=] µm/min.
            % k2:       Soil dissolution removal rate [=] µm/min.


clearvars -except data1
close all
clc;

E1 = data1;                                     % Matrix to use in further calculations.

%% INTIAL DEFINITIONS
% Initial conditions
exptime = input('Experimental time (min): ');   % Time vector. [min].
h    = 0.59e-4;                                 % Dry sample thickness. [m].
h0   = 1.15*h;                                  % Initial experimental sample thickness. [m].

% Stretch
lambda_0   = h0/h;                              % Initial stretch.


% Obtention of equilibrium thickness.
hmax1 = input('Equilibrium thickness (µm): ');  % Equilibrium thickness. [µm].
hmax1 = hmax1/1e6;                              % Equilibrium thickness. [m].
lambda_inf = hmax1/h;                           % Equilibrium stretch.


%Parameters for non-linear swelling equation.
display('Check your non-linear theory parameters')

chi   = 0.9;                                    % Interaction parameter.
n     = 6e26;                                   % Effective number of polymer chains per unit volume.
[chains/m3].
omega = 3e-29;                                  % Volume per solvent molecule. [m3/water.molecule].
D_s   = 2.5e-10;                                % Diffusion coefficient. [m2/s].


% Timings - LINEAR INCREASE FOR REMOVAL (1/2)
tremoval  = 7.5;                                % Time for removal to start. [min].
tincrease = 7;                                  % Increasing time to get to maximum removal. [min].
tmaximum  = tremoval + tincrease;               % Time to reach maximum removal rate. [min].



% Theoretical layers and PDE criteria
nz        = input ('number of theoretical layers considered: ');        % Number of grid points in z
domain
nz1       = nz;                                                         % Number of layers still
available.

delta_z   = h/nz;                               % Size of each grid point. [m].
z_d       = [0:delta_z:h];                      % Discretised spatial domain. [m].
delta_t   = 0.5*delta_z^2/D_s                   % Time step to match stability criteria. [s].
t         = exptime*60;                         % Experimental time. [s].
t_d       = [0:delta_t:t];                      % Time vector. [s].



% Timings - LINEAR INCREASE FOR REMOVAL (1/2)
a = find(t_d >= tremoval*60);                   % Find time value for end of lag time. [s].
a1 = a(1);
clear a

a = find(t_d >= tmaximum*60);                   % Find time value for end of increase of removal
rate.†[s].
a2 = a(1);
clear a
```

```
% Layer Thickness matrix
z_s_0  = h/nz;                                  % Initial thickness of the layers. [m].
z_inf  = hmax1/nz;                              % Maximum stretch per layer. [m].
z_s_01 = z_s_0 * 1000;                          % Initial thickness of theoretical layers. [mm].
z_inf1 = z_inf * 1000;                          % Maximum thickness of a theoritical layer. [mm].
z_s  = zeros(length(t_d),length(z_d));          % Layer thickness vector. OUTPUT MATRIX.


% Other possible outputs.
rho_h20 = 1;                                    % Water density. [g/cm3].
m_sat =  rho_h20 * (z_inf1 - z_s_01) / 10;      % Saturation mass of a theoretical layer. [g/cm2].

eggyolk_mass = 1.66;                            % Egg Yolk mass per tile. [g].
tile_area    = 12*10;                           % CFT tile area. [cm2].
eggyolk_mass_area  = eggyolk_mass/tile_area;    % Egg Yolk mass per tile area. [g/cm2].
eggyolk_mass_layer = eggyolk_mass_area / nz;    % Egg Yolk mass per area and per layer. [g/cm2 per
layer].
eggyolk_remaining  = zeros(size(t_d,2),2);      % Egg Yolk remaining matrix. OUTPUT MATRIX.

m_s = zeros(size(z_s,1),size(z_s,2));           % Water mass per layer. [g/cm2 per layer]
water_mass      = zeros(length(t_d)-1,1);       % Total water mass. [g].

cum_water_mass          = zeros (size(z_s,1),size(z_s,2));  % Cumulative water content per layer.
[g].
cum_thickness           = zeros (size(z_s,1),size(z_s,2));  % Cumulative thickness. [mm].
cum_water_mass_sat      = zeros (size(z_s,1),size(z_s,2));  % Cumulative saturated water content per
layer. [%].
relative_cum_water_mass = zeros (size(z_s,1),size(z_s,2));  % Relative cumulative total water mass.
[%].


% Output matrices.
thickness    = zeros(length(t_d),2);            % OUTPUT MATRIX [s mm].
total_mass   = zeros(length(t_d),2);            % OUTPUT MATRIX [s g].
removal      = zeros(length(t_d),4);            % OUTPUT MATRIX [s removal_rate layers_remaining
removal_carryover].
state_matrix = zeros(size(t_d,2),4);            % OUTPUT MATRIX [min cumulative_saturation
removal_rate frequency_function].


thickness(:,1) = t_d';                          % Time. [s].
thickness(1,2) = h*1000;                        % Thickness. [mm].

eggyolk_remaining(:,1) = t_d';                                  % Time. [s].
eggyolk_remaining(1,2) = nz1 * eggyolk_mass_layer * tile_area;  % Egg Yolk mass. [g].

total_mass(:,1) = t_d';                                         % Time. [s].
total_mass(1,2) = nz * eggyolk_mass_layer * tile_area;          % Total (soil + solvent) mass. [g].

removal(:,1) = t_d';                            % Time. [s].
state_matrix (:,1) = t_d';                      % Time. [s].



% Frequency function definitions
        interval_shear_start = 1.45;            % Start time of application of shear. [min].
        interval_shear_end   = 2;               % End time of application of shear.   [min].
        total_shear_interval = 3;               % Time length of repetition interval. [min].
        related_interval_shear_start = interval_shear_start / total_shear_interval;
        related_interval_shear_end   = interval_shear_end / total_shear_interval;


% Removal Rates definitions
k1 = input ('shear stress removal rate (µm/min): ');    % Shear stress removal rate. [µm/min].
k2 = input ('dissolution removal rate (µm/min): ');     % Soil dissolution removal rate. [µm/min].


% Initial boundary conditions
lambda_s      = zeros(length(t_d),length(z_d));  % Stretch matrix.
lambda_s(1,:) = lambda_0;                        % INITIAL BOUNDARY CONDITION (t=0).
z_s (1,:) = lambda_s(1,:) * z_s_0;               % INITIAL BOUNDARY CONDITION (t=0).


% Number of loops and counter
loops = length (t_d)                            % Number of loops.
counter = 1;


%% ALGORITHM
tic
for i=1:length(t_d)-1                           % LOOP FOR SOLVING PDE AND INTEGRATE MECHANISMS
    if nz1 >= 1
        %if thickness(i,2) > 0

    % BOUNDARY CONDITIONS
            if nz1<nz                                   % BOUNDARY CONDITION 1. INSTANT EQUILIBRIUM
AT UPPER LAYER.
                lambda_s(i+1,nz1+1) = lambda_s(i,nz1+1);
%               lambda_s(i+1,nz1+1) = (lambda_s(i,nz1)+lambda_s(i,nz1+1))/2;
```

```
%             lambda_s(i+1,nz1+1) = (lambda_s(i,nz1+1)+lambda_inf)/2;
            else
               lambda_s(i+1,nz1+1) = lambda_inf;
            end

            if i>1                                      % BOUNDARY CONDITION 2. NO FLUX AT BOTTOM
LAYER.
                lambda_s(i,1) = lambda_s(i-1,2);
                z_s (i,1) = z_s(i-1,2);
            end


    % SWELLING - NONLINEAR THEORY
            for j = 2:nz1
       %z_s(i+1,j) =  z_s(i,j) + (D_s*delta_t/delta_z^2)*(z_s(i,j+1)-2*z_s(i,j)+z_s(i,j-1));  % m

            % Non-linear equation solver.
                lambda_A = (lambda_s(i,j+1)+lambda_s(i,j))/2;
                lambda_B = (lambda_s(i,j)+lambda_s(i,j-1))/2;

                xiA = (1/(lambda_0^2 * lambda_A^4)) - ((2*chi*((lambda_0^2 * lambda_A)-
1))/(lambda_0^4 * lambda_A^5)) + (n*omega*((lambda_0^2 * lambda_A)-1)*((lambda_A^2)+1))/(lambda_0^2 *
lambda_A^4);
                xiB = (1/(lambda_0^2 * lambda_B^4)) - ((2*chi*((lambda_0^2 * lambda_B)-
1))/(lambda_0^4 * lambda_B^5)) + (n*omega*((lambda_0^2 * lambda_B)-1)*((lambda_B^2)+1))/(lambda_0^2 *
lambda_B^4);
                lambda_s(i+1,j) = lambda_s(i,j) +
((D_s*(lambda_0^2)*delta_t)/delta_z^2)*((xiA*(lambda_s(i,j+1)-lambda_s(i,j))) - xiB*(lambda_s(i,j)-
lambda_s(i,j-1)));
            end

                z_s (i+1,:) = lambda_s(i+1,:)* z_s_0;                   % [m].


    % WATER CONTENT IN SAMPLE OVER TIME
        % Water mass per layer.
            for j = 1:nz1+1
                m_s(i+1,j) =  rho_h20 * (z_s(i+1,j)-z_s_0) * 100;       % Water mass per layer.
[g/cm2].
            end

        % Total water mass in sample
            water_mass(i+1,1) = (sum(m_s(i+1,:))) * tile_area;          % Total water mass. [g].

        % Cumulative water content
            for j = 1:nz1+1
                cum_water_mass_sat (i+1,j) = m_sat * ((nz1+1)-(j-1));   % Cumulative water
saturation. [g/cm2].
            end

            for j = 1:nz1+1
                mini_m_s = zeros(1,(nz1+1)-(j-1));
                mini_cum_thickness = zeros(1,(nz1+1)-(j-1));

                mini_m_s = m_s(i,j:(nz1+1));
                mini_cum_thickness = z_s(i,j:(nz1+1)) * 1000;           % From top of the layer.
[mm].

                cum_water_mass (i+1,j) = sum (mini_m_s);                % Cumulative water mass (top
to bottom). [g/cm2].
                cum_thickness  (i+1,j) = sum (mini_cum_thickness);      % Cumulative thickness  (top
to bottom). [mm].

                clear mini_m_s; clear mini_cum_thickness;

                % Relative cumulative water content
                relative_cum_water_mass (i+1,j)= (cum_water_mass(i+1,j)/ cum_water_mass_sat(i+1,j)) *
100; % Saturation percentage. [%].
            end


     % FREQUENCY FUNCTION

            if i > 1
            interval_counter = ceil ((t_d(i+1)/(60*total_shear_interval)));  % [min/min].
            else
            interval_counter = 1;
            end

            inner_interval_time = ((t_d(i+1)/60)-((interval_counter-
1)*total_shear_interval))/total_shear_interval;

            if inner_interval_time >= related_interval_shear_start && inner_interval_time <=
related_interval_shear_end
                phiSS = 1;
                phiEA = 0;
            else
                phiSS = 0;
                phiEA = 1;
            end
```

```
    % SOIL DISSOLUTION

            if i > a1 && i < a2
                ke = (-k2/tincrease)*((t_d(i)-(tremoval*60))/60)/1000;  % Soil dissolution rate at
increase period. [mm/min].
                %ke = 0;  %[mm/min]
            elseif i > a1 && i > a2
                ke = -k2/1000;  %[mm/min]                               % Soil dissolution rate.
[mm/min].
            else
                ke = 0;
            end


    % SHEAR STRESS

            if i > a1 && i < a2
                kss = (-k1/tincrease)*((t_d(i)-(tremoval*60))/60)/1000; % Shear Stress rate at
increase period. [mm/min].
                %kss = 0;  %  [mm/min]
            elseif i > a1 && i > a2
                kss = -k1/1000; % [mm/min]                              % Shear Stress rate.
[mm/min].
            else
                kss = 0;
            end


 %% 3 - INTEGRATION OF DIFFERENT RATES

            removal(i+1,2)   = (phiSS*kss + phiEA*ke) * delta_t/60;     % Net removal in the loop.
[mm].
            thickness(i+1,2) = cum_thickness(i+1,1) + removal(i+1,2) ;  % Net thickness in the loop.
[mm].


            removal(i+1,3) = nz1;                                       % Number of layers remaining.
            c = find (removal(:,3) == nz1);
            %cum_shear_removal = zeros(c,1);
            cum_shear_removal = removal(c,2);
            removal(i+1,4) = sum(cum_shear_removal);
            clear cum_shear_removal


        % Output matrixes
            state_matrix (i+1,2) = relative_cum_water_mass (i+1,1);     % Saturation. [%]
            state_matrix (i+1,3) = removal(i+1,2);                      % Net removal in the loop.
[mm].
            state_matrix (i+1,4) = phiSS;                               % Frequency function.

            eggyolk_remaining(i+1,2) = nz1 * eggyolk_mass_layer * tile_area;    % Soil remaining.
[g].

            total_mass(i+1,2) = nz1 * eggyolk_mass_layer * tile_area + water_mass(i+1);  % Total
mass. [g].


        % Removal of theoretical layers
            d = find (cum_thickness(i+1,:) <= abs(removal(i+1,4)));

            if size(d,1) == 0
                nz1 = nz1;
            else
                d(2,:)= z_s(i+1,d);
                e = find(d(2,:) > 0);
                nz1 = nz1 - size(e,2);
            end
            clear d

        %end

    %end
     end


            % Evolution of the fitting.
        if counter == ceil(loops/10)
            disp('10% COMPLETE')
        elseif counter == ceil(2*loops/10)
            disp('20% COMPLETE')
        elseif counter == ceil(3*loops/10)
            disp('30% COMPLETE')
        elseif counter == ceil(4*loops/10)
            disp('40% COMPLETE')
        elseif counter == ceil(5*loops/10)
            disp('50% COMPLETE')
        elseif counter == ceil(6*loops/10)
            disp('60% COMPLETE')
```

```
        elseif counter == ceil(7*loops/10)
            disp('70% COMPLETE')
        elseif counter == ceil(8*loops/10)
            disp('80% COMPLETE')
        elseif counter == ceil(9*loops/10)
            disp('90% COMPLETE')
        end

        counter = counter + 1;

end
time = toc;

% g. moisture / g. dry solid.
moisture_content      = zeros(size(total_mass,1),size(total_mass,2));
moisture_content(:,1) = total_mass(:,1);                                                    % Time.
[min].
moisture_content(:,2) = (total_mass(:,2)-eggyolk_remaining(:,2))./eggyolk_remaining(1,2);   %
Moisture content. [g.water/g.soil].

% Cleaning percentage.
cleaning_percentage         = zeros(size(eggyolk_remaining,1),size(eggyolk_remaining,2));
cleaning_percentage (:,1)   = eggyolk_remaining(:,1);                                       % Time.
[min].
cleaning_percentage (:,2)   = ((eggyolk_remaining(1,2)-
eggyolk_remaining(:,2))./eggyolk_remaining(1,2))*100;  % Cleaning percentage. [%].



%% GOODNESS-OF-FIT SIMULATION

    thickness (:,1) = thickness(:,1)/60;     % Time into minutes. [min].
    B  = thickness;                          % Simulation matrix. [s mm].
%   E1(:,1)= E1(:,1) * 60;      % Time in seconds (s).

    % Time limitation. Fitting only when thickness is >0
    s1 = find(E1(:,2) < 0);
    s2 = E1(s1,1);
    s3 = find(B(:,1) > s2(1));

    if length (s3) > 0
    B(s3(1):end,:) = [];
    E1((s1+1):end,:) = [];
    end


    % Create more values for original experimental data matrix. Increase R2
    % sensitivity.
    % Interpolation 1
    t_new = linspace(E1(1,1),E1(end,1),2*size(E1,1)-1);
    thickness_new = interp1(E1(:,1), E1(:,2), t_new);
    E2(:,1) = t_new';                                   % Time. [min].
    E2(:,2) = thickness_new';                           % Thickness. [mm].


    % Interpolation 2
    t_new2 = linspace(E2(1,1),E2(end,1),2*size(E2,1)-1);
    thickness_new2 = interp1(E2(:,1), E2(:,2), t_new2);
    E3(:,1) = t_new2';                                  % Time. [min].
    E3(:,2) = thickness_new2';                          % Thickness. [mm].


    % Interpolation 3
    t_new3 = linspace(E3(1,1),E3(end,1),2*size(E3,1)-1);
    thickness_new3 = interp1(E3(:,1), E3(:,2), t_new3);
    E4(:,1) = t_new3';                                  % Time. [min].
    E4(:,2) = thickness_new3';                          % Thickness. [mm].



  % Find closest value and create new matrix.
    B1 = zeros (size(E4,1),2);    % New simulation matrix. [s mm].
    Btmp = zeros (size(B,1),1);   % Temporary matrix.


    for j = 1:size(E4,1)
        val = E4(j,1);             % Value to find
        Btmp = abs(B(:,1)-val);    % Temporaty matrix.
        [idx idx] = min(Btmp);     % Index of closest value.

        B1(j,1) = B(idx,1);        % Time. [s].
        B1(j,2) = B(idx,2);        % Thickness. [mm].
    end


    % R-squared
    yresid  = E4(:,2) - B1(:,2);
    SSresid = sum(yresid.^2);
    SStotal = (length(E4(:,2))-1) * var(E4(:,2));
    rsq = 1 - SSresid/SStotal;     % Coefficient of determination.
```

```
%% PLOTS
close all


    %PLOT 1
    %Swelling over time
figure(1)
axes('FontSize',24,'FontName','Calibri')
set(gcf,'Color',[1,1,1])
plot(thickness(:,1),thickness(:,2),'.','markersize',8,'Color',[0 0 0])
hold on
plot(data1(:,1),data1(:,2),'.','markersize',8,'Color',[0 0 0])
% title('THICKNESS OVER TIME','FontWeight','bold','FontSize',20,'FontName','Calibri',...
%     'FontAngle','normal')
xlabel('Time (min)','FontWeight','bold','FontSize',24,'FontName','Calibri',...
    'FontAngle','normal')
ylabel('Thickness (mm)','FontWeight','bold','FontSize',24,'FontName','Calibri',...
    'FontAngle','normal')
% ylim([0 0.5])
% xlim([0 35])
% h=legend('Model prediction','Experimental data', 'Location', 'NorthEast');
%     set(h,'FontSize',22,'FontName','Calibri','FontAngle','normal')
hold on


    %PLOT 2
    %Total mass over time
total_mass(:,1)=total_mass(:,1)/60;      % Time into minutes.

figure(2)
axes('FontSize',24,'FontName','Calibri')
set(gcf,'Color',[1,1,1])
plot(total_mass(:,1),total_mass(:,2),'.','markersize',10,'Color',[0 0 0])
hold on
% plot(Aexpdata1(:,1),Aexpdata1(:,2),'.r','markersize',8)
% hold on
%xlim([0 10000])
%ylim([0 1])
% title('TOTAL MASS OVER TIME','FontWeight','bold','FontSize',20,'FontName','Calibri',...
%     'FontAngle','normal')
xlabel('Time (min)','FontWeight','bold','FontSize',20,'FontName','Calibri',...
    'FontAngle','normal')
ylabel('Total mass (g)','FontWeight','bold','FontSize',20,'FontName','Calibri',...
    'FontAngle','normal')
% ylim([0 0.8])
% h=legend('Model prediction','Experimental data', 'Northeast');
%     set(h,'FontSize',22,'FontName','Calibri','FontAngle','normal')
hold on


    %PLOT 3
    %Egg yolk remaining over time
eggyolk_remaining(:,1) = eggyolk_remaining(:,1)/60;     % Time into minutes.

figure(3)
axes('FontSize',24,'FontName','Calibri')
set(gcf,'Color',[1,1,1])
plot(eggyolk_remaining(:,1),eggyolk_remaining(:,2),'.','markersize',10,'Color',[0 0 0])
hold on
% plot(Aexpdata1(:,1),Aexpdata1(:,2),'.r','markersize',8)
% hold on
%xlim([0 10000])
%ylim([0 1])
% title('EGG YOLK REMAINING OVER TIME','FontWeight','bold','FontSize',20,'FontName','Calibri',...
%     'FontAngle','normal')
xlabel('Time (min)','FontWeight','bold','FontSize',20,'FontName','Calibri',...
    'FontAngle','normal')
ylabel('Egg Yolk remaining (g)','FontWeight','bold','FontSize',20,'FontName','Calibri',...
    'FontAngle','normal')
% ylim([0 0.8])
% h=legend('Model prediction','Experimental data', 'Northeast');
%     set(h,'FontSize',22,'FontName','Calibri','FontAngle','normal')
hold on


    %PLOT 4
    %Cleaning percentage
cleaning_percentage(:,1) = cleaning_percentage(:,1)/60;     % Time into minutes.

figure(4)
axes('FontSize',24,'FontName','Calibri')
set(gcf,'Color',[1,1,1])
plot(cleaning_percentage(:,1),cleaning_percentage(:,2),'.','markersize',10,'Color',[0 0 0])
hold on
% plot(Aexpdata1(:,1),Aexpdata1(:,2),'.r','markersize',8)
% hold on
%xlim([0 10000])
```

```
%ylim([0 1])
% title('CLEANING PERCENTAGE','FontWeight','bold','FontSize',20,'FontName','Calibri',...
%     'FontAngle','normal')
xlabel('Time (min)','FontWeight','bold','FontSize',20,'FontName','Calibri',...
    'FontAngle','normal')
ylabel('Cleaning percentage (%)','FontWeight','bold','FontSize',20,'FontName','Calibri',...
    'FontAngle','normal')
% ylim([0 0.8])
% h=legend('Model prediction','Experimental data', 'Northeast');
%     set(h,'FontSize',22,'FontName','Calibri','FontAngle','normal')
hold on



    %PLOT 5
    %Saturation over time.
state_matrix(:,1) = state_matrix(:,1)/60;      %Time into minutes.

figure(6)
axes('FontSize',24,'FontName','Calibri')
set(gcf,'Color',[1,1,1])
plot(state_matrix(:,1),state_matrix(:,2),'.','markersize',10,'Color',[0 0 0])
hold on
% xlim([0 6000])
%ylim([0 1])
%set(gca,'XDir','reverse');
% title('%SATURATION OVER TIME','FontWeight','bold','FontSize',20,'FontName','Calibri',...
%     'FontAngle','normal')
xlabel('Time (min)','FontWeight','bold','FontSize',20,'FontName','Calibri',...
    'FontAngle','normal')
ylabel('% Sample saturation','FontWeight','bold','FontSize',20,'FontName','Calibri',...
    'FontAngle','normal')
hold on


%% CLEAN OUTPUT

clearvars -except data1 time chi rsq cleaning_percentage eggyolk_mass eggyolk_remaining h0 ke kss
lambda_s m_s moisture_content nz nz1 omega removal state_matrix thickness total_mass z_s

display ('SIMULATION FINISHED')
time
```

A.5. Appendix

This appendix focuses on the description of a procedure to evaluate cleaning via Black and White (B&W) imaging. The method is suitable for soils showing adhesive failure when cleaned, that is, the detachment of soil patches of different sizes from the substrate. This behaviour is typically seen, for example, in tomato paste soils (carbohydrate based).

To set-up an experiment, the operator must ensure enough contrast between the substrate and the soil used (i.e. red soil vs. transparent/white substrate). Images of the soil sample analysed must be taken at different times, at the most uniform lighting conditions possible and at a fixed distance. For its use in ADWs it is possible to take pictures while the wash cycle is running, as done for the colour change IA shown in *Chapter 7, section 7.2* or outside the appliance. The latest set-up offers less noise as the camera is not located in a water environment but requires the interruption of the cleaning sequence for pictures to be taken. The placement of a camera inside the ADW allows collecting more data but the quality of the images is not as good.

Figure A5.1 shows the images taken from a test run to illustrate the technique presented. 40g of ketchup were sprayed across the surface of a circular and transparent Perspex substrate. Samples were dried for 24h in an oven at 60ºC before placing them into a Miele G1222 SC ADW at the left side of the bottom basket. A 'Quick Wash' programme was set and pictures were taken outside the ADW at intervals of 1 minute for the first 10 minutes of the wash cycle. Colour images were transformed into B&W images by using the Matlab routine included at the end of the appendix. To calculate the removal achieved at any time, a comparison between the initial number of black pixels, (representing the area covered by the soil at time 0) and the number of pixels at time 't' (representing the area covered by the soil at time 't') is necessary. Following Eq.1 it is possible to estimate the SRI at any time.

$$SRI\ (\%) = \left(1 - \frac{Black\ Pixels_{\ t=t}}{Black\ Pixels_{\ t=0}}\right) \cdot 100 \qquad (1)$$

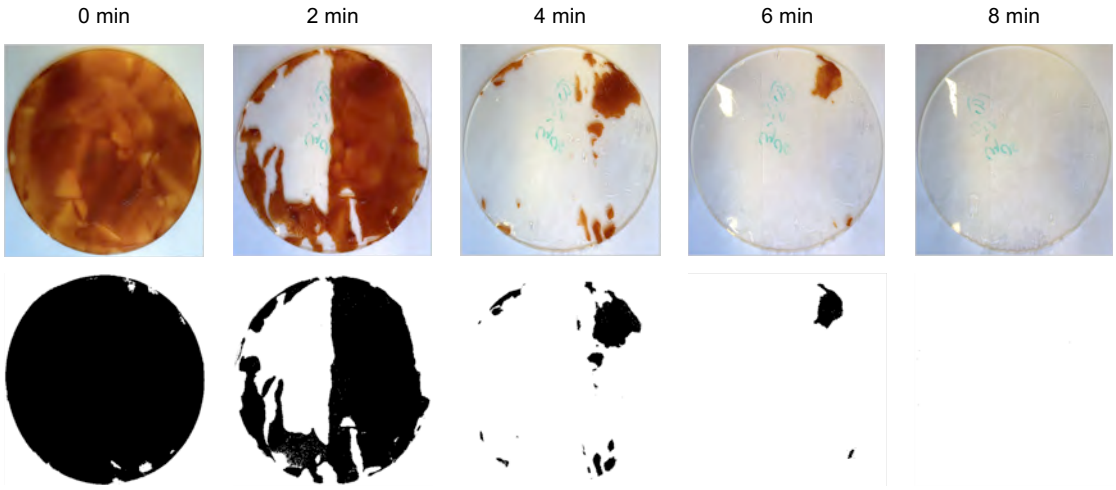

Figure A5.1. Example of the cleaning pattern shown by a tomato ketchup deposit over a Perspex substrate and the transformation of the pictures to B&W images.

In **Figure A5.2** SRI values calculated from the example shown below are plotted.

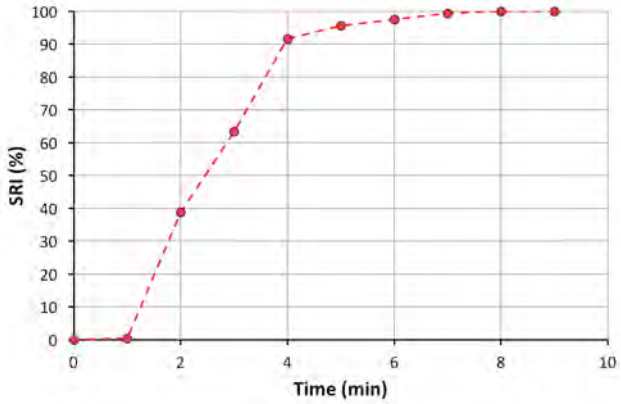

Figure A5.2. Cleaning profile over time for the example previously shown.

As observed, the technique offers a simple and straightforward system of measuring cleaning of soils that show an adhesive failure.

MATLAB routine

```
%% Script to analyse cleaning via B&W images
       % Pictures should be preloaded to MATLAB workspace
       % Note: Pictures should be numbered consecutively (i.e. NAME_01; NAME_02;
       NAME_03...)

clc
close all


%% 1.- Load images & create cropped area.
n = input ('Introduce number of images: ');


    % Load first image & crop.
tic
k=1;
jpgFilename = strcat('NAME_', num2str(k),'.JPG');
A = imread(jpgFilename);

[I2 RECT] = imcrop(A);
close all

imageData = zeros(size(I2,1),size(I2,2),size(I2,3),n,'uint8');  %Pre-allocation.
imageData(:,:,:,1) = I2;

toc

 % Load all images & crop.
tic
if n > 1
   for k = 2:n
   jpgFilename = strcat('NAME_', num2str(k),'.JPG');
   C           = imread(jpgFilename);
   [D]         = imcrop(C,RECT);
   imageData (:,:,:,k) = D;
   end
end
toc

%% 2.- Convert RGB to B&W and Calculate cleaning percentage

threshold = graythresh(A);
C = im2bw(A,threshold);                     C --> Black % White image
figure, imshow(C)

D = imresize(C, [1800 1800]);               E --> Resized image

b = find(D==0);
total = size(b);
total = total(1,1);


i=1;
k=1;
for k = 1:n
    F = imageData(:,:,:,k);

       G = im2bw(F);
       H = imresize(G, [1800 1800]);
       c = find(H==0);
       total1 = size(c);
       total1 = total1(1,1);

       cleaning(i) = ((total-total1)/total)*100;   % SRI results

       i=i+1;
end

disp('DONT FORGET TO SAVE THE RESULTS')
```